Coupled thermomechanical fluid-structure interaction in the secondary air system of aircraft engines

Yannick Muller

ED 072 – UNIV LILLE NORD DE FRANCE
ÉCOLE DOCTORALE REGIONALE SCIENCES POUR L'INGENIEUR

THESE

présentée en vue de l'obtention du titre de

DOCTEUR

de l'**UNIVERSITE DE VALENCIENNES ET DU HAINAUT CAMBRESIS**

Spécialité : **Mécanique et Énergétique**

par

YANNICK MULLER

Ingénieur ENSICA

COUPLED THERMO-MECHANICAL FLUID-STRUCTURE INTERACTION IN THE SECONDARY AIR SYSTEM OF AIRCRAFT ENGINES

CONTRIBUTION TO AN INTEGRATED DESIGN METHOD

Interaction fluide-structure par couplage thermo-mécanique dans le système d'air secondaire de turbo-réacteurs Contribution à une méthode de conception intégrée

soutenance prévue le 30 septembre 2009

devant la Commission d'examen

Prof. G. Descombes	Conservatoire National de Arts et Métiers de Paris	Rapporteur
Prof. F. Leboeuf	École Centrale de Lyon	Rapporteur
Prof. T. Arts	von Karman Institute of Fluid Dynamics, Belgique	Examinateur
Prof. B. Desmet	Université de Valenciennes	Examinateur
Dr. G. Dhondt	MTU Aero Engines, Munich	Examinateur
J. Kutz	MTU Aero Engines, Munich	Invité
f. F. Monnoyer	Université de Valenciennes	Directeur de thèse

Acknowledgement

The present project has been carried out from November 2005 to September 2008 in the department "Air and Oil system" of MTU Aero engines GmbH (MTU Aero engines GmbH Dachauer Str. 665 80995 Munich Germany) and under the tutelage of Valenciennes University (Laboratoire de Mécanique et Energétique de l'Université de Valenciennes - Le Mont Houy F-59313 Valenciennes CEDEX 9). The financial aspects of this research project have been entirely covered by MTU Aero Engines GmbH whom I thank for authorising to proceed with this thesis.

My first thoughts go naturally to Dr. H. P. Hackenberg and A. Kammerer who initiated this project. I hereby sincerely thank them for having placed their confidence in me to carry out this study. I also thank Pr. Desmet, former head of the L.M.E. Valenciennes.

I would like to thank Dr. J. Kutz (MTU Aero Engines GmbH) for sharing his precious insights on the secondary air system, his knowledge on the physical description of the different flow elements implemented, as well as his explanations on the current air system tool used at MTU Aero Engines. I also thank him especially for the many suggestions regarding the present report.

I thank Dr. G. Dhondt (MTU Aero Engines GmbH) for his support concerning all the mathematical and programming aspects of the thesis. Dr. Dhondt is the creator of the Finite Element Software CalculiX. I count myself privileged to have met him and worked with him on a daily basis.

I express my sincere gratitude to Dr. E. Reile and F. Cottier (MTU Aero Engines GmbH) for their help with the SAS-thermomechanical coupled computation and CFD applications.

I thank Pr. F. Monnoyer de Galland (L.M.E Valenciennes University) for his help, advice and critical role played in the composition as well as in the examination of the present report.

I thank all the people of the Air and Oil System and Heat transfer analysis department.

Last but not least, all my love goes to Hélène, who supported me at all time, through all difficulties, and gave me the necessary drive to thrive and continuously improve myself.

Coupled thermomechanical fluid-structure interaction in the secondary air system of aircraft engines: contribution to an integrated design method.

Yannick Muller

This document was created using $LaTeX2\varepsilon$

Presented at:

2^{nd} **GACM Colloquium on Computational Mechanics.**, October 10-12, 2007 Munich

ASME Turbo Expo 2008 Gas Turbine Technical Congress and Exposition., June 9-13, 2008 Berlin, Germany

ASME Turbo Expo 2009 Gas Turbine Technical Congress and Exposition., June 8-12, 2009 Orlando, FL, USA

Publications:

Secondary Air System Model for Integrated Thermomechanical Analysis of a Jet Engine.

Proceedings of ASME Turbo Expo 2008 ASME GT2008-50078

Integrated Fluid Network-Thermomechanical Approach for the Coupled Investigation of a Jet Engine.

Proceedings of ASME Turbo Expo 2009 ASME GT2009-59104

Objectives

In jet engines, the secondary air system or SAS takes care of a variety of important functions such as high pressure turbine blade cooling, turbine disc cavity sealing against hot gas ingress and bearing chamber sealing. Moreover secondary air streams also control metal temperatures and thus the thermal expansion of the engine parts, especially gaps and seal clearances.

In order to check the fulfilment of these functions in the design phase of an engine, gas temperatures, pressures and mass flow rates must be accurately calculated. Up to now, aerodynamic calculations leading to mass flow rates, flow pressures and temperatures, thermal calculations yielding material temperatures and structural analysis computations yielding material deformations are performed separately. In practice, however, a lot of interactions exists, which are currently not considered and would require a lot of time consuming iterations. Indeed, a change in material temperature leads to a modification of the expansion of the interacting parts yielding significant changes in the geometry of the gaps between them. Since the gap width drives the pressure loss, interaction between the aerodynamics, thermal and solid mechanics solutions is strong.

The purpose of the present investigation is to take the interactions into account in a robust analysis tool, combining secondary air system, thermal analysis and mechanical calculations. The challenge is to create an integrated program suite allowing to calculate these effects in steady state for the special purpose of design applications. The basic concept is a network consisting of nodes representing the chambers and connected by elements which can be interpreted as pressure loss devices. The network is to be linked to a thermomechanical finite element model of the engine within the free software finite element software CalculiX [13]. This can be done in the form of a dedicated module in which gas pressures, temperatures and mass flow rates are calculated. For coupled thermomechanical secondary air system applications the process is iterative: secondary air variables are computed based on the structural temperatures and deformations of the previous iteration and serve as boundary conditions to the thermomechanical problem for the next

iteration.

The work is divided into the following subtasks:

- based on given structural temperatures and deformations and appropriate inlet conditions, determine the stationary gas temperature, pressure and mass flow rates using the principle of conservation of mass, conservation of momentum and conservation of energy. In general this will result in a system of nonlinear equations to be solved by appropriate liberalization. This includes the treatment of compressible flow and the possibility of sonic speed conditions in part of the network. All pressure loss devices relevant to an aircraft engine such as different seal types, pipes, orifices and nozzles shall be treated.

- using an updated topological network representation, a method to obtain one unique model starting from both the air system and the thermomechanical model shall be developed. A way to force the different analysis modules to communicate internally and without human intervention must be implemented for a smooth and efficient computational process.

- coupled computations using CalculiX shall be performed for realistic engine parts and conditions and compared to results obtained using the traditional process with the aim of highlighting the interactions between the different disciplines.

5

Contents

Nomenclature

Latin symbols

A	m^2	surface/cross section
c_p	$\frac{J}{kgK}$	specific heat capacity at constant pressure
C_t	$\frac{m}{s}$	tangential velocity
c_v	$\frac{J}{kgK}$	specific heat capacity at constant volume
D, d	m	diameter
f	N	vector of field forces
h	$\frac{J}{kg}$	specific enthalpy
h^θ	$\frac{W}{kg}$	heat generation per unit of mass
h_c	$\frac{W}{m^2K}$	heat transfer coefficient
l	m	pipe length
M	$-$	Mach number
$\dot{m}$	$\frac{kg}{s}$	mass flow rate
p	Pa	pressure
$\dot{Q}$	$\frac{W}{m^2}$	heat flux
R_u	$\frac{J}{molK}$	universal gas constant
R	$\frac{J}{kgK}$	specific ideal gas constant
r	m	radius
Re	$-$	Reynolds number
s	m	labyrinth seal gap
T	K	temperature
v	$\frac{m}{s}$	velocity
V	m^3	volume

Greek symbols

δ_{ij}	$-$	Kronecker symbol
η	$\frac{kg}{ms}$	dynamic viscosity
κ	$-$	isentropic exponent
λ	$-$	friction coefficient
λ_c	$\frac{W}{m^2 K}$	thermal conductivity
ν	$\frac{m^2}{s}$	kinematic viscosity
ρ	$\frac{kg}{m^3}$	density
ζ	$-$	pressure loss coefficient
σ	$\frac{N}{m^2}$	stress tensor

Subscripts

abs	absolute
crit	critical
ctrl	control (for surface and volume)
eff	effective (for cross section)
flow	relative to the flow
ideal	ideal value
in	inlet, incoming flow
out	outlet, outgoing flow
$,i = \frac{\partial}{\partial x_i}$	partial derivative with regards to coordinate x_i
rel	relative
s	static
t	total

Abbreviates

CFD	Computational Fluid Dynamics
COF	Carry Over Factor
IP	Intermediate Pressure
LP	Low Pressure
HP	High Pressure

OEM	Original Engine Manufacturer
SFC	Specific Fuel Consumption
SAS	Secondary Air System
TET	Turbine Entry Temperature

Einstein summation convention.

In mathematics, especially in applications of linear algebra to physics, the **Einstein notation** or **Einstein summation convention** is a notational convention useful when dealing with coordinate formulas. It was introduced by Albert Einstein in 1916.

When specified, all indices appearing by pairs are representing a sum over all spatial dimensions:

$$\begin{aligned} y &= C_1 x_1 + C_2 x_2 + C_3 x_3 + ... + C_n x_n \\ &= \sum_i^n C_i x_i \\ &= C_i x_i \end{aligned}$$

Whenever explicitely stated, Einstein summation convention is used throught this document.

Background and state of the art

During the last fifty years, the exchange of people and goods have steadily increased due to the creation of new free trade spaces or trade agreements (Economic European Community 1957 and successive enlargements, Association of South East Asian Nations 1967, North American Free Trade Area 1994), the emergence of new markets in Asia (China and India), as well as the increase of salaries and leisure time. One of the success stories of transport in the 20^{th} century and continuing today is the explosion of public commercial air transportation all over the world. As presented in Fig.1 over the last 40 years, traffic growth (revenue passenger km) has suffered from only three stagnation phases: the first Gulf War and the rise of oil prices in 1991, the aftermath of the terrorist attacks of September 2001, and more recently the second Gulf war and the emergence of cases of Severe Acute Respiratory Syndrome in south east Asia in 2003.

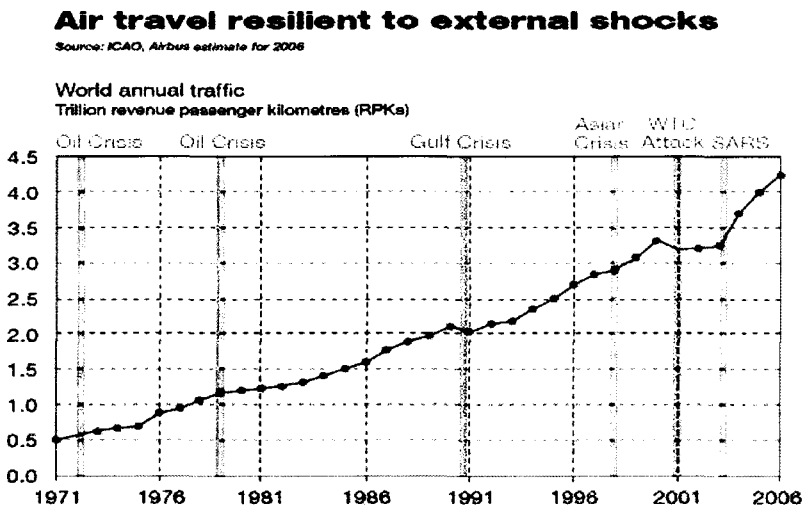

Figure 1: Evolution of air travel for the period 1971-2006.

The average growth over the period 1990-2005 is set at 5.2% per year. Future market estimations envision a yearly 5% progression for passenger traffic and even more for freight transportation in the years to come, despite tensions in the Middle East, talks of fuel shortage and oil prices rising. This implies an increase in the number of aircrafts in operation or/and an increase in aircraft movements. In turn this phenomenon

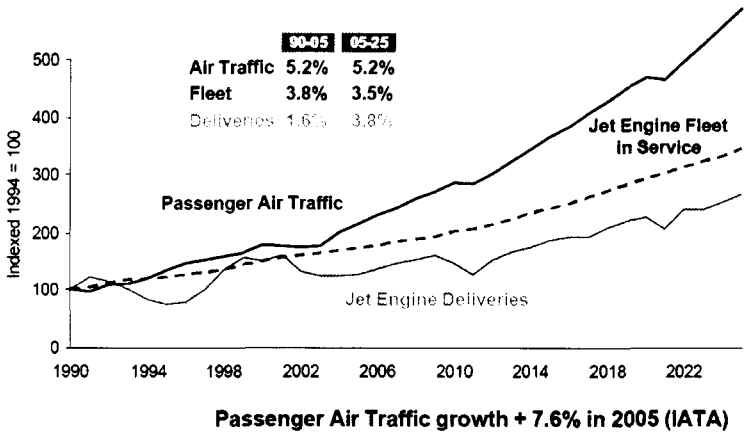

Figure 2: Estimated traffic growth in terms of passenger, aircrafts and engines.

is responsible for increased engine deliveries and/or an accentuation of maintenance repair and overhaul operations (see in Fig.2). Such predictions underline the growing importance of improving cost efficiency, performance, environmental friendliness as well as air transport reliability and safety.

In order to meet the challenges and needs of the air traffic market, advanced aero engines and the related technology have to be developed.

Although the Kyoto Protocol of 1997, committing members to cutting greenhouse gas emission by 12.5% of the 1990 levels by 2012, excluded international aviation, concerns about the influence of global aviation on climate change and global warming have nonetheless been voiced. Under the pressure of environmental lobbies/ governments and driven by customer demands for cost efficiency, aero engines manufacturers must continuously reduce fuel consumption as well as pollutant emissions, even though the proportion of air transport fuel consumption and pollutant emissions is small compared to other transportation systems (8% of total fuel consumption and 3,2% of total NOx pollution).

Air traffic emissions (water vapours, carbon dioxide and monoxide, nitrogen oxides) delivered at very high altitude are suspected of having a large impact on the global warming effect. In Europe, by 2010, the targets to be met by aero engine manufacturers in terms of fuel consumption and pollutant emissions are already challenging and even more restrictive for the decade to come.

- **-10%** SFC_{2000} for 2010 and **-50%** SFC_{2000} for 2020
- **-33%** NOx_{2000} for 2010 and **-80%** NOx_{2000} for 2020

Noise is also an important factor to be reckoned with. Both airport facility development (new facilities, traffic increase) and urban growth are responsible for higher population densities in the immediate vicinity of airports. Noise levels between 90db and 100db (take-off) are both psychologically and physically dam-

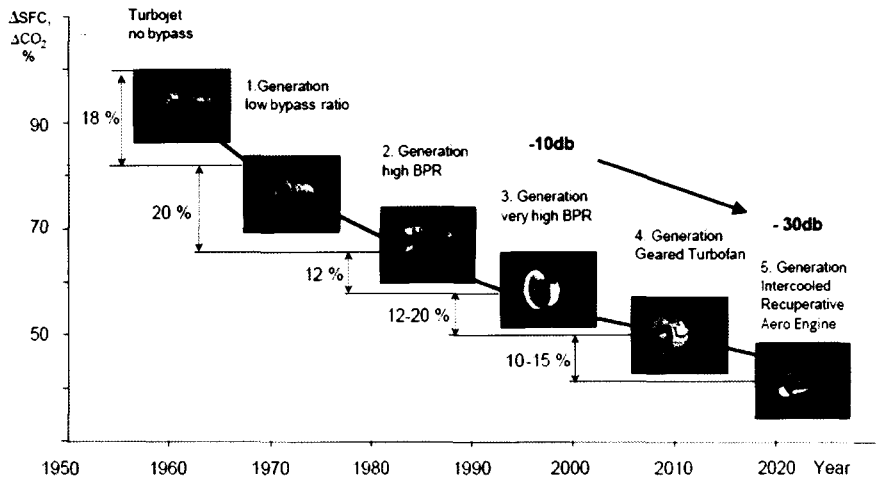

Figure 3: Evolution of engine characteristics. Adapted from [4]

aging to exposed populations. To tackle this growing public health problem, public transport organisations have issued ever more drastic rules over the years, e.g. noisy aircrafts are charged with more airport fees. Therefore, airline demands for quieter aircrafts drive engine manufacturers to reduce engine noise levels. Considerable improvements have been achieved in terms of SFC reduction, noise levels and pollution over the past sixty years (see Fig.3) but much remains to be done to achieve the objectives set for the next decade. Last but not least, the late liberalisation of the airline market and the multiplication of low-cost airlines led to a tremendous growth of air traffic. This plays a serious role on the saturation of airport facilities and the overloading of air traffic control. To overcome this problem, two solutions are therefore envisioned:

- increasing the number of airports and/or developing already existing airport facilities, which is problematic in densely populated areas like most industrialised countries.
- building larger aircrafts to accommodate more passengers, which need more powerful engines complying with all the aforementioned political, economical and environmental constraints.

For engine manufacturers, the need to come up with ever more efficient engines with regard to customers requirements is obvious. One result is a drive towards reducing design and life cycle cost. To achieve these objectives, new design methods must be developed to come up with new concepts ensuring both reliability and efficiency of the improved solution.

At MTU Aero engines GmbH Munich, new simulation tools are under development, aiming at ever more accuracy in future engine design. In the frame of this development policy, the present research project deals with a specific engine subsystem: the Secondary Air System or SAS.

In jet engines, the secondary air system takes care of a variety of vital functions such as cooling the blades in the high pressure turbine, preventing hot gas ingestion into turbine disc cavities or sealing the bearing

chambers. Secondary air streams also control material temperatures and consequently thermal expansion and gaps/seal clearances.

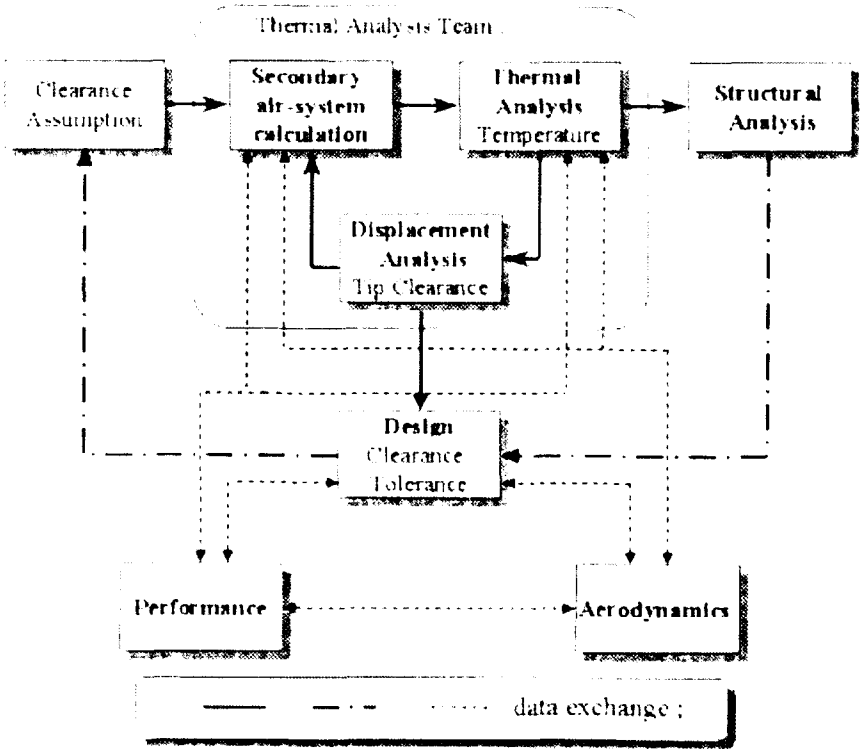

Figure 4: The Secondary Air System Analysis in the design process. [46]

Designing an engine is a very complex task. The global engine design process widely used by most of the engine manufacturers is presented in Fig.4. In order to simplify the design effort and make it more efficient, the process is subdivided into fields of competence each dealing with a special aspect of the engine as is pictured in Fig.4. There are 5 such fields of competence, namely

- performance defining engine requirements in terms of overall efficiency
- aerodynamics analysing the flow in the engine main flow path and designing the main flow path in order to meet performance definition
- secondary air system design fluid analysis
- thermal analysis aiming at obtaining the temperature repartition on the structure and in the secondary air system
- structural analysis predicting stresses and displacements under mechanical and thermal loads

As pictured in Fig.4, performance definition and a specified configuration of the flow path specify the requirements of the secondary air system in terms of air consumption. To achieve the specified consumption

target which is controlled by the clearances and tolerances in the air system, the SAS analysis is embedded in a chain of analyses including thermal and mechanical analysis.

The current procedure at MTU to perform a secondary air system analysis is based on a sequential iterative process. As the first analysis in the chain, using input from performance, design and aerodynamics departments, secondary air system calculations aim at determining mass-flow rates, flow pressures and temperatures. These results are used as an input for the thermal model yielding the material temperature distribution. In turn the material temperature repartition is used as an additional constraint for the structural calculation, yielding material deformations which are subsequently used to update the geometrical definition of the flow model. This constitutes an iterative process to be repeated until all the specifications are met.

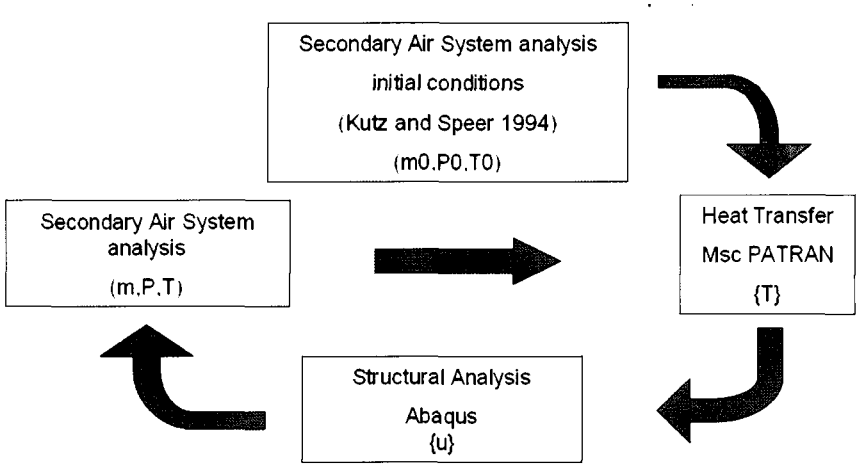

Figure 5: Current SAS-thermal-mechanical analysis process.

The current process may be improved. As shown in Fig.5, it requires one model for secondary air flow, one thermal model and one mechanical model. For each model a dedicated software is used: the Kutz and Speer flow network solver [26] for the SAS, QTRAN for the thermal calculations and Abaqus for structural deformations. Results are transferred from one model to the next one either by hand or using dedicated interfacing tools. According to Roychoudhary and al. [47], this explains why design completion is usually based on a maximum of two iterations. The existing interactions occurring between flow and structure are thus disregarded leading to very expensive and time consuming redesign efforts in case of discrepancies during model/data matching.

Observations and tests have shown that thermomechanical coupling effects occurring in the secondary air system can be strong and have therefore a significant impact on the design solution. The temperature gradients in the structure induce thermal stresses and, in conjunction to mechanical loads, deformations modify gap and clearance shapes and sizes. Since gap definition has an important influence on pressure losses and subsequently on mass-flow rates, it is expected that the interaction between the aerodynamic thermal and

solid mechanics solution of the problem is important. The study by Roychoudhary [47] performed on a low pressure turbine sealing arrangement confirms this fact. It shows the importance of coupling effects on the SAS in operating conditions and confirms the need to include them in the design process. Consequently, the classical sequential procedure has to be replaced by an iterative procedure requiring seamless data transfer at the interfaces between the modules.

The purpose of the present investigation is to create a robust analysis tool, coupling fluid, thermal analysis and mechanical deformation in the secondary air system to take this interaction into account.

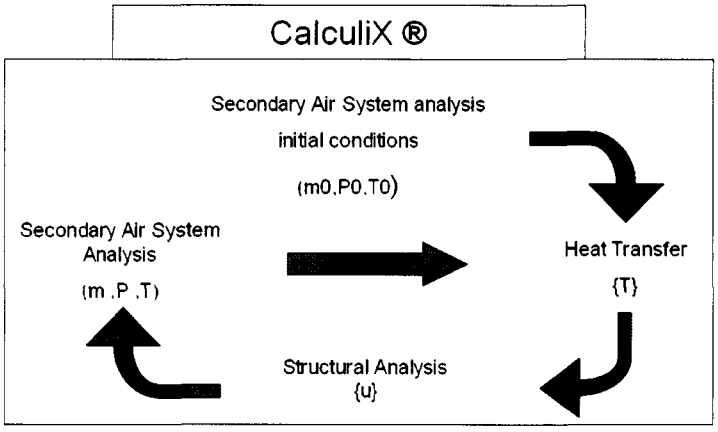

Figure 6: Envisioned SAS-thermal-mechanical analysis process.

One strategy is to gather the different analyses in one unique mainframe as presented in Fig.6. This leads to simplified communication between the different types of analysis performed on the system, as well as enables to overcome the difficulties described by Roychoudhary and al. [47]. SAS, thermal and structural capabilities are implemented in a modular form into a common frame. The free finite element software CalculiX has been chosen to play this role. CalculiX already features structural and thermal analysis. A secondary air system analysis module as well as the communication between this module and the two others remain to be created.

To simulate and analyse the secondary air system flow, the basic concept is to use a fluid network. It is thereafter directly integrated into a thermomechanical finite element model of the engine to form one unique SAS-thermal-mechanical model used to perform coupled computations.

The present thesis report structure is the following:

- The literature review shows the state of the research on SAS. A first section highlights the SAS functions and implications with regard to engine performances, providing a close insight on this particular engine subsystem. The second part presents and justifies the way to model and perform an analysis of this system. It introduces the concept of 1D flow networks and details the solution methods.

- The second chapter of the thesis deals with the implementation of the method. It focuses on the development of the constitutive equations and details the implementation of the solution algorithm and the different elements. The last section shows the validation aspects of the software.

- The third chapter deals with the coupling of the network and thermomechanical analysis tool. The way the coupling between flow and structure properties is performed is presented. Modifications necessary to accommodate the requirements of the coupled process are explained and justified. Examples of calculations are presented to illustrate the improvements brought by the new tool. The examples illustrate the coupling between SAS-heat transfer and structural analysis on increasingly complex models and details the contribution of each discipline to the coupled effects.

Chapter 1

Literature review

1.1 Introduction

Engine design and manufacturing is a domain where research and development costs are steadily increasing. Therefore, technological research projects are either placed under the aegis of institutional investors (Advisory Council for Aeronautics Research in Europe), or carried out under joint ventures enabling the different partners to share both risks/costs during the development phase as well as the technological fallouts.

Multiple EU funded projects in the specific field of aero engine design focus on improving engine overall efficiency and SFC, reducing noise and pollutant emissions. A review of all current European research projects has been performed by Coutrot [8] and gives an insight of the different industrial/academic partnerships involved as well as the technological aspects investigated. Concerning specifically the secondary air systems ICAS-GT (Internal Cooling Air Systems for Gas Turbines) [50], ICAS-GT2 and MAGPI focus on turbine rim seals, rotating cavities, compressor stator wells, turbine pre-swirl and compressor drive cones. The studies provide a better understanding of specific topics by means of Computational Fluid Dynamic (CFD) simulations and subsequent testing on rigs.

Studies have been carried out in the field of secondary air system coupled analysis, taking into account fluid-solid or fluid-solid-heat transfer interaction. Verdicchio [57], Chunhua [7],Chmielniak [6], Errera [17] or Heselhaus [20] have investigated the reciprocating effects of fluid properties on material temperature and deformation in the secondary air system.

Roychoudhary and Jlidi [47], showed that current methods and ways used to compute coupled SAS thermomechanical problems could be greatly improved, bringing a higher degree of prediction accuracy. A dedicated tool, tackling the complex multi-physics problem, would lead to more realistic and accurate simulations.

The first part of this literature review presents the jet engine secondary air system (SAS) as it is understood

in the aero engine and gas turbine field of application.

The second part, dedicated to the theoretical aspects related to the SAS, presents the way the secondary air system is modeled. The major methods used to solve the SAS/network problems are described.

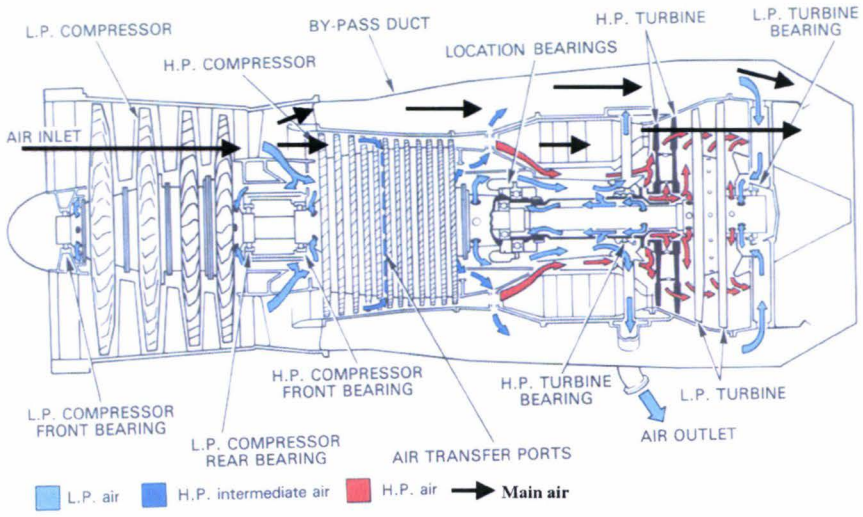

Figure 1.1: General overview of the main air system and secondary air flow pattern of a jet engine. [10]

1.2 Basics of aero engine Secondary Air System

1.2.1 Presentation of the air system

In an aero engine, a distinction is made between primary or main air system and secondary air system. The primary air system, represented by black arrows on Fig.1.1, encompasses the flows governing the gas turbine cycle. This includes the flows going through the engine core comprised of the compressor, the combustion chamber and the turbine as well as the air going thought the bypass channel.

The amount of air diverted from the primary air system and which therefore does not contribute to either thrust or shaft power creation constitutes the secondary air system. Secondary flows, usually bled from the compressor, are used in almost all engine and aircraft components as illustrated in Fig.1.1. The light blue, blue and red arrows show at which engine stage the main air is diverted and its applications in the engine. Secondary flows are either recombined with the main flow at highest possible pressure level in the high pressure turbine, or released over board toward the rear of the engine where a small performance recovery can be achieved or used to supply the aircraft pneumatic system. The SAS is consequently further subdivided into internal air system and external air system.

The external air system provides for all the needs not directly related to engine operation. This comprises the air supply of the aircraft systems such as de-icing of the lifting surfaces, wing leading edges and engine pods, air conditioning of both pilot and passenger cabins, fuel tank pressurisation and accessory cooling. The amount of secondary air used for external purposes is labelled air outlet on Fig.1.1.

In contrast to that, the internal air system, thereafter called secondary air system, provides for a variety of tasks inside the engine. The purpose of the secondary air system is described in detail by Moore in [36],

Turner in [53] as well as in [10].

1.2.2 Functions of the Internal Air System

The main task of the secondary air system is to provide adequate cooling air for three different applications. For the high pressure turbine blades and vanes, placed directly after the combustion chamber in the main hot stream, temperatures may locally exceed the structurally acceptable temperature, triggering creep phenomena or even cause local burning of the alloy. This explains why HPT blades and vanes, location 1 on Fig.1.2 are internally cooled and protected from the hot stream by film cooling techniques. Combustion chamber casings are also cooled for the same reasons. Excessive temperature gradient on loaded parts is responsible for thermal fatigue. The cooling air system is therefore used to mitigate temperatures in the whole engine and to achieve an even temperature distribution thus improving material life expectancy by preventing high temperature gradients in the material. The level of temperatures encountered in the engine lead to geometrical modification of gap and clearance definition through thermal expansion. This phenomenon is sensitive when material displacements and clearances are about the same order of magnitude. Cooling air is used as an expansion regulator for instance for blade tip clearances in the fan and compressor as shown by item 3 on Fig.1.2.

Another task of the secondary air system is to insulate the hot gas path from the rest of the engine. The cooling air system provides for the sealing of cavities between rotating discs and walls in the engine turbine (item 1 and 2 on Fig.1.2) to prevent any hot air ingress which may reach as far as the engine shaft. This is done by ensuring a positive pressure difference between secondary air system and main air stream so that the leakage are always flowing towards the main flow path. The same technique is used for bearing chamber sealing shown in Fig.1.2 item 4. Thus oil is prevented from leaking inside the engine, contaminating the cooling air flow and potentially leading to oil coking or oil fire.

The last task of the secondary air system is to balance the gas loads at the bearing chambers. The compressor exerts an axial force in the forward direction and the turbine an axial force in the rearward direction. The shaft between compressor and turbine is therefore always under tension. The difference between these two loads constitutes the axial bearing load which must be kept within acceptable limits at high engine power and never fall below zero at low power. The internal air system must be designed to counterbalance the bearing load and may be used at several locations as shown by item 4 in Fig.1.2.

Flows in the secondary air system are regulated by metered orifices and by seals, most particularly labyrinth seals. The seals, through gap and clearance definition, drive the amount of air tapped from the main stream for the purposes of the secondary air system and therefore secondary air system consumption. It is then

crucial from a design point of view to accurately predict the seal behaviour during operation.

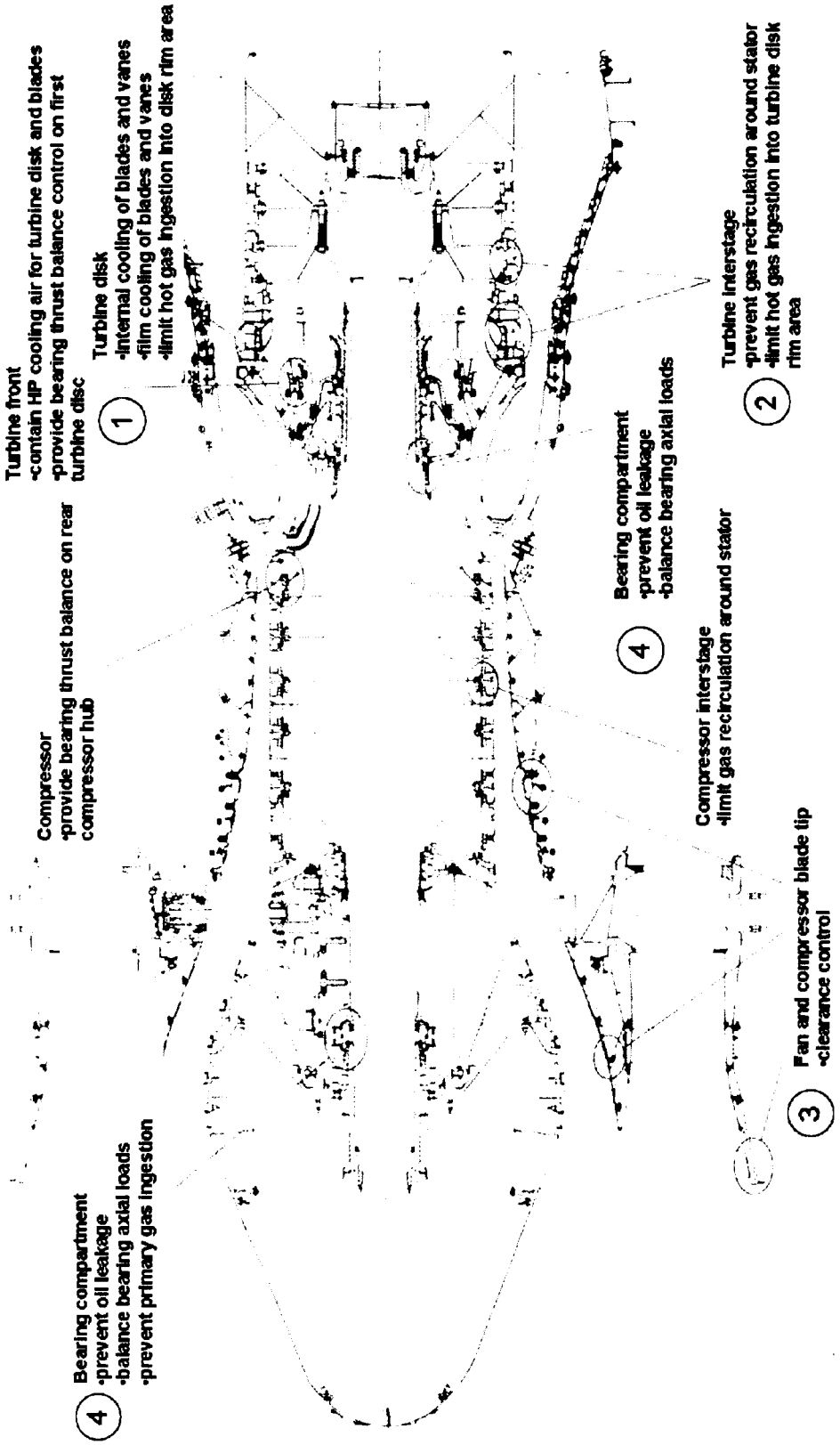

Figure 1.2: General arrangement of the PW-JT9D turbo fan engine showing various SAS functions. Adapted from [36]

1.2.3 Overall impact of the SAS on engine performance

Up to 30% of the main flow may be extracted from the compressor for secondary air system purposes. To minimise performance losses, the amount of work performed on the secondary air must be kept to a minimum. The best practice is to tap air from the low pressure compressor or intermediate pressure compressor.

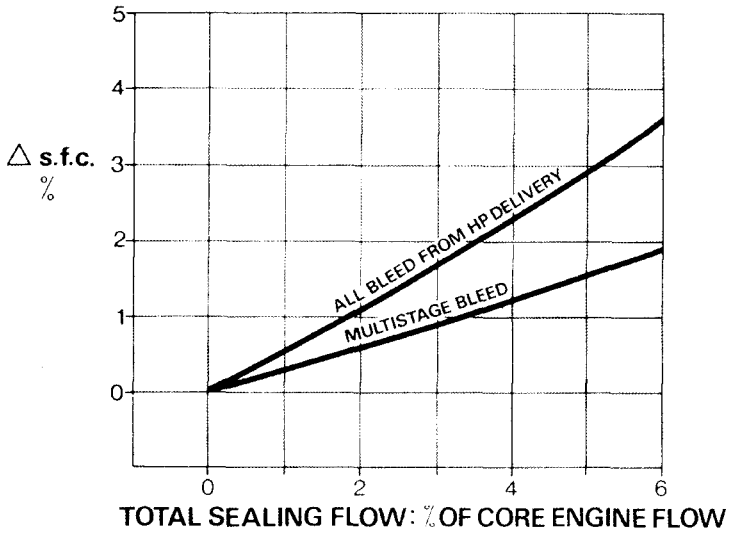

Figure 1.3: Influence of sealing flow and tapping location on Specific Fuel Consumption for a transport engine.

Fig.1.3 shows the impact of the amount of air used for sealing purposes on the overall engine specific fuel consumption. At equivalent amount of sealing flow, tapping the core main flow at several locations tends to mitigate the effects of secondary air on the SFC.

It is estimated that 1% coolant bleed in excess results in an SFC increase by 0.4% to 0.6%. According to Turner [53], a reduction of 1% SFC amounts to a reduction of about 0.5% in the direct engine operating costs.

As for sealing purposes, cooling applications also impact the aerodynamic cycle requirements. Fig.1.4 shows the variation of specific fuel consumption and specific thrust with the compressor pressure ratio and the bypass ratio at two given turbine entry temperatures for a subsonic aircraft. To increase engine performance, there are three main parameters to reckon with:

- compressor pressure ratio
- bypass ratio
- turbine entry temperature or TET

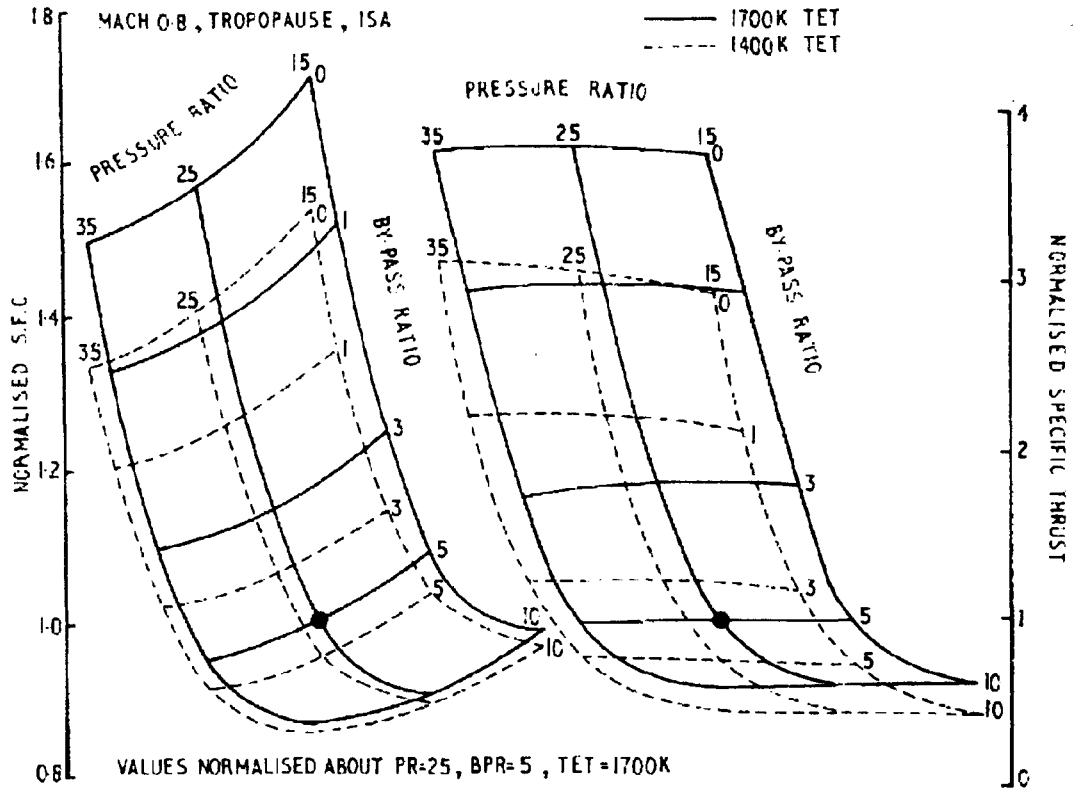

Figure 1.4: Influence of turbine entry temperature, bypass ratio and pressure ratio on SFC and specific thrust variations.[36].

Fig1.4 shows the advantages of using high values of compressor pressure ratio and bypass ratio to improve SFC and a high turbine entry temperature for specific thrust considerations. The current improvements to achieve better SFC and specific thrust values also have an impact on the cooling requirements.

Increasing the pressure ratio in the compressor also increases the cooling air temperature thus reducing its cooling potential. The increase in pressure also increases the heat flux the cooling fluid has to absorb.

For the engine manufacturer, the engine size is limited by the ground clearance. This distance is set by the aircraft manufacturer. At given aircraft design, increasing the bypass ratio necessary reduces the size of the gas generator. The manufacturing is therefore more complex due to smaller blades and vanes as well as a more compact cooling system. In addition to a greater value of the bypass ratio one gets an increase in the number of low pressure turbine stages which is responsible for a higher demand for cooling air. The reduction of the engine size is responsible for higher temperatures in the different engine parts. Since mechanical strains, deformations and tolerances do not reduce as scale does, downsizing is responsible for induced geometrical variations detrimental to the air sealing gaps and clearance control systems [36].

A higher turbine entry temperature requires stronger cooling of the elements located in the main hot stream [28]. This includes internal as well as external cooling on the surface of the blade and vanes which modifies

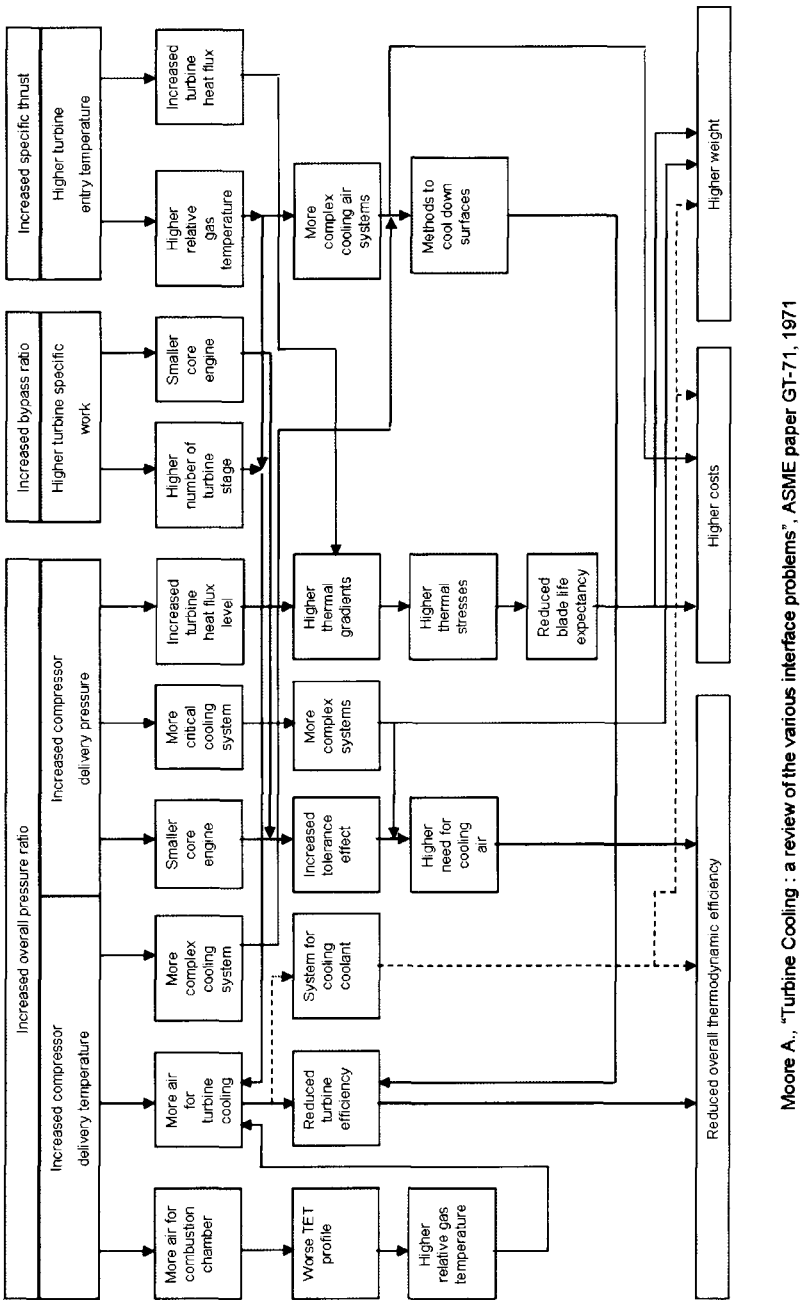

Figure 1.5: An overview of cooling requirements on engine thermodynamic parameters. [35]

their aerodynamic properties and affects the turbine efficiency. The improvement of the jet engine thermodynamic cycle is therefore difficult to achieve as it implies additional turbine cooling, using higher cooling air temperatures and an increase of smaller blades the cooling of which is more complex.

The intricate relationships between the thermodynamic parameters, the cooling requirements as well as their impact on the engine in terms of thermodynamic efficiency, cost and weight are summarised in Fig.1.5.

1.3 Modelling the secondary air system

1.3.1 General modelling

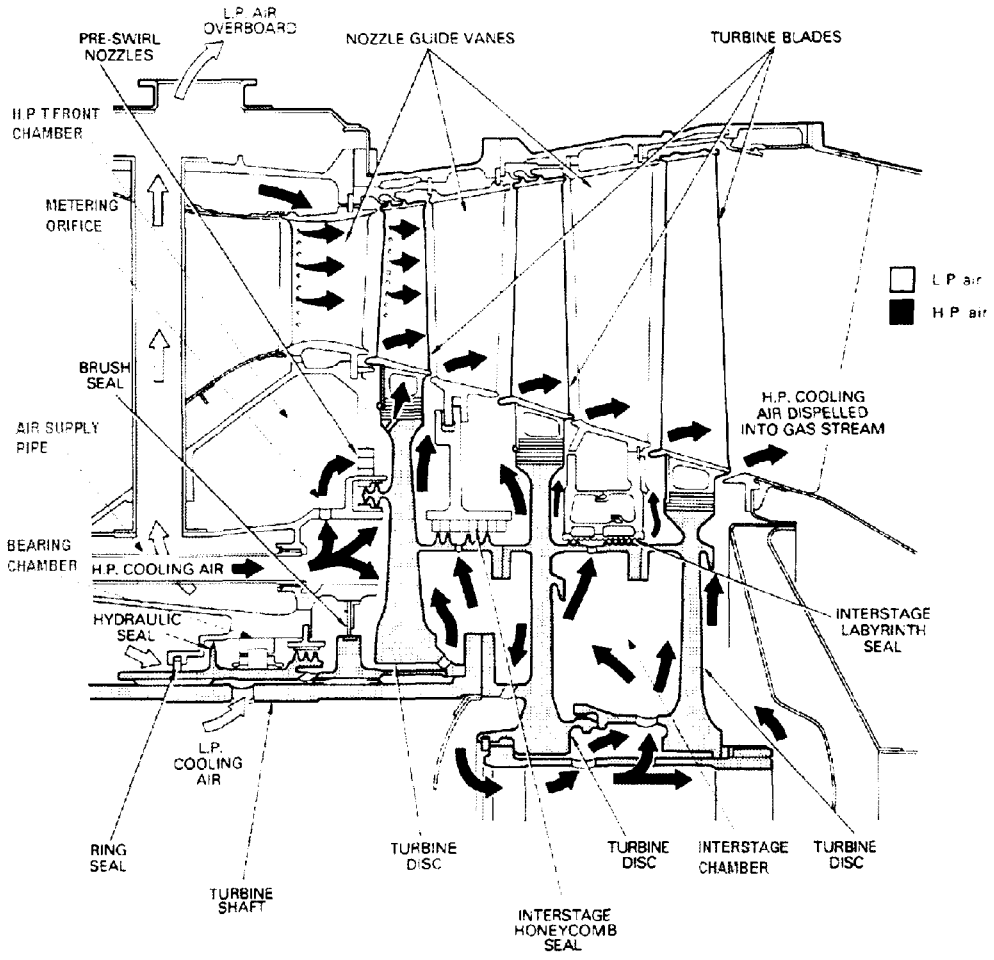

Figure 1.6: General arrangement of an aero engine turbine with SAS flows and relevant design elements.[10]

An engine secondary air system general arrangement of a High Pressure Turbine is shown in Fig.1.6. From the secondary air system perspective this high pressure turbine configuration is viewed as a succession of chambers linked by flow passages. Chambers are shown in Fig.1.6.They are typically locations where the structure encloses a volume of air such as the stator/disc cavities. By comparison, flow passages are defined whenever the space attributed to the fluid is small. The air flows, represented by fat arrows, going from one chamber to another must go through one or several flow passages.

At the crossing of a flow passage, the state of the fluid is modified from a given state at a specified initial location to a different state at another location. Flow passages such as orifices, pipes or seals are indicated in Fig.1.6. A flow passage is therefore best represented by an inlet and an outlet where the state of the fluid is defined and, in-between, a device the purpose of which is to provide the change of state. Such a

representation is given Fig.1.7.

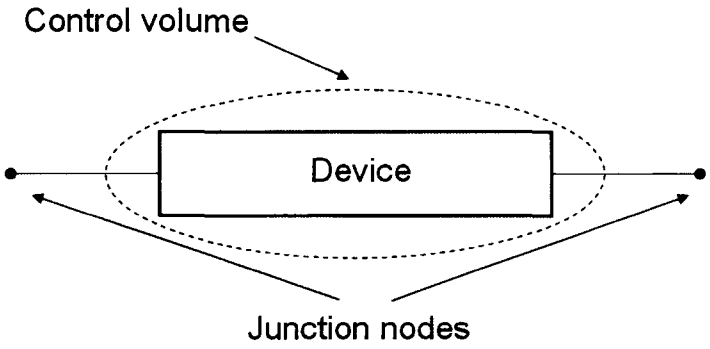

Figure 1.7: General model of a flow passage.

At an inlet and an outlet, the state of the fluid is completely defined by two independent state variables. The state variables mainly used to characterise the state of the fluid in the literature are **total pressure and total temperature in the static reference frame**. Though, unlike static pressure and temperature, both chosen variables depend on the reference frame, it enables to obtain directly the value of the total head loss. The device responsible for the change of state is characterised by a geometry and a quantity of matter going from inlet to outlet. The variable usually selected are **the through-flow area and the mass flow rate**.

A nodal representation is used for inlet and outlet. Inlets and outlets can be connected by several flow passages, they are subsequently indiscriminately called **junction nodes**.

Connecting flow passages at their junction nodes enables to create a one-dimensional network. The topology of the network is only dictated by the relation between the different flow passages and is therefore independent of the actual geometrical arrangement of the secondary air system. The secondary air system thus modelled is a succession of flow passages, comprised of junction nodes where the state of the fluid is defined and of devices through which the SAS air flows. The secondary air system network model of the previous low pressure turbine arrangement presented in Fig.1.6 is visualised in Fig.1.8 showing both junction nodes and devices.

A transformation from one state to an other one is characterised by at least a modification of one of the state variables. Historically speaking, the first networks were used in hydrostatics to model water distribution. The aim was to ensure sufficient water supply by predicting the pressure repartition between source and drain. The device responsible for the change of state between the junction nodes of a given flow passage is thereafter called **pressure loss device**, the flow passage is thereafter called **pressure loss element**.

The SAS network is therefore made up of interconnected circuits. The circuits are divided into smaller entities, pressure loss elements, related to an elementary function. Each pressure loss element is characterised by two junction nodes, connecting it to its neighbours, and a pressure loss device.

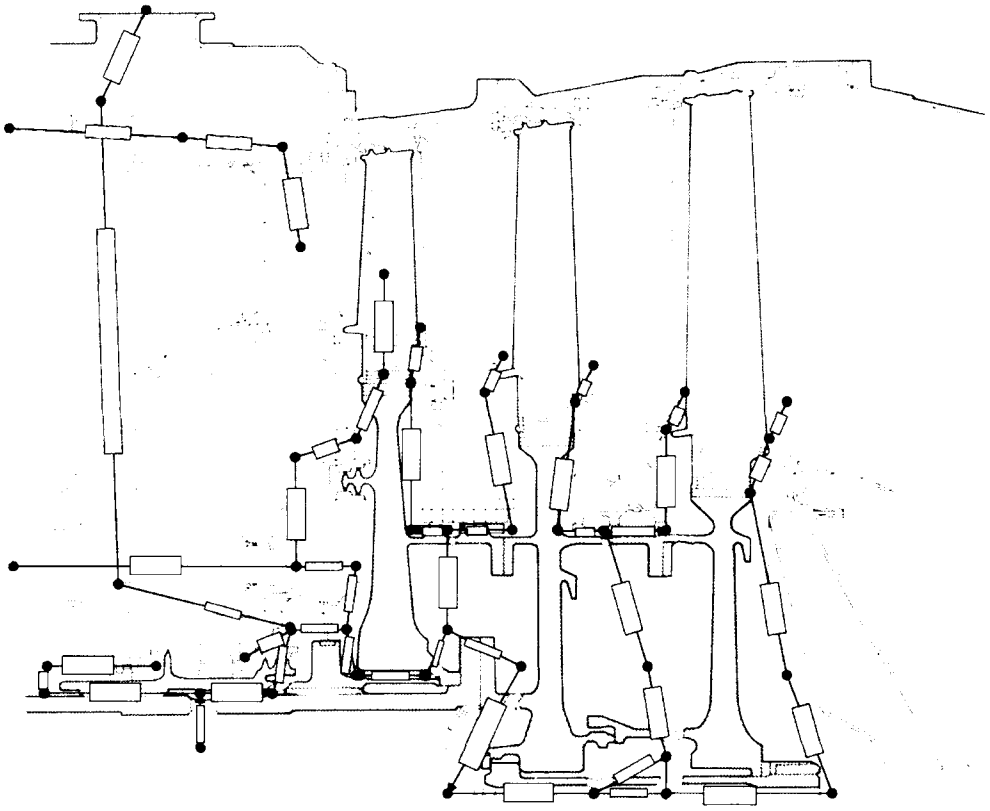

Figure 1.8: SAS network model of the HPT configuration.

The aim of the secondary air system calculation is to obtain pressures, temperatures in all the junction nodes of the network as well as all the mass flow rates in the pressure loss elements knowing the geometrical definition of the flow passages and for a given set of prescribed inlet and outlet conditions. The boundary conditions are usually specified at inlet(s) and outlet(s) of the system. According to the problem description, boundary conditions are defined in terms of pressure or temperature at the junction nodes and mass flow rates in the pressure loss elements. Usually, the boundary conditions are specified at the system interface, in term of sources where the flow is entering the system or drains where the flow is leaving the system.

1.3.2 The one-dimensional approximation

The one-dimensional approach applies to flows in which all fluid properties are considered uniform over any cross section of the flow. In a one-dimensional flow the rate of change of fluid properties normal to the streamline direction is very small compared to the rate of change along the streamline. In fluid network, for instance when addressing pressure losses as it is the case in the secondary air system, the one-dimensional approximation is often used [58]. Many authors, such as Shapiro in [49] or Benedict [3], state that the errors in predicting the change of rate along the streamline are small if:

- the fractional rate of change of area with respect to distance along the axis of the duct is small: $\frac{dA}{Adx} << 1$
- the radius of curvature is large compared with the hydraulic diameter: $\frac{A}{R^2} << 1$.

Under the one-dimensional approximation, the three conservation equations governing the network, mass energy and momentum conservation, are written in their respective integral forms. The fluid properties are the averaged properties taken on a mean streamline.

1.3.3 Problem conditioning

In a global network approach, the pressure loss element is a control volume in between two junction nodes for which the momentum balance is expressed. The junction nodes are locations where the thermodynamical state of the fluid is described independently of the direction of the flow. The mass and energy balance are written at the junction nodes.

There are 3 variables in the system

- 2 state variables, pressure and temperature, at the junction nodes
- 1 variable, the mass flow rate, attached to the pressure loss device

and 3 balance equations

- momentum balance in the pressure loss device
- mass and energy balance in the junction nodes

The system is not completely defined until boundary conditions are specified in the network, setting the constraints for the solution. Boundary conditions are values set either at the junction nodes for temperature and pressure or defined for the pressure loss element in term of mass flow rate. Once the boundary conditions are specified, the network problem can be solved. It remains to be determined if the problem is mathematically well-conditioned: how many equations are describing the problem, how many unknowns are there, how many boundary conditions are required, do all the configurations have a solution?

Let N_j denote the number of junction nodes in the system and N_e the number of elements. Three network configurations are presented in Fig.1.9.

In the case of a linear network, with neither closed loops nor branchings, the maximum of elements present in the network is given by

$$N_e = N_j - 1 \tag{1.1}$$

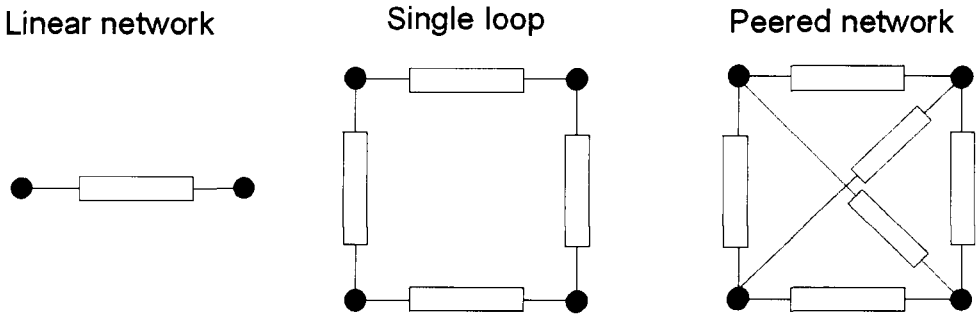

Figure 1.9: Three basic network configurations.

This leads to $N_e = N_j - 1$ mass flow rates in the elements, N_j pressures and N_j temperatures in the junction nodes. It gives a total of $3N_j - 1$ variables. There are $N_e = N_j - 1$ loss equations, N_j equations for mass conservation and the same number for energy conservation, which amounts to $3N_j - 1$ equations. Let suppose that boundary conditions are defined in terms of inlet pressure, inlet temperature and outlet pressure. The total of unknowns is therefore $3N - 4$. As inlet and outlet pressures are known the number of loss equations available is $Ne = N_j - 3$. Setting the inlet temperature as boundary condition cancels the energy equation in the first node. The amount of equations is therefore $N_j - 3$ loss equations, $N_j - 1$ energy equations and N_j mass equations which amounts exactly to the number of unknown variables.
In the case of a simple loop there are an equal number of pressure loss elements and junction nodes. This leads to an equal amount $3N_j$ of unknown variables and equations. In the case of peer connection, where each element has the maximum possible number of neighbours

$$N_e = \frac{N_j\,(N_j - 1)}{2} \tag{1.2}$$

The number of variables is written under the general form

$$N_{var} = 2N_j + N_e \tag{1.3}$$

The number of available equations is distributed as follows

- one equation for the mass balance in each junction node
- one equation for the energy conservation in each junction node
- one equation for the momentum balance for each element.

The number of equations is therefore $N_{eq} = N_e + 2N_j$ and equal to the number of unknowns.

Boundary conditions must be specified in the system to obtain a solution. The general number of boundary conditions is noted N_b The number of unknowns in the system is given by

$$N_{un} = 2N_j + N_e - N_b \tag{1.4}$$

The number of available equations is decreased by the number of specified boundary conditions. The number of available equations is therefore given by

$$N_{eq} = 2N_j + N_e - N_b \tag{1.5}$$

and equal to the number of unknowns.

1.4 Solving the network problem

In the frame of the present work only steady-state analysis is addressed. Steady-state computations are crucial in engineering as they enable to study the system for design conditions in relationship with efficiency and life cycle. Transient phenomena are generally taken into account once the steady state results have been obtained in order to predict the response of the system to a time dependent variation of the boundary conditions.

Under steady state condition the three types of equations are described in the network as

- mass conservation: the sum of all mass flow rates entering or leaving a node is equal to zero
- energy conservation: the sum of all heat heat flow entering or leaving a node is equal to zero
- momentum conservation: for each flow passage there is a relationship between inlet state variables, outlet state variables, mass flow rate and geometry.

The set of equations defined above is nonlinear because the loss equation in the loss element is a nonlinear function of pressure, temperature and mass flow rate. This loss equation is obtained using the energy conservation and the momentum conservation on the element as used by Majumdar and al. in [30] and in [29] as well as by Kutz and Speer in [26] or again Ebenhoch in [15].

The solution method of the nonlinear system of equations is therefore iterative, each iteration yielding a better approximation of the solution until the accuracy of the iterated variables is deemed acceptable. In this case convergence is achieved and the iterative process stops. It proceeds as follows

- linearise the nonlinear system of equations

- using linear algebra techniques solve the linear system of equations
- check the solution obtained with the set of nonlinear equations.

Solving the nonlinear system of equations is therefore described under the form of an optimisation problem: finding the values of the system variables which satisfy the nonlinear system of equations with the desired accuracy.

In the literature the most widely used method for solving nonlinear equations is the Newton-Raphson method and its derivatives. [9], [30], [29], [26], [15].

1.4.1 The Newton-Raphson method

In numerical analysis, Newton's method (also known as the Newton-Raphson method or Newton-Fourier method) is an efficient root finding algorithm for a real valued function.

Let f be a differentiable function defined on the interval [a, b] in the real space $\Re$.

Let $\Delta x = x - x_n$. The Taylor expansion for f can be written as follows:

$$f(x_n) + \frac{df}{dx}\Delta x + \frac{1}{2}\frac{d^2f}{dx^2}|_{\epsilon_n}\Delta x^2 = 0 \tag{1.6}$$

with ϵ_n lying between x_n and x. An approximation of the first order of Eq.1.6 is

$$f(x_n) + \frac{df}{dx}|_{x_n}\Delta x = 0 \tag{1.7}$$

which is a linear equation solved using linear algebra and yielding the correction term Δx used to obtain a new value x_{n+1}. An illustration of Newton root finding algorithm is given in Fig.1.10

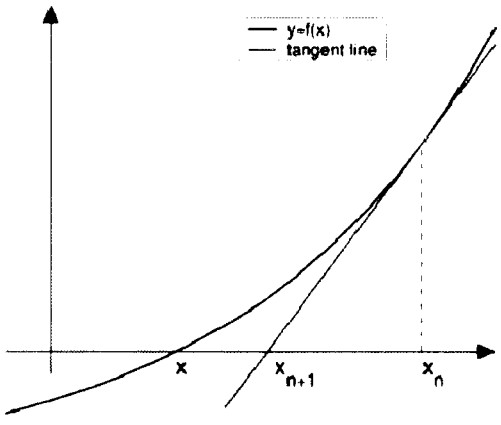

Figure 1.10: Illustration of the Newton-Raphson method with a one dimensional real-value function.

Solving Eq.1.6 exactly for x gives

$$x = x_n - \frac{f(x_n)}{f'(x_n)} - \Delta x^2 . \frac{f''(\epsilon)}{2f'(x_n)} \tag{1.8}$$

Or by definition of Δx

$$x = x_n - \frac{f(x_n)}{f'(x_n)} - (x - x_n)^2 . \frac{f''(\epsilon)}{2.f'(x_n)} \tag{1.9}$$

Therefore the error after $n+1$ iterations is proportional to the square of the error after n iterations showing quadratic convergence [24]. The Newton-Raphson method is therefore iterative and requires an initial value of the function. A useful strategy devised to provide reliable convergence even when a close estimate is not available is to use an over/under relaxation factor. Eq.1.7 is written

$$x_{n+1} = x_n - \delta_n \tag{1.10}$$

with

$$\delta_n = \frac{f(x_n)}{f'(x_n)} \tag{1.11}$$

The relaxation factor Θ is introduced yielding

$$x_{n+1} = x_n - \Theta_n \delta_n \tag{1.12}$$

Compared to the original Newton-Raphson, this method retains the direction of propagation of the convergence algorithm, δ_n, but changes the size of the step Δx predicted by the classical method by a factor Θ_n. Θ_n is usually calculated to ensure monotonic convergence of the correction.
Two methods are widely used, namely the method developed by Davidon-Fletcher-Powell, and subsequently called DFP and the method developed by Broyden-Fletcher-Goldfarb-Shanno, BFGS. Both methods are described in [5].

1.4.2 The Newton-Raphson method in fluid network problems

Numerous authors have used the Newton-Raphson method to solve nonlinear sets of equations related to network problems. The applications of the Newton-Raphson method when addressing fluid networks are of three types:

- type 1: The Newton-Raphson is applied to closed loops in the network
- type 2: the Newton-Raphson algorithm is applied only to solve the nonlinear loss equation

- type 3: the system of equations is considered globally and the Newton-Raphson method is used to build a global matrix.

Illustration of type 1 methods: Hardy Cross

The first and widely used method for analysing pipe networks is the Hardy Cross method [9] developed in the 1930s for hand generated solutions of water distribution pipe networks and therefore for incompressible flow. Even today many computer programs are based on this method, such as the one described by Prasad in [45]. Temperature is not considered as an unknown in the original Hardy Cross problem. In addition to the nonlinear loss equation relating mass flow rate to pressure drop for flow passages, two types of equations are used

- mass conservation at the junction nodes
- continuity of potential is applied to a closed loop stating that the total change in potential along a closed path is zero

The Hardy Cross method divides the global network into smaller sub-networks by considering only one portion of the circuit at a time. The scale of the sub-network is generally a loop. The continuity and potential errors are determined for the selected loop using the Newton-Raphson algorithm. This yields mass flow rate and pressure corrections used to update the variables in the loop. Another adjacent loop is subsequently selected and the same process is started again until the whole circuit is completed thus propagating the correction to the complete network. The sequential process is repeated until the continuity and potential equation errors are minimised in each loop of the circuit. The topology is therefore very important in the choice of the equations since the equations are based on the existence of loops. According to several authors like Jeppson [24] or Wood and Rayes in [62], although well suited for small networks, the Hardy Cross method can be very slow and even fails to converge when used to analyse larger networks.

Illustration of type 2 methods: Kutz and Speer algorithm

A publication often referred to when dealing with flow network problems is the paper entitled "Simulation of the secondary air system of Aero Engines", written by K.J. Kutz and T.M. Speer [26].This method is the one currently in use at MTU Aero engines for SAS analysis. The solution retained by Kutz and Speer was, with due regard to the problem size, to adopt a hierarchical algorithm instead of trying to solve the whole system of equations at once. A rough outline of the nested structure adopted by Kutz and Speer is given in Fig.1.11. Network nodes are defined only at branchings, when more than two loss elements meet. To retain

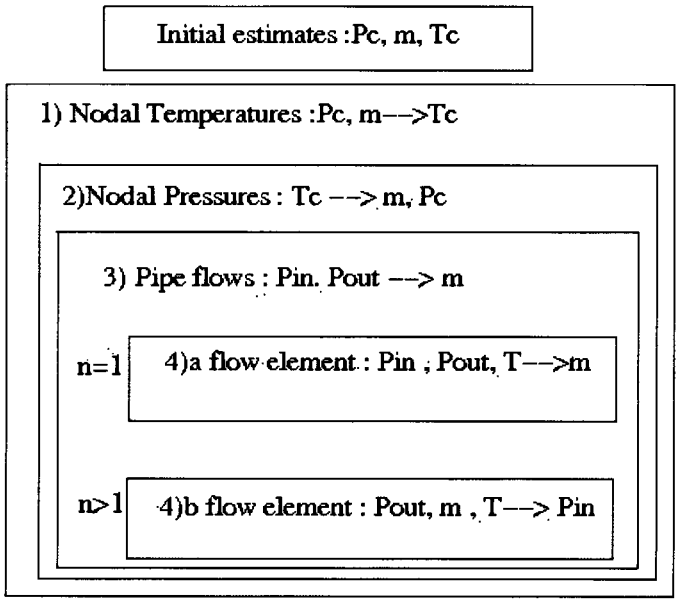

Figure 1.11: Nested iteration algorithm.[26]

the terminology used, the topology is comprised of pipes with two junction nodes containing one or several loss elements in series.

In the first level of the iterative process, only the energy equation is considered. This equation states that the sum of the heat flows going in and out of the junction nodes plus the contribution of discrete heat flows external to the network is balanced. Solving this linear equation at nodal level, gives a value of the enthalpy for each junction node and yields nodal temperatures in the network. At iteration level 2, the nonlinear loss equation is solved in terms of pressures. To this aim a variant of the Newton-Raphson method developed by Powell in [44] and [43] is used. For flow computation, performed at iteration level 3, the Kutz and Speer procedure relies on the topology and discriminates between pipes containing only one loss element and pipes consisting of a succession of loss elements. The two cases are dealt with separately at iteration level 4.

- If a single element is considered: using the inlet and outlet pressures and temperatures from iteration level 1 and 2 in conjunction with the pressure loss equation gives the value of the mass flow rate.

- If a series of flow elements is found: given the nodal temperature obtained at level 1, the outlet pressure obtained at iteration level 2 and a value of the mass flow rate, a distribution of pressure for each loss element in the pipe is created. This pressure distribution satisfies the loss equation. Using a secant method the pressure distribution is varied until the nodal inlet pressure determined at iteration level 2 and the nodal value of the varying pressure distribution meet.

Illustration of type 3 methods: Majumdar and al.

Majumdar and al. [30], [29] published two papers describing their method and applying it to the investigation of the internal flow of a rocket engine turbo pump. This method is the direct application of the Newton-Raphson algorithm for multi-variable functions. The system is considered from a global point of view and the global system of equations is considered to solve all equations simultaneously.Mass and energy equations are written for the junction nodes and loss equation for each element. The Newton-Raphson scheme is used on each equation for mass flow rate, temperature and pressure thus yielding a system of linear equations, the solution of which yields corrections for all three variables through the whole network. Using the updated variables, new mass, energy and loss equations are written and the process is repeated until the set of equations is satisfied. Other authors, such as Miedema et al.[32] or Desideri and DiMaria [11] successfully used this global approach.

1.5 Conclusion

The Secondary Air System is a complex and essential part of an aero engine which greatly influences engine performance. It is best modelled by a **network** of pressure loss elements comprised of junction nodes representing the state of the fluid at a given location and pressure loss devices defining the amount of fluid flowing from one junction node to the other. For the purposes of SAS computations, temperature and pressure are used as variables to define the state of the fluid in the nodes, and the mass flow rate is used as the transport variable in the pressure loss element. The set of equations formed by mass and energy conservation in the nodes and loss equation in the loss elements is nonlinear. The Newton-Raphson method and its derivatives is used by the majority of the authors to solve the set of nonlinear equations. Different methods enabling to obtain mass flow rates, total pressures and total temperatures in the network, have been reviewed along with the one currently in use at MTU Aero engines GmbH described in [26].

Since the influence of gas properties on engine metal parts is important, parameters obtained at the end of the Secondary Air System calculation serve as boundary conditions for a subsequent thermomechanical analysis. Literature sources attest of the growing interest for coupled analysis. Currently, at MTU Aero Engines, three distinct models and three different software must be used to perform a coupled analysis therefore deteriorating the accuracy of the results. The iterative analysis process is often stopped before global convergence is reached disregarding many interactions between the fluid, thermal and structural problem. The need for a new software integrating secondary air system and thermomechanical approach in view of more accurate design analysis and subsequent test data matching is therefore substantiated.

Chapter 2

Theoretical developments

2.1 Modelling the secondary air system: formulation

2.1.1 Element topology

As highlighted in the literature review, the secondary air system of aero engines is best represented by a one-dimensional network. The network consists of pressure loss elements connecting at junction nodes. The state of the fluid is defined by two state variables, the total pressure and the total temperature in the static reference frame, in the junction nodes and the mass flow rate in the pressure loss device.

The network representation has proved well adapted, reliable and has been used for years by the different engine manufacturers.

The proposal in the present thesis, consists in **blending together secondary air system network and finite element thermomechanical model in one unique finite element model**. Topological compatibility between the secondary air system model and the thermomechanical finite element mesh is therefore required to ensure an efficient and reliable data exchange between the different modules. Accordingly, it has been decided to use a topological representation of the loss element that satisfies the requirements of the finite element program.

The topology proposed for the new loss element is a three node element as represented in Fig.2.1. As for the

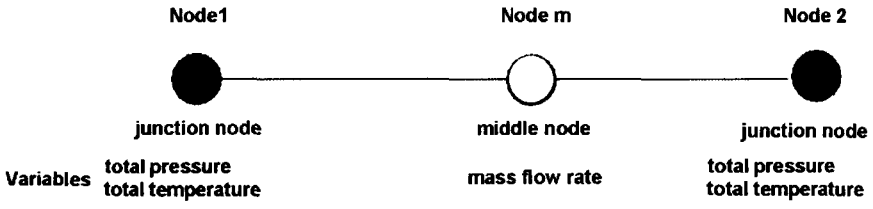

Figure 2.1: Loss element topology.

former topology node1 and node2 are the junction nodes where the fluid state is defined by total pressure and total temperature. The middle node, labelled Node m, replaces the pressure loss device and accommodates information on the mass flow rate. The loss element represents a basic brick for the construction of the network and stands for one single flow passage.

2.1.2 Boundary element

Boundary conditions for air system flow networks, must be specified in terms of total pressures, total temperatures or mass flow rates.

For this purpose a special element has been developed. As pictured in Fig.2.2 the boundary element is a

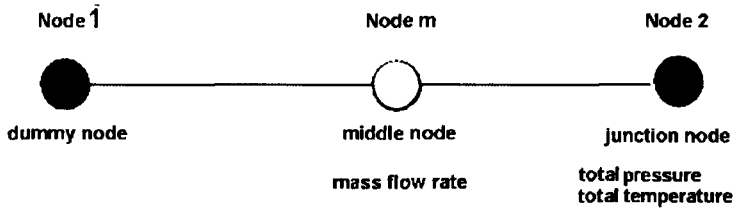

Figure 2.2: Representation of a boundary element topology.

variation of the previously presented loss element. A boundary element is connected to the network by only one of the junction nodes, the other remaining free. The junction node 2 in Fig.2.2 is used to implement boundary conditions in terms of pressure and temperature. Boundary conditions in terms of mass flow rate are implemented at the middle node. As the equation for mass conservation is applied to the junction nodes, a boundary element with two regular junction nodes cannot be used. Indeed, there is only one mass flow rate coming in or out of the junction node 1 in Fig.2.2 depending on whether the boundary element is a source or a drain. The mass conservation cannot be taken into account at such nodes as there is creation respectively disappearance of mass. Therefore the junction node of connectivity 1, although present in the network, is not considered for the creation of the system of equations.

2.2 The governing equations

2.2.1 Hypotheses and constitutive equations

The scope of the applications of the flow solver specify the hypotheses concerning the properties, physical characteristics and behaviour of the flow.

1. In the secondary air system, air is considered as a Newtonian fluid

2. Air is considered as an ideal gas governed by the equation of state:

$$\frac{p}{\rho} = R.T \tag{2.1}$$

where p is the static pressure, ρ is the density , T is the static temperature and R is the specific gas constant. The perfect gas approximation is valid when temperature variations within the fluid are small. In the case of secondary air system typical variations of temperature over a complete module may range from 100 K up to a maximum of 200 K. Between two junction nodes of a given loss element, temperature changes are much smaller.

The variations of specific heat capacity at constant pressure with temperature are pictured in Fig.2.3.

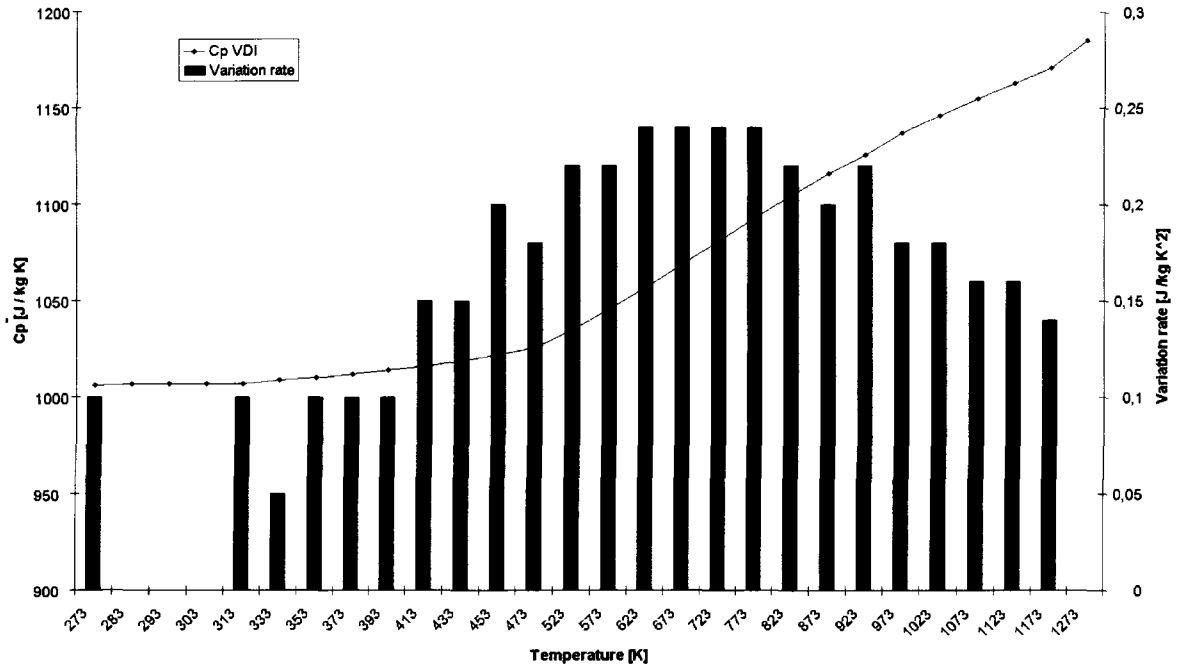

Figure 2.3: Variation of C_p in $[Jkg^{-1}K^{-1}]$ in function of temperature in $[K]$ from [56] and variation rate

From this figure it can be seen that with small temperature variations lead to small variations of the

heat capacity. For temperatures between 473K and 1273K, the usual range of application for the SAS, the maximum rate of variation of C_p is about $0.25JKg^{-1}K^{-2}$. A variation of 200K amounts therefore to a maximum of $50JKg^{-1}K^{-1}$ or a relative change of 5% of the C_p value.

3. Only steady state phenomena are considered in the network

4. Outside irreversibility zones such as boundary layers, wakes and shock waves the flow is considered isentropic. The flows are in the elements are considered isentropic with pressure losses and force works modelled under an integral form as correction factors.

The underlying conservation principles are:

- Conservation of mass at junction nodes
- Conservation of energy at junction nodes
- loss equation in the loss elements

Viscosity induced pressure losses exist in the network and must be properly addressed.
The main goal of this section is to show more in details the equations governing the network, how they have been obtained and how they are used to obtain total nodal pressure, total nodal temperature, and mass flow rate.

2.2.2 Notations and conventions.

In order to express the conservation principles under the present assumptions a convention has been chosen. In Fig.2.4, a junction node, labelled i, is considered. Node i is fixed in space and has a finite volume V_i. The node i connectivity may comprise from 1 to n neighbouring junction nodes labelled j_k, $k = 1, .., n$. Lines between node i and its neighbours are noted with a subscript ij_k and $\dot{m}_{ij_k}$ is the absolute value of the mass flow rate flowing through the line. A reference vector $\overrightarrow{e}_{ij_k}$ is defined for each line from i to j_k. The flow goes in and out of node i through a section denoted A_{ij_k}. The total area comprised of the inlet and outlet sections of the control volume is called $A_i = \bigcup_{k=1}^{n} A_{ij_k}$. The sign convention for the mass flow rate is the following:

- $\overrightarrow{\dot{m}}_{ij_k} = +\dot{m}_{ij_k}\overrightarrow{e}_{ij_k}$ for an outflow
- $\overrightarrow{\dot{m}}_{ij_k} = -\dot{m}_{ij_k}\overrightarrow{e}_{ij_k}$ for an inflow
- $\dot{m}_{ij_k} = ||\overrightarrow{\dot{m}}_{ij_k}||$.

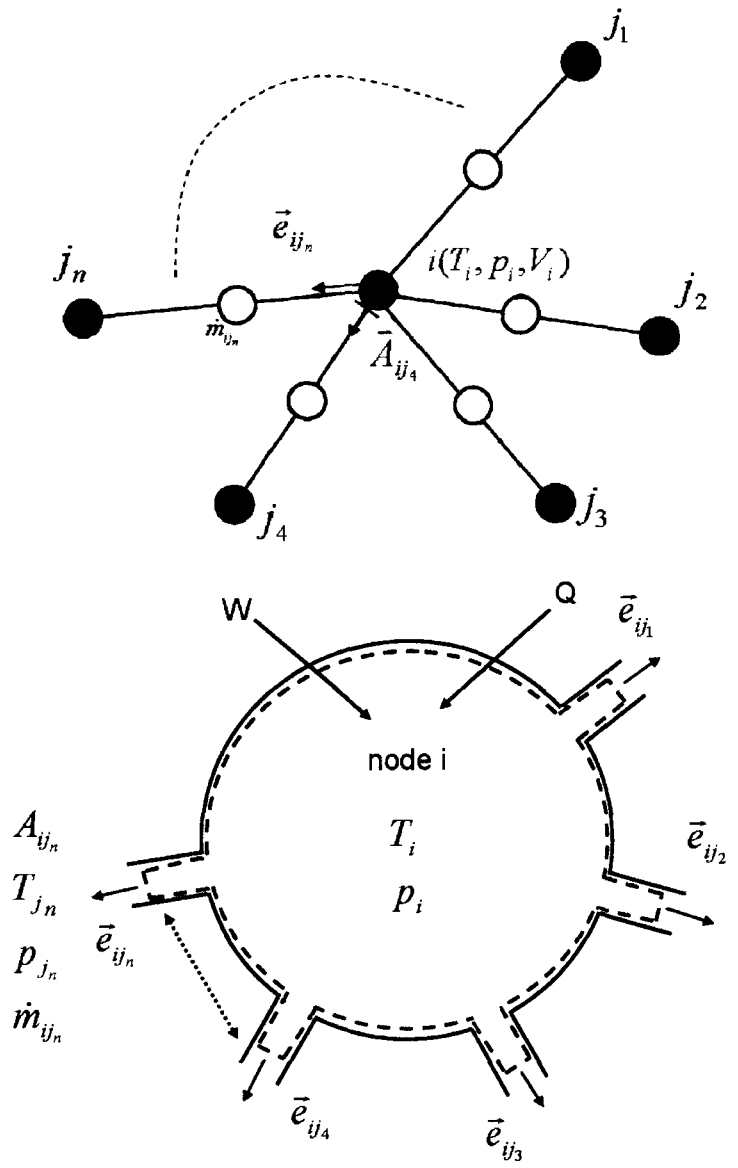

Figure 2.4: Notations, conventions and definition of the control volume

.

W is the global amount of work of the external forces acting on the control volume such as the work of a shaft or a rotating disc stirring the fluid. Q refers to the global amount of heat exchanged between the control volume and its surroundings.

2.2.3 Conservation of mass.

The general equation for mass conservation under steady state conditions applied to a compressible flow is written in the static frame, using Einstein convention $l = 1, ., 3$, under the following form

$$(\rho v^l)_{,l} = 0 \tag{2.2}$$

Let i stands for the index of a given gas node of finite volume, V_i, fixed in space. Integrating Eq.2.2 over the control volume yields

$$\int_{V_i} (\rho v^l)_{,l} dV = 0 \tag{2.3}$$

Using the divergence theorem to transform the second integral term into a surface integral yields

$$\int_{A_i} \rho v^l dA_{ij_k l} = 0 \tag{2.4}$$

,where A_i stands for the control surface corresponding to the volume V_i. For one junction node one can write

$$\int_{A_{ijk}} \rho v^l dA_{ij_k l} = \dot{m}_{ij_k} \tag{2.5}$$

Consequently, Eq.2.4 amounts to

$$\boxed{-\sum_{k \in in} \dot{m}_{ij_k} + \sum_{k \in out} \dot{m}_{ij_k} = 0} \tag{2.6}$$

2.2.4 Conservation of energy

The general principle of energy conservation presented in Annex B 3.4 is written as:

$$\rho \frac{de_t}{dt} = \rho v^k f^k + \left(v^k \sigma^{kl}\right)_{,l} - q^k_{,k} \tag{2.7}$$

The total enthalpy is defined by

$$h_t = e_t + \frac{p}{\rho} \tag{2.8}$$

Using Eq.2.8 in Eq.2.7 yields

$$\begin{aligned} \rho \frac{de_t}{dt} &= \rho \left[\frac{dh_t}{dt} - \frac{d}{dt}\left(\frac{p}{\rho}\right) \right] \\ &= \rho \frac{dh_t}{dt} - \frac{dp}{dt} + \frac{p}{\rho}\frac{d\rho}{dt} \end{aligned} \tag{2.9}$$

Using the principle of mass conservation $\frac{d\rho}{dt} = -\rho v^k_{,k}$ and by definition $\frac{dp}{dt} = \frac{\partial p}{\partial t} + v^k p_{,k}$. Eq.2.9 is transformed into

$$\rho \frac{de_t}{dt} = \rho \frac{dh_t}{dt} - \frac{\partial p}{\partial t} - (v^k p)_{,k} \tag{2.10}$$

According to the hypothesis and the Newton Stokes assumptions for the mechanical behaviour of the fluid (see Annex B 3.4), the stress tensor is separated into $\sigma^{kl} = -p\delta^{kl} + \tau^{kl}$ where τ^{kl} is the tensor of viscous

stresses. Using the Newton-Stokes assumption and Eq.2.10, Eq.2.7 becomes

$$\rho\frac{dh_t}{dt} = \frac{\partial p}{\partial t} + \rho v^k f^k + \left(v^l\,\tau^{kl}\right)_{,k} - q^k_{,k} \tag{2.11}$$

Eq.2.11 is the Lagrangian formulation of the energy equation. The Reynolds theorem is applied to the total enthalpy

$$\begin{aligned}\rho\frac{dh_t}{dt} &= \rho\left(\frac{\partial h_t}{\partial t} + v^k h_{t,k}\right)\\ &= \frac{\partial \rho h_t}{\partial t} + \left(\rho v^k h_t\right)_{,k} - h_t\left(\frac{\partial \rho}{\partial t} + \left(\rho v^k_{,k}\right)\right)\\ &= \frac{\partial \rho h_t}{\partial t} + \left(\rho v^k h_t\right)_{,k}\end{aligned} \tag{2.12}$$

The Eulerian formulation is therefore

$$\frac{\partial \rho h_t}{\partial t} + \left(\rho v^k h_t\right)_{,k} = \frac{\partial p}{\partial t} + \rho v^k f^k + \left(v^l\,\tau^{kl}\right)_{,k} - q^k_{,k} \tag{2.13}$$

Under steady state conditions and in the stationary frame, the equation is formulated as

$$\boxed{\left(\rho v^k h_t\right)_{,k} = \rho v^k f^k + \left(v^l\,\tau^{kl}\right)_{,k} - q^k_{,k}} \tag{2.14}$$

Considering the control volume attached to node i, Eq.2.14 is integrated over the fixed control volume V_i. Transforming the volumes integrals containing the divergence terms into surface integrals yields:

$$\int_{A_i} \rho h_t v^k dA_k = \int_{A_i} -q^k dA_k + \int_{A_i} v^k \tau^{kl} dA_k + \int_{V_i} \rho v^k f^k dV \tag{2.15}$$

or using the nomenclature presented in Fig.2.4, Eq.2.15 is written

$$\int_{A_i} \rho h_t v^k dA_k = Q + W_{\text{viscous}} + W_{\text{field}} \tag{2.16}$$

where $W_{viscous}$ is the work delivered by the viscous or shear forces acting on the control volume and W the work delivered by field forces. As the control volume has been chosen to match exactly the chamber walls, the viscous phenomenon are therefore internal to the control volume. At the inlet and outlet cross section A_{ij_k} the contribution of the viscous stress tensor is negligible. Two case must be considered:

- if the chamber walls are non rotating, due to the slow velocities (subsonic) in the fluid nodes, the work of the viscous forces is neglected in front of the contribution of other phenomena such as conductive

heat transfer in the energy equation.

- if the chamber walls are rotating at high rotation speed, as is often the case in turbomachinery applications, the work of the viscous forces cannot be neglected anymore as it is responsible for frictional heating. This phenomenon is responsible in the immediate vicinity of the walls for the existence of a thermal boundary layer. In the 1D model the thermal boundary layer is not explicitly solved. Therefore the term representing the work of the viscous form is represented as an integral source term in the energy equation.

Furthermore, it is assumed that the amount of work of the external field forces such as gravity on the control volume is mostly negligible. The area of the convective term is now split into areas with inflow and areas with outflow:

$$\int_{A_i} \rho h_t v^k dA_k = \sum_{k \in in} h_{tij_k} \int_{A_{ij_k}} \rho v^k dA_{ij_k} + \sum_{k \in out} h_{tij_k} \int_{A_{ij_k}} \rho v^k dA_{ij_k} \tag{2.17}$$

Using Eq.2.5 yields

$$\int_{A_i} \rho h_t v^k dA_k = - \sum_{k \in in} h_{tij_k} \dot{m}_{ij_k} + \sum_{k \in out} h_{tij_k} \dot{m}_{ij_k} \tag{2.18}$$

Substituting the definition of enthalpy in Eq.2.18

$$\begin{aligned} \int_{A_i} \rho h_t v^k dA_k &= - \sum_{k \in in} \int_0^{T_i} C_p dT \dot{m}_{ij_k} + \sum_{k \in out} \int_0^{T_i} C_p dT \dot{m}_{ij_k} && (2.19) \\ &= - \sum_{k \in in} \left(\int_0^{T_{ref}} C_p dT + \int_{T_{ref}}^{T_i} C_p dT \right) \dot{m}_{ij_k} \\ &\quad + \sum_{k \in out} \left(\int_0^{T_{ref}} C_p dT + \int_{T_{ref}}^{T_i} C_p dT \right) \dot{m}_{ij_k} && (2.20) \end{aligned}$$

,where T_{ref}, reference total temperature, may be freely chosen. C_p is constant over a loss element.It is therefore taken out of the integral.

$$\begin{aligned} \int_{A_i} \rho h_t v^k dA_k &= h_{ref} \underbrace{\left(- \sum_{k \in in} \dot{m}_{ij_k} + \sum_{k \in out} \dot{m}_{ij_k} \right)}_{=0 \text{ by mass conservation}} \\ &\quad - \sum_{k \in in} C_p \left(T_i - T_{ref} \right) \dot{m}_{ij_k} + \sum_{k \in out} C_p \left(T_i - T_{ref} \right) \dot{m}_{ij_k} && (2.21) \end{aligned}$$

Choosing $T_{\text{ref}} = T_{j_k}$ yields

$$\int_{A_i} \rho h_t v^k dA_k = -\sum_{k \in in} C_p (T_i - T_{j_k}) \dot{m}_{ij_k} + \sum_{k \in out} C_p (T_i - T_{j_k}) \dot{m}_{ij_k} \tag{2.22}$$

The term on the right hand side of Eq.2.16 models the heat exchange between the control volume and its surroundings. This term models the heat exchange between wall and fluid (surface A_{iw}).

$$\int_{A_i} q^k dA_k = \int_{A_i w} q^k_{conv} dA_k + \int_{A_i f} q^k dA_k \tag{2.23}$$

This term is represented by a source term

$$\begin{aligned} \int_{A_i} q^k dA_k &= [h_c (T_w - T_i)] A_i \\ &= \overline{h_c}(T_w - T_i) \end{aligned} \tag{2.24}$$

where h_c is the convective heat transfer coefficient between the wall with temperature T_w and the fluid inside the control volume with temperature T_i, and is function of the geometry of the Reynolds number and the Prandtl number. The heat transfer coefficient is a simplified approach to take into account the conduction phenomena occurring in the boundary layer between fluid and structure when the boundary layer is not explicitely solved as is the case in the 1D model presented.Finally the principle of energy conservation is written, under steady state assumptions, as

$$\boxed{-\sum_{k \in in} C_p (T_i - T_{j_k}) \dot{m}_{ij_k} + \sum_{k \in out} C_p (T_i - T_{j_k}) \dot{m}_{ij_k} + \overline{h_c}(T_w - T_i) + Q_i + W_{\text{viscous}i} = 0} \tag{2.25}$$

Eq.2.25 expresses that the change of heat energy at node i is caused by heat flows from the adjacent nodes and thermal interaction between the fluid nodal temperature and the material. In absence of interaction with the surroundings, fluid or loss elements may be therefore seen as an energy carrier.

2.2.5 Loss equations

The loss element equations, modeling pressure losses in a loss element, are expressed in terms of total nodal pressures and temperatures and mass flow rate. The loss equation represents the physical behaviour of each flow element. Because different flow passage geometries yield different physical behaviour, the loss equation is not unique. Therefore several the classes of elements have been considered to classify the different types of loss equations. In the junction nodes, energy and continuity conservation are expressed.

The loss equation is solved for each flow element. The loss equation is called G and described in the most general case:

$$G(T_i, T_j, p_i, p_j, \dot{m}_{ij}) \tag{2.26}$$

The different classes of loss elements and their respective mathematical models are further described in the following sections.

2.3 Implementing the Newton-Raphson method

In the previous section the constitutive equations have been derived. This section deals more practically with the implementation of the solver algorithm. It presents the way the system of linear equations is obtained from the equations developed in the previous section, the way the system is solved and all relevant aspects of the Newton-Raphson method.

2.3.1 The algorithm

Considering one loss element as represented in Fig.2.1, the unknown in the equations are

- mass flow rate : $\dot{m}_{ij}$
- inlet total temperature : T_i
- inlet total pressure : p_i
- outlet total temperature: T_j
- outlet total pressure : p_j

Let $f = f(T_i, T_j, p_i, p_j, \dot{m}_{ij})$ be a general nonlinear function of the problem variables, continuous or semi-continuous and differentiable over the definition domain. The aim of the problem is to find a root of function f using the Newton-Raphson algorithm. A Taylor expansion about the solution in iteration l yields

$$\underbrace{f({T_i}^l, {T_j}^l, {p_i}^l, {p_j}^l, \dot{m}_{ij}^l)}_{residual} + \frac{\partial f}{\partial T_i}|_l \Delta {T_i}^l + \frac{\partial f}{\partial T_j}|_l \Delta {T_j}^l + \frac{\partial f}{\partial p_i}|_l \Delta {p_i}^l + \frac{\partial f}{\partial p_j}|_l \Delta {p_j}^l + \frac{\partial f}{\partial \dot{m}_{ij}}|_l \Delta \dot{m}_{ij}^l = 0 \quad (2.27)$$

This general principle has been applied to the three constitutive equations which, grouped together form a system of nonlinear equations. The following system is then built and solved in terms of variable corrections at iteration l:

$$\{R\}^l + [A]^l \{\Delta X\}^l = 0 \quad (2.28)$$

which is another form of writing Eq.2.27 using matrix formalism.

$\{R\}$ is the vector containing the residuals of each equation of the system, $[A]$ is the Jacobian matrix containing the first derivatives of each equation with respect to each variable and $\{\Delta X\}$ is the vector containing the correction for each variable.

The linear system of equations is solved using a collection of subroutines written in FORTRAN dedicated to solve large and sparse linear algebra problems [54], relying on the PLU decomposition of matrix $[A]$. The

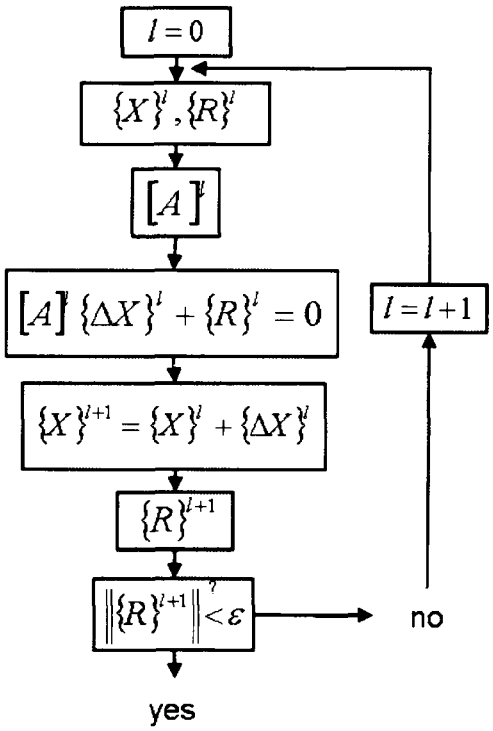

Figure 2.5: Newton-Raphson algorithm as implemented in CalculiX.

LU decomposition with partial pivoting and row interchanges is used to factor $[A]$ as

$$[A] = [P]\,[L]\,[U] \tag{2.29}$$

where $[P]$ is a permutation matrix, $[L]$ is unit lower triangular, and $[U]$ is upper triangular. The factored form of $[A]$ is then used to solve the system of equations $[A]\,\{X\} = \{B\}$. The overall algorithm is illustrated in Fig.2.5

2.3.2 Determining the initial/starting conditions

As represented in Fig.2.5, initial estimates of the unknown variables of the system are needed at the very beginning of the iterative process.

The nodal temperature is the first variable to be estimated.

Then the nodal pressures are determined. Unknown pressures are determined from the pressure boundary conditions using a Laplacian law of repartition: every unknown total pressure is calculated as the mean value of the total pressures of the adjacent nodes.

Once the initial nodal temperature and pressure values have been determined in the whole network, it is possible to compute the mass flow rate in each flow element using the corresponding loss equations Eq.2.26.

2.3.3 Computing the residuals and filling the $[A]$ matrix

As presented in Fig.2.5 the next step consists in computing the residuals. This is readily achieved once nodal pressures and temperatures as well as mass flow rates have been determined throughout the network. Eq.2.6 is used to obtain the residual for the nodal mass equations, Eq.2.25 for the nodal energy conservations and Eq.2.26 for the loss equations.

The method developed in this thesis is comparable to the one used by Majumdar in [30] and described in the literature review. Accordingly the equations of mass and energy conservation as well as loss equation must be linearised. The partial first derivatives of each equation with regard to each parameter must be obtained. Once computed, the values of the partial derivatives of each equation with regard to each variable taken at the present iteration constitute Jacobian matrix of the system, $[A]$.

The principle for mass conservation as been expressed for a given node i by Eq.2.6: The different partial derivatives of the function at iteration l are:

$$\frac{\partial f}{\partial \dot{m}_{ijk}}|_l = -\sum_{k\in in} 1 + \sum_{k\in out} 1 \tag{2.30}$$

Hence, the complete equation for steady state mass conservation modified to suit the Newton-Raphson requirements is written as

$$\underbrace{-\sum_{k\in in} \dot{m}_{ijk}{}^l + \sum_{k\in out} \dot{m}_{ijk}{}^l}_{residual} - \sum_{k\in in} \Delta\dot{m}_{ijk}{}^l + \sum_{k\in out} \Delta\dot{m}_{ijk}{}^l = 0 \tag{2.31}$$

The principle for energy conservation is written for a given node i in the form presented for Eq.2.25:

$$f = -\sum_{k\,\in\, in} C_p \left(T_i^l - T_{j_k}{}^l\right) \dot{m}_{ijk}{}^l + \sum_{k\,\in\, out} C_p \left(T_i^l - T_{j_k}{}^l\right) \dot{m}_{ijk}{}^l + \overline{h_c}(T_w - T_i^l) = 0 \tag{2.32}$$

The partial derivatives of function f at iteration l are:

$$\frac{\partial f}{\partial T_i}|_l = \sum_{k\in in} C_p \dot{m}_{ijk}{}^l - \sum_{k\in out} C_p \dot{m}_{ijk}{}^l + \overline{h_c} \tag{2.33}$$

$$\frac{\partial f}{\partial T_{j_k}}|_l = -\sum_{k\in in} C_p \dot{m}_{ijk}{}^l + \sum_{k\in out} C_p \dot{m}_{ijk}{}^l \tag{2.34}$$

$$\frac{\partial f}{\partial \dot{m}_{ij_k}}|_l = -\sum_{j\in in} Cp \left(T_i^l - T_{j_k}{}^l\right) + \sum_{k\in out} Cp \left(T_i^l - T_{j_k}{}^l\right) \tag{2.35}$$

The energy conservation is expressed under steady state conditions as:

$$
\begin{aligned}
0 = & \underbrace{-\sum_{k\,\in\,in} C_p\left(T_i^l - T_{jk}^l\right)\dot{m}_{ij_k}^l + \sum_{k\,\in\,out} C_p\left(T_i^l - T_{jk}^l\right)\dot{m}_{ij_k}^l + \overline{h_c}\left(T_w - T_i{}^l\right)}_{residual} \\
& - \left(\sum_{k\in in} C_p\dot{m}_{ij_k}^l - \sum_{k\in out} C_p\dot{m}_{ij_k}^l - \overline{h_c}\right)\Delta T_i^l \\
& - \left(\sum_{k\in in} C_p\dot{m}_{ij_k}^l - \sum_{k\in out} C_p\dot{m}_{ij_k}^l\right)\Delta T_{j_k}^l \\
& - \left(\sum_{j\in in} Cp\left(T_i^l - T_{j_k}^l\right) - \sum_{k\in out}\left(CpT_i^l - T_{j_k}^l\right)\right)\Delta\dot{m}_{ij_k}^l
\end{aligned}
\tag{2.36}
$$

For the loss equation, which are the only nonlinear equations in the system of equations, the transformation of Eq.2.26 into a linear equation by the Newton-Raphson method gives Eq.2.27. Each of the loss equation is dealt with in detail in the following section.

2.3.4 Convergence criteria.

To find the solution at the end of a given increment a set of nonlinear equations has to be solved. In order to do so, the Newton-Raphson method is applied, i.e. the set of equations is locally linearised and solved. If the solution does not satisfy the original nonlinear equations, the latter are linearised again at the new solution. This procedure is repeated until the solution satisfies the original nonlinear equations within a certain margin. Suppose iteration l has been performed and convergence is to be checked. Let us introduce the following quantities:

- $\tilde{q}_l^\alpha$: the iteration-averaged residual value for equation α for all iterations up to but not including iteration l.

- $r_{l,max}^\alpha$: the largest residual value (in absolute value) of equation α at the end of iteration l. For its calculation each equation is considered independently:

$$
r_\alpha^{k,max} = \max_e \max_{n_e} |\delta q_k^\alpha|, \tag{2.37}
$$

  where δ denotes the change due to iteration l, e represents all elements and n_e all nodes belonging to a given element.

- $\Delta u_{l,max}^\beta$: the largest change in solution (in absolute value) of variable β over all iterations including

iteration l. :

$$\Delta u^{\beta}_{l,max} = \max_{e} \max_{n_e} |\Delta u^{\beta}_{l}|, \tag{2.38}$$

- $c^{\beta}_{k,max}$: the largest change in solution (in absolute value) of variable β in iteration l.

$$c^{\beta}_{l,max} = \max_{e} \max_{n_e} |\delta u^{\beta}_{l}|. \tag{2.39}$$

The constant c_1 is used to check convergence of the residual and c_2 is used to check convergence of the solution. Both values may be specified by the user.

Convergence is obtained **if** the largest value of the residual is small compared to the iteration averaged of residual for equation α

$$r^{\alpha}_{l,max} \leq c_1 \, \tilde{q}^{\alpha}_{l} \tag{2.40}$$

and if the largest correction to the solution is also small compared to the largest incremental change corresponding to the solution variable:

$$c^{\beta}_{l,max} \leq c_2 \, \Delta u^{\beta}_{l,max} \tag{2.41}$$

2.3.5 Automatic increment size reduction

Sometimes the correction computed by the Newton-Raphson algorithm is too large for the solution to converge at all - the initial state is outside the radius of convergence of the system of equation. This condition can be detected by observing the behaviour of the largest residuals, r^{α}_{max}. In some cases, these will not decrease from iteration to iteration. It is assumed that if the largest residuals fail to decrease over two consecutive iterations, the iterations should be reattempted with a smaller increment size. This relaxation technique has been described in more general terms in the literature review. Thus if

$$\begin{aligned} r^{\alpha}_{k-1,max} &> r^{\alpha}_{k-2,max} \\ r^{\alpha}_{k,max} &> r^{\alpha}_{k-2,max} \\ r^{\alpha}_{k,max} &> c_1 \, \tilde{q}^{\alpha}_{k} \end{aligned} \tag{2.42}$$

the increment size is modified. This check is first performed at the end of the fourth iteration. With automatic relaxation monitoring, the size of the increment is adapted using the relaxation factor $d\theta = d\theta D_F$, where $D_F = 0.25$. The iteration of the increment is subsequently restarted. This subdivision continues until a successful increment size is found or the minimum increment size is reached.

2.4 Element description and implementation

As the following pages focus on loss elements and not on junction node i anymore, the subscript k indicating node i connectivity is subsequently dropped. i respectively in and j respectively out are used as subscripts for inlet and outlet nodes.

It has been shown that the energy equation Eq.2.25 is solved only in the junction nodes, which are the actual inlets/outlets of a flow element. Energy input or output happens in the junction nodes.

The types of loss element implemented are:

- **orifices:** typically used as pressure or mass flow rate regulation devices
- **labyrinth seals:** labyrinth seals are especially important since they control SAS in/out flows.
- **straight pipes:** the pipe element takes into account frictional effects
- **frame of reference change:** from a static frame of reference to a rotating frame of reference or vice versa.
- **vortices:** in order to assess radial pressure losses.
- **total head loss elements:** inlet and outlet losses, enlargements, contractions, bends.
- **branches:** joining and splitting.

With a library containing these loss elements, complex secondary air system configurations can be modelled. In the limited time frame of the present project, it has been decided to use as often as possible already existing literature material to model the different types of loss elements. The first immediate advantage is to be able to focus on the solver development as specified in the statement of work. The second and less immediate advantage is to be able to offer freely on the internet a version of CalculiX containing the final SAS algorithm developed in this thesis.

Numerous theoretical as well as empirical studies have been performed on most flow passages. They were included in order to provide the correlations for the loss element models described in this thesis.

2.4.1 Analysis of choked flow

As shown in [58], throughout an isentropic flow, total temperature, total pressure and total density are constant. In more general flows, the surface shear stresses, heat exchange between the fluid and its surroundings, or the presence of shock waves will lead to entropy changes, irreversibilities, and therefore the total quantities will vary axially along the flow. Even so, in such cases, it is often useful to apply the concept of the

total conditions locally within the flow. The local total temperature respectively pressure and density is defined as the temperature respectively pressure, density, that would be attained if the gas were brought to rest isentropically. Certain general flow relations which are independent of the boundary conditions can be set down in terms of local flow properties, and it is convenient to consider them. In the present case according to the hypothesis formulated, it is assumed that the fluid is an ideal gas and the processes occurring in the fluid are isentropic.

For a steady state, one dimensional flow, the equation of continuity is written as

$$\rho A v = \dot{m} = constant \tag{2.43}$$

By definition, the Mach number is defined as

$$M = \frac{v}{a} \tag{2.44}$$

and the relation for the velocity of sound is given by

$$a^2 = \kappa RT = \left(\frac{\partial p}{\partial \rho}\right)_{\text{isentropic}} \tag{2.45}$$

Using the state equation for a perfect gas, defined in Eq.2.1, and the previous relationships, yields

$$\frac{\dot{m}\sqrt{RT}}{Ap\sqrt{\kappa}} = M \tag{2.46}$$

which applies to any location within the flow. This equation is a restatement of the equation of continuity in terms of local temperature, pressure and Mach number. The local total temperature is given by

$$T_t = T\left(1 + \frac{\kappa - 1}{2} M^2\right) \tag{2.47}$$

and the local total pressure is

$$p_t = p\left(1 + \frac{\kappa - 1}{2} M^2\right)^{\frac{\kappa}{\kappa - 1}} \tag{2.48}$$

Replacing these expressions in Eq.2.46 results in

$$\frac{\dot{m}\sqrt{RT_t}}{Ap_t\sqrt{\kappa}} = M\left(1 + \frac{\kappa - 1}{2} M^2\right)^{-\frac{\kappa+1}{2(\kappa-1)}} \tag{2.49}$$

which is a general relationship applicable to all locations within the flow. This equation is known as the

reduced flow equation. On the left hand side is the term called reduced mass flow rate based on the total temperature and total pressure. As no limitation has been placed on the boundary conditions of the flow, this relation applies therefore locally within any steady state one-dimensional flow, no matter whether or not heat exchange, surface friction, normal shock waves are present and/or considered.

If the values of $\dot{M}, A, T_t, p_t$ are known at any section of the flow, which in the present case are the inlet/outlet junction nodes, then for given values of κ, R, Eq.2.49 provides a convenient means of evaluating the mass flow rate in the fluid element. Differentiating Eq.2.49 with respect to M shows that the mass flow function has a maximum value at M=1, given by

$$\left(\frac{\dot{m}\sqrt{RT_t}}{Ap_t\sqrt{\kappa}}\right)_{max} = \left(\frac{2}{\kappa+1}\right)^{\frac{\kappa+1}{2(\kappa-1)}} \tag{2.50}$$

The conditions evaluated at $M = 1$ are written using an asterisk as supescript

$$\dot{m}_{max} = \left(\frac{2}{\kappa+1}\right)^{\frac{\kappa+1}{2(\kappa-1)}} \frac{A^* p_t^* \sqrt{\kappa}}{\sqrt{RT_t^*}} \tag{2.51}$$

When the condition of maximum mass flow rate is reached within a flow, for given upstream conditions, the flow is said to be **choked**. Under this circumstances there are no changes which can be made to the flow conditions downstream of the sonic point, either in pressure or temperature, which can result in a further increase in mass flow rate.

Differentiating logarithmically the equation of continuity Eq.2.43 yields

$$\frac{d\rho}{\rho} + \frac{dv}{v} + \frac{dA}{A} = 0 \tag{2.52}$$

For an adiabatic steady and uniform flow

$$\begin{aligned} h + \frac{v^2}{2} &= cte \\ dh + vdv &= 0 \end{aligned} \tag{2.53}$$

Enthalpy is written under differential form as

$$dh = dq + Vdp = dq + \frac{1}{\rho}dp \tag{2.54}$$

For an isentropic flow, $dq = 0$, which yields

$$vdv + \frac{dp}{\rho} = 0 \tag{2.55}$$

also called Euler's equation of motion for inviscid fluid in steady state. The definition of the Mach number and speed of sound presented in Eq.2.44 and Eq.2.45 enable to write

$$\left(1 - M^2\right) \frac{dv}{v} + \frac{dA}{A} = 0 \tag{2.56}$$

which relates the variations of speed to the variations of section or using only Mach number and section

$$\frac{dM}{M} = -\frac{1 + \frac{\kappa-1}{2} M^2}{1 - M^2} \frac{dA}{A} \tag{2.57}$$

This equation is also known as Hugoniot's equation and can be interpreted as follows:

- if $0 < M < 1$ an increase in section leads to a decrease in flow velocity and vice versa.
- if $M > 1$ the variations of speed are proportional to the variations of section.
- if $M = 1$ the sonic velocity is reached and $(1 - M^2) = 0$. As speed is a finite quantity it results that $\frac{dA}{A} = 0$, which is to say sonic conditions can only been achieved at an extremum of section. Using the second derivative of Eq.2.57 enables to conclude that the extremum is a minimum of the section or a throat.

Consider a fluid element, comprised of an inlet junction node and an outlet junction node and representing a discrete pressure loss in the network. Inlet/outlet sections are defined for each junction nodes and the variation of section between inlet and outlet is a priori not known. Therefore choking conditions, if reached, may only occur at the minimum of either inlet or outlet section, depending on their relative geometrical specifications and may not occur elsewhere in the element.

As mentioned, if the flow is choked in the element, no variation of the downstream conditions will yield to an increase in mass flow rate. Knowing that the element is choked, knowing the choked section and knowing the inlet conditions, using the continuity equation enables to determine exactly the downstream conditions for which the element was choked.

2.4.2 Dimensional analysis

The Buckingham pi theorem is formulated as follows: Let K equal the number of fundamental dimensions required to describe the physical variables. Let $P_1, P_2..., P_N$ represent N physical variables in the physical

relation

$$f_1(P_1, P_2, ..., P_N) = 0 \tag{2.58}$$

Then, the physical relation described by Eq.2.58 may be written as a relation of $N - K$ dimensionless products called Π product.

$$f_2(\Pi_1, \Pi_2, ..., \Pi_{N-K}) = 0 \tag{2.59}$$

where each Π product is a dimensionless product of a set of K physical variables plus one other physical variable. Let $P_1, P_2, ...P_K$ be the selected set of K physical variables. Then

$$\Pi_1 = f_3(P_1, P_2, ..., P_K, P_{K+1}) = 0 \tag{2.60}$$

$$\Pi_2 = f_4(P_1, P_2, ..., P_K, P_{K+2}) = 0 \tag{2.61}$$

$$..... \tag{2.62}$$

$$\Pi_{N-K} = f_5(P_1, P_2, ..., P_K, P_N) = 0 \tag{2.63}$$

The choice of the repeating variables $P_1, P_2, ..., P_K$ should be such that they include all the K dimensions used in the problem. The dependent variable should appear in only one of the Π products.

In the SAS physics, if one considers the three equations of conservation established in 2.2, there are a total of 8 variables used $p, T, \rho, p_t, T_t, \dot{m}, v, A$. Following the Buckingham pi theorem the fundamental dimensions are

$$\begin{aligned} m &= \text{dimension of mass} \\ l &= \text{dimension of length} \\ T &= \text{dimension of temperature} \\ t &= \text{dimension of time} \end{aligned}$$

Therefore $K = 4$. The physical variables and their dimensions are

$$\begin{aligned}
[p_t] &= ml^{-1}t^{-2} \\
[p] &= ml^{-1}t^{-2} \\
[T_t] &= T \\
[T] &= T \\
[\dot{m}] &= mt^{-1} \\
[A] &= l^2 \\
[v] &= lt^{-1} \\
[\rho] &= ml^{-3} \\
[C_p] &= ml^{-2}t^{-2} \\
[C_v] &= ml^{-2}t^{-2}
\end{aligned}$$

Therefore $N = 8$. According to Buckingham pi theorem, there are 4 dimensionless Π products Using the principal variables, $p_t, T_t, \dot{m}, A$, four non-dimensional variables are created

$$M = \frac{v}{\sqrt{\kappa RT}} = \frac{\dot{m}\sqrt{RT}}{Ap\sqrt{\kappa}} \tag{2.64}$$

$$\tilde{\rho} = \frac{\rho RT_t}{p_t} \tag{2.65}$$

$$\tilde{\dot{m}} = \frac{\dot{m}\sqrt{RT_t}}{Ap_t\sqrt{\kappa}} \tag{2.66}$$

$$\Pi = \frac{p}{p_t} \tag{2.67}$$

The constitutive equations for the state of a perfect gas are written

$$p = \rho RT \tag{2.68}$$

$$c = \sqrt{\kappa RT} \tag{2.69}$$

$$\dot{m} = \rho Av \tag{2.70}$$

$$\frac{p_t}{p} = \left(\frac{\rho_t}{\rho}\right)^{\kappa} = \left(\frac{p_t}{p}\right)^{\frac{\kappa}{\kappa+1}} \tag{2.71}$$

$$C_p - C_v = R \tag{2.72}$$

$$\frac{C_p}{C_v} = \kappa \tag{2.73}$$

$$T_t = T + \frac{v^2}{2C_p} \tag{2.74}$$

enables to further reduce the non-dimensional equations into

$$\frac{T}{T_t} = \left(1 + \frac{\kappa - 1}{2} M^2\right)^{-1} \tag{2.75}$$

$$\Pi = \frac{p}{p_t} = \left(1 + \frac{\kappa - 1}{2} M^2\right)^{-\frac{\kappa}{\kappa - 1}} \tag{2.76}$$

$$\tilde{\rho} = \frac{\rho R T_t}{p_t} = \left(1 + \frac{\kappa - 1}{2} M^2\right)^{-\frac{1}{\kappa - 1}} \tag{2.77}$$

$$\tilde{m} = \frac{\dot{m}\sqrt{RT_t}}{A p_t \sqrt{\kappa}} = M \left(1 + \frac{\kappa - 1}{2} M^2\right)^{-\frac{1}{2}\frac{\kappa + 1}{\kappa - 1}} \tag{2.78}$$

Eq.2.75 to Eq.2.78 are four supplementary relationships using four independent dimensions of mass, force, temperature and time. The Buckingham pi theorem states therefore that they can be all expressed as function of an unique non-dimensional variable and gives the non dimensional coefficients. According to the classical gas dynamics theory and physical reasons, the Mach number is chosen. It is therefore possible to use only dimensionless parameters depending only on the Mach number. The Newton-Raphson method can be readily applied to the new system of dimensionless equations. Obtaining the principal variable of the problem is possible through the use of the Jacobian matrix of the transformation. This method enables to simplify and homogenise the formalism of the equations. From a computational point of view however the cost generated by the use of dimensionless equations is necessarily greater than that of the direct method:

- As boundary conditions and initial estimates are given in terms of the principal variables, the computation of each nodal Mach number from the principal variables in order to obtain the dimensionless equations must be performed at least once
- the computation of the global Jacobian matrix of the transformation requires to compute the values of the partial derivatives of the Mach number relative to total pressure, total temperature and mass flow rate for the whole system

- The Jacobian matrix of the transformation must be applied at least once in order of obtain results in terms of the principal problem variables.

As it was not deemed possible in the time frame of the present work to implement and compare both methods, in view of the additional requirements of the dimensionless method, it has been chosen to keep the equations explicitly in terms of the principal problem variables.

2.4.3 Orifices

Orifices are generally used as flow regulating devices or pressure adjustment/regulation mean.

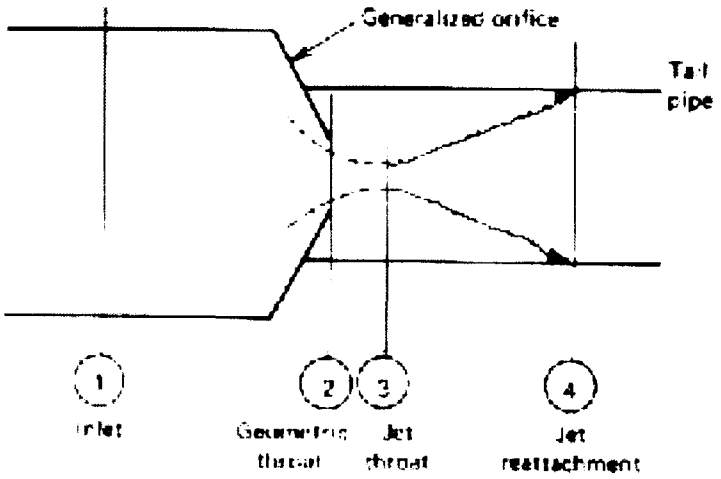

Figure 2.6: Representation of a general orifice, showing axial sections and flow pattern under steady state assumption and high Reynolds number (4×10^3).

Physical model

According to Shapiro [49], for short ducts, as is the case for orifices, nozzles and diffusers, the viscous effects are small as well as the heat exchange during the crossing of the orifice. The flow is isentropic and therefore adiabatic reversible in the free jet stream. The isentropic discharge of a compressible gas out of a pressure tank is in its process similar to an orifice flow. Considering two sections, one upstream of the orifice inlet in the pipe containing the orifice, labelled with subscript $_{in}$, and one at the smallest section of the orifice outlet,labelled with subscript $_{out}$, the equation of continuity for compressible flow is written

$$\rho_{in} A_{in} v_{in} = \rho_{out} A_{out} v_{out} \tag{2.79}$$

The equation of energy for the conditions given is written as the conservation of total enthalpy of the fluid along a streamline

$$\frac{\kappa}{\kappa - 1} \frac{p_{in}}{\rho_{in}} + \frac{v_{in}^2}{2} = \frac{\kappa}{\kappa - 1} \frac{p_{out}}{\rho_{out}} + \frac{v_{out}^2}{2} \tag{2.80}$$

Moreover the fluid in the free jet stream is considered isentropic, and therefore

$$\frac{p_{in}}{\rho_{in}^{\kappa}} = \frac{p_{out}}{\rho_{out}^{\kappa}} \tag{2.81}$$

From Eq.2.80 and Eq.2.81 one obtains

$$\frac{v_{out}^2}{2} - \frac{v_{in}^2}{2} = \frac{\kappa}{\kappa - 1}\frac{p_{in}}{\rho_{in}}\left(1 - \left(\frac{p_{out}}{p_{in}}\right)^{\frac{\kappa-1}{\kappa}}\right) \tag{2.82}$$

Using Eq.2.79 and Eq.2.81 yields

$$v_{in}^2 = \left(\frac{\rho_{out}}{\rho_{in}}\frac{A_{out}}{A_{in}}v_{out}\right)^2 = \left(\frac{p_{out}}{p_{in}}\right)^{\frac{2}{\kappa}}\left(\frac{A_{out}}{A_{in}}\right)^2 v_{out}^2 \tag{2.83}$$

The order of magnitude of the inlet/outlet surface ratio enables to neglect the inlet velocity. In turn one obtains the following formula of the outflow called after Saint-Venant and Wantzel

$$\frac{v_{out}^2}{2} = \frac{\kappa}{\kappa - 1}\frac{p_{in}}{\rho_{in}}\left(1 - \left(\frac{p_{out}}{p_{in}}\right)^{\frac{\kappa-1}{\kappa}}\right) \tag{2.84}$$

Transforming the outlet velocity enables to write

$$\frac{\dot{m}^2}{2\rho_{out}^2 A_{out}^2} = \frac{\kappa}{\kappa - 1}\frac{p_{in}}{\rho_{in}}\left(1 - \left(\frac{p_{out}}{p_{in}}\right)^{\frac{\kappa-1}{\kappa}}\right) \tag{2.85}$$

and in turn using Eq.2.81

$$\dot{m}^2 = A_{out}^2 p_{in}\rho_{in}\left(\frac{p_{out}}{p_{in}}\right)^{\frac{2}{\kappa}}\frac{2\kappa}{\kappa - 1}\left(1 - \left(\frac{p_{out}}{p_{in}}\right)^{\frac{\kappa-1}{\kappa}}\right) \tag{2.86}$$

Subsequently, the non-dimensional reduced mass flow rate is written

$$\frac{\dot{m}\sqrt{RT_{in}}}{A_{out}p_{in}} = \sqrt{\frac{2\kappa}{\kappa - 1}\left(\frac{p_{out}}{p_{in}}\right)^{\frac{2}{\kappa}}\left(1 - \left(\frac{p_{out}}{p_{in}}\right)^{\frac{\kappa-1}{\kappa}}\right)} \tag{2.87}$$

The discharge coefficient of an real orifice, or C_d, is defined as the ratio of the ideal isentropic mass flow rate flowing through the orifice and the real mass flow rate and accounts for the losses and irreversibilities generated while the fluid flows through the orifice. The discharge coefficient is therefore always less than 1 and models the resistance of the flow through the orifice. Therefore $(C_d\ A)$ is an equivalent section and called effective section A_{eff} .

$$C_d = \frac{\dot{m}_{real}}{\dot{m}_{is}} \tag{2.88}$$

$$\frac{\dot{m}\ \sqrt{R\ T_{in}}}{A_{eff}\ p_{in}\ \sqrt{\kappa}} - \sqrt{\frac{2}{\kappa - 1}\left(\frac{p_{out}}{p_{in}}\right)^{\frac{2}{\kappa}}\left(1 - \left(\frac{p_{out}}{p_{in}}\right)^{\frac{\kappa-1}{\kappa}}\right)} = 0 \tag{2.89}$$

Discharge coefficient values are depending on a number of factors such as geometrical parameters of the orifice or Reynolds number. The geometrical parameters which control the discharge coefficient for an orifice

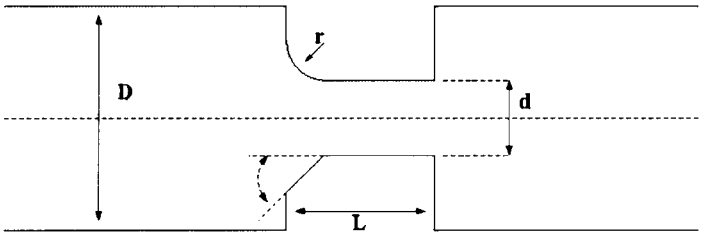

Figure 2.7: Orifice with the relevant geometric parameters affecting the discharge coefficient.

configuration are represented in Fig.2.7. Empirical correlations depending on the geometrical parameters are numerous in the literature. Hay presents a method to compute pressure losses with regard to hole geometrical specifications [19]. The inclination of the hole with regard to the flow direction has been studied by Idris in [23]. The influence of the inlet geometry of the hole (sharp, rounded hole edges, chamfer) is described by Mcgreehan and Schotsch [31]. Parker in [41] and Lichtarowicz [27] add orifice length to the problem as relevant parameter. Rotating holes are also well documented. Several studies have been performed on the subject by Alexiou, [2], Zimmermann [63], or Weissert [59]. Studies by Hasan [18], Dittmann [14]and Popp [42] have been dedicated to special design such as cover plates, and pre-swirl nozzles, concentrating on several aspects of rotating holes.

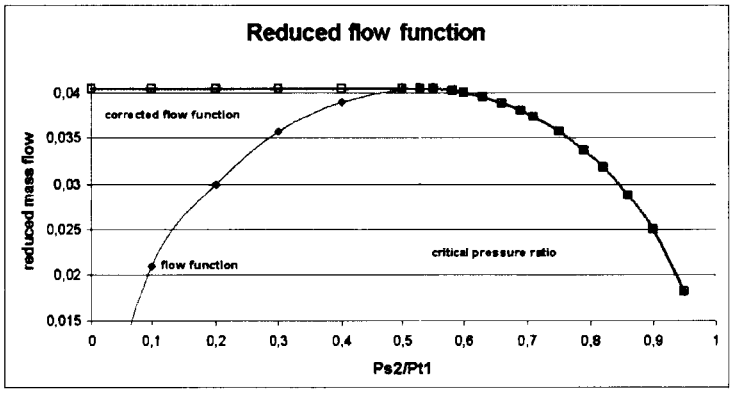

Figure 2.8: Orifice flow characteristic as function of the outlet/inlet pressure ratio under steady state conditions.

The mathematical model described by Eq.2.87, and represented in Fig.2.8 by the diamond-shaped dots, is not consistent with choking. Indeed, after having reached its maximum value, the mass flow rate decreases with decreasing pressure ratio. To take this fact into account, the mass flow rate is defined by two equations over the two domains separated by $\left(\frac{p_{s_{out}}}{p_{t_{in}}}\right)_{crit}$. The domain where $\left(\frac{p_{s_{out}}}{p_{t_{in}}}\right)$ is greater than $\left(\frac{p_{s_{out}}}{p_{t_{in}}}\right)_{crit}$ is called sub-critical domain, the other comprised between $\left(\frac{p_{s_{out}}}{p_{t_{in}}}\right)_{crit}$ and zero is called supercritical domain.

Over the supercritical domain, the reduced mass flow is constant, and over the subcritical domain the reduced mass flow rate follows Eq.2.87. The value of the critical pressure ratio corresponds to the maximum mass flow rate given by Eq.2.87

$$\left(\frac{p_{s_{out}}}{p_{t_{in}}}\right)_{crit} = \left(\frac{2}{\kappa+1}\right)^{\frac{\kappa}{\kappa-1}} \tag{2.90}$$

for this value the corresponding mass flow rate is

$$\dot{m}_{crit} = \frac{A_{eff}\, p_{in}}{\sqrt{T_{in}}}\sqrt{\frac{\kappa}{R}\left(\frac{\kappa+1}{2}\right)^{-\frac{\kappa+1}{\kappa-1}}} \tag{2.91}$$

Under these conditions the mathematical model for an orifice can be summed up as:
If $\frac{p_{s_{out}}}{p_{t_{in}}} \leq \left(\frac{2}{\kappa+1}\right)^{\frac{\kappa}{\kappa-1}}$ then

$$\left(\frac{\dot{m}\,\sqrt{T_{in}R}}{A_{eff}\, p_{in}\,\sqrt{\kappa}}\right) - \sqrt{\left(\frac{\kappa+1}{2}\right)^{-\frac{\kappa+1}{\kappa-1}}} = 0 \tag{2.92}$$

If $\frac{p_{s_{out}}}{p_{t_{in}}} > \left(\frac{2}{\kappa+1}\right)^{\frac{\kappa}{\kappa-1}}$ then

$$\frac{\dot{m}\,\sqrt{R\,T_{in}}}{A_{eff}\, p_{in}\sqrt{\kappa}} - \sqrt{\frac{2}{\kappa-1}\left(\frac{p_{out}}{p_{in}}\right)^{\frac{2}{\kappa}}\left(1-\left(\frac{p_{out}}{p_{in}}\right)^{\frac{\kappa-1}{\kappa}}\right)} = 0 \tag{2.93}$$

Differentiating the orifice constitutive equation

The constitutive equation for the orifice has been described in the previous paragraph. This equation is a function of $\dot{m}, T_{in}, p_{in}$,and p_{out}. The differentiation of Eq.2.92 and Eq.2.93 yields:

- In the critical case,

$$f = \left(\frac{\dot{m}\,\sqrt{R\,T_{in}}}{A_{eff}\, p_{in}\,\sqrt{\kappa}}\right)_{crit} - \sqrt{\left(\frac{\kappa+1}{2}\right)^{-\frac{\kappa+1}{\kappa-1}}} = 0 \tag{2.94}$$

$$\frac{\partial f}{\partial T_{in}} = \frac{1}{2}\frac{\dot{m}}{A_{eff}\, p_{in}\,\sqrt{T_{in}}}\sqrt{\frac{R}{\kappa}} \tag{2.95}$$

$$\frac{\partial f}{\partial p_{in}} = -\frac{\dot{m}\,\sqrt{T_{in}}}{A_{eff}\, p_{in}^2}\sqrt{\frac{R}{\kappa}} \tag{2.96}$$

$$\frac{\partial f}{\partial \dot{m}} = \frac{\sqrt{T_{in}}}{A_{eff}\, p_{in}}\sqrt{\frac{R}{\kappa}} \tag{2.97}$$

  All other derivatives of this function are zero.

- in the subcritical case

$$f = \frac{\dot{m}\sqrt{R\,T_{in}}}{A_{eff}\,p_{in}\sqrt{\kappa}} - \sqrt{\frac{2}{\kappa-1}\left(\frac{p_{out}}{p_{in}}\right)^{\frac{2}{\kappa}}\left(1-\left(\frac{p_{out}}{p_{in}}\right)^{\frac{\kappa-1}{\kappa}}\right)} = 0 \tag{2.98}$$

$$\frac{\partial f}{\partial T_{in}} = \frac{1}{2}\frac{\dot{m}}{A_{eff}\,p_{in}\,\sqrt{T_{in}}}\sqrt{\frac{R}{\kappa}} \tag{2.99}$$

$$\frac{\partial f}{\partial p_{in}} = -\frac{\dot{m}\sqrt{RT_{in}}}{A_{eff}\,p_{in}^2\sqrt{\kappa}} + \sqrt{\frac{2}{(\kappa-1)}}\frac{1}{p_{in}}\left(\frac{p_{out}}{p_{in}}\right)^{\frac{1}{\kappa}}\sqrt{1-\left(\frac{p_{out}}{p_{in}}\right)^{\frac{\kappa-1}{\kappa}}}\left(\frac{1}{\kappa}-\frac{\kappa-1}{2\kappa}\frac{\left(\frac{p_{out}}{p_{in}}\right)^{\frac{\kappa-1}{\kappa}}}{1-\left(\frac{p_{out}}{p_{in}}\right)^{\frac{\kappa-1}{\kappa}}}\right) \tag{2.100}$$

$$\frac{\partial f}{\partial \dot{m}} = \frac{\sqrt{T_{in}}}{A_{eff}\,p_{in}}\sqrt{\frac{R}{\kappa}} \tag{2.101}$$

$$\frac{\partial f}{\partial p_{out}} = -\sqrt{\frac{2}{(\kappa-1)}}\frac{1}{p_{out}}\left(\frac{p_{out}}{p_{in}}\right)^{\frac{1}{\kappa}}\sqrt{1-\left(\frac{p_{out}}{p_{in}}\right)^{\frac{\kappa-1}{\kappa}}}\left(\frac{1}{\kappa}-\frac{\kappa-1}{2\kappa}\frac{\left(\frac{p_{out}}{p_{in}}\right)^{\frac{\kappa-1}{\kappa}}}{1-\left(\frac{p_{out}}{p_{in}}\right)^{\frac{\kappa-1}{\kappa}}}\right) \tag{2.102}$$

Discharge coefficients

Three methods have been implemented for the calculation of the discharge coefficient of plain orifices. The Parker and Kercher method is described in detail in [41]. Mcgreehan and Schotsch have developed their method in [31]. Both methods rely on the Reynolds number similitude, and take non-dimensional geometrical representative parameters such as the aspect ratio in order to compute the discharge coefficient. The Parker and Kercher method takes compressibility into account, while Mcgreehan and Schotsch implemented a way to consider rotation without compressibility effects. The Mcgreehan and Schotsch method for rotation has been implemented in Parker and Kercher method.

2.4.4 Labyrinth Seals

The most common type of seal encountered in a jet engine is the labyrinth seal. A labyrinth seal comprises a rotating part with one or several fins and a stator as presented in Fig.2.9. There are two types of labyrinth seal: straight or stepped. Seals play an essential role in the secondary air system as they act as flow metering devices. To control efficiently the amount of flow going in and out of the air system, seals usually have small gaps. As gap definition and deformations induced by thermal expansion and mechanical loads are about the same order of magnitude, the thermomechanical effect on seal leakage is deemed to be significant. It is therefore extremely important to predict accurately the coupling between SAS and thermomechanical phenomena on seals.

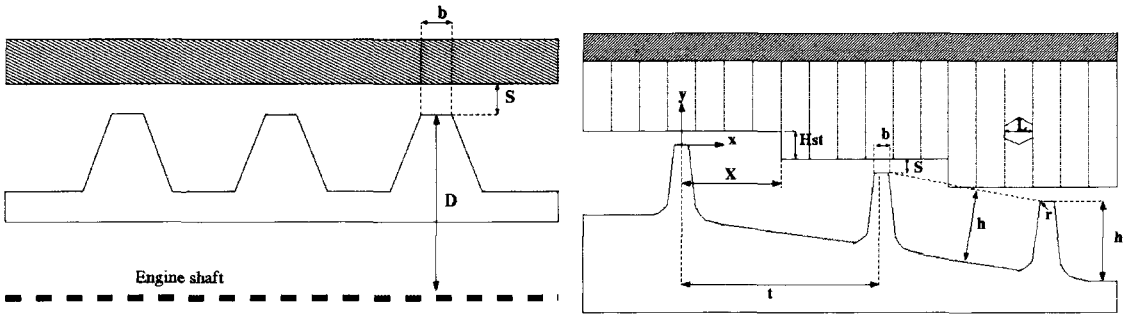

Figure 2.9: Straight and stepped labyrinth seals.

Straight and stepped labyrinth seals

The flow function for the ideal labyrinth has been derived by Egli [16] considering a series of restrictions with a complete dynamic head loss downstream of each fin. The labyrinth flow equation is given by

$$\frac{\dot{m}_{ideal}\sqrt{R\,T_{in}}}{A\,p_{in}} = \sqrt{\frac{1-\left(\frac{p_{out}}{p_{in}}\right)^2}{\left(n-ln\left(\frac{p_{out}}{p_{in}}\right)\right)}} \tag{2.103}$$

A is defined as the annulus area comprised between the stator and the rotor. Fig.2.10 shows the different flow characteristic of a labyrinth as a function of the outlet/inlet pressure ratio and the number of fins. The critical pressure ratio of a labyrinth seal, is given by the formula

$$\left(\frac{p_{out}}{p_{in}}\right)_{crit} = \frac{1}{\sqrt{1+2n-ln\left(\frac{p_{out}}{p_{in}}\right)^2_{crit}}} \tag{2.104}$$

which is obtained by derivating Eq.2.103 with regards to $\frac{p_{out}}{p_{in}}$ This equation is solved iteratively for several values of n from 1 to 9 as displayed below.

fin number	1	2	3	4	5	6	7	8	9
$\frac{p_{out}}{p_{in}}$	0.4711	0.3797	0.3293	0.2957	0.2710	0.2519	0.2365	0.2236	0.2127

Labyrinth reduced mass flow function of the pressure ratio and number of fins.

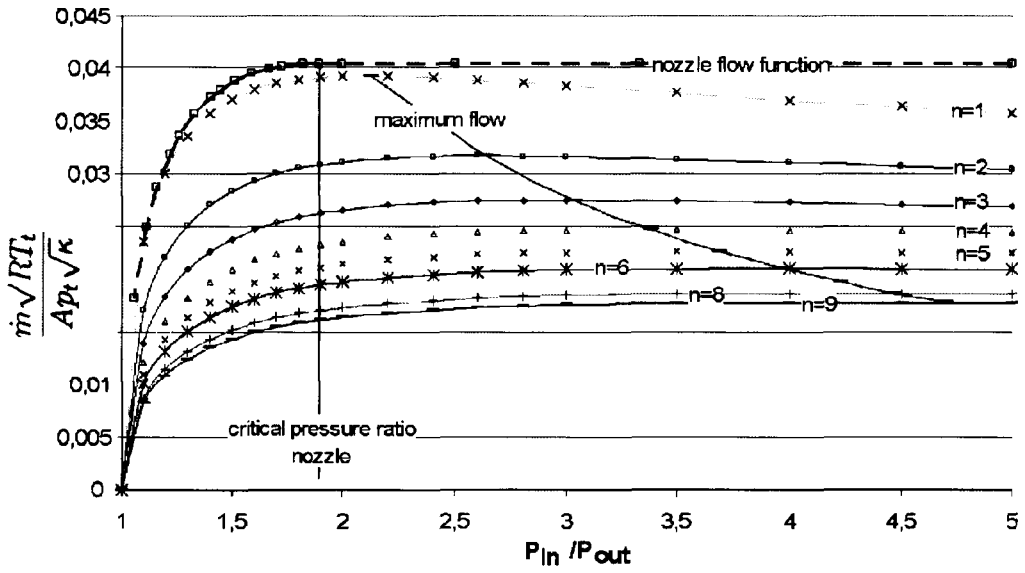

Figure 2.10: Labyrinth reduced mass flow function of the pressure ratio and number of fins under steady state conditions.

Carry Over Factor. The ideal labyrinth flow function (Fig.2.10) implies a complete dynamic head pressure loss downstream of each fin. The carry-over factor, COF, should account for the effect that only a fraction of the dynamic head is lost if the fins are spaced too closely. This effect depends on the number of fins, fin inter-spacing and seal gap. Fig.2.11 shows the carry-over factor for different numbers of fins as a function of the nondimensional ratio t/s, space between two consecutive fins and gap, from Hodkinson [21]. The carry-over factor proposed by Hodkinson is:

$$k = \sqrt{\frac{1}{1 - \frac{n-1}{n}\frac{s/t}{s/t + 0.02}}} \tag{2.105}$$

With the correction factor from [61]

$$k_1 = \sqrt{\frac{n}{n-1}} \tag{2.106}$$

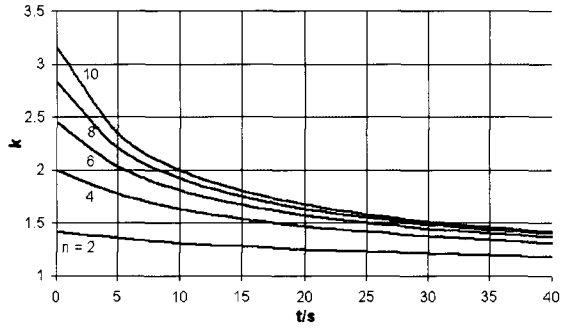

Figure 2.11: Carry-Over Factor from Hodkinson.[21].

a revised carry-over factor k_2, which, according to Zimmermann, better correlates the cumulated effects of the number of fin than the correlation k from Hodkinson is obtained by:

$$k_2 = k_1\, k \tag{2.107}$$

Carry-over factors derived from CFD calculations as tabulated in Zimmermann and Wolff [64] compared with those from equivalent conditions in Fig.2.11, are of the same order of magnitude.

Coefficient of discharge and geometric parameters. As presented in Fig.2.9 several geometrical parameters have an impact on the through-flow capacity of labyrinth seals. The height and width of the fins, their number, the breadth of fin tips used, the distance between two fins, the geometry of the cavities all have been studied by Hodkinson [21]. Willenborg and Wittig [60] studied the impact of stator lining material such as honeycombs on labyrinth seal pressure losses. Wolff and Zimmermann, in [61], review most of the different aspects of labyrinth seals, with either stepped or straight design, and the influence of different geometrical parameters on the discharge coefficient. The data given by Wolff and Zimmermann compare well with MTU proprietary test data and the correlations have therefore been chosen for the labyrinth model.

Differentiating the constitutive equation

Eq.2.103 in the subcritical domain, with $C_1 = COF\ A$, is written as

$$f\left(p_{in}, p_{out}, T_{in}, \dot{m}\right) = \frac{\dot{m}\sqrt{R\,T_{in}}}{p_{in}} - C_1 \sqrt{\frac{1 - \left(\frac{p_{out}}{p_{in}}\right)^2}{\left(n - ln\left(\frac{p_{out}}{p_{in}}\right)\right)}} \tag{2.108}$$

And subsequently the partial derivatives are

$$\frac{\partial f}{\partial T_{in}} = \frac{1}{2}\frac{\dot{m}\sqrt{R}}{p_{in}\sqrt{T_{in}}} \tag{2.109}$$

$$\frac{\partial f}{\partial p_{in}} = -\frac{\dot{m}\sqrt{T_{in}R}}{p_{in}^2} - \frac{C_1}{2}\sqrt{\frac{\left[n - ln\left(\frac{p_{out}}{p_{in}}\right)\right]}{1-\left[\frac{p_{out}}{p_{in}}\right]^2}}\left(\frac{2\frac{p_{out}^2}{p_{in}^3}}{\left[n - ln\left(\frac{p_{out}}{p_{in}}\right)\right]} - \frac{1-\left(\frac{p_{out}}{p_{in}}\right)^2}{\left[n - ln\left(\frac{p_{out}}{p_{in}}\right)\right]^2}\frac{1}{p_{in}}\right) \tag{2.110}$$

$$\frac{\partial f}{\partial p_{out}} = -\frac{C_1}{2}\sqrt{\frac{\left[n - ln\left(\frac{p_{out}}{p_{in}}\right)\right]}{1-\left[\frac{p_{out}}{p_{in}}\right]^2}}\left(\frac{-2\frac{p_{out}}{p_{in}^2}}{\left[n - ln\left(\frac{p_{out}}{p_{in}}\right)\right]} + \frac{1+\left(\frac{p_{out}}{p_{in}}\right)^2}{\left[n - ln\left(\frac{p_{out}}{p_{in}}\right)\right]^2}\frac{1}{p_{out}}\right) \tag{2.111}$$

$$\frac{\partial f}{\partial \dot{m}} = \frac{\sqrt{T_{in}R}}{p_{in}} \tag{2.112}$$

In the critical case the flow function for labyrinth seals reduces to

$$f\left(p_{in}, T_{in}, \dot{m}\right) = \frac{\dot{m}\sqrt{T_{in}R}}{p_{t_{in}}} - C_2 \tag{2.113}$$

with $C_2 = C_1\sqrt{\frac{1-\left(\frac{p_{out}}{p_{in}}\right)_{crit}^2}{\left(n-ln\left(\frac{p_{out}}{p_{in}}\right)_{crit}\right)}}$

The partial derivatives of Eq.2.113 are

$$\frac{\partial f}{\partial T_{in}} = \frac{1}{2}\frac{\dot{m}\sqrt{R}}{p_{in}\sqrt{T_{in}}} \tag{2.114}$$

$$\frac{\partial f}{\partial p_{in}} = -\frac{\dot{m}\sqrt{T_{in}R}}{p_{in}^2} \tag{2.115}$$

$$\frac{\partial f}{\partial p_{out}} = 0 \tag{2.116}$$

$$\frac{\partial f}{\partial \dot{m}} = \frac{\sqrt{T_{in}R}}{p_{in}} \tag{2.117}$$

2.4.5 Pipes with friction and constant section

This type of element enables to model pipe flows with friction in several thermal configurations. Inlet and outlet losses are not considered in this part.

Physical formulation

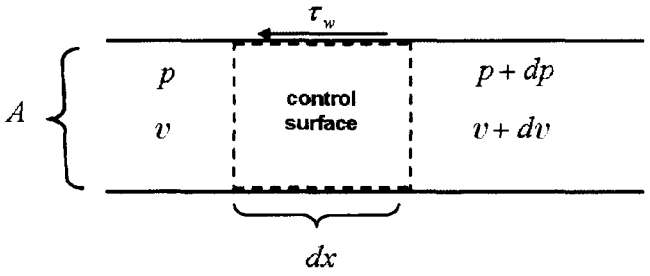

Figure 2.12: Balance of forces acting on a pipe element.

Considering Fig.2.12, the balance of the forces acting on the control volume is

$$Ap - A\left(p + dp\right) - \tau_w dA_w = \rho A v \left(v + dv\right) - \rho A v v \tag{2.118}$$

$$- Adp - \tau_w dA_w + = \rho A v dv \tag{2.119}$$

Using the definition of the wall shear stress $\tau_w = \frac{\lambda}{4}\frac{\rho}{2}v^2$, where λ is the Darcy friction factor and dividing by A gives

$$- dp - \frac{\lambda}{4}\frac{\rho}{2}v^2\frac{dA_w}{A} = \rho\frac{dv^2}{2} \tag{2.120}$$

As $\frac{dA_w}{A} = \frac{\pi D dx}{\frac{D^2}{\pi\frac{}{4}}}$, the momentum equation is written as

$$\boxed{\rho\frac{dv^2}{2} + dp + \frac{\lambda}{D}\frac{\rho}{2}v^2 dx = 0} \tag{2.121}$$

For pipe flow with friction two conditions of practical importance are discussed in the present context: adiabatic and isothermal flows. At low velocities the effect of natural heat transfer tends to be more important, resulting in an isothermal process, while at high velocities, the quick change of energy generating fast changes in temperature over a short length of duct is predominant over the natural heat transfer effect. Under these circumstances adiabatic conditions are approximated.

In order to obtain the governing equations for pipe flow with friction in both cases, the following equations are used:

- state equation under differential form

$$\frac{dp}{d\rho} + \frac{dT}{T} + \frac{dp}{p} = 0 \tag{2.122}$$

- mass conservation

$$\frac{d\rho}{\rho} + \frac{dv}{v} + \frac{dA}{A} = 0 \tag{2.123}$$

- conservation of energy

$$vdv + C_p dT = dQ \tag{2.124}$$

- conservation of momentum, Eq.2.121.

Adiabatic case

Under adiabatic flow conditions and with a constant section $dQ = 0$ and $dA = 0$. From Eq2.123 one gets

$$\frac{d\rho}{\rho} = -\frac{dv}{v} \tag{2.125}$$

Using Eq.2.122 and Eq.2.125yields

$$\frac{dp}{p} = -\frac{dv}{v} + \frac{dT}{T} \tag{2.126}$$

Using Eq.2.124 one obtains

$$CpdT = -vdv \tag{2.127}$$

which is transformed into

$$\frac{\kappa}{\kappa - 1} RT \frac{dT}{T} = -v^2 \frac{dv}{v} \tag{2.128}$$

and in turn

$$\frac{dT}{T} = -\left(\kappa - 1\right) \frac{v^2}{\kappa RT} \frac{dv}{v} \tag{2.129}$$

Introducing the Mach number

$$M = \frac{v}{\sqrt{\kappa RT}} \tag{2.130}$$

leads to

$$\frac{dT}{T} = -\left(\kappa - 1\right) M^2 \frac{dv}{v} \tag{2.131}$$

Combining Eq.2.126 and Eq.2.131 yields

$$\frac{dp}{p} = -\frac{dv}{v} - (\kappa - 1) M^2 \frac{dv}{v} \tag{2.132}$$

$$\frac{dp}{p} = -\left[1 + (\kappa - 1) M^2\right] \frac{dv}{v} \tag{2.133}$$

Using Eq.2.121 leads to

$$v^2 \frac{dv}{v} + RT \frac{dp}{p} + \frac{\lambda}{2} v^2 \frac{dx}{D} = 0 \tag{2.134}$$

and using Eq.2.133 in Eq.2.134 we get

$$v^2 \frac{dv}{v} - RT\left[1 + (\kappa - 1) M^2\right] \frac{dv}{v} + \frac{\lambda}{2} v^2 \frac{dx}{D} = 0 \tag{2.135}$$

$$\frac{dv}{v}\left[v^2 - \kappa RT \frac{1}{\kappa}\left[1 + (\kappa - 1) M^2\right]\right] + \frac{\lambda}{2} v^2 \frac{dx}{D} = 0 \tag{2.136}$$

$$\frac{dv}{v}\left[M^2 - \frac{1}{\kappa}\left[1 + (\kappa - 1) M^2\right]\right] + \frac{\lambda}{2} M^2 \frac{dx}{D} = 0 \tag{2.137}$$

$$\frac{dv}{v} \frac{1}{\kappa}\left(M^2 - 1\right) + \frac{\lambda}{2} M^2 \frac{dx}{D} = 0 \tag{2.138}$$

$$\frac{dv}{v} - \kappa \frac{M^2}{M^2 - 1} \frac{\lambda}{2} \frac{dx}{D} = 0 \tag{2.139}$$

$$\tag{2.140}$$

From Eq.2.130 one obtains

$$\frac{dM}{M} = \frac{dv}{v} - \frac{1}{2} \frac{dT}{T} \tag{2.141}$$

Using Eq.2.131 in Eq.2.141 leads to

$$\frac{dM}{M} = \frac{dv}{v}\left(1 + \frac{\kappa - 1}{2} M^2\right) \tag{2.142}$$

Using Eq.2.142 in Eq.2.140 yields the constitutive equation

$$\boxed{\frac{dM}{M} = \frac{\kappa M^2 \left(1 + \frac{\kappa - 1}{2} M^2\right)}{2\left(1 - M^2\right)} \lambda \frac{dx}{D}} \tag{2.143}$$

Eq.2.143 is now written as

$$\frac{-2\left(1 - M^2\right)}{\kappa M^3 \left(1 + \frac{\kappa - 1}{2} M^2\right)} dM + \frac{\lambda dx}{D} = 0 \tag{2.144}$$

Since $\frac{\lambda dx}{D}$ is positive, the following conclusions can be drawn:

$$M < 1 \qquad \frac{dM}{dx} > 0 \tag{2.145}$$

$$M = 1 \qquad \frac{dM}{dx} \to \infty \tag{2.146}$$

$$M > 1 \qquad \frac{dM}{dx} < 0 \tag{2.147}$$

In both subsonic and supersonic cases the effect of friction is to get the Mach number to approach unity. Therefore, an initially subsonic flow will never achieve supersonic conditions and a supersonic flow will never become subsonic. The sonic condition cannot occur part way of the tube and the only place where it may be reached is at the downstream extremity of the tube, provided that the cross section downstream of the tube is greater than the cross section of the tube.

In order to proceed to its integration, Eq.2.143 is transformed using

$$\frac{dM}{M} = \frac{1}{2}\frac{dM^2}{M^2} \tag{2.148}$$

$$\int_0^L \frac{1-M^2}{\kappa M^2\left(1+\frac{\kappa-1}{2}M^2\right)}\frac{dM^2}{M^2} = \int_0^L \lambda\frac{dx}{D} \tag{2.149}$$

$$= \lambda\frac{L}{D} \tag{2.150}$$

In order to integrate the left hand side, M^2 is replaced by Z and a partial fraction extension of the integrand is performed.

$$\begin{aligned}\frac{1-Z}{Z^2\left(1+\frac{\kappa-1}{2}Z\right)} &= \frac{1}{Z^2\left(1+\frac{\kappa-1}{2}Z\right)} - \frac{1}{Z\left(1+\frac{\kappa-1}{2}Z\right)} \\ &= -\frac{\kappa-1}{2Z} + \frac{1}{Z^2} + \frac{\left(\frac{\kappa-1}{2}\right)^2}{1+\frac{\kappa-1}{2}Z} - \frac{1}{Z} + \frac{\frac{\kappa-1}{2}}{1+\frac{\kappa-1}{2}Z} \\ &= -\frac{\kappa+1}{2}\frac{1}{Z} + \frac{1}{Z^2} + \frac{\kappa-1}{2}\frac{\kappa+1}{2}\frac{1}{1+\frac{\kappa-1}{2}Z}\end{aligned} \tag{2.151}$$

$$\begin{aligned}\int \frac{1-Z}{Z^2\left(1+\frac{\kappa-1}{2}Z\right)}dZ &= -\frac{\kappa+1}{2}lnZ - \frac{1}{Z} + \frac{\kappa+1}{2}ln\left(1+\frac{\kappa-1}{2}Z\right) \\ &= -\frac{1}{Z} + \frac{\kappa+1}{2}ln\left(\frac{1+\frac{\kappa-1}{2}Z}{Z}\right)\end{aligned} \tag{2.152}$$

A solution of Eq.2.143 is therefore

$$\boxed{\frac{1}{\kappa}\left(\frac{1}{M_1^2}-\frac{1}{M_2^2}\right)+\frac{\kappa+1}{2\kappa}ln\left(\frac{1+\frac{\kappa-1}{2}M_2^2}{1+\frac{\kappa-1}{2}M_1^2}\frac{M_1^2}{M_2^2}\right)=\lambda\frac{L}{D}} \tag{2.153}$$

As already shown, at the end extremity of the pipe the Mach number M_2 cannot exceed 1. Therefore, in the limit case Eq.2.153 becomes

$$\boxed{\frac{1-M_{1max}^2}{\kappa M_{1max}^2}+\frac{\kappa+1}{2\kappa}ln\left(\frac{\frac{\kappa+1}{2}M_{1max}^2}{1+\frac{\kappa-1}{2}M_{1max}^2}\right)=\lambda\frac{L}{D}} \tag{2.154}$$

Both Eq.2.153 and Eq.2.154 are mentioned by Ward-Smith in [58] and by Shapiro in [49]. In order to obtain Eq.2.153 as a function of the problem variables the Mach number is first transformed using

$$\begin{aligned} M &= \frac{v}{\sqrt{\kappa RT}} \\ &= \frac{\dot{m}}{\rho A\sqrt{\kappa RT}} \\ &= \frac{\dot{m}\sqrt{RT}}{\sqrt{\kappa}Ap} \end{aligned} \tag{2.155}$$

and combined with the isentropic relationship

$$\frac{T_t}{T}=(1+\frac{\kappa+1}{2}M^2) \tag{2.156}$$

which gives

$$\frac{A^2}{R\dot{m}^2}\left(\frac{p_1^2}{T_1}-\frac{p_2^2}{T_2}\right)+\frac{\kappa+1}{2\kappa}ln\left(\frac{T_{t2}}{T_2}\frac{T_1}{T_{t1}}\frac{p_2^2T_1}{P_1^2T_2}\right)=\frac{\lambda L}{D} \tag{2.157}$$

In order to make the total pressure appear in the equation, the isentropic relationship is used $p=p_t\left(\frac{T}{T_t}\right)^{\frac{\kappa}{\kappa-1}}$. This yields

$$\boxed{f=\frac{A^2}{R\dot{m}^2}\left(\frac{p_{t1}^2T_1^{\frac{\kappa+1}{\kappa-1}}}{T_{t1}^{\frac{2\kappa}{\kappa-1}}}-\frac{p_{t2}^2T_2^{\frac{\kappa+1}{\kappa-1}}}{T_{t2}^{\frac{2\kappa}{\kappa-1}}}\right)+\frac{\kappa+1}{2\kappa}ln\left(\frac{T_{t2}}{T_2}\frac{T_1}{T_{t1}}\frac{p_{t2}^2T_2^{\frac{\kappa+1}{\kappa-1}}}{T_{t2}^{\frac{2\kappa}{\kappa-1}}}\frac{T_{t1}^{\frac{2\kappa}{\kappa-1}}}{p_{t1}^2T_1^{\frac{\kappa+1}{\kappa-1}}}\right)-\frac{\lambda L}{D}=0} \tag{2.158}$$

Once this equation is obtained it is further differentiated with regard to all the variables in order to comply with the Newton-Raphson method, which gives

$$\frac{\partial f}{\partial\dot{m}}=-\frac{2A^2}{R\dot{m}^3}\left(\frac{p_{t1}^2T_1^{\frac{\kappa+1}{\kappa-1}}}{T_{t1}^{\frac{2\kappa}{\kappa-1}}}-\frac{p_{t2}^2T_2^{\frac{\kappa+1}{\kappa-1}}}{T_{t2}^{\frac{2\kappa}{\kappa-1}}}\right) \tag{2.159}$$

$$\frac{\partial f}{\partial p_{t1}} = \frac{A^2}{R\dot{m}^2}\left(\frac{2p_{t1}T_1^{\frac{\kappa+1}{\kappa-1}}}{T_{t1}^{\frac{2\kappa}{\kappa-1}}}\right) - \frac{\kappa+1}{\kappa}\frac{1}{p_{t1}} \tag{2.160}$$

$$\frac{\partial f}{\partial p_{t2}} = \frac{A^2}{R\dot{m}^2}\left(\frac{-2p_{t2}T_2^{\frac{\kappa+1}{\kappa-1}}}{T_{t2}^{\frac{2\kappa}{\kappa-1}}}\right) + \frac{\kappa+1}{\kappa}\frac{1}{p_{t2}} \tag{2.161}$$

$$\frac{\partial f}{\partial T_{t1}} = \frac{A^2}{R\dot{m}^2}\left(-\frac{2\kappa}{\kappa-1}\frac{p_{t1}^2T_1^{\frac{\kappa+1}{\kappa-1}}}{T_{t1}^{\frac{2\kappa}{\kappa-1}}}\frac{1}{T_{t1}}\right) + \frac{\kappa+1}{2\kappa}\left(-\frac{1}{T_{t1}} + \frac{2\kappa}{\kappa+1}\frac{1}{T_{t1}}\right) \tag{2.162}$$

$$\frac{\partial f}{\partial T_{t2}} = \frac{A^2}{R\dot{m}^2}\left(\frac{2\kappa}{\kappa-1}\frac{p_{t2}^2T_1^{\frac{\kappa+1}{\kappa-1}}}{T_{t2}^{\frac{2\kappa}{\kappa-1}}}\frac{1}{T_{t2}}\right) + \frac{\kappa+1}{2\kappa}\left(\frac{1}{T_{t2}} - \frac{2\kappa}{\kappa-1}\frac{1}{T_{t2}}\right) \tag{2.163}$$

$$\frac{\partial f}{\partial T_1} = \frac{A^2}{R\dot{m}^2}\left(\frac{\kappa+1}{\kappa-1}\frac{p_{t1}^2T_1^{\frac{\kappa+1}{\kappa-1}}}{T_{t1}^{\frac{2\kappa}{\kappa-1}}}\frac{1}{T_1}\right) + \frac{\kappa+1}{2\kappa}\left(\frac{1}{T_1} - \frac{\kappa+1}{\kappa-1}\frac{1}{T_1}\right) \tag{2.164}$$

$$\frac{\partial f}{\partial T_2} = \frac{A^2}{R\dot{m}^2}\left(-\frac{\kappa+1}{\kappa-1}\frac{p_{t2}^2T_2^{\frac{\kappa+1}{\kappa-1}}}{T_{t2}^{\frac{2\kappa}{\kappa-1}}}\frac{1}{T_2}\right) + \frac{\kappa+1}{2\kappa}\left(-\frac{1}{T_2} + \frac{\kappa+1}{\kappa-1}\frac{1}{T_2}\right) \tag{2.165}$$

In the critical case Eq.2.154 is written as

$$\boxed{f = \frac{1}{\kappa}\left(\frac{A^2\kappa}{R\dot{m}^2}\frac{p_{t1}^2T_1^{\frac{\kappa+1}{\kappa-1}}}{T_{t1}^{\frac{2\kappa}{\kappa-1}}} - 1\right) + \frac{\kappa+1}{2\kappa}\left(ln\left(\frac{T_1}{T_{t1}}\right) - ln\left(\frac{2}{\kappa+1}\frac{A^2\kappa}{R\dot{m}^2}\frac{p_{t1}^2T_1^{\frac{\kappa+1}{\kappa-1}}}{T_{t1}^{\frac{2\kappa}{\kappa-1}}}\right)\right) - \frac{\lambda L}{D} = 0} \tag{2.166}$$

The partial derivatives of this equation are

$$\frac{\partial f}{\partial \dot{m}} = \frac{2}{\dot{m}}\left(-\frac{A^2}{R\dot{m}^2}\frac{p_{t1}^2T_1^{\frac{\kappa+1}{\kappa-1}}}{T_{t1}^{\frac{2\kappa}{\kappa-1}}} + \frac{\kappa+1}{2\kappa}\right) \tag{2.167}$$

$$\frac{\partial f}{\partial p_{t1}} = \frac{2}{p_{t1}}\left(\frac{A^2}{R\dot{m}^2}\frac{p_{t1}^2T_1^{\frac{\kappa+1}{\kappa-1}}}{T_{t1}^{\frac{2\kappa}{\kappa-1}}} - \frac{\kappa+1}{2\kappa}\right) \tag{2.168}$$

$$\frac{\partial f}{\partial T_{t1}} = \frac{2\kappa}{\kappa-1}\frac{1}{T_{t1}}\left(-\frac{A^2}{R\dot{m}^2}\frac{p_{t1}^2T_1^{\frac{\kappa+1}{\kappa-1}}}{T_{t1}^{\frac{2\kappa}{\kappa-1}}} + 1\right) - \frac{\kappa+1}{2\kappa}\frac{1}{Tt1} \tag{2.169}$$

$$\frac{\partial f}{\partial T_1} = \frac{\kappa+1}{\kappa-1}\frac{1}{T_1}\left(\frac{A^2}{R\dot{m}^2}\frac{p_{t1}^2T_1^{\frac{\kappa+1}{\kappa-1}}}{T_{t1}^{\frac{2\kappa}{\kappa-1}}} - 1\right) + \frac{\kappa+1}{2\kappa}\frac{1}{T1} \tag{2.170}$$

Isothermal case

In the case of an isothermal flow in a pipe with constant section $dT = 0$ and $dA = 0$.

From Eq.2.122 and Eq.2.123 one gets

$$\frac{dv}{v} = -\frac{dp}{\rho} = -\frac{dp}{p} \tag{2.171}$$

Using Eq.2.121 and Eq.2.171 and replacing velocity by Mach number yields

$$-\kappa RTM^2\frac{dp}{p} + RT\frac{dp}{p} + \lambda\kappa RT\frac{M^2}{2}\frac{dx}{D} = 0 \tag{2.172}$$

$$\frac{dp}{p}\left(1-\kappa M^2\right) + \lambda\kappa\frac{M^2}{2}\frac{dx}{D} = 0 \tag{2.173}$$

and finally

$$\frac{dp}{p} = -\frac{\kappa M^2}{1-\kappa M^2}\frac{\lambda}{2}\frac{dx}{D} = 0 \tag{2.174}$$

The relationship $v = \sqrt{\kappa RT}M$ yields for isothermal flow $\frac{dv}{v} = \frac{dM}{M}$. Using this formula in Eq.2.174 yields

$$\frac{dM}{M} = \frac{\kappa M^2}{1-\kappa M^2}\frac{\lambda}{2}\frac{dx}{D} = 0 \tag{2.175}$$

and in turn

$$\frac{1-\kappa M^2}{\kappa M^2}\frac{dM^2}{M^2} = \frac{\lambda}{2}\frac{dx}{D} \tag{2.176}$$

Eq.2.176 is written as

$$-\frac{2\left(1+\kappa M^2\right)}{\kappa M^3}dM + \frac{\lambda dx}{D} = 0 \tag{2.177}$$

Since $\frac{\lambda dx}{D}$ is positive the following conclusions apply

$$\kappa M^2 < 1 \qquad \frac{dM}{dx} > 0 \tag{2.178}$$

$$\kappa M^2 = 1 \qquad \frac{dM}{dx} \to \infty \tag{2.179}$$

$$\kappa M^2 > 1 \qquad \frac{dM}{dx} < 0 \tag{2.180}$$

In comparison with adiabatic flow the change occurring in the flow depends on the magnitude of κM^2 compared to unity. Independent of whether the flow Mach number is greater or less than $\frac{1}{\sqrt{\kappa}}$, the effect of friction in isothermal flow is to let the Mach number tend towards the limit $\frac{1}{\sqrt{\kappa}}$. Eq.2.177 shows that the condition $M = \frac{1}{\sqrt{\kappa}}$ may only occur at the downstream extremity of the pipe.

In order to integrate Eq.2.176 the same substitution used for the adiabatic case is applied, $Z = M^2$ and the left hand side is decomposed into a partial fraction which yields

$$\frac{1-\kappa Z}{\kappa Z}\frac{dZ}{Z} = \frac{1}{\kappa}\frac{dZ}{Z^2} - \frac{dZ}{Z} \tag{2.181}$$

and Eq.2.176 is integrated leading to the following form

$$\boxed{\frac{1}{\kappa}\left(\frac{1}{M_1^2}-\frac{1}{M_2^2}\right)+ln\left(\frac{M_1^2}{M_2^2}\right)=\frac{\lambda L}{D}} \tag{2.182}$$

In the critical case, where $M_{2max}=\frac{1}{\sqrt{\kappa}}$ Eq.2.182 reduces to

$$\boxed{\frac{1-\kappa M_{1max}^2}{\kappa M_{1max}^2}+ln\left(\kappa M_{1max}^2\right)=\frac{\lambda L}{D}} \tag{2.183}$$

Both Eq.2.182 and Eq.2.183 are mentioned by Ward-Smith in [58] and by Shapiro in [49].

Eq.2.182 is in turn written as

$$\boxed{f=\frac{A^2}{R\dot{m}^2}\left(\frac{p_{t1}^2T_1^{\frac{\kappa+1}{\kappa-1}}}{T_{t1}^{\frac{2\kappa}{\kappa-1}}}-\frac{p_{t2}^2T_2^{\frac{\kappa+1}{\kappa-1}}}{T_{t2}^{\frac{2\kappa}{\kappa-1}}}\right)+ln\left(\frac{p_{t2}^2T_2^{\frac{\kappa+1}{\kappa-1}}}{T_{t2}^{\frac{2\kappa}{\kappa-1}}}\right)-ln\left(\frac{p_{t1}^2T_1^{\frac{\kappa+1}{\kappa-1}}}{T_{t1}^{\frac{2\kappa}{\kappa-1}}}\right)-\frac{\lambda L}{D}=0} \tag{2.184}$$

Once Eq.2.184 is obtained it is further differentiated with regard to all the variables, which gives

$$\frac{\partial f}{\partial\dot{m}}=-\frac{2A^2}{R\dot{m}^3}\left(\frac{p_{t1}^2T_1^{\frac{\kappa+1}{\kappa-1}}}{T_{t1}^{\frac{2\kappa}{\kappa-1}}}-\frac{p_{t2}^2T_2^{\frac{\kappa+1}{\kappa-1}}}{T_{t2}^{\frac{2\kappa}{\kappa-1}}}\right) \tag{2.185}$$

$$\frac{\partial f}{\partial p_{t1}}=\frac{A^2}{R\dot{m}^2}\left(\frac{2p_{t1}T_1^{\frac{\kappa+1}{\kappa-1}}}{T_{t1}^{\frac{2\kappa}{\kappa-1}}}\right)-\frac{2}{p_{t1}} \tag{2.186}$$

$$\frac{\partial f}{\partial p_{t2}}=\frac{A^2}{R\dot{m}^2}\left(\frac{-2p_{t2}T_2^{\frac{\kappa+1}{\kappa-1}}}{T_{t2}^{\frac{2\kappa}{\kappa-1}}}\right)+\frac{2}{p_{t2}} \tag{2.187}$$

$$\frac{\partial f}{\partial T_{t1}}=\frac{A^2}{R\dot{m}^2}\left(-\frac{2\kappa}{\kappa-1}\frac{p_{t1}^2T_1^{\frac{\kappa+1}{\kappa-1}}}{T_{t1}^{\frac{2\kappa}{\kappa-1}}}\frac{1}{T_{t1}}\right)+\frac{2\kappa}{\kappa+1}\frac{1}{T_{t1}} \tag{2.188}$$

$$\frac{\partial f}{\partial T_{t2}}=\frac{A^2}{R\dot{m}^2}\left(\frac{2\kappa}{\kappa-1}\frac{p_{t2}^2T_2^{\frac{\kappa+1}{\kappa-1}}}{T_{t2}^{\frac{2\kappa}{\kappa-1}}}\frac{1}{T_{t2}}\right)-\frac{2\kappa}{\kappa-1}\frac{1}{T_{t2}} \tag{2.189}$$

$$\frac{\partial f}{\partial T_1}=\frac{A^2}{R\dot{m}^2}\left(\frac{\kappa+1}{\kappa-1}\frac{p_{t1}^2T_1^{\frac{\kappa+1}{\kappa-1}}}{T_{t1}^{\frac{2\kappa}{\kappa-1}}}\frac{1}{T_1}\right)+\frac{\kappa+1}{\kappa-1}\frac{1}{T_1} \tag{2.190}$$

$$\frac{\partial f}{\partial T_2}=\frac{A^2}{R\dot{m}^2}\left(-\frac{\kappa+1}{\kappa-1}\frac{p_{t2}^2T_2^{\frac{\kappa+1}{\kappa-1}}}{T_{t2}^{\frac{2\kappa}{\kappa-1}}}\frac{1}{T_2}\right)-\frac{\kappa+1}{\kappa-1}\frac{1}{T_2} \tag{2.191}$$

In the critical case, Eq.2.183 is written as

$$\boxed{f = \left(\frac{A^2}{R\dot{m}^2} \frac{p_{t1}^2 T_1^{\frac{\kappa+1}{\kappa-1}}}{T_{t1}^{\frac{2\kappa}{\kappa-1}}} - 1 \right) - ln \left(\frac{A^2}{R\dot{m}^2} \frac{p_{t1}^2 T_1^{\frac{\kappa+1}{\kappa-1}}}{T_{t1}^{\frac{2\kappa}{\kappa-1}}} \right) - \frac{\lambda L}{D} = 0} \tag{2.192}$$

and the related first derivatives are

$$\frac{\partial f}{\partial \dot{m}} = \frac{2}{\dot{m}} \left(-\frac{A^2}{R\dot{m}^2} \frac{p_{t1}^2 T_1^{\frac{\kappa+1}{\kappa-1}}}{T_{t1}^{\frac{2\kappa}{\kappa-1}}} + 1 \right) \tag{2.193}$$

$$\frac{\partial f}{\partial p_{t1}} = \frac{2}{p_{t1}} \left(\frac{A^2}{R\dot{m}^2} \frac{p_{t1}^2 T_1^{\frac{\kappa+1}{\kappa-1}}}{T_{t1}^{\frac{2\kappa}{\kappa-1}}} - 1 \right) \tag{2.194}$$

$$\frac{\partial f}{\partial T_{t1}} = \frac{2\kappa}{\kappa-1} \frac{1}{T_{t1}} \left(-\frac{A^2}{R\dot{m}^2} \frac{p_{t1}^2 T_1^{\frac{\kappa+1}{\kappa-1}}}{T_{t1}^{\frac{2\kappa}{\kappa-1}}} + 1 \right) \tag{2.195}$$

$$\frac{\partial f}{\partial T_1} = \frac{\kappa+1}{\kappa-1} \frac{1}{T_1} \left(\frac{A^2}{R\dot{m}^2} \frac{p_{t1}^2 T_1^{\frac{\kappa+1}{\kappa-1}}}{T_{t1}^{\frac{2\kappa}{\kappa-1}}} - 1 \right) \tag{2.196}$$

Static temperatures

In both adiabatic and isothermal cases the equations obtained are a function of inlet/outlet static temperatures. Therefore for both adiabatic and isothermal cases, the Newton-Raphson method is written at iteration k in the form

$$\begin{aligned} & f(\dot{m}, T_{t1}, T_{t2}, p_{t1}, p_{t2}, T_1, T_2)_k + \left(\frac{\partial f}{\partial \dot{m}}\right)_k \Delta \dot{m}_k \\ & + \left(\frac{\partial f}{\partial T_{t1}}\right)_k \Delta T_{t1k} + \left(\frac{\partial f}{\partial T_{t2}}\right)_k \Delta T_{t2k} \\ & + \left(\frac{\partial f}{\partial p_{t1}}\right)_k \Delta p_{t1k} + \left(\frac{\partial f}{\partial p_{t2}}\right)_k \Delta p_{t2k} \\ & + \left(\frac{\partial f}{\partial T_1}\right)_k \Delta T_{1k} + \left(\frac{\partial f}{\partial T_2}\right)_k \Delta T_{2k} \end{aligned} \tag{2.197}$$

Since the static temperature is not a primary variable, the equations previously obtained are supplemented by the relationship between static and total temperatures either at pipe inlet or outlet

$$T_t = T + \frac{v^2}{2C_p} \tag{2.198}$$

Reformulating this expression using the equation of state, mass conservation and the isentropic relationship yields

$$T_t = T + \frac{\dot{m}^2 R^2 T^2}{2C_p A^2 p_t^2 \left(\frac{T}{T_t}\right)^{\frac{2\kappa}{\kappa-1}}} \tag{2.199}$$

which in turn can be transformed into

$$g\left(T,Tt,pt,\dot{m}\right)=\left(T_t-T\right)\left(2C_pA^2p_t^2\left(\frac{T}{T_t}\right)^{\frac{2\kappa}{\kappa-1}}\right)-\dot{m}^2R^2T^2=0 \tag{2.200}$$

This equation is of the form $g\left(T,Tt,pt,\dot{m}\right)=0$. The Newton-Raphson differentiation leads to

$$g\left(T^0,T_t^0,p_t^0,\dot{m}^0\right)+\frac{\partial g}{\partial T_0}\Delta T+\frac{\partial g}{\partial T_{t\,0}}\Delta T_t+\frac{\partial g}{\partial p_{t\,0}}\Delta p_t+\frac{\partial g}{\partial \dot{m}\,0}\Delta\dot{m}\backsimeq 0 \tag{2.201}$$

ΔT is subsequently expressed as

$$\Delta T=-\frac{g\left(T^0,T_t^0,p_t^0\dot{m}^0\right)+\frac{\partial g}{\partial T_t\,0}\Delta T_t+\frac{\partial g}{\partial p_{t\,0}}\Delta p_t+\frac{\partial g}{\partial \dot{m}\,0}\Delta\dot{m}}{\frac{\partial g}{\partial T\,0}} \tag{2.202}$$

The derivatives of Eq.2.200 coefficients are developed hereafter.

$$\frac{\partial g}{\partial T_t}=2C_pA^2p_t^2\left(\frac{T}{T_t}\right)^{\frac{2\kappa}{\kappa-1}}\left[1-\frac{2\kappa}{\kappa-1}\left(1-\frac{T}{T_t}\right)\right] \tag{2.203}$$

$$\frac{\partial g}{\partial T}=2C_pA^2p_t^2\left(\frac{T}{T_t}\right)^{\frac{2\kappa}{\kappa-1}}\left[\frac{2\kappa}{\kappa-1}\frac{T}{T_t}-1\right]-2\dot{m}^2R^2T \tag{2.204}$$

$$\frac{\partial g}{\partial p_t}=4C_pA^2p_t\left(T_t-T\right)\left(\frac{T}{T_t}\right)^{\frac{2\kappa}{\kappa-1}} \tag{2.205}$$

$$\frac{\partial g}{\partial \dot{m}}=-2\dot{m}R^2T^2 \tag{2.206}$$

Eq.2.202 holds for inlet conditions as well as outlet conditions. Replacing Eq.2.202 in Eq.2.197 , ΔT_{in} and ΔT_{out} can be eliminated. This leads to Eq.2.207, properly conditioned and written only in terms of total parameters increments: ΔT_{tin},ΔT_{tout}, Δp_{tin}, Δp_{tout} and $\Delta\dot{m}$.

$$\begin{aligned}
&\underbrace{f\left(T_{t1}^0,T_{t2}^0,T_1^0,T_2^0,p_{t1}^0,p_{t2}^0,\dot{m}^0\right)-\frac{g\left(T_1^0,T_t^0{}_1,p_{t1}^0,\dot{m}^0\right)}{\frac{\partial g}{\partial T_1\,0}}\frac{\partial f}{\partial T_{in\,0}}-\frac{g\left(T_2^0,T_t^0{}_2,p_{t2}^0,\dot{m}^0\right)}{\frac{\partial g}{\partial T_{out}\,0}}\frac{\partial f}{\partial T_{2\,0}}}_{residual}\\
&+\left(\frac{\partial f}{\partial T_{t1\,0}}-\frac{\partial f}{\partial T_{1\,0}}\frac{\frac{\partial g}{\partial T_{t1\,0}}}{\frac{\partial g}{\partial T_{1\,0}}}\right)\Delta T_{t1}+\left(\frac{\partial f}{\partial T_{t2\,0}}-\frac{\partial f}{\partial T_{2\,0}}\frac{\frac{\partial g}{\partial T_{t2\,0}}}{\frac{\partial g}{\partial T_{2\,0}}}\right)\Delta T_{t2}\\
&+\left(\frac{\partial f}{\partial p_{t1\,0}}-\frac{\partial f}{\partial T_{1\,0}}\frac{\frac{\partial g}{\partial p_{t1\,0}}}{\frac{\partial g}{\partial T_{1\,0}}}\right)\Delta p_{t1}+\left(\frac{\partial f}{\partial p_{t2\,0}}-\frac{\partial f}{\partial T_{2\,0}}\frac{\frac{\partial g}{\partial p_{t2\,0}}}{\frac{\partial g}{\partial T_{2\,0}}}\right)\Delta p_{t2}\\
&+\left(\frac{\partial f}{\partial \dot{m}\,0}-\frac{\partial f}{\partial T_{1\,0}}\frac{\frac{\partial g}{\partial \dot{m}\,0}}{\frac{\partial g}{\partial T_{1\,0}}}-\frac{\partial f}{\partial T_{2\,0}}\frac{\frac{\partial g}{\partial \dot{m}_0}}{\frac{\partial g}{\partial T_{2\,0}}}\right)\Delta\dot{m}\backsimeq 0
\end{aligned} \tag{2.207}$$

The dependence of Eq.2.197 on static temperatures increment ΔT_{in} and ΔT_2 is resolved. Total nodal pressures, total nodal temperatures and mass flow rates are directly determined during the iterative process.

However, for the present type of element, inlet and outlet static temperatures remain to be computed. During the iterative process, at iteration k, T_{t1k},p_{t1k}, T_{t2k}, p_{t2k}, and $\dot{m}_k$ are considered known. Examining Eq.2.200, the only remaining unknown is either the static inlet or the static outlet temperature depending whether the equation is written for inlet respectively outlet conditions. Eq.2.200 is a nonlinear equation in the variable T_{static} and can be solved using the Newton Raphson algorithm. This task is performed in a module separated from the main iterative process.

Friction coefficient

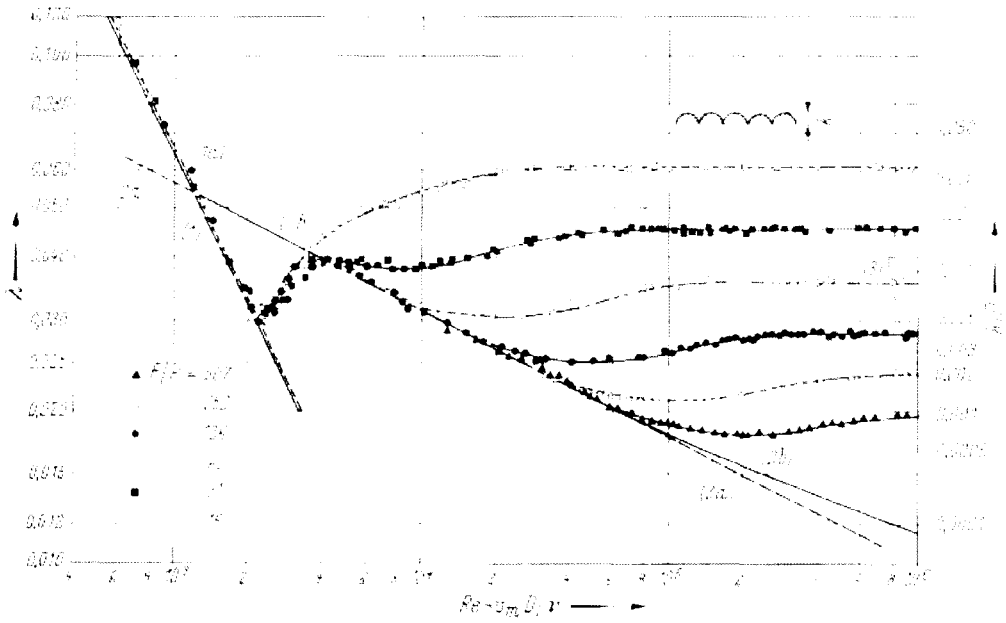

Figure 2.13: Friction factor values experimentally obtained for artificially roughened pipes, theoretical relationship for smooth pipe. (1) smooth laminar, (1a) rough turbulent, (2a) smooth turbulent, (2b) smooth turbulent, (3) sand-roughened turbulent. [52]

As shown by measurements performed by Keenan and Neumann [25], over a range of Mach numbers between 0 and 1, compressible and incompressible friction coefficients do not differ for smooth circular pipes. A similar result has been obtained for rough circular pipes by Mills and Coles [34]. Therefore, the incompressible friction model is applied in the present case. In order to be able to use the friction correlations, the flow is supposed fully established in the pipe. Considering Fig.2.13, discrimination between the different types of fully developed flows is done as follows:

- Laminar flow, using Couette-Poiseuille with form factor correction, for Reynolds numbers below 2300

$$\lambda = \phi \frac{64}{Re} \tag{2.208}$$

- Turbulent flow using White-Colebrook equation for values of Reynolds over 4000

$$\frac{1}{\sqrt{\lambda}} = -2\, log_{10}\left(\frac{2.51}{Re\sqrt{\lambda}} + 0.27\frac{\epsilon}{D}\right) \tag{2.209}$$

- Transition flow regime approximated by a linear interpolation.

$$log\,(\lambda) = log\,(\lambda_{2300}) + \frac{log\left(\frac{\lambda_{4000}}{\lambda_{2300}}\right)}{log\left(\frac{Re_{4000}}{Re_{2300}}\right)}\, log\left(\frac{Re}{Re_{2300}}\right) \tag{2.210}$$

2.4.6 Change of the reference frame

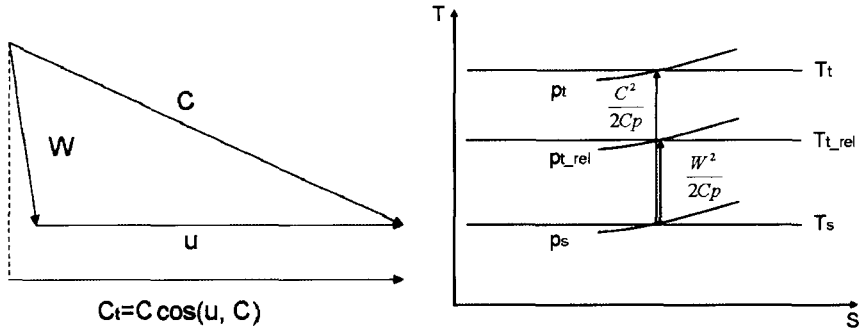

Figure 2.14: Velocity triangle and associated temperature-entropy diagram.

The present element enables to transform total pressure and total temperature from the static frame of reference into the rotating frame and vice versa. Considering Fig.2.14, the total temperature in the relative system is written as

$$T_{t,rel} = T + \frac{W^2}{2C_p} \tag{2.211}$$

and the static temperature is expressed as

$$T = T_t - \frac{C^2}{2C_p} \tag{2.212}$$

where W is the velocity in the relative frame of reference, C is the velocity in the absolute reference frame (for instance at a pre-swirl nozzle outlet) and u the circumferential velocity. Combining Eq.2.211 and Eq.2.212 yields

$$T_{t,rel} = T_t + \frac{W^2}{2C_p} - \frac{C^2}{2C_p} \tag{2.213}$$

Considering Fig.2.14, $W^2 = u^2 + C^2 - 2\ u\ C\ cos\,(u, C)$. Consequently Eq.2.213 can be written as

$$T_{t,rel} = T_t \left(1 + \frac{u^2 - 2u\ C\ cos\,(u, C)}{2C_p T_t}\right) \tag{2.214}$$

Since $Ccos\,(u, C) = C_t$, the fluid tangential velocity one obtains

$$T_{t,rel} = T_t \left(1 + \frac{u^2 - 2\ u\ C_t}{2C_p T_t}\right) \tag{2.215}$$

$$p_{t,rel} = p_t \left(1 + \frac{u^2 - 2\ u\ C_t}{2C_p T_t}\right)^{\frac{\kappa}{\kappa - 1}} \tag{2.216}$$

where u is the circumferential velocity. For a transition from the absolute frame of reference to the moving

frame one gets

$$T_t = T_{t,rel}\left(1 - \frac{u^2 - 2\,u\,C_t}{2C_pT_{t,rel}}\right) \tag{2.217}$$

$$p_t = p_{t,rel}\left(1 - \frac{u^2 - 2\,u\,C_t}{2C_pT_{t,rel}}\right)^{\frac{\kappa}{\kappa-1}} \tag{2.218}$$

The transition from one system to the other occurs over one flow element: the properties of the inlet and outlet nodes are described in different frames of reference without affecting the mass flow rate. The temperature change from one reference to the other is taken as an additional input in the energy balance of the outlet node to this end. Eq.2.217 is transformed into

$$C_p\left(T_t - T_{t,rel}\right)\dot{m}_{ij} = -\frac{u^2 - 2\,u\,C_t}{2}\dot{m}_{ij} \tag{2.219}$$

For the absolute to relative transition, Eq.2.215 can be written as

$$f = \frac{p_{t_{out}}}{p_{t_{in}}} - \left(1 + \frac{u^2 - 2\,u\,C_t}{2C_pT_{t_{in}}}\right)^{\frac{\kappa}{\kappa-1}} = 0 \tag{2.220}$$

The partial derivatives of Eq.2.220 are

$$\frac{\partial f}{\partial p_{t_{in}}} = -\frac{p_{t_{out}}}{p_{t_{in}}^2} \tag{2.221}$$

$$\frac{\partial f}{\partial p_{t_{out}}} = \frac{1}{p_{t_{in}}} \tag{2.222}$$

$$\frac{\partial f}{\partial T_{t_{in}}} = -\frac{\kappa}{\kappa-1}\left(\frac{u^2 - 2\,u\,C_t}{2C_pT_{t_{in}}^2}\right)\left(1 + \frac{u^2 - 2\,u\,C_t}{2C_pT_{t_{in}}}\right)^{\frac{\kappa}{\kappa-1}-1} \tag{2.223}$$

For the relative to absolute transition, Eq.2.218 can be written as

$$f = \frac{p_{t_{out}}}{p_{t_{in}}} - \left(1 - \frac{u^2 - 2\,u\,C_t}{2C_pT_{t_{in}}}\right)^{\frac{\kappa}{\kappa-1}} = 0 \tag{2.224}$$

The partial derivatives of Eq.2.224 are

$$\frac{\partial f}{\partial p_{t_{in}}} = -\frac{p_{t_{out}}}{p_{t_{in}}^2} \tag{2.225}$$

$$\frac{\partial f}{\partial p_{t_{out}}} = \frac{1}{p_{t_{in}}^2} \tag{2.226}$$

$$\frac{\partial f}{\partial T_{t_{in}}} = -\frac{\kappa}{\kappa-1}\left(\frac{u^2 - 2\,u\,C_t}{2C_pT_{t_{in}}^2}\right)\left(1 - \frac{u^2 - 2\,u\,C_t}{2C_pT_{t_{in}}}\right)^{\frac{\kappa}{\kappa-1}-1} \tag{2.227}$$

2.4.7 Vortex elements

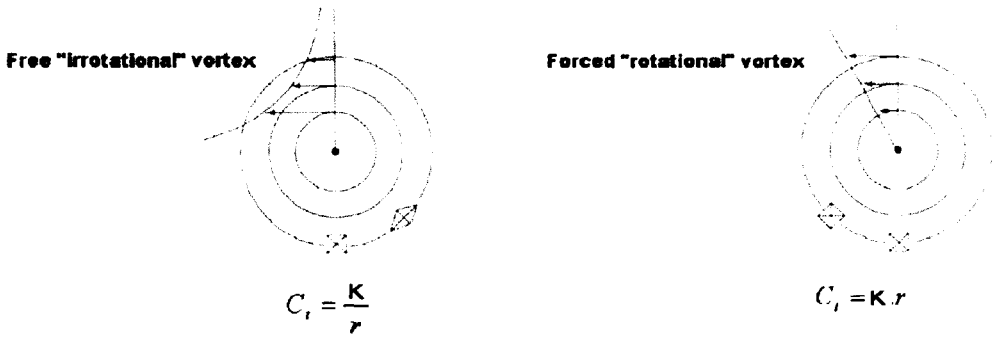

Figure 2.15: Two types of vortex.

Due to the presence of numerous rotating parts (discs, shafts), swirling flows are often encountered in the secondary air system. These swirling flows are most often approximated by either a free or a forced (solid body) vortex. The type of flow is controlled by the turbulent flow parameter λ_t.

$$\begin{aligned} \lambda_t &= \frac{C_w}{Re_\phi^{0.8}} \\ C_w &= \frac{\dot{m}}{\eta r_{out}} \\ Re_\phi &= \frac{\omega r_{out}^2}{\nu} \end{aligned}$$

where η is the cinematic viscosity, C_w is the flow rate coefficient and Re_ϕ is the circumferential Reynolds number. Flows displaying large values of λ_t (important mass flow rates, small rotation speed) tend more to the free vortex type whereas flows with 'low' λ_t value (small mass flow rate, high rotation speed) tend more to the forced vortex type in rotor-stator spaces. This leads to the following possible discrimination in the case of the SAS have two different origins:

- Forced vortices are created in rotor-stator spaces when the fluid is flowing radially and the turbulent flow parameter, λ_t is low.
- Free vortices are mainly induced by swirl creating elements, as pre-swirl nozzles, which provide a relatively high flow and thus a large λ_t value .

Detailed information exists in the literature and gives a better understanding of the physical phenomenon (see Owen [40]).

In the case of vortices, for the special purpose of secondary air system calculations, only the radial pressure difference is taken into account. No additional heat is imparted to the fluid and moreover the domain of flow

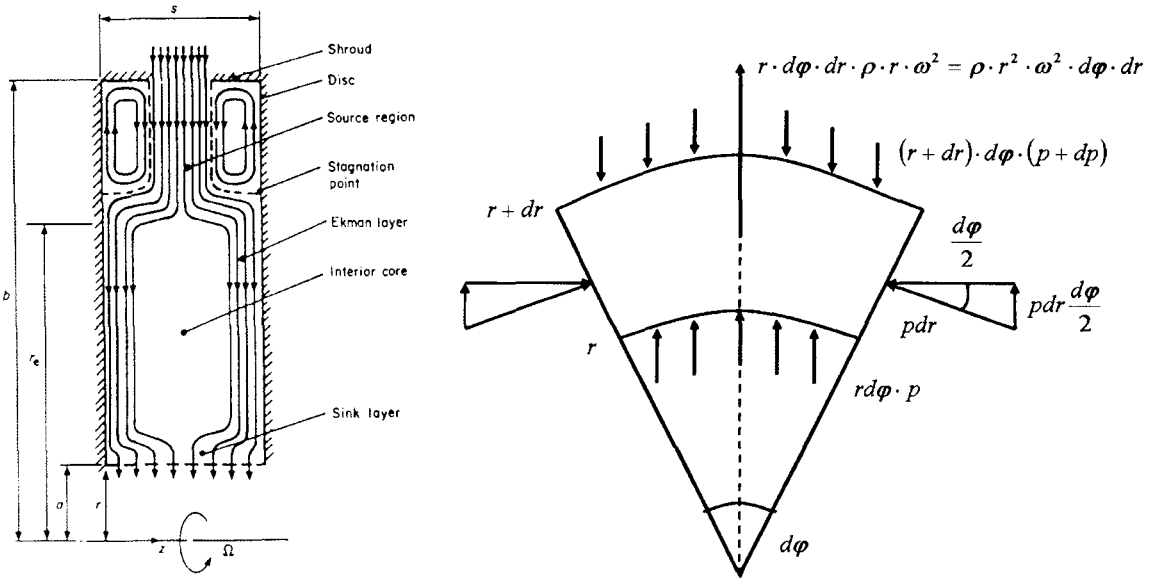

Figure 2.16: Schematic diagram of rotating cavity with radial fluid inflow from Owen and al.[37] (left) and balance of forces acting on a rotating flow element away from the Eckmann layers (right).

considered excludes the Eckmann layers and the sink layer represented in Fig.2.16. As stated by Owen in [39], for single disc in a fluid of large extend or for a rotor-stator system whose clearance is sufficiently large, viscous and turbulent effects are negligible except in thin boundary layers near the discs. The core of the fluid is therefore considered as inviscid. It follows that the process in the domain considered is isentropic. Therefore

$$T = T_{ref}\left(\frac{p}{p_{ref}}\right)^{\frac{\kappa-1}{\kappa}} \tag{2.228}$$

where the reference point may be freely chosen.

Constitutive equation

This analysis is valid for both free and forced vortices. It is aimed at determining the pressure gradient in the radial direction of the vortex. Following Owen assumption, the core is considered inviscid. Under this assumption the momentum equation projected in the orthoradial direction is written

$$v_r \frac{\partial}{\partial r}(rv_\phi) + v_z \frac{\partial}{\partial z}(rv_\phi) = 0 \tag{2.229}$$

z being the direction if the rotation axis. This yields two results:

- either $v_r = 0$: no radial component of the velocity inside the core and all the fluid has been entrained into the boundary layers
- or rv_ϕ is independent of the axial direction and there still remains some radial flow in the core and

$$rv_\phi = constant$$

It is considered that $v_r = 0$ or $v_r << v_\phi$ in the core region. Considering Fig.2.16, the balance of forces acting on small volume of fluid projected following the radial direction yields

$$(r + dr)\, d\phi\, (p + dp) - r d\phi p - 2pdr\frac{d\phi}{2} = \rho r^2 w^2 d\phi dr \tag{2.230}$$

Simplifying Eq.2.230 and neglecting the second order terms by comparison with the first order terms yields

$$rdp = \rho r^2 w^2 dr \tag{2.231}$$

Using the definition of the tangential velocity $C_t = \omega\, r$

$$\frac{1}{\rho}\frac{\partial p}{\partial r} = \frac{r^2 w^2}{r} = \frac{C_t^2}{r} \tag{2.232}$$

This equation is consistent with Owen and al. [38] and is valid for the source region away from the Eckman layers and in the internal core represented in Fig.2.16 (left). If the sink layer is ignored, Eq.2.232 is used to calculate the pressure drop that occurs as the fluid moves from the source toward the sink.

In the present situation, pressure p and temperature T are static values. The tangential velocity component in the upstream element is small enough to consider that $p_t \simeq p$ and $T_t \simeq T$. Using the equation of state and Eq.2.228 gives

$$\rho = \frac{p}{RT_{ref}}\left(\frac{p_{ref}}{p}\right)^{\frac{\kappa-1}{\kappa}} = \frac{p_{ref}^{\frac{\kappa-1}{\kappa}}}{RT_{ref}}\left(\frac{1}{p}\right)^{\frac{1}{\kappa}} \tag{2.233}$$

Using Eq.2.233 and Eq.2.232 yields

$$\frac{1}{\rho}\frac{\partial p}{\partial r} = \frac{RT_{ref}}{p_{ref}^{\frac{\kappa-1}{\kappa}}}\left(\frac{1}{p}\right)^{\frac{1}{\kappa}}\frac{dp}{dr} \tag{2.234}$$

which enables to write

$$\frac{RT_{ref}}{p_{ref}^{\frac{\kappa-1}{\kappa}}}\left(\frac{1}{p}\right)^{\frac{1}{\kappa}}\frac{dp}{dr} = \frac{C_t^2}{r} \tag{2.235}$$

Separating the variables, Eq.2.235 is integrated

$$\frac{RT_{ref}}{p_{ref}^{\frac{\kappa-1}{\kappa}}}\int_{p_{ref}}^{p_{out}}\frac{1}{p^{\frac{1}{\kappa}}}\partial p = \int_{r_{ref}}^{r_{out}}\frac{C_t^2}{r}\partial r \tag{2.236}$$

which yields

$$\frac{RT_{ref}}{p_{ref}^{\frac{\kappa-1}{\kappa}}}\frac{\kappa}{\kappa-1}\left[p_{out}^{\frac{\kappa}{\kappa-1}}-p_{ref}^{\frac{\kappa}{\kappa-1}}\right]=\int_{r_{ref}}^{r_{out}}\frac{C_t^2}{r}\partial r \tag{2.237}$$

Taking the inner radius as reference point enables to write

$$\frac{RT_{in}}{p_{in}^{\frac{\kappa-1}{\kappa}}}\frac{\kappa}{\kappa-1}\left[p_{out}^{\frac{\kappa}{\kappa-1}}-p_{in}^{\frac{\kappa}{\kappa-1}}\right]=\int_{r_{in}}^{r_{out}}\frac{C_t^2}{r}\partial r \tag{2.238}$$

and further

$$\boxed{\frac{p_{out}}{p_{in}}=\left[1+\frac{\kappa-1}{\kappa}\frac{1}{RT_{in}}\int_{r_{in}}^{r_{out}}\frac{C_t^2}{r}\partial r\right]^{\frac{\kappa}{\kappa-1}}} \tag{2.239}$$

Forced solid body vortex. For a forced solid body vortex, by definition $\frac{C_t}{r}=K$, where K is a constant therefore Eq.2.239 is written as

$$\frac{p_{out}}{p_{in}}=\left[1+\frac{\kappa-1}{\kappa}\frac{1}{RT_{in}}\int_{r_{in}}^{r_{out}}K^2r\partial r\right]^{\frac{\kappa}{\kappa-1}} \tag{2.240}$$

Which in turn yields

$$\frac{p_{out}}{p_{in}}=\left[1+\frac{1}{2C_pT_{in}}K^2r_{in}^2\left(\left(\frac{r_{out}}{r_{in}}\right)^2-1\right)\right]^{\frac{\kappa}{\kappa-1}} \tag{2.241}$$

$K^2=(\frac{C_t}{r})^2$ and in particular $K^2=(\frac{C_{tin}}{r_{in}})^2$ which finally gives

$$\boxed{f\left(p_{in},p_{out},T_{in},\dot{m}\right)=\frac{p_{out}}{p_{in}}-\left[1+\frac{C_{tin}^2}{2C_pT_{in}}\left(\left(\frac{r_{out}}{r_{in}}\right)^2-1\right)\right]^{\frac{\kappa}{\kappa-1}}} \tag{2.242}$$

The partial derivatives of Eq.2.242 with regard to temperatures pressures and mass flow rate are:

$$\frac{\partial f}{\partial p_{in}}=-\frac{p_{out}}{p_{in}^2} \tag{2.243}$$

$$\frac{\partial f}{\partial p_{out}}=-\frac{1}{p_{in}} \tag{2.244}$$

$$\frac{\partial f}{\partial \dot{m}}=0 \tag{2.245}$$

$$\frac{\partial f}{\partial T_{in}}=\frac{\kappa}{\kappa-1}\frac{C_{tin}^2}{2C_pT_{in}^2}\left(\left(\frac{r_{out}}{r_{in}}\right)^2-1\right)\left(1+\frac{C_{tin}^2}{2C_pT_{in}}\left(\left(\frac{r_{out}}{r_{in}}\right)^2-1\right)\right)^{\frac{1}{\kappa-1}} \tag{2.246}$$

Free vortex. For a free vortex, by definition $C_t\, r = K$, therefore using a development similar to the one performed for the solid body vortex, Eq.2.239 becomes

$$\boxed{f\left(p_{in}, p_{out}, T_{in}, \dot{m}\right) = \frac{p_{out}}{p_{in}} - \left[1 + \frac{C_{t_{in}}^2}{2C_p T_{in}}\left(1 - \left(\frac{r_{in}}{r_{out}}\right)^2\right)\right]^{\frac{\kappa}{\kappa-1}}} \tag{2.247}$$

For free vortices, the tangential velocity C_{tin} comes from an upstream element.

Partial derivatives of Eq.2.247 with regard to temperatures pressures and mass flow rate are:

$$\frac{\partial f}{\partial p_{in}} = -\frac{p_{out}}{p_{in}^2} \tag{2.248}$$

$$\frac{\partial f}{\partial p_{out}} = -\frac{1}{p_{in}} \tag{2.249}$$

$$\frac{\partial f}{\partial \dot{m}} = 0 \tag{2.250}$$

$$\frac{\partial f}{\partial T_{in}} = \frac{\kappa}{\kappa - 1}\frac{C_{t_{in}}^2}{2C_p T_{in}^2}\left(1 - \left(\frac{r_{in}}{r_{out}}\right)^2\right)\left(1 + \frac{C_{t_{in}}^2}{2C_p T_{in}}\left(1 - \left(\frac{r_{in}}{r_{out}}\right)^2\right)\right)^{\frac{1}{\kappa-1}} \tag{2.251}$$

2.4.8 Total head loss elements

Total head loss elements form a loss element class including several element types:

- long orifices in a pipe, long orifices in wall sections complementing the orifice family
- sudden enlargements, sudden contractions with and without chamfer
- sharp and soft bends of pipes with either square or round cross sections

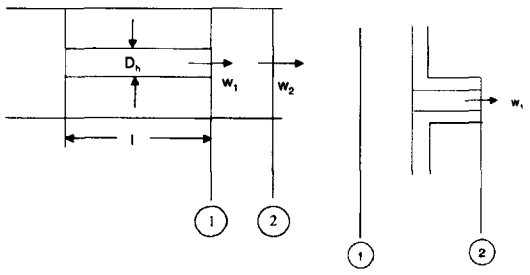

Figure 2.17: Definition of a long orifice element (left) and long orifice in a wall (right) [22].

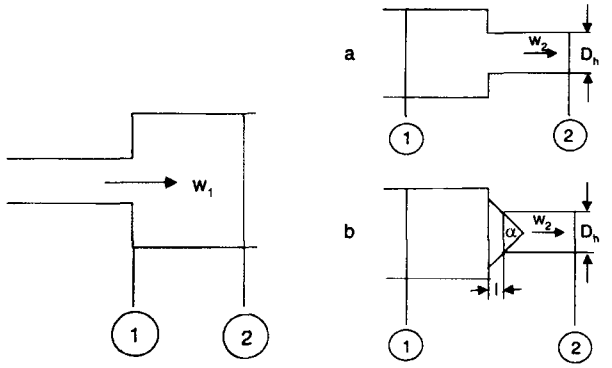

Figure 2.18: Definition of sudden expansion and sudden contraction elements [22].

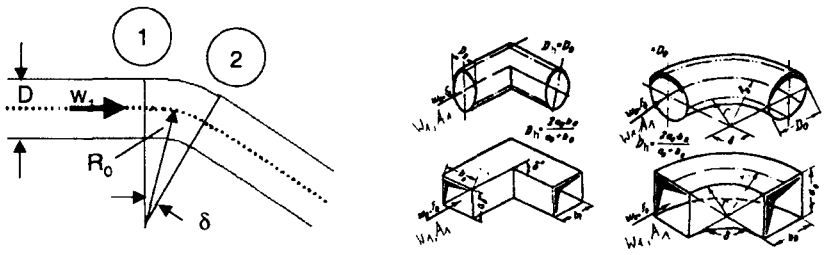

Figure 2.19: Definition of a bend element by Miller [33](left) and Idelchik [22](right)

The methods implemented in CalculiX for the determination of the pressure loss coefficients have been taken from Idelchik [22] and Miller [33].

Mathematical developments

For incompressible flows, the total head loss of the aforementioned elements is characterised by

$$\Delta p_t = p_{t1} - p_{t2} = \zeta \frac{\rho}{2} c^2 \tag{2.252}$$

For compressible flows three problems arise.

1. The loss coefficient is usually determined for incompressible flow , a way must be found to apply this coefficient to compressible flows too.

2. For compressible flow, choking of the element may occur in either inlet or outlet cross section.

3. The reference velocity for the total head is taken at the inlet of the element. If inlet and outlet cross sections differ, the reference velocity is taken at the smallest cross section. It might be the inlet as in the case of an enlargement or the outlet in the case of a sudden contraction.

Inlet, outlet and reference cross sections are therefore always to be specified.

- either reference plane 1 in which case $\Delta p = \zeta_1 \frac{\rho}{2} c_1^2$
- either reference plane 2 in which case $\Delta p = \zeta_2 \frac{\rho}{2} c_2^2$

Eq.2.252 must be adapted for compressible flows. The approach developed by Scholz in [48] is used. The

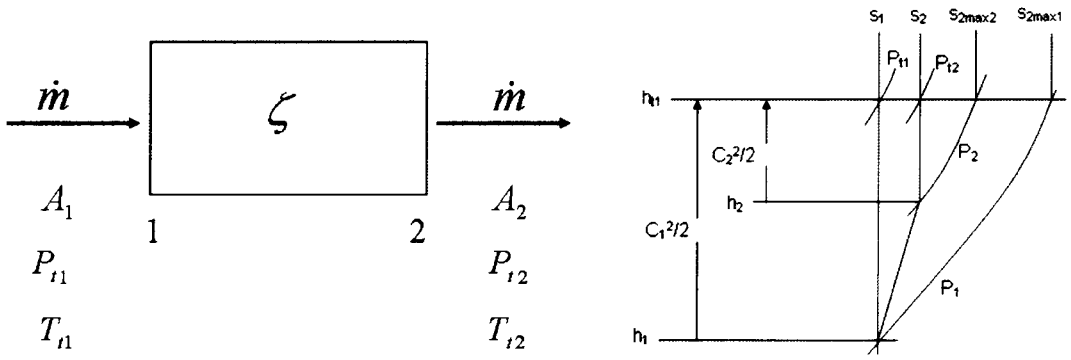

Figure 2.20: Total head loss element representation and Scholz diagram ([48])

loss factor ζ can either be based on inlet speed, c_1 or outlet speed, c_2. And therefore for an incompressible flow $\Delta p_t = p_{t1} - p_{t2} = \zeta_1 \frac{\rho}{2} c_1^2$ or $\Delta p_t = p_{t1} - p_{t2} = \zeta_2 \frac{\rho}{2} c_2^2$. According to Fig.2.20, the loss factor is defined as the ratio between actual entropy increase over the element and the maximum entropy increase over the element (reached if the outlet velocity is zero). Therefore two definitions of the loss factor are possible:

- based on inlet conditions : $\zeta_1 = \frac{S_2 - S_1}{S_{2_{max1}} - S_1}$

- based on outlet conditions : $\zeta_2 = \frac{S_2 - S_1}{S_{2_{max2}} - S_2}$

The total head loss family can be subdivided in two families, namely type ζ_1 total head losses concerning flow elements for which the inlet section is smaller than or equal to the outlet section and type ζ_2 total head losses for which the outlet section is smaller than the inlet section. Using the entropy definition, the following equation is derived:

$$S_2 - S_1 = \frac{\kappa}{\kappa - 1} R\, ln\left(\frac{T_2}{T_1}\right) - R\, ln\left(\frac{p_2}{p_1}\right) \tag{2.253}$$

Assuming adiabatic conditions of flow over the element one obtains

$$S_2 - S_1 = R\, ln\frac{p_1}{p_2} \tag{2.254}$$

According to Fig.2.20, both $S_{2_{max1}} - S_1$ and $S_{2_{max2}} - S_1$ are respectively written as

$$S_{2_{max1}} - S_1 = R\, ln\left(\frac{p_{t1}}{p_2}\right) \tag{2.255}$$

and

$$S_{2_{max2}} - S_1 = R\, ln\left(\frac{p_{t2}}{p_2}\right) \tag{2.256}$$

Using Eq.2.254, 2.255 and 2.256 leads to two expressions of the pressure ratio based on inlet respectively outlet conditions. For inlet conditions, using the inlet Mach number

$$\frac{p_{t1}}{p_{t2}} = \left(\frac{p_{t1}}{p_1}\right)^{\zeta_1} = \left(1 + \frac{\kappa - 1}{2} M_1^2\right)^{\zeta_1 \frac{\kappa}{\kappa - 1}} \tag{2.257}$$

and for outlet conditions

$$\frac{p_{t1}}{p_{t2}} = \left(\frac{p_{t2}}{p_2}\right)^{\zeta_2} = \left(1 + \frac{\kappa - 1}{2} M_2^2\right)^{\zeta_2 \frac{\kappa}{\kappa - 1}} \tag{2.258}$$

It can be shown by expansion of Eq.2.257 or Eq.2.258 into a Taylor series, that for small Mach numbers the incompressible equation Eq.2.252 is recovered.

ζ_1 -type elements. The inlet cross section A_1 is smaller than or equal to the outlet cross section A_2 and the pressure ratio is defined according to Eq.2.257. Let us suppose at first that neither inlet nor outlet section

is critical,

$$M_1 = \sqrt{\frac{2}{\kappa - 1}\left(\left(\frac{p_{t1}}{p_{t2}}\right)^{\frac{\kappa-1}{\zeta_1(\kappa)}} - 1\right)} \tag{2.259}$$

Using the flow equation

$$\dot{m}_{red1} = \frac{\dot{m}\sqrt{R\,T_{t1}}}{A_1\,p_{t1}\,\sqrt{\kappa}} = M_1\,\left(1 + \frac{\kappa - 1}{2}M_1^2\right)^{-\frac{\kappa+1}{2(\kappa-1)}} \tag{2.260}$$

and including Eq.2.259 in Eq.2.260, one finally arrives at

$$f\left(\dot{m}, T_{t1}, p_{t1}, p_{t2}\right) = \frac{\dot{m}\sqrt{R\,T_{t1}}}{A_1\,p_{t1}\,\sqrt{\kappa}} - \sqrt{\frac{2}{\kappa - 1}\left(\left(\frac{p_{t1}}{p_{t2}}\right)^{\frac{\kappa-1}{\zeta_1\kappa}} - 1\right)}\,\left(\frac{p_{t1}}{p_{t2}}\right)^{-\frac{(\kappa+1)}{2\zeta_1\kappa}} = 0 \tag{2.261}$$

The partial derivatives of Eq.2.261 are

$$\begin{aligned}\frac{\partial f}{\partial p_{t1}} = & -\frac{\dot{m}\sqrt{R\,T_{t1}}}{A_1\,p_{t1}^2\,\sqrt{\kappa}} + \frac{1}{p_t 1}\left(\frac{p_{t1}}{p_{t2}}\right)^{\frac{(\kappa+1)}{2\zeta_1\kappa}}\left(\frac{2}{\kappa-1}\left(\left(\frac{p_{t1}}{p_{t2}}\right)^{\frac{\kappa-1}{\zeta_1\kappa}} - 1\right)\right)^{\frac{1}{2}} \\ & \left[\frac{(\kappa+1)}{2\zeta_1\kappa} - \frac{1}{\zeta_1\kappa}\left(\frac{p_{t1}}{p_{t2}}\right)^{\frac{\kappa-1}{\zeta_1\kappa}}\left(\frac{2}{\kappa-1}\left(\left(\frac{p_{t1}}{p_{t2}}\right)^{\frac{\kappa-1}{\zeta_1\kappa}} - 1\right)\right)^{-1}\right]\end{aligned} \tag{2.262}$$

$$\frac{\partial f}{\partial T_{t1}} = \frac{1}{2}\frac{\dot{m}\sqrt{R}}{A_1\,p_{t1}\,\sqrt{\kappa T_{t1}}} \tag{2.263}$$

$$\frac{\partial f}{\partial \dot{m}} = \frac{\sqrt{RT_{t1}}}{A_1\,p_{t1}\,\sqrt{\kappa}} \tag{2.264}$$

$$\begin{aligned}\frac{\partial f}{\partial p_{t2}} = & \frac{1}{p_{t2}}\left(\frac{p_{t1}}{p_{t2}}\right)^{\frac{(\kappa+1)}{2\zeta_1\kappa}}\left(\frac{2}{\kappa-1}\left(\left(\frac{p_{t1}}{p_{t2}}\right)^{\frac{\kappa-1}{\zeta_1\kappa}} - 1\right)\right)^{\frac{1}{2}} \\ & \left[\frac{-(\kappa+1)}{2\zeta_1\kappa} + \frac{1}{\zeta_1\kappa}\left(\frac{p_{t1}}{p_{t2}}\right)^{\frac{\kappa-1}{\zeta_1\kappa}}\left(\frac{2}{\kappa-1}\left(\left(\frac{p_{t1}}{p_{t2}}\right)^{\frac{\kappa-1}{\zeta_1\kappa}} - 1\right)\right)^{-1}\right]\end{aligned} \tag{2.265}$$

Let us suppose now that A_2 is still not critical but that critical conditions are reached at A_1 The critical pressure ratio is given by

$$\left(\frac{p_{t1}}{p_{t2}}\right)_{critical} = \left(1 + \frac{\kappa - 1}{2}\right)^{\zeta_1\frac{\kappa}{\kappa-1}} \tag{2.266}$$

in turn using 2.266 in 2.261

$$f\left(\dot{m}, T_{t1}, p_{t1}, p_{t2}\right) = \frac{\dot{m}\sqrt{R\,T_{t1}}}{A_1\,p_{t1}\sqrt{\kappa}} - \underbrace{\sqrt{\frac{2}{\kappa-1}\left(\left(\frac{p_{t1}}{p_{t2}}\right)_{critical}^{\frac{\kappa-1}{\zeta_1\kappa}} - 1\right)}\,\left(\frac{p_{t1}}{p_{t2}}\right)_{critical}^{-\frac{(\kappa+1)}{2\zeta_1\kappa}}}_{constant} = 0 \tag{2.267}$$

The partial derivatives of Eq.2.267 are

$$\frac{\partial f}{\partial p_{t1}} = -\frac{\dot{m}\sqrt{R\,T_{t1}}}{A_1\,p_{t1}^2\,\sqrt{\kappa}} \tag{2.268}$$

$$\frac{\partial f}{\partial T_{t1}} = \frac{1}{2}\frac{\dot{m}\sqrt{R}}{A_1\,p_{t1}\,\sqrt{\kappa T_{t1}}} \tag{2.269}$$

$$\frac{\partial f}{\partial \dot{m}} = \frac{\sqrt{RT_{t1}}}{A_1\,p_{t1}\,\sqrt{\kappa}} \tag{2.270}$$

$$\frac{\partial f}{\partial p_{t2}} = 0 \tag{2.271}$$

If section A_2 is critical, which can only occur in the case of large pressure losses, then

$$\dot{m}_{red1} = \frac{\dot{m}\sqrt{R\,T_{t1}}}{A_1\,p_{t1}\sqrt{\kappa}} = M_1\,\left(1+\frac{\kappa-1}{2}M_1^2\right)^{-\frac{\kappa+1}{2(\kappa-1)}} \tag{2.272}$$

and

$$\dot{m}_{red2} = \frac{\dot{m}\sqrt{R\,T_{t2}}}{A_2\,p_{t2}\,\sqrt{\kappa}} = M_2\,\left(1+\frac{\kappa-1}{2}M_2^2\right)^{-\frac{\kappa+1}{2(\kappa-1)}} \tag{2.273}$$

Combining Eq.2.272 and Eq.2.273 yields under the assumption that the flow is adiabatic

$$\frac{p_{t1}}{p_{t2}} = \frac{A_2}{A_1}\frac{M_2\,\left(1+\frac{\kappa-1}{2}M_2^2\right)^{-\frac{\kappa+1}{2(\kappa-1)}}}{M_1\,\left(1+\frac{\kappa-1}{2}M_1^2\right)^{-\frac{\kappa+1}{2(\kappa-1)}}} \tag{2.274}$$

Since section A_2 is critical $M_2 = 1$, using the definition of M_1 Eq.2.259, Eq.2.274 simplifies into

$$\frac{p_{t1}}{p_{t2}} = \frac{A_2}{A_1}\frac{\left(\frac{p_{t1}}{p_{t2}}\right)^{\frac{\kappa+1}{2\zeta_1\kappa}}}{\sqrt{\frac{2}{\kappa-1}\left(\left(\frac{p_{t1}}{p_{t2}}\right)^{\frac{\kappa-1}{\zeta_1\kappa}}-1\right)\left(\frac{\kappa+1}{2}\right)^{\frac{\kappa+1}{2(\kappa-1)}}}} \tag{2.275}$$

Eq.2.275 is solved iteratively separately from the main iterative process to determine the critical value of p_{t2}. This value is then inserted in Eq.2.261

ζ_2-type elements A_1 being larger than A_2, only one critical case occurring at A_2 is possible. If A_2 is not critical then

$$f\left(\dot{m}, T_{t1}, p_{t1}, p_{t2}\right) = \frac{\dot{m}\sqrt{R\,T_{t2}}}{A_2\,p_{t2}\,\sqrt{\kappa}} - \sqrt{\frac{2}{\kappa-1}\left(\frac{p_{t1}}{p_{t2}}^{\frac{\kappa-1}{\zeta_2\kappa}}-1\right)}\left(\frac{p_{t1}}{p_{t2}}\right)^{-\frac{(\kappa+1)}{2\zeta_2\kappa}} = 0 \tag{2.276}$$

The partial derivatives of Eq.2.276 are

$$\frac{\partial f}{\partial p_{t1}} = \frac{1}{p_t 1}\left(\frac{p_{t1}}{p_{t2}}\right)^{\frac{(\kappa+1)}{2\zeta_2\kappa}}\left(\frac{2}{\kappa-1}\left(\left(\frac{p_{t1}}{p_{t2}}\right)^{\frac{\kappa-1}{\zeta_2\kappa}}-1\right)\right)^{\frac{1}{2}} \left[\frac{(\kappa+1)}{2\zeta_2\kappa}-\frac{1}{\zeta_2\kappa}\left(\frac{p_{t1}}{p_{t2}}\right)^{\frac{\kappa-1}{\zeta_2\kappa}}\left(\frac{2}{\kappa-1}\left(\left(\frac{p_{t1}}{p_{t2}}\right)^{\frac{\kappa-1}{\zeta_2\kappa}}-1\right)\right)^{-1}\right] \tag{2.277}$$

$$\frac{\partial f}{\partial T_{t2}} = \frac{1}{2}\frac{\dot{m}\sqrt{R}}{A_2\, p_{t2}\,\sqrt{\kappa T_{t2}}} \tag{2.278}$$

$$\frac{\partial f}{\partial \dot{m}} = \frac{\sqrt{RT_{t2}}}{A_2\, p_{t2}\,\sqrt{\kappa}} \tag{2.279}$$

$$\frac{\partial f}{\partial p_{t2}} = -\frac{\dot{m}\sqrt{R\,T_{t2}}}{A_2\, p_{t2}^2\,\sqrt{\kappa}}+\frac{1}{p_{t2}}\left(\frac{p_{t1}}{p_{t2}}\right)^{\frac{(\kappa+1)}{2\zeta_2\kappa}}\left(\frac{2}{\kappa-1}\left(\left(\frac{p_{t1}}{p_{t2}}\right)^{\frac{\kappa-1}{\zeta_2\kappa}}-1\right)\right)^{\frac{1}{2}} \left[\frac{-(\kappa+1)}{2\zeta_2\kappa}+\frac{1}{\zeta_2\kappa}\left(\frac{p_{t1}}{p_{t2}}\right)^{\frac{\kappa-1}{\zeta_2\kappa}}\left(\frac{2}{\kappa-1}\left(\left(\frac{p_{t1}}{p_{t2}}\right)^{\frac{\kappa-1}{\zeta_2\kappa}}-1\right)\right)^{-1}\right] \tag{2.280}$$

Otherwise A_2 is critical and

$$\left(\frac{p_{t1}}{p_{t2}}\right)_{critical} = \left(1+\frac{\kappa-1}{2}\right)^{\zeta_2\frac{\kappa}{\kappa-1}} \tag{2.281}$$

and in turn

$$f\left(\dot{m}, T_{t1}, p_{t1}, p_{t2}\right) = \frac{\dot{m}\sqrt{R\,T_{t2}}}{A_2\, p_{t2}\,\sqrt{\kappa}} - \underbrace{\sqrt{\frac{2}{\kappa-1}\left(\left(\frac{p_{t1}}{p_{t2}}\right)_{critical}^{\frac{\kappa-1}{\zeta_2\kappa}}-1\right)}\left(\frac{p_{t1}}{p_{t2}}\right)_{critical}^{-\frac{(\kappa+1)}{2\zeta_2\kappa}}}_{constant} = 0 \tag{2.282}$$

The partial derivatives of Eq.2.282 are

$$\frac{\partial f}{\partial p_{t1}} = 0 \tag{2.283}$$

$$\frac{\partial f}{\partial T_{t1}} = \frac{1}{2}\frac{\dot{m}\sqrt{R}}{A_2\, p_{t2}\,\sqrt{\kappa T_{t2}}} \tag{2.284}$$

$$\frac{\partial f}{\partial \dot{m}} = \frac{\sqrt{RT_{t2}}}{A_2\, p_{t2}\,\sqrt{\kappa}} \tag{2.285}$$

$$\frac{\partial f}{\partial p_{t2}} = -\frac{\dot{m}\sqrt{R\,T_{t2}}}{A_2\, p_{t2}^2\,\sqrt{\kappa}} \tag{2.286}$$

ζ coefficient determination Both ζ_1- or ζ_2-type have been implemented using methods found in Idelchik [22] or Miller [33]. ζ_1-type elements

- Long orifice in a pipe ([22] Idelchik p.140) Fig.2.17

- Sudden expansion (Idelchik p128), Fig.2.18.
- Bends from Miller (p141 [33]) and Idelchik (p206-208 and p215-216 [22]), Fig.2.19

ζ_2-type elements

- Sudden contraction with and without chamfer (Idelchik p96, 98, 99)[22], Fig.2.18.
- Long orifice in a wall (Idelchik p.143) Fig.2.17

2.4.9 Branches

Branches, either joining or dividing flows, are special types of ζ elements. The section in each branch is constant and the element branch is the superposition of two ζ-type elements. The computation of the ζ loss coefficients for both elements is performed as previously seen for total head loss elements and the constitutive equations as well as the partial derivatives remain the same.

$$\Delta p_{0-i} = \zeta_{0-i}\frac{\rho}{2}v_0^2 = f(v_i, v_0) \tag{2.287}$$

where subscript i stands for the joining/dividing branches, and 0 for the main branch. Two loss coefficients are defined, ζ_{0-1} and ζ_{0-2}, one in each branch and ζ_{0-i} depends on the geometry, the mass flow rate repartition in the branches and the density in each branches. Eq.2.287 is not suitable for the pressure loss calculation of branches. With this representation, the pressure loss coefficient in the combining/dividing branches 1 and 2 would only depend on the flow in the main branch which is not the case. Therefore Eq.2.287 is transformed into

$$\Delta p_{0-i} = \zeta_{0-i}(\frac{v_0}{v_i})^2\frac{\rho}{2}v_i^2 = \overline{\zeta_{0-i}}\frac{\rho}{2}vi^2 \tag{2.288}$$

The computational procedure described for total head losses remains the same for each branch. Several converging and diverging configurations are presented in Fig2.21. The methods can be found in the works of Idelchik [22], and Vazsonyi [55].

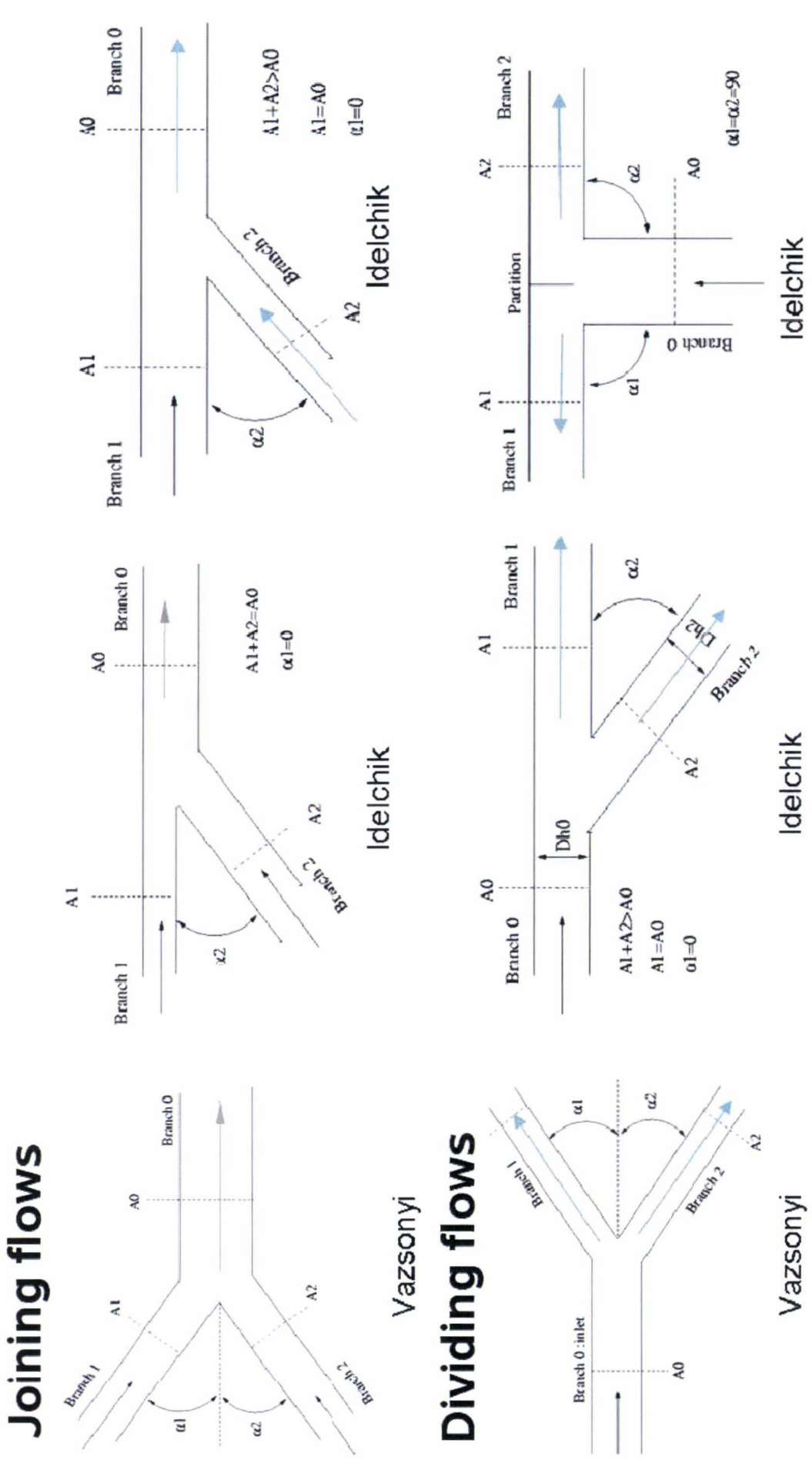

Figure 2.21: Summary of the methods implemented in CalculiX

2.5 Testing

To this day, no public/open source benchmark has been found to test the new Secondary Air System tool on large models.

2.5.1 Current secondary air system program

In the absence of external benchmark, the program currently in use at the MTU Aero engines Air and oil system department, has been used as reference. Two additional facts are provided to back up this choice:

- First of all, the MTU current S.A.S. program has been used to design a variety of air systems for both commercial (V2500, GP7000) and military (RB199, EJ200, MTR390, TP400) engines, power generation turbines (LM2500) as well as technology projects (ATFI, CLEAN, NEWAC) for over 20 years. During the development phase of these numerous projects, the program has been used as tool for the analysis of test results which proved the validity of the program for modelling large complex models.
- In several European military projects, the opportunity arose to compare the current program results with those of the partner companies giving very good agreement.

The physical models for the flow elements used in CalculiX and those used in MTU proprietary code are comparable though not similar. For instance, MTU proprietary code uses proprietary correlations for the correction factors while MTU flow models and correlations have been found in the literature. Moreover, the way the system of equations is considered and solved is also significantly different, as highlighted in the literature review in section 1.4.2.

2.5.2 Test Model

The model chosen to perform tests and subsequent comparisons between the CalculiX S.A.S. module and the current Air System program is the final version of an existing secondary air system powering a real aircraft. The secondary air system model is composed of 4 different models:

- the Low Pressure Turbine (hereafter LPT) air system,
- the High Pressure (hereafter HP) air system,
- the Intermediate Pressure- Low Pressure air system (hereafter IP-LP),
- the third stage air system.

The networks have been obtained directly from the air system department and processed 'as received' with CalculiX thanks to the interfacing process developed during this project and presented in Annex A 3.4. Results are shown using the MTU proprietary Graphical User Interface. It presents different elements which are interpreted as follows:

- Circles represent boundary conditions, squares represent chambers. They contain:
  - the nodal boundary condition/chamber label,
  - the nodal total pressure in Bar,
  - the nodal total Temperature in Kelvin.
- Lines with associated tokens representing air flows and flow elements.
  - The lines mass flow rates ($kg.s^{-1}$) are written next to the line name.
  - Flow elements are designated by a single capital letter:
    * F: total head losses
    * R: orifices/restrictors
    * S: Labyrinth seals
    * V: vortices
    * W: pipes with friction.

2.5.3 Secondary air System Networks and results

All parts of the air system are represented on the engine cut Fig.2.22. The four models contain a variety of flow elements from each flow element class presented in the previous section with geometrical specifications.

The complexity of the network topologies and the variety of flow elements and configurations vouch for an extensive and thorough testing of CalculiX capabilities. Fig.2.23 to Fig.2.26 show the results obtained with CalculiX and post-processed with the Graphical User Interface for the four models used.

Comparison is provided between the proprietary version of CalculiX and the current version of the secondary air system tool.

LPT air system. (Fig.2.25). This model is composed of 31 flow elements, including 10 boundary condition elements. Convergence is reached after 48 iterations. CPU time upon completion is 0.0469s. For the same model and the same precision, the reference current software CPU time is 0.053s.

HP air system.(Fig.2.24). This model is composed of 37 flow elements, including 10 boundary condition elements. Convergence is reached after 209 iterations. CPU time upon completion is 0.19597s. For the same model and the same precision, the reference current software CPU time is 0.095s.

3^{rd} stage system.(Fig.2.23). This model is composed of 62 flow elements, including 17 boundary condition elements. Convergence is reached after 47 iterations. CPU time upon completion is 0.073s. For the same model and the same precision, the reference current software CPU time is 0.072s.

IP-LP air system. (Fig.2.26). This model is composed of 142 flow elements,including 17 boundary condition elements. Convergence is reached after 529 iterations. CPU time upon completion is 2.657s For the same model and the same precision, the reference current software CPU time is 0.465s.

Commentary From the previous elements it can be seen that, except in the last case (IP-LP) the CPU time needed by both software to reach convergence is of the same order of magnitude.
From the user point of view however, no notable increase in waiting time is envisioned, convergence times remaining insignificant.
For all four models, the maximum relative difference observed between CalculiX and the current SAS tool in terms of temperatures, mass flow rates, and pressures is less than 5% of the affected value.

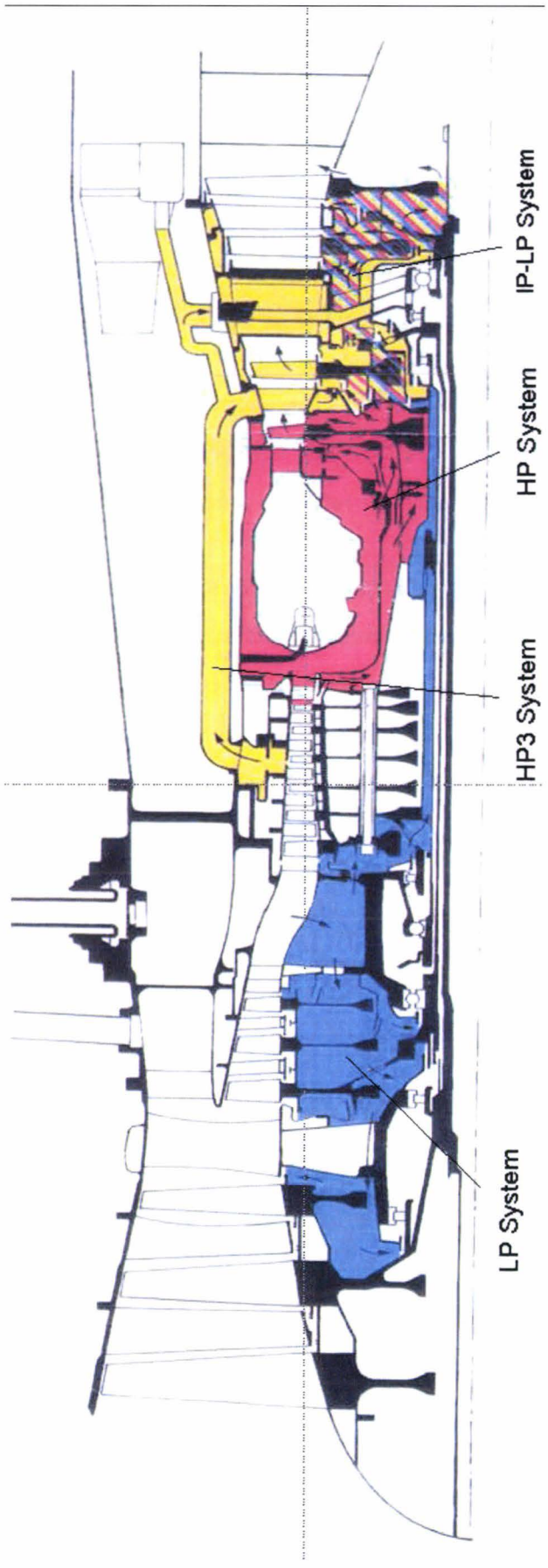

Figure 2.22: An overview of the engine secondary air system with the different air systems.

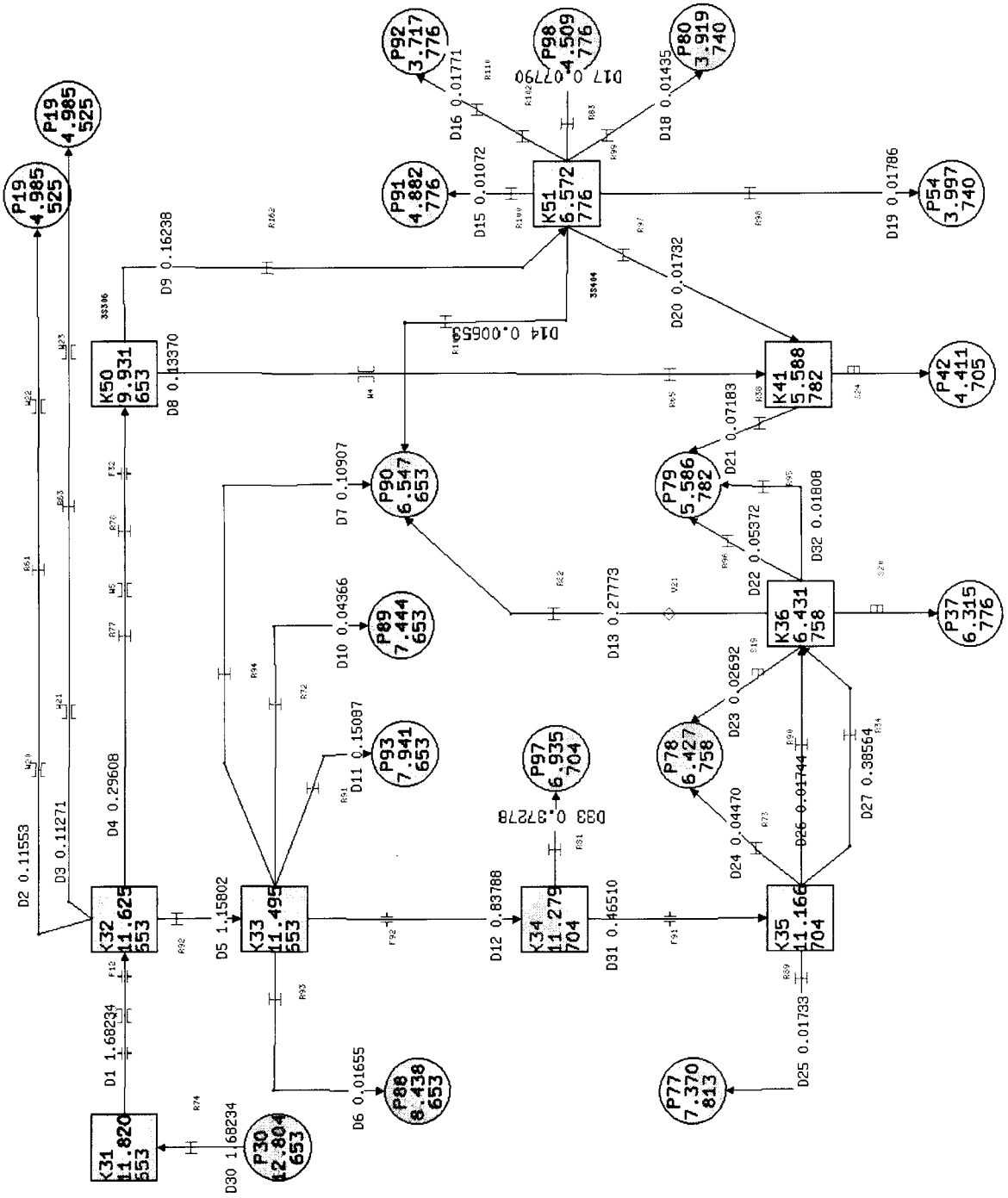

Figure 2.23: 3^{rd} stage air system.

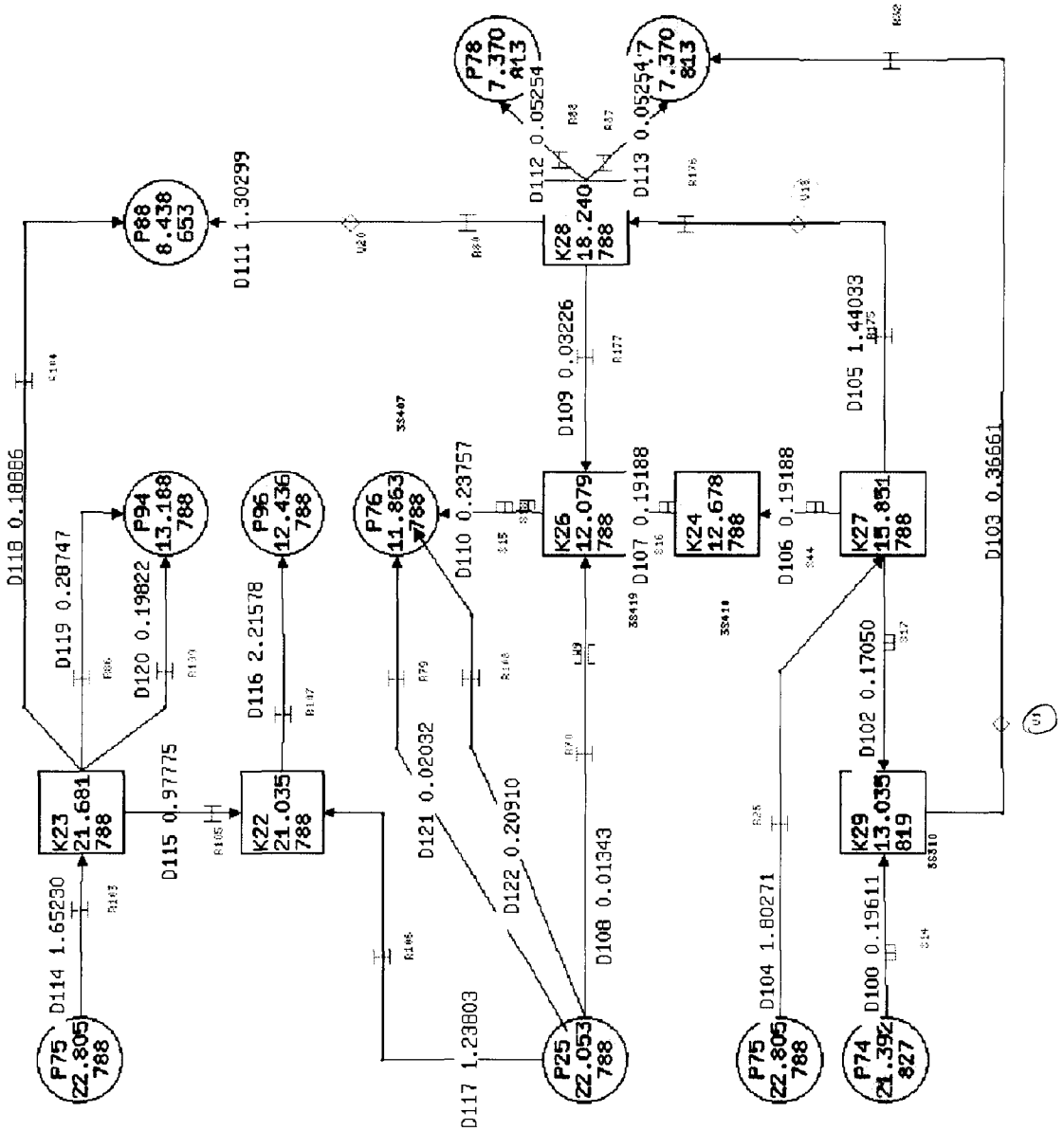

Figure 2.24: HP air system.

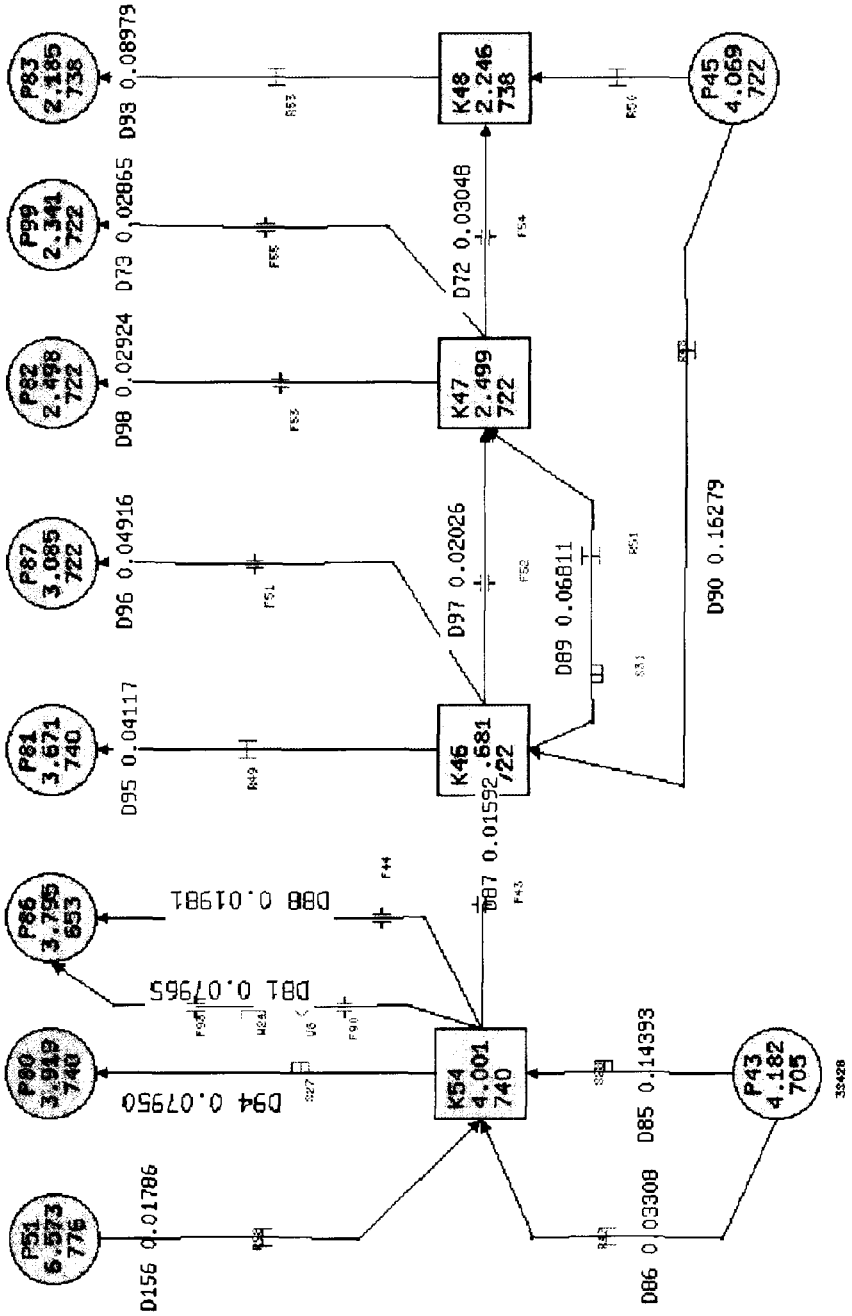

Figure 2.25: LPT air system.

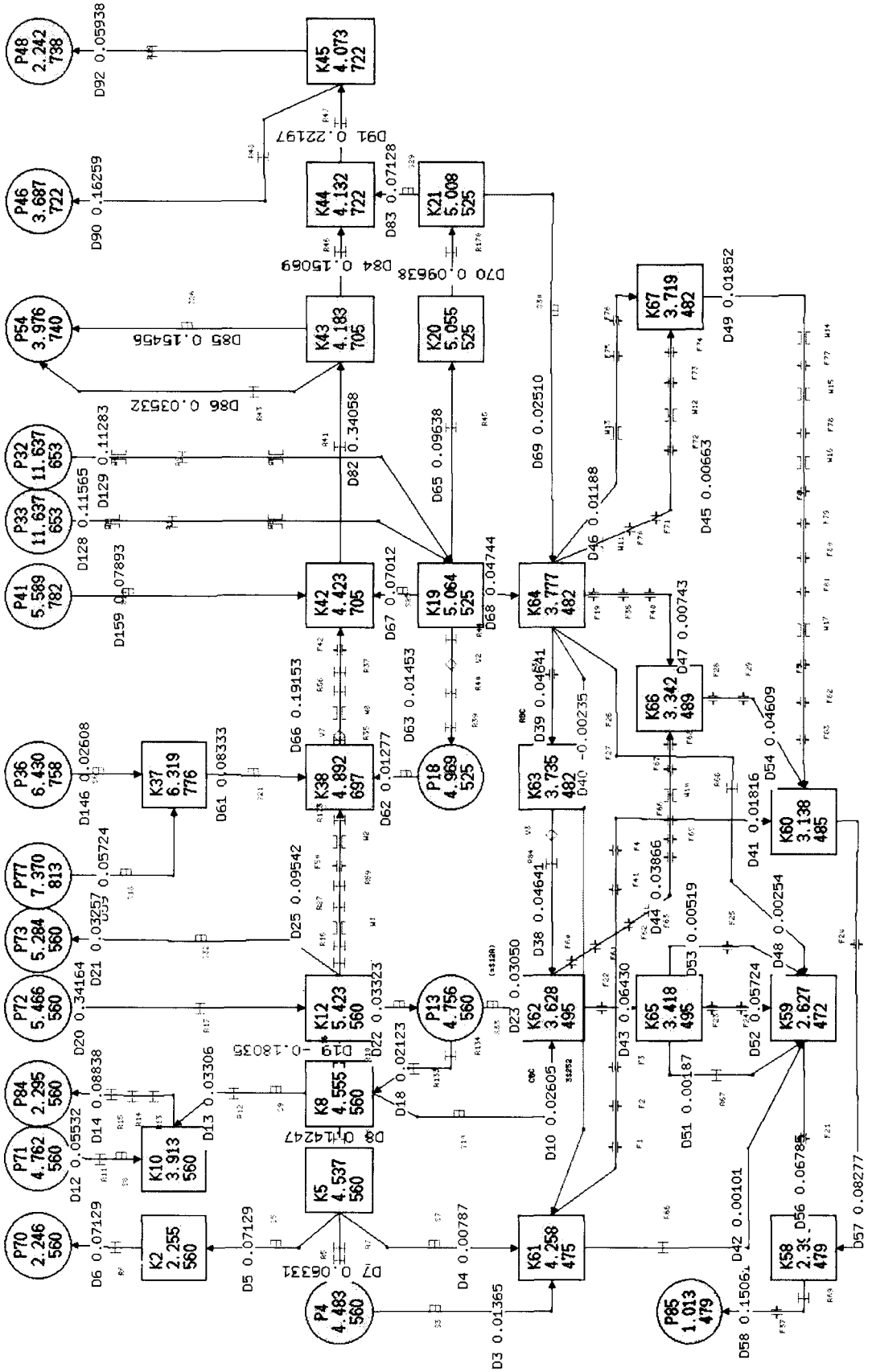

Figure 2.26: IP-LP air system.

2.6 Conclusion

The second part of the thesis, dedicated to flow networks, showed step by step the design of the new Secondary Air System module implemented in CalculiX. The creation of a new topology for the flow elements and subsequently for the network model necessary for coupled computations has been highlighted. The modification of the constitutive equations towards a suitable form for CalculiX have been presented and subsequently, the implementation of the Newton-Raphson method necessary to obtain a set of linear equations has been described both theoretically and practically.

For every class of loss elements implemented, background information has been provided along with the mathematical models and the linearisation of the constitutive equations. The classes of loss elements are:

- orifices/restrictors
- labyrinth seals
- pipes with friction
- reference change and vortex
- total head losses: contractions, enlargements, orifice in walls, bends and branches

A sequential process has been developed (see Annex A 3.4) to couple CalculiX and the existing graphical user interface which enables to create and modify the network topology with ease as well as graphically display the results.

The new secondary air system module and the interfacing process have been tested on different existing secondary air systems. Results for a complete real model have been presented. Very good agreement has been found between the results obtained with CalculiX (MTU version) and the ones obtained with the current MTU secondary air system tool on the model presented as well as other test models not included in this thesis. Computation times are of the same order of magnitude and remain small (order of magnitude 0.5 min) as required in the specifications.

Further computations, tests, and validations are necessary to approve the new SAS tool for productive use. Furthermore, sensitivity studies are planned to assess to what extend the new tool is sensitive to initial condition/geometrical definition variations.

For the continuation of the study, the new SAS module is assumed to be functional. The successful testing of the CalculiX secondary air system module is an important milestone in the project and enables to envision more specifically coupled SAS flows and thermomechanical analysis.

Chapter 3

Secondary Air System-thermomechanical coupling

3.1 Introduction

In the secondary air system, thermomechanical effects, estimated to be strong (and all the stronger for labyrinth seals), must be precisely addressed to come up with a valid design. Flow temperature, flow pressure and mass flow rates greatly influence material temperatures, which in turn generate thermal loads responsible for geometrical changes of the engine parts (Fig.3.1). This effect, redefining blade tip clearance and seal gap characteristics, modifies the pressure losses and mass flow rates in the secondary air system considerably. Conversely, they have an impact on the flow and material temperatures.

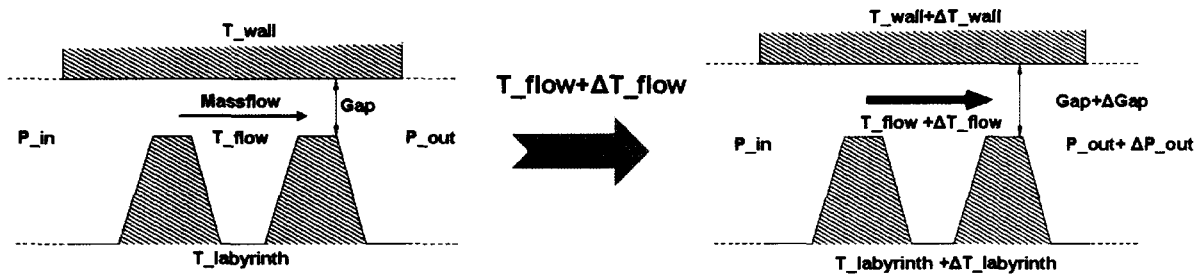

Figure 3.1: Example of thermomechanical effects on a straight labyrinth seal.

The aim is to join thermomechanical finite element model and secondary air system network model, up to now separated, within one single model and subsequently perform a fully coupled analysis using one single software code.

The thermal and mechanical modules have already been successfully implemented. CalculiX enables to perform thermal, mechanical and fully coupled thermomechanical analysis. The related theory as well

as the method implemented is described in details in [12], [13] and Annex C (3.4). The creation of the secondary air system module has been presented in Chapter 2.

This chapter explains the coupling method and presents some illustrations and results obtained with the new coupling process.

3.2 Coupling the models

The thermomechanical analysis process has been sketched in Fig.6 on page 4. The process is iterative and hierarchized, each separated analysis module performs its task and provides automatically the next module with the updated results relevant for the analysis.

Aerodynamic networks are solved separately from the structural equation system. Networks generally lead to small sets of inherently asymmetric equations. If solved together with the structural system, the small network contribution would lead to a complete asymmetric matrix and increase the computational time significantly. Moreover aerodynamic networks are very nonlinear and require more iterations than structural nonlinearities. Consequently, the small network contribution would also lead to a lot more iterations. Therefore, the matrices of networks are set up and solved on their own.

Thanks to the new flow element topology, it is possible to integrate directly the secondary air system network in the finite element thermal model. Such an integrated model can be seen Fig.3.2. The 2D axisymmetric

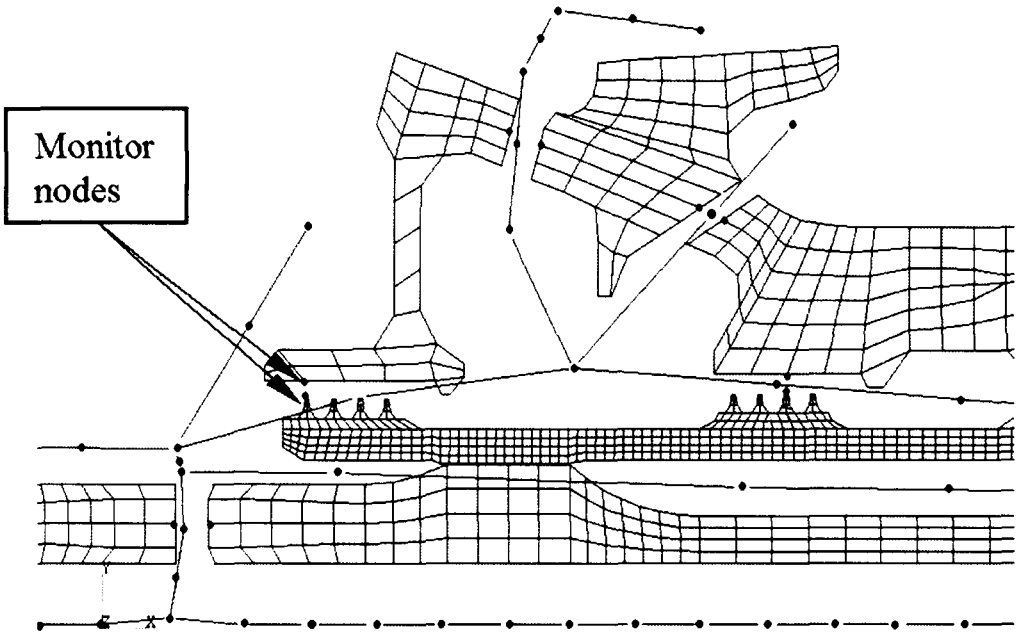

Figure 3.2: Example of flow network integrated in a thermomechanical model.

thermal model displays a variety of flow passages such as labyrinths, orifices and pipes and illustrates how

the coupling mechanism operates between the secondary airflow and the structural parts. The coupling is, however, not restricted to 2D models.

3.2.1 Thermal coupling

As detailed in Annex E, thermal interactions are taken into account between fluid and structure. Convection is defined as a heat flux between the junction nodes of the flow and the material nodes of the finite element mesh characterised by:

$$\dot{Q} = \overline{h_c}\,(T_{wall} - T_{fluid}) \tag{3.1}$$

,where $\overline{h_c}$ is the convective heat transfer coefficient, T_{wall} respectively T_{fluid} the material respectively the fluid nodal temperature. The heat transfer coefficient is an approximation of the conduction phenomena occurring between a solid and a fluid in movement inside the boundary layer when the boundary layer is not explicitly resolved as is the case with the 1D fluid model chosen.
Material temperatures are changed through the heat exchange by convection between structure and fluid and in turn fluid temperatures are changed by the thermal solution.

3.2.2 Mechanical coupling

Flow elements are defined by four main characteristics:

- a label
- the ordered triplet of nodes defining the local flow direction and subsequently inlet and outlet node
- a type relating the flow element to a general flow element class
- a set of properties linking the discrete flow element to its physical counterpart.

In the set of properties, most interesting at this point of the discussion, are the geometrical properties of the flow element, e.g. the gap in the case of seals and the hydraulic diameter and the length in the case of pipes. These properties are set at the very beginning of the calculation according to the geometrical specifications measured on a on a non-rotating engine. In the previous chapter, they were set once for the complete computation and required an user intervention to modify their definition.
In order to accommodate material displacements due to thermal dilatation or pressures, the gap width is no longer given by the user but instead, two nodes, subsequently called monitor nodes, are chosen on the thermomechanical finite element mesh on either side of the gap of the flow element. The radial distance between the two monitor nodesrepresents the gap width. Such monitor nodes can be seen represented on the

labyrinth seals in Fig.3.2. One monitor node is set on the stator part, the other one is selected on the rotor, in the present case at the tip of a fin. With the introduction of geometrical definitions based on the relative position of the monitor node geometrical properties are updated after each iteration.

In the course of the main iterative process the flow parameters are calculated first and the thermomechanical analysis, yielding material temperatures and displacements, is carried out. Along with the other nodes of the FE mesh, the predefined monitor nodes are undergoing axial and radial displacements, which modify their relative position. The variation of distance between the two monitor nodes is estimated. In turn, the set of properties corresponding to the involved flow element in the secondary air system network is updated taking into account the diameter and length variation. The next iteration may then begin, with new temperatures and new geometrical definitions.

Gap definition of all flow elements (with the exception of vortex and reference change elements) may be subject to variation, though thermomechanical phenomena affect some elements more than others. Seals, for instance, are undergoing significant geometrical changes since gap definition and rotor/stator displacements are about the same order of magnitude which has a strong impact on the flow characteristics and modifies the thermal problem.

3.3 Applications

3.3.1 Flow through a flexible pipe

This section is dedicated to the coupled computations for a simple, reproducible and illustrative example as well as its validation.

Model description.

The model chosen represents a pipe, the physical characteristics of which are the following:

- **Geometry:**
  - length: 1 m
  - diameter: 0.01 m
  - wall thickness : 0.001 m
  - perfectly smooth inner wall
- **Material: isotropic linear elastic material (rubber-like)**
  - density (ρ): 1550 $kg.m^{-3}$
  - Young's modulus (E): 0.016 GPa
  - Poisson's ratio (ν): 0.3

The material has been chosen especially for its low Young's modulus in order to to illustrate the effects of material deformations due to mechanical loads, in the present case introduced by the fluid static pressure. An overview of the model, showing the global geometry and presenting the different boundary conditions implemented on the model, is shown in Fig.3.3.

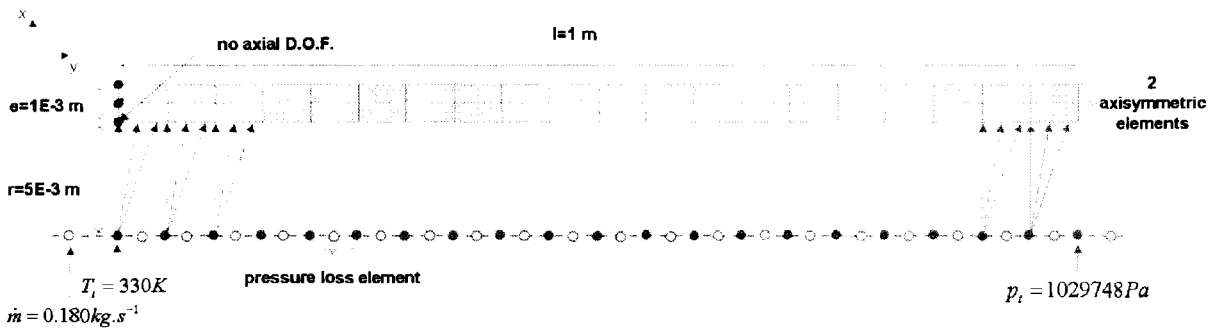

Figure 3.3: Representation of the model.

The model is axisymmetric (radial direction along the x axis, longitudinal direction along the y axis). The material is composed of two layers of 400 eight-node 0.0025-by-0.0005 axisymmetric elements of type CAX8. The aspect ratio of the mesh elements is 5.

The fluid canal is composed of 22 fluid elements (including 2 boundary condition elements) belonging to the element type pipe with friction and constant section presented in section 2.4.5. Each pipe element is 0.05m long and corresponds to 20 wall elements on the mechanical model. The model has therefore 21 nodes with pressure/temperature degrees of freedom and 22 nodes with a mass flow rate degree of freedom.

The left hand nodes of the pipe are fixed in the longitudinal direction, the rest of the pipe is let free to deform in either radial or axial direction under the fluid pressure constraints. The initial diameter of the pipe is 0.01m and the roughness parameter is set to 0 for a perfectly smooth surface.

Inlet conditions are set at the left extremity of the fluid canal as a constant mass flow rate of 0.180 $kg.s^{-}1$ and a temperature of 330K. The outlet boundary condition is set as a total pressure of 10 bar at the right extremity of the fluid canal. This leaves the repartition of the total and static pressures throughout the pipe free to change in agreement with geometrical definition modifications.

Fluid total pressures are computed at each fluid element junction node using the algorithm developed and presented in Chapter 2. For the structural problem however, only the static pressures are relevant as boundary conditions. Using the Mach numbers at each junction nodes, total pressures are converted into static pressures by the gas dynamic function:

$$\frac{p_s}{p_t} = (1 + \frac{\kappa - 1}{2} M^2)^{\frac{-\kappa}{\kappa - 1}} \tag{3.2}$$

Fluid static pressures are used as distributed load boundary conditions on the inner face of the tube elements. For the purpose of the modelling, the static pressure defined at a given fluid node is applied on the face of the 20 structural elements located directly downstream of the fluid node. The static pressure level acting on the pipe wall is therefore redefined every 20 structural elements which corresponds to the inlet/outlet of each fluid element.

Three steady state calculations have been performed.

The **structural** computation aims at predicting the deformation of the pipe under the pressure of the fluid on the inner wall. This computation is the first computation of the iterative process and its results serve as basis for comparison with the coupled computations. It is subsequently called **baseline computation** and corresponds to the **first iteration** of the coupling process.

Two **coupled fluid-mechanical** computations have been performed to illustrate the reciprocal interactions between fluid and material. The first computation only considers diameter variations as relevant parameter

in order to update the geometrical definition of the pipe elements, iteration after iteration. In the second one both diameter and length variations are taken into account. Iterations are performed until convergence of both mechanical and fluid models is achieved.

The relevant parameters for each computation are total and static pressure repartition at inlet and outlet of each pipe element as well as radial and axial displacements of the nodes belonging to the inner side of the wall. To this end 20 nodes, called monitor nodes, have been chosen on the pipe wall to estimate the radial variation for each group of 20 elements and an additional monitor node has been added to evaluate the length variations.

The baseline computation

As the influence of the structural deformation is not taken into account to update the geometrical definition of the pipe, the fluid problem can be considered separately from the structural computation. Nodal total pressures, nodal static pressures and corresponding Mach numbers are displayed in Fig.3.4.

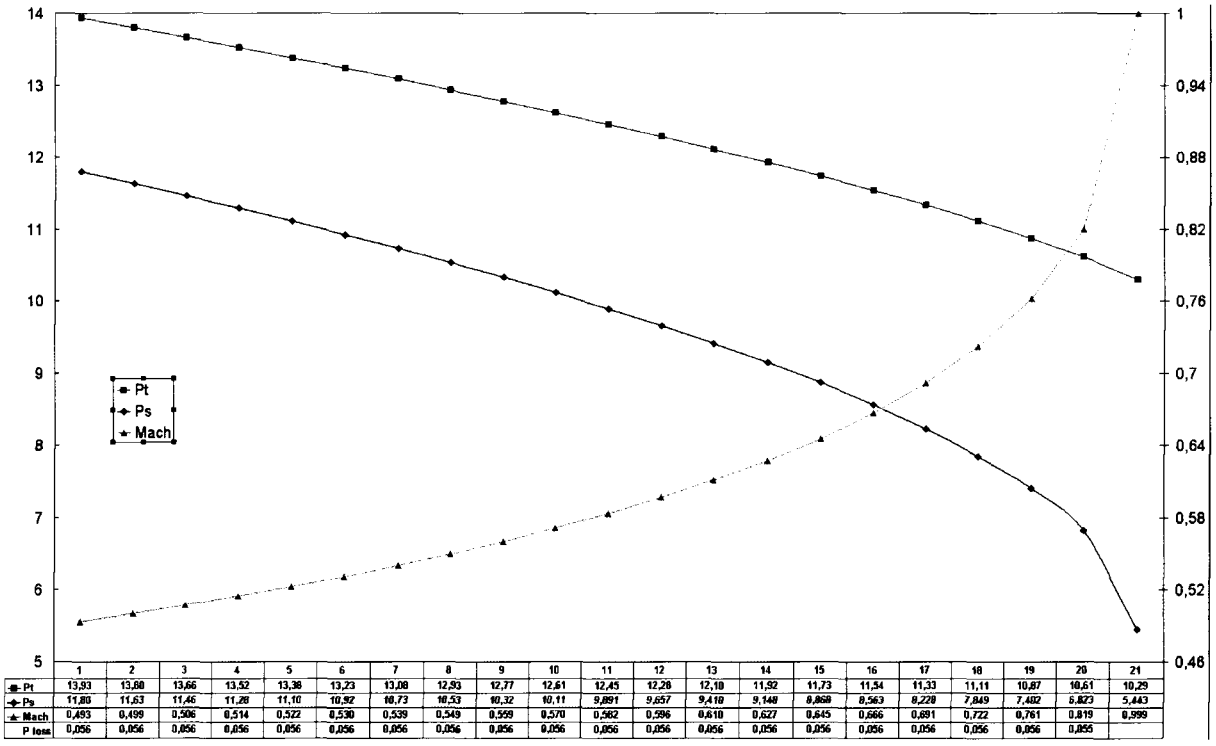

	1	2	3	4	5	6	7	8	9	10	11	12	13	14	15	16	17	18	19	20	21
Pt	13,93	13,80	13,66	13,52	13,38	13,23	13,08	12,93	12,77	12,61	12,45	12,28	12,10	11,92	11,73	11,54	11,33	11,11	10,87	10,61	10,29
Ps	11,80	11,63	11,46	11,28	11,10	10,92	10,73	10,53	10,32	10,11	9,891	9,657	9,410	9,148	8,869	8,563	8,228	7,849	7,402	6,823	5,443
Mach	0,493	0,499	0,506	0,514	0,522	0,530	0,539	0,549	0,559	0,570	0,582	0,596	0,610	0,627	0,645	0,666	0,691	0,722	0,761	0,819	0,999
P loss	0,056	0,056	0,056	0,056	0,056	0,056	0,056	0,056	0,056	0,056	0,056	0,056	0,056	0,056	0,056	0,056	0,056	0,056	0,056	0,055	

Figure 3.4: Fluid node total and static pressures [Bar] and Mach numbers predicted by CalculiX for the baseline model.

At the end of the computation the residual values for the energy equation, the mass conservation equation and the pressure loss equation are all below 1E-6.

The convergence of the flow model can be verified a-posteriori using inlet and outlet Mach numbers and pressure loss coefficients $\frac{\lambda L}{d}$ presented in Fig.3.4 and computing for each pipe element the value of the

residual given by

$$residual = \frac{1}{\kappa}\left(\frac{1}{M_1^2} - \frac{1}{M_2^2}\right) + \frac{\kappa+1}{2\kappa} ln\left(\frac{1+\frac{\kappa-1}{2}M_2^2}{1+\frac{\kappa-1}{2}M_1^2}\frac{M_1^2}{M_2^2}\right) - \frac{\lambda l}{d} \tag{3.3}$$

which has been explained in section 2.4.5.

The fluid model shows that with the geometry and boundary conditions used, the Mach number value starts about 0.49 at the pipe inlet to reach almost sonic conditions at the pipe outlet. This is responsible for an increasingly important difference between static and total pressure along the pipe.

In turn this has an impact on the mechanical problem, the solution of which is presented in Fig.3.5 as nodal displacements. The monitor nodes have been taken at the beginning of each pipe segment. The shape of

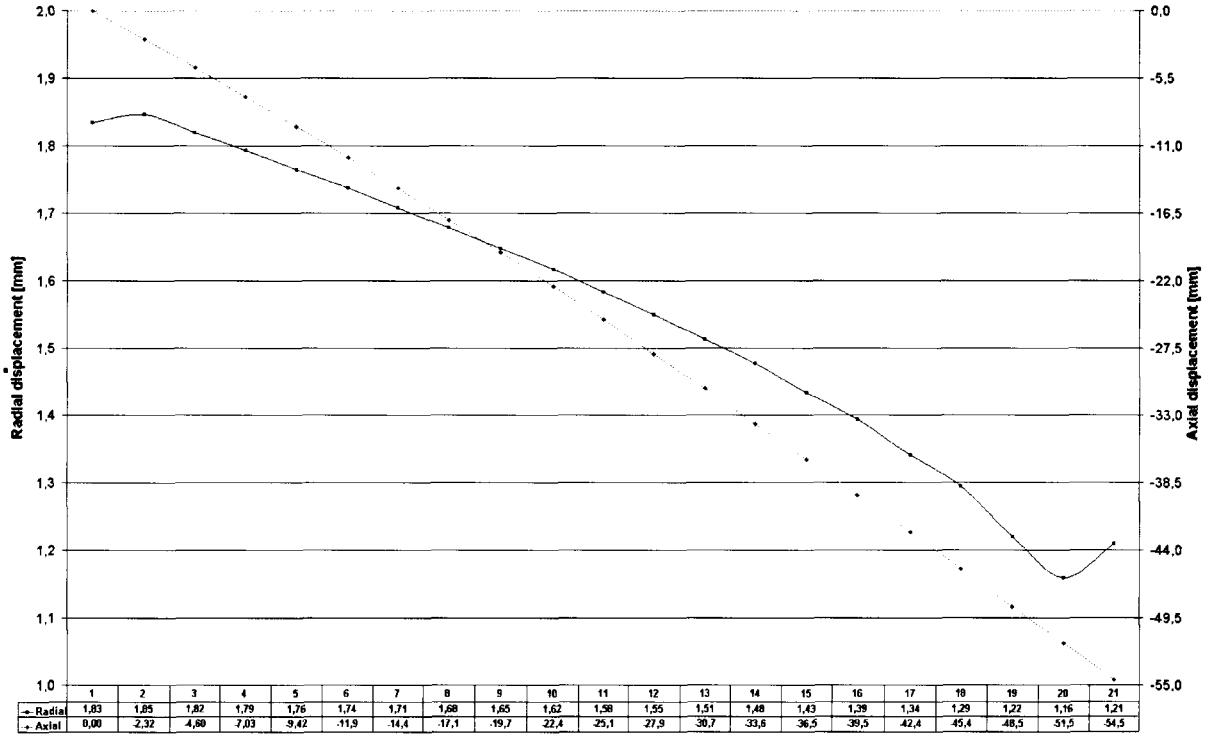

	1	2	3	4	5	6	7	8	9	10	11	12	13	14	15	16	17	18	19	20	21
Radial	1,83	1,85	1,82	1,79	1,76	1,74	1,71	1,68	1,65	1,62	1,58	1,55	1,51	1,48	1,43	1,39	1,34	1,29	1,22	1,16	1,21
Axial	0,00	-2,32	-4,69	-7,03	-9,42	-11,9	-14,4	-17,1	-19,7	-22,4	-25,1	-27,9	-30,7	-33,6	-36,5	-39,5	-42,4	-45,4	-48,5	-51,5	-54,5

Figure 3.5: Nodal radial and axial displacements [mm] predicted by CalculiX for the baseline model.

the radial displacement is in agreement with the static pressure repartition in the fluid canal. Nevertheless the first and last monitor points, respectively first and last nodes of the pipe, display radial displacements which are not in agreement with the general trend of the radial displacement curve nor in agreement with the repartition of static pressures in the flow canal. For the first group of CAX8 elements the nodal displacements are about 0.7% less than the next group. Between the last group and its preceding group the difference reaches 4%. This difference may be attributed to the fact that both group of nodes belong each to the free ends of the pipe.

Coupled computations.

The results for the fluid model of the two coupled computations are displayed in Fig.3.6. Using the results

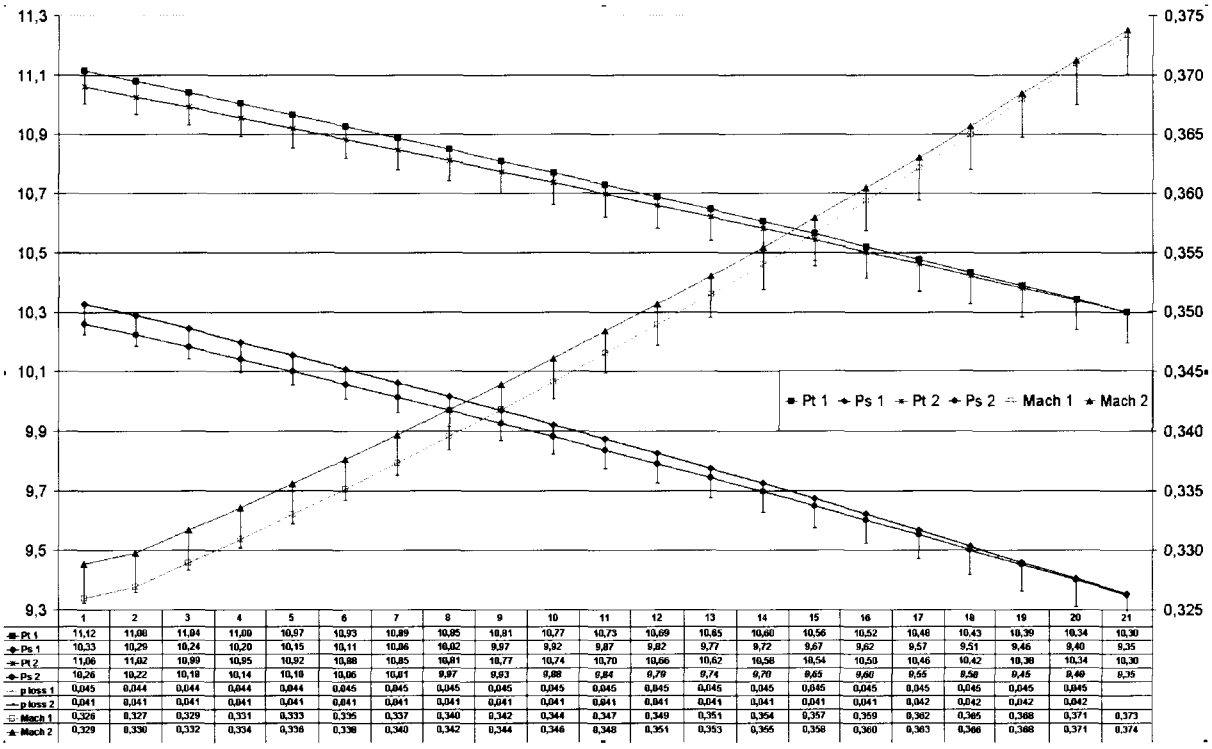

	1	2	3	4	5	6	7	8	9	10	11	12	13	14	15	16	17	18	19	20	21
Pt 1	11,12	11,08	11,04	11,00	10,97	10,93	10,89	10,85	10,81	10,77	10,73	10,69	10,65	10,60	10,56	10,52	10,48	10,43	10,39	10,34	10,30
Ps 1	10,33	10,29	10,24	10,20	10,15	10,11	10,06	10,02	9,97	9,92	9,87	9,82	9,77	9,72	9,67	9,62	9,57	9,51	9,46	9,40	9,35
Pt 2	11,06	11,02	10,99	10,95	10,92	10,88	10,85	10,81	10,77	10,74	10,70	10,66	10,62	10,58	10,54	10,50	10,46	10,42	10,38	10,34	10,30
Ps 2	10,26	10,22	10,19	10,14	10,10	10,06	10,01	9,97	9,93	9,88	9,84	9,79	9,74	9,70	9,65	9,60	9,55	9,50	9,45	9,40	9,35
p loss 1	0,045	0,044	0,044	0,044	0,044	0,045	0,045	0,045	0,045	0,045	0,045	0,045	0,045	0,045	0,045	0,045	0,045	0,045	0,045	0,045	0,045
p loss 2	0,041	0,041	0,041	0,041	0,041	0,041	0,041	0,041	0,041	0,041	0,041	0,041	0,041	0,041	0,041	0,041	0,042	0,042	0,042	0,042	0,042
Mach 1	0,326	0,327	0,329	0,331	0,333	0,335	0,337	0,340	0,342	0,344	0,347	0,349	0,351	0,354	0,357	0,359	0,362	0,365	0,368	0,371	0,373
Mach 2	0,329	0,330	0,332	0,334	0,336	0,338	0,340	0,342	0,344	0,346	0,348	0,351	0,353	0,355	0,358	0,360	0,363	0,366	0,368	0,371	0,374

Figure 3.6: Fluid node total and static pressures [Bar], Mach numbers and pressure loss coefficients predicted by CalculiX for the two coupled models. 1% difference indicator

presented in Fig.3.6 and using Eq.3.3, as a first validation the residuals may be computed to verify the convergence of the flow model, using the method previously explained for the baseline model. The influence of the length variation on the pressure drop is deemed to be marginal as the difference in total and static pressures is less than 1%. This is confirmed by Fig.3.8 showing the radial displacements. Considering the static pressure level equivalent for the two models, the variation of diameter are equivalent and in turn the Reynolds number and the friction coefficient (which is a function of both Reynolds number and diameter) is equivalent. As the diameter increases, the length of the pipe decreases as shown in Fig.3.9 which explains the smaller pressure loss coefficient for the model taking pipe length into consideration.

Compared to the baseline model, the final radius of the pipe has been increased by an average of 31% with an average radius of 6.55E-2 m and its length has been decreased by 7.5% at 0.9249 m. In this model diameter variations are obviously the relevant parameter which drives the coupled solution. Again, the same behaviour for the first and last segment of the pipe concerning radial displacements is observed with this time much less difference between the neighbouring segments due to the lower static level in the pipe and therefore the smaller radial displacement level.

Fig.3.7 shows total and static nodal pressures of the fluid nodes for all three models. In order to illustrate

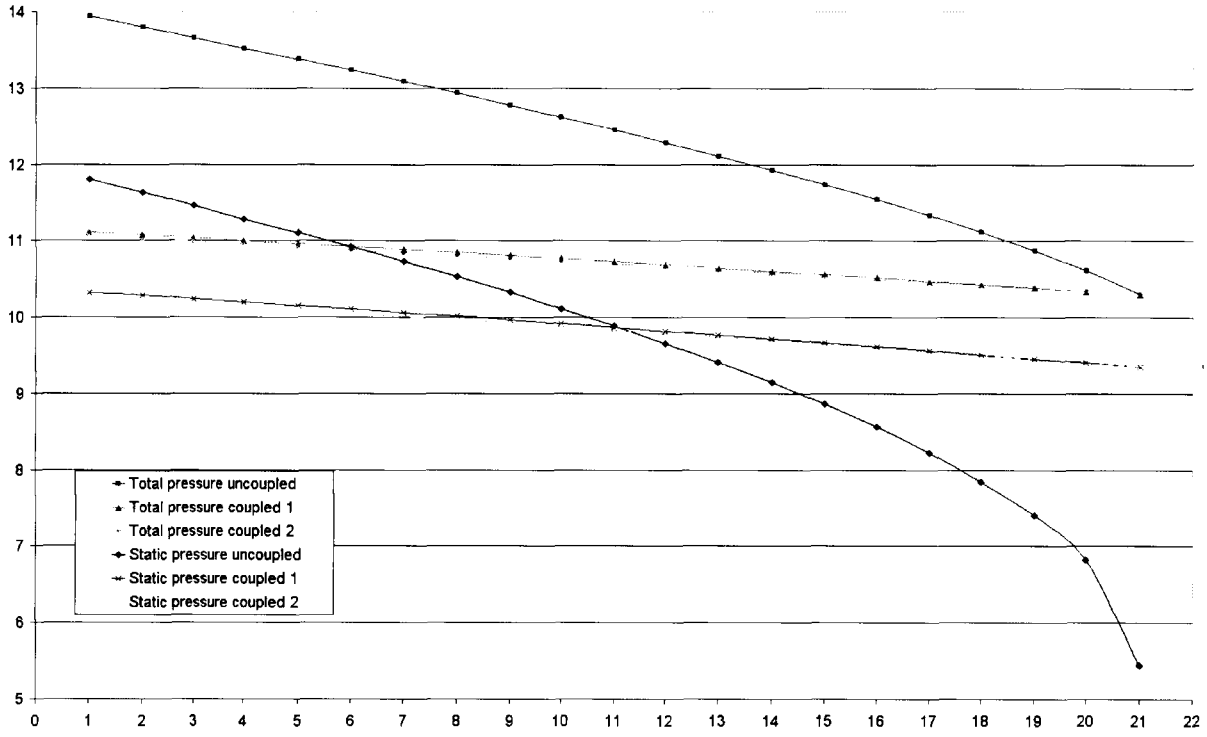

Figure 3.7: Fluid node total and static pressures [Bar] predicted by CalculiX for all three models.

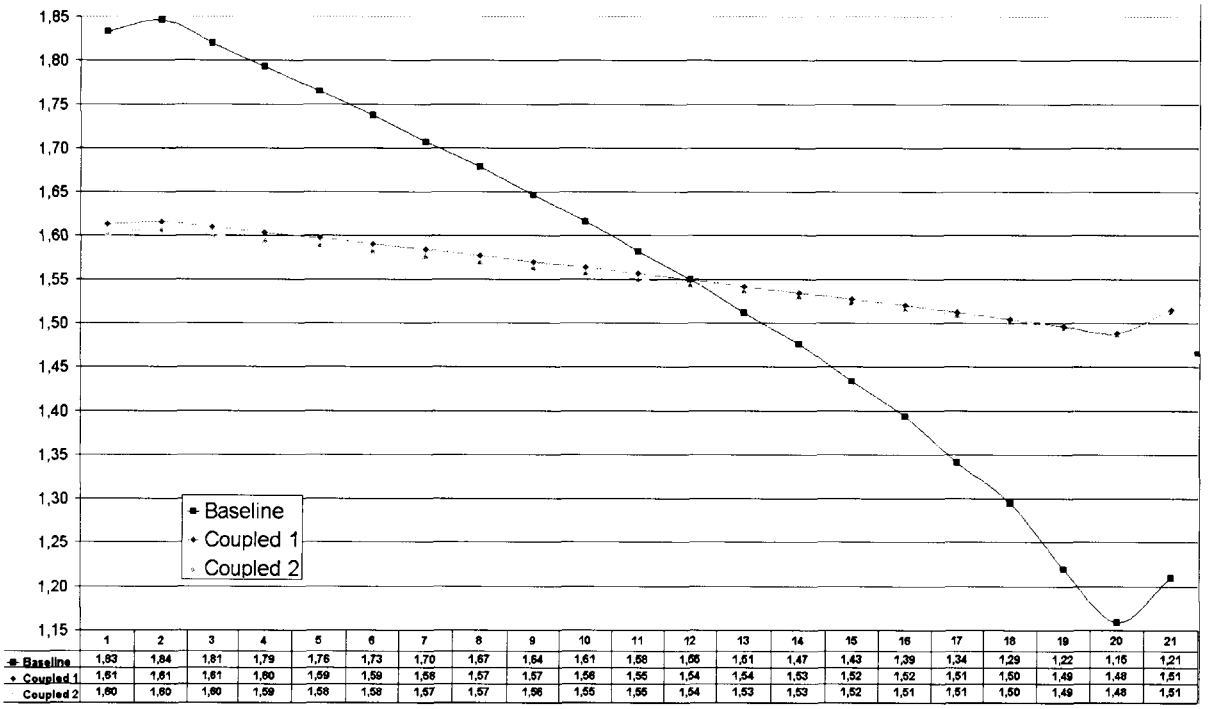

	1	2	3	4	5	6	7	8	9	10	11	12	13	14	15	16	17	18	19	20	21
Baseline	1,83	1,84	1,81	1,79	1,76	1,73	1,70	1,67	1,64	1,61	1,58	1,55	1,51	1,47	1,43	1,39	1,34	1,29	1,22	1,15	1,21
Coupled 1	1,61	1,61	1,61	1,60	1,59	1,59	1,58	1,57	1,57	1,56	1,55	1,54	1,54	1,53	1,52	1,52	1,51	1,50	1,49	1,48	1,51
Coupled 2	1,60	1,60	1,60	1,59	1,58	1,58	1,57	1,57	1,56	1,55	1,55	1,54	1,53	1,53	1,52	1,51	1,51	1,50	1,49	1,48	1,51

Figure 3.8: Radial nodal displacements [mm] predicted by CalculiX for all three models.

better what happens during the coupled computation, Fig.3.10 shows the local pipe radius at 3 positions

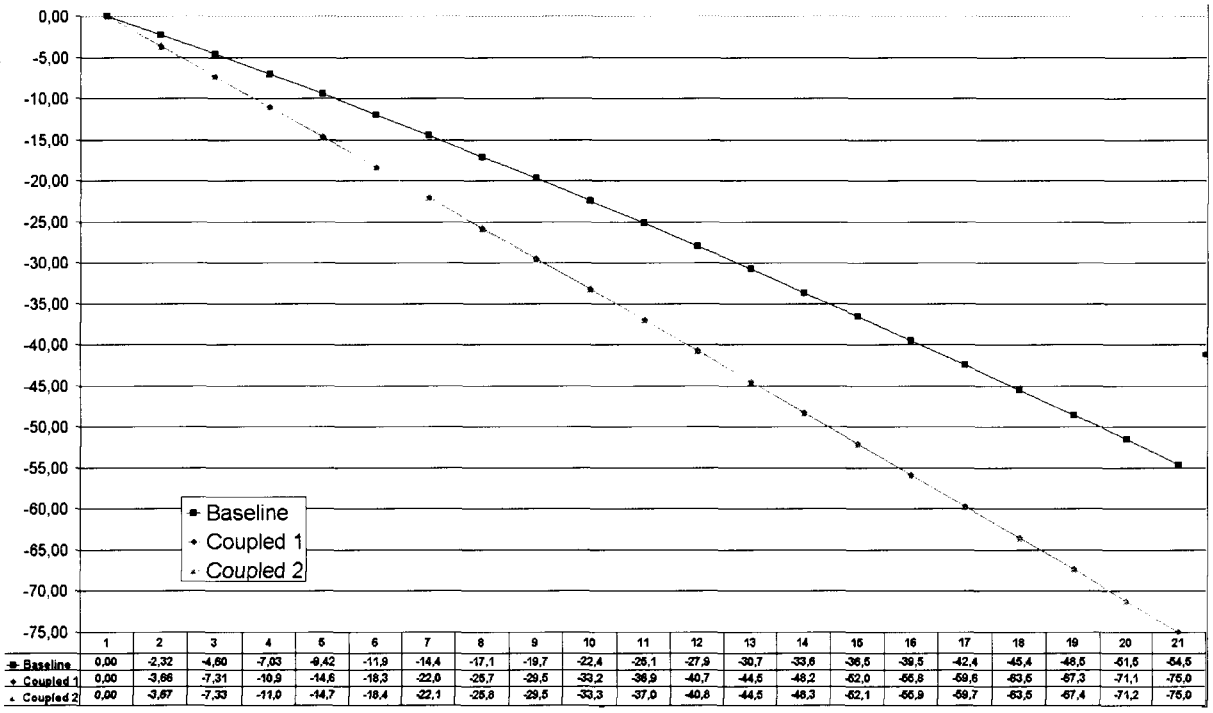

	1	2	3	4	5	6	7	8	9	10	11	12	13	14	15	16	17	18	19	20	21
Baseline	0,00	-2,32	-4,60	-7,03	-9,42	-11,9	-14,4	-17,1	-19,7	-22,4	-25,1	-27,9	-30,7	-33,6	-36,5	-39,5	-42,4	-45,4	-48,5	-51,5	-54,5
Coupled 1	0,00	-3,66	-7,31	-10,9	-14,6	-18,3	-22,0	-25,7	-29,5	-33,2	-36,9	-40,7	-44,5	-48,2	-52,0	-55,8	-59,6	-63,5	-67,3	-71,1	-75,0
Coupled 2	0,00	-3,67	-7,33	-11,0	-14,7	-18,4	-22,1	-25,8	-29,5	-33,3	-37,0	-40,8	-44,5	-48,3	-52,1	-55,9	-59,7	-63,5	-67,4	-71,2	-75,0

Figure 3.9: Axial nodal displacements [mm] predicted by CalculiX for all three models.

located at the both ends of the pipe and at the middle as well as the static pressure level for the first coupled model. Starting with the fluid computation, the diameter of the pipe is set at its initial value of 1×10^{-2}

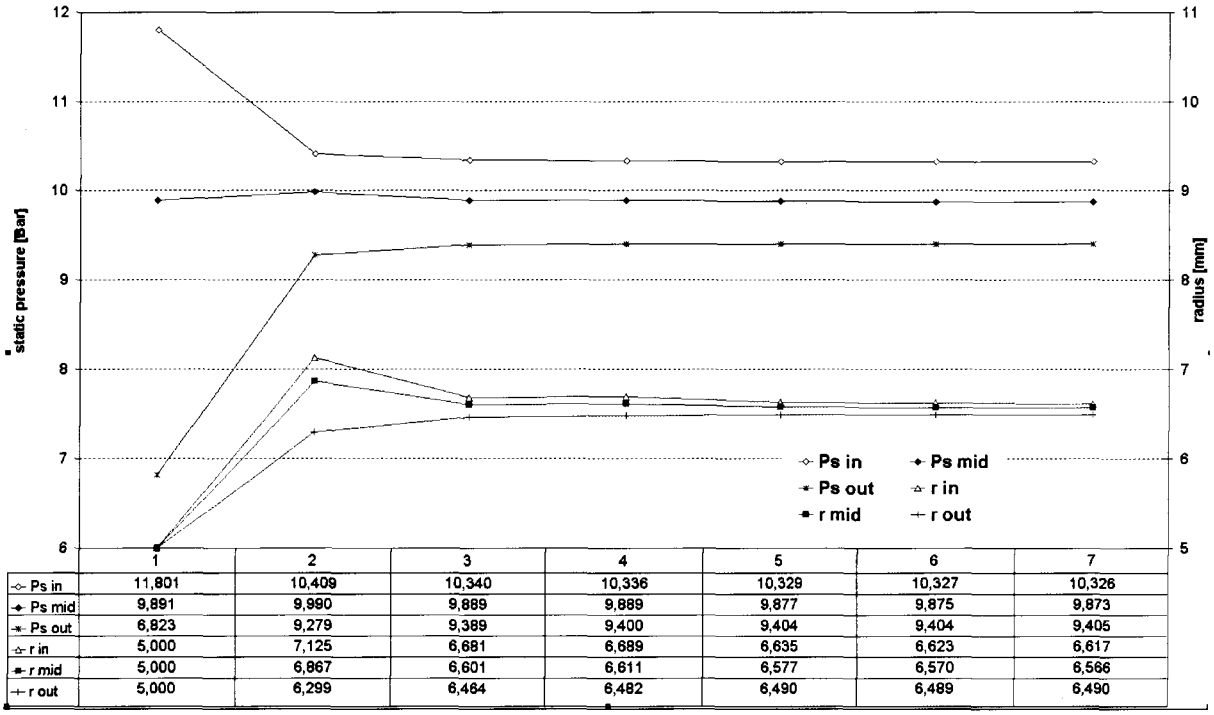

	1	2	3	4	5	6	7
Ps in	11,801	10,409	10,340	10,336	10,329	10,327	10,326
Ps mid	9,891	9,990	9,889	9,889	9,877	9,875	9,873
Ps out	6,823	9,279	9,389	9,400	9,404	9,404	9,405
r in	5,000	7,125	6,681	6,689	6,635	6,623	6,617
r mid	5,000	6,867	6,601	6,611	6,577	6,570	6,566
r out	5,000	6,299	6,464	6,482	6,490	6,489	6,490

Figure 3.10: Static pressures [Bar] and radial nodal displacements [mm] predicted by CalculiX model after each iteration for the first coupled model.

m and naturally, both fluid and subsequent mechanical solution mirror the results already presented for the baseline computation. As the diameter is increased, at given mass flow rate, the pressure loss coefficient due to friction is decreased as well as the local Mach number leading to a redistribution of the static pressure as shown in the second fluid iteration. The reduction of static pressure yields a reduction of the radial forces acting on the pipe wall and the diameter of the pipe is again reduced.

At the end of the computation, the diameter of the pipe has been globally increased by an average of 30%. From iterations to iterations it can be seen that the process converges swiftly.

Validation

Validation of the fluid model The solution of the three computations for the flow model used in CalculiX is straightforward since the residuals of the pipe flow equation Eq.3.3, which can be found in several references books such as Ward-Smith [58] and Shapiro [49], have been minimised. As already mentioned in section 2.4.5 this equation has been obtained under the assumptions of compressible pipe flow with friction in the special case of an adiabatic flow.

In order to provide a further validation of the flow model, the results obtained by CalculiX have been compared with the method described by Idelchik in [22] for circular tubes with smooth walls, stabilised flows and friction. The Idelchik method is mostly based on experimental data.

Idelchik states that most of the resistance coefficients and methods given in the handbook of hydraulic resistance were obtained for $M \leq 0.3$. Even if according to Keenan and Neumann [25], and also mentioned by Idelchik, the resistance coefficient values can be extended well into the transonic regime: they may not be used when compressibility effects are becoming important.

The results obtained by CalculiX on the converged fluid solution of the coupled model show that the Mach number in the pipe is located between 0.3 and 0.4. Therefore Idelchik's method is used for comparison purposes.

Computational procedure of Idelchik method The total pressure losses in a straight conduit of constant cross section due to friction is defined using the Darcy-Weisbach equation

$$\begin{aligned} \Delta p_{fr} &= p_{t1} - p_{t2} \\ &= \frac{\lambda l}{d} \rho_0 \frac{v_0^2}{2} \\ &= \zeta_{fr} \rho_0 \frac{v_0^2}{2} \end{aligned} \tag{3.4}$$

where subscript 0 denotes the governing inlet cross section and ζ_{fr} is the pressure loss coefficient. In the turbulent regime for which the Reynolds number is greater than 1E5, Idelchik recommends the use of the following formula to determine the friction coefficient

$$\lambda = \frac{1}{(1.8 * logRe - 1.64)^2} \tag{3.5}$$

The difference between the friction coefficient determined using Idelchik's method and the friction coefficient determined using the nonlinear White-Colebrook equation is about 3% over a range of Reynolds numbers comprised between 1×10^5 and 1.45×10^6 as shown in Fig.3.11.

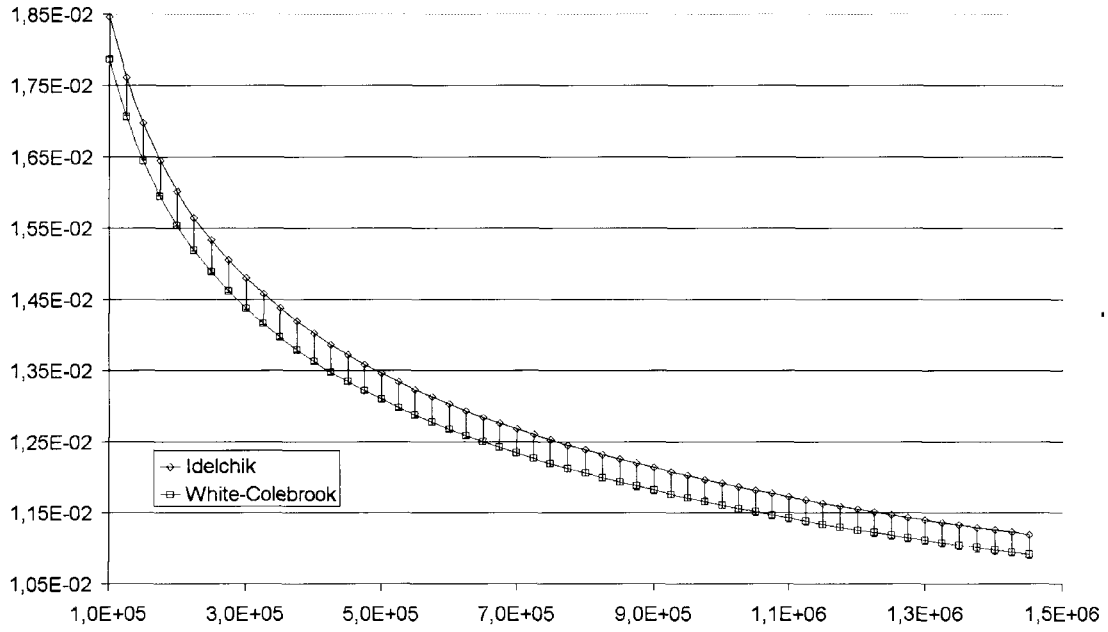

Figure 3.11: Friction coefficient as a function of the Reynolds number for White-Colebrook and Idelchik friction models. 3% difference indicator

The method used to obtain a solution using Idelchik is the following. Since the Idelchik pressure loss is determined in the flow direction, the inlet total pressure, the inlet total temperature and the inlet Mach number are supposed known and take the values determined by CalculiX. Using the total pressure respectively the total temperature and the Mach number, the static pressures respectively temperatures are computed using the isentropic relationships

$$\frac{p}{p_t} = \left(1 + \frac{\kappa - 1}{2} M^2\right)^{\frac{-\kappa}{\kappa - 1}} \tag{3.6}$$

and

$$\frac{T}{T_t} = \left(1 + \frac{\kappa - 1}{2} M^2\right)^{-1} \tag{3.7}$$

The static pressure and temperature are used in the equation of state to determine the fluid density. Using

the Sutherland equation enables to compute the dynamic viscosity

$$\mu = 1.712 \times 10^{-5} \sqrt{\frac{T}{273.15}} \frac{1 + \frac{113}{273.15}}{1 + \frac{113}{T}} \tag{3.8}$$

and in turn the Reynolds number is computed using

$$Re = \frac{\dot{m} d}{\mu A} \tag{3.9}$$

Using Eq.3.5 enables to determine the friction factor and subsequently the pressure loss coefficient. The velocity of sound in the fluid is determined using

$$a = \sqrt{\kappa R T} \tag{3.10}$$

which enables, using the Mach number, to compute the velocity of the fluid at the inlet section. Subsequently, the total pressure can be determined for the outlet section using Eq.3.4. The reduced mass flow is expressed at a given section as

$$\frac{\dot{m}\sqrt{RT_t}}{Apt\sqrt{\kappa}} = \frac{M}{\left(1 + \frac{\kappa-1}{2} M^2\right)^{\frac{\kappa+1}{2(\kappa-1)}}} \tag{3.11}$$

Writing the expression of the reduced mass flow at both inlet and outlet leads, in the case of an adiabatic process, to

$$\frac{A_2 p_{t_2}}{A_1 p_{t_1}} - \frac{M1 \left(1 + \frac{\kappa-1}{2} M_2^2\right)^{\frac{\kappa+1}{2(\kappa-1)}}}{M_2 \left(1 + \frac{\kappa-1}{2} M_1^2\right)^{\frac{\kappa+1}{2(\kappa-1)}}} = 0 \tag{3.12}$$

This non-linear equation in M_2 is solved using the Newton Raphson method.

The next segment of pipe is dealt with as described for the first pipe using M_2 and p_{t_2} as inlet values and the procedure is repeated for all the pipes segments.

Two such computations have been performed and compared with the solution of the two fluid computations performed with CalculiX on the coupled models.

Results and comparison For the two coupled computations where the Mach number is about 0.3, predicted total and static pressure levels as well as Mach numbers are in very good agreement for both CalculiX and Idelchik models, with relative differences less than 2% on both static and total pressures and less than 1% difference on Mach number values. Comparison curves for static, total pressures and Mach numbers are presented Fig.3.12 for the first coupled model.

In the light of Fig.3.12, the method used in CalculiX correlates well with the Idelchik method in the incompressible domain. Results predicted by CalculiX for total pressures, Mach numbers and static pressures

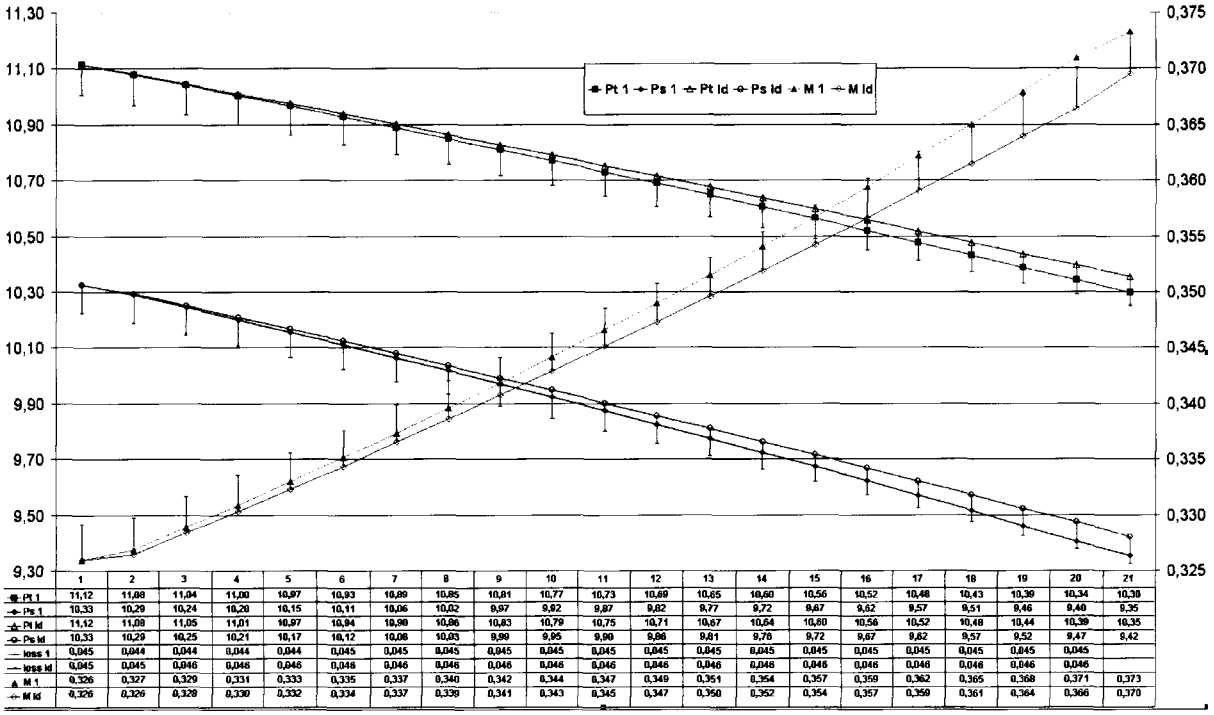

	1	2	3	4	5	6	7	8	9	10	11	12	13	14	15	16	17	18	19	20	21
Pt 1	11,12	11,08	11,04	11,00	10,97	10,93	10,89	10,85	10,81	10,77	10,73	10,69	10,65	10,60	10,56	10,52	10,48	10,43	10,39	10,34	10,30
Ps 1	10,33	10,29	10,24	10,20	10,15	10,11	10,06	10,02	9,97	9,92	9,87	9,82	9,77	9,72	9,67	9,62	9,57	9,51	9,46	9,40	9,35
Pt Id	11,12	11,08	11,05	11,01	10,97	10,94	10,90	10,86	10,83	10,79	10,75	10,71	10,67	10,64	10,60	10,56	10,52	10,48	10,44	10,39	10,35
Ps Id	10,33	10,29	10,25	10,21	10,17	10,12	10,08	10,03	9,99	9,95	9,90	9,86	9,81	9,76	9,72	9,67	9,62	9,57	9,52	9,47	9,42
loss 1	0,045	0,044	0,044	0,044	0,044	0,045	0,045	0,045	0,045	0,045	0,045	0,045	0,045	0,045	0,045	0,045	0,045	0,045	0,045	0,045	
loss Id	0,045	0,045	0,046	0,046	0,046	0,046	0,046	0,046	0,046	0,046	0,046	0,046	0,046	0,046	0,046	0,046	0,046	0,046	0,046	0,046	
M 1	0,326	0,327	0,329	0,331	0,333	0,335	0,337	0,340	0,342	0,344	0,347	0,349	0,351	0,354	0,357	0,359	0,362	0,365	0,368	0,371	0,373
M Id	0,326	0,326	0,328	0,330	0,332	0,334	0,337	0,339	0,341	0,343	0,345	0,347	0,350	0,352	0,354	0,357	0,359	0,361	0,364	0,366	0,370

Figure 3.12: Fluid node total and static pressures [Bar] and Mach number predicted by CalculiX and Idelchik method for the first coupled model. 1% difference indicator

display less than 1% difference with the results found by Idelchik. The same process has been used to compare the second coupled model results with Idelchik, yielding similar results, which is consistent because the two coupled model solutions are very close to one another. The second comparison does not bring further information and is therefore not presented. Consequently, a validation of the fluid model used by CalculiX by comparison with the incompressible method proposed by Idelchik was performed and the correctness of the fluid results was ascertained.

Validation of the mechanical model. In order to verify the mechanical aspect of the problem in terms of radial and axial displacements the following method is used. From a strictly mechanical point of view the model can be represented as a tube with an internal pressure as in Fig.3.13. The radial force F_r resulting from the pressure on the pipe wall is written as

$$\begin{aligned} F_r &= P A_{proj} \\ &= P\, d\, l \end{aligned} \tag{3.13}$$

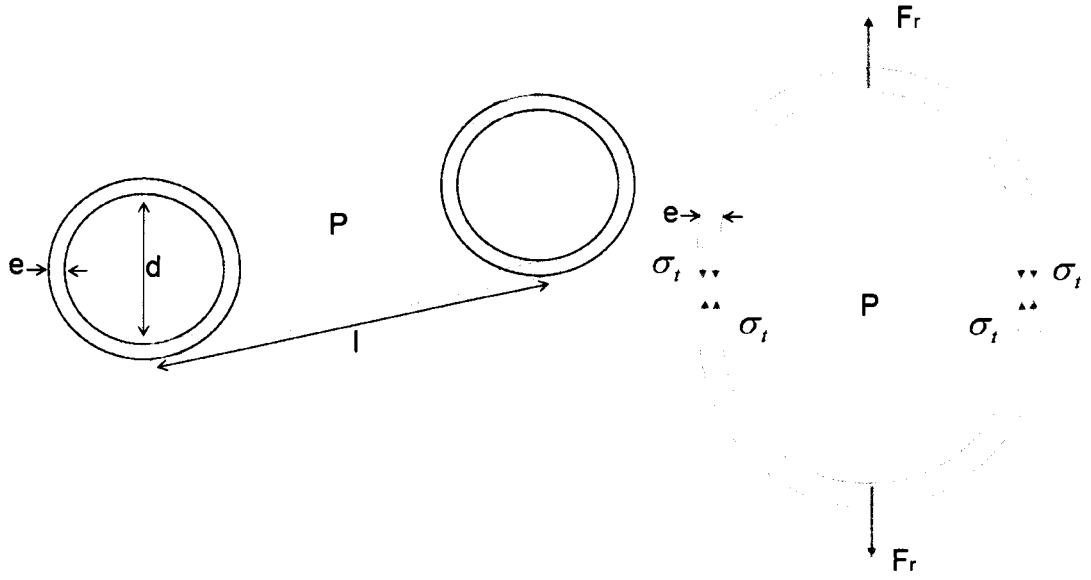

Figure 3.13: Representation of the mechanical model.

Subsequently the value of the tangential stress in the pipe is given by

$$\begin{aligned} \sigma_t &= \frac{F_r}{A_{wall}} \\ &= \frac{P\,d\,l}{2\,e\,l} \\ &= \frac{P\,d}{2\,e} \end{aligned} \tag{3.14}$$

Linear elasticity theory yields the value of the corresponding strain as

$$\epsilon_t = \frac{\sigma_t}{E} \tag{3.15}$$

In turn, the variation of radius Δr is given by

$$\begin{aligned} \Delta r &= r - r_0 \\ &= \epsilon_t r_0 \end{aligned} \tag{3.16}$$

Radial nodal displacements predicted both by CalculiX and using the linear elasticity theory on all but the first and last group of elements in the pipe are represented in Fig.3.14 and Fig.3.15. On all cited figures a difference indicator representing 1% of the nodal radial displacement value obtained using the linear elasticity theory is represented. All figures show good agreement, with less than 2% absolute difference between CalculiX and the linear elasticity theory. This tends to give credit to the fact that the radial displacements

due to the fluid pressure acting on the tube wall are in agreement with the linear elasticity theory. Again, as

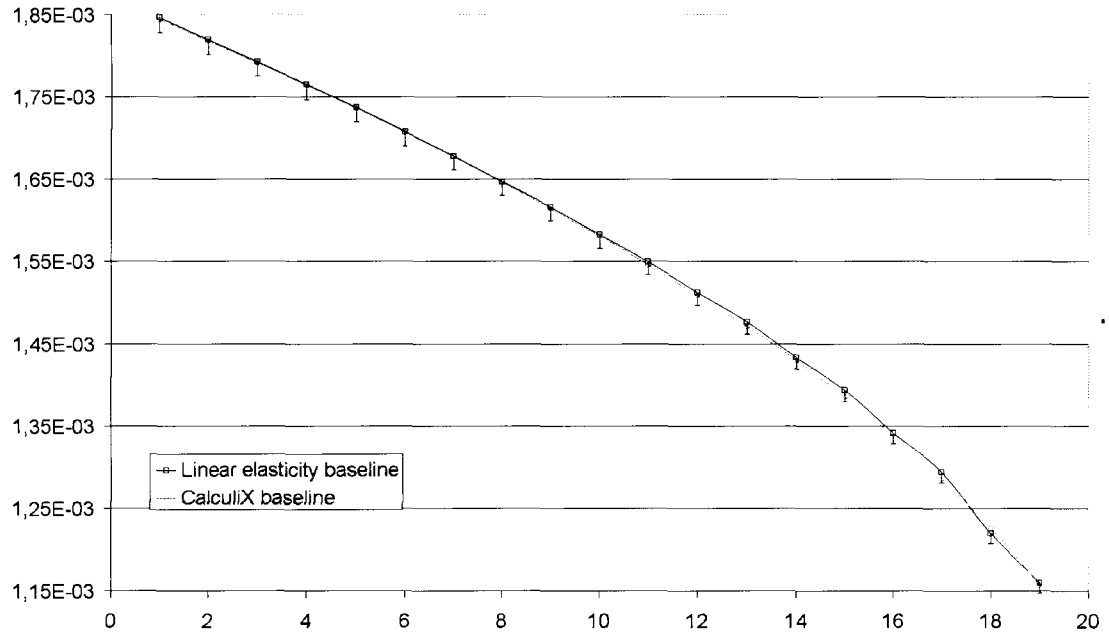

Figure 3.14: Nodal radial displacements[m] predicted using CalculiX and the linear elasticity method for the uncoupled model. 1% difference indicator

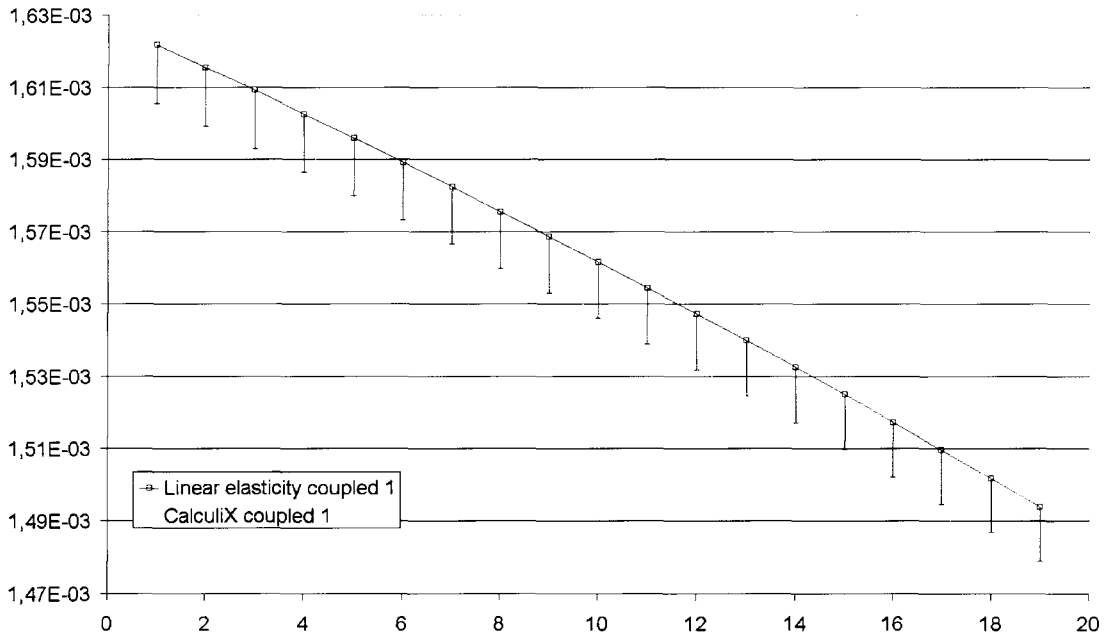

Figure 3.15: Nodal radial displacements[m] predicted using CalculiX and the linear elasticity method for the first coupled model. 1% difference indicator

first and second coupled results are very close to one another for the fluid as well as the mechanical aspect, the comparison between linear theory and the second coupled model results is not presented here as it does not provide any further validation.

Conclusion

Air flowing through a rubber pipe has been considered for validation. In this model, the fluid pressure acts on the rubber wall of the pipe deforming it, which in turn modifies radius and length definition and has an impact on the flow problem redefining fluid pressures and therefore wall deformations. The problem has been solved using the fluid solver developed in this thesis and coupled with the mechanical solver in CalculiX in order to be able to compute the mutual interactions between fluid and solid. Results show that at the end of the iterative process, which takes 7 iterations to converge, the radius of the pipe has grown by 31% and its length has been reduced by 7.5%. Both fluid and mechanical results have been compared with established theories, the Idelchik incompressible correlations in the case of the fluid and linear elasticity for the structural radial displacements. The results predicted by CalculiX are in very good agreement with the simplified theories used which enables to validate both fluid and structural models.

3.3.2 Parametric study on a labyrinth seal

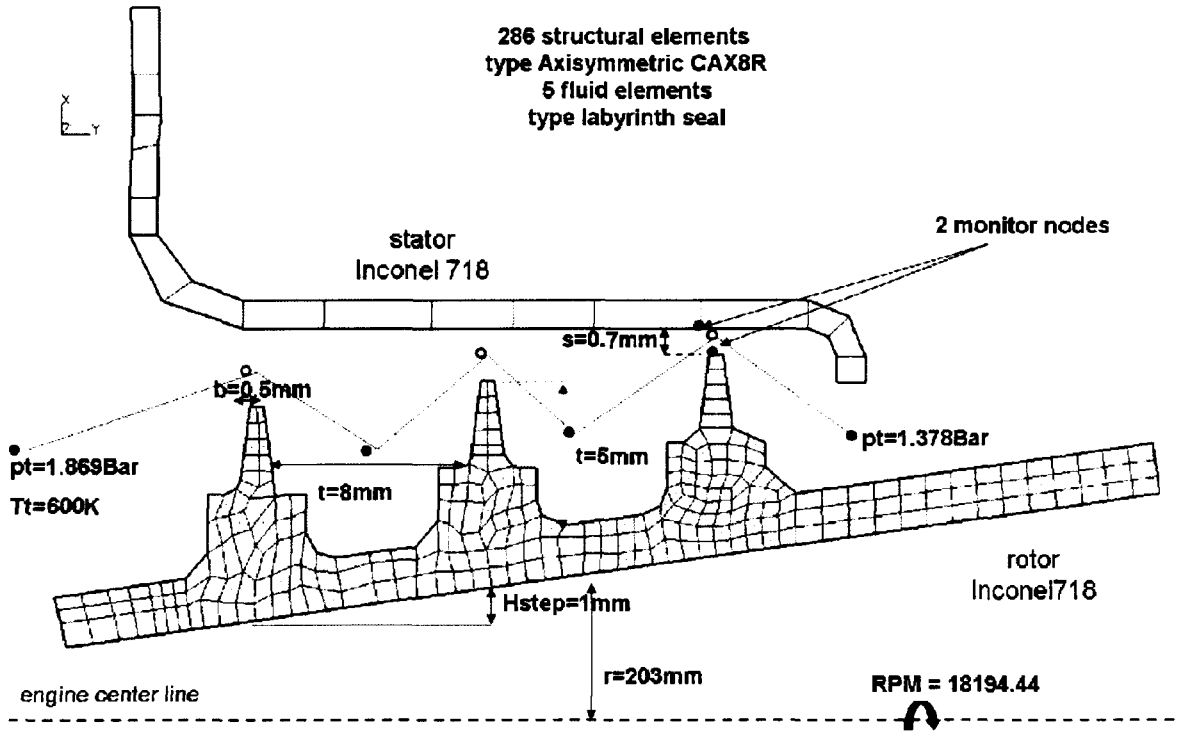

Figure 3.16: Finite element model of the three-fin-stepped labyrinth seal.

Model presentation

As presented in Fig3.16, the 2D axisymmetric finite element model represents the stator and rotor part of a 3-fin-stepped labyrinth seal.

The structural model is composed of 286 CAX8R quadratic elements. The fluid channel representing the flow through the labyrinth is modeled by 5 flow elements, 3 of which are represented in Fig.3.16 plus two boundary condition elements.

Labyrinth seals are used to control the amount of flow entering and leaving the secondary air system. Due to centrifugal forces, thermal expansion and deformation the geometrical characteristics of the labyrinth seal, like the gap, are modified. In order to characterise the labyrinth seal properties, the mass flow rate value has been chosen as variable for the SAS aspect of the model. Boundary conditions for the fluid channel are given as an inlet pressure of 1.869 bar, an inlet temperature of 600K and an outlet pressure of 1.378 bar. The conditions correspond to the operating regime of the labyrinth seal.

In order to model the bolt fixing the upper part of the stator of the labyrinth seal, the upper end of the plate is constrained at its top end in direction x and y. The rotor is constrained in directions x and y at its left extremity to simulate the attachment to the foot of the middle blade, and at its right extremity to simulate

the attachment to the third blade disc.

The stepped labyrinth seal geometrical properties are defined as follows:

- initial gap: **0.7 mm** (initial radial distance between monitor nodes)
- diameter: **406 mm**
- fin-tip breadth: **0.5 mm**
- fin height: **5 mm**
- number of fins: **3**
- inter-fin spacing: **8 mm**
- step height: **1 mm**
- stator thickness: **11 mm**
- stator length: **57.1mm**
- rotor thickness: **20 mm**
- rotor length: **59.8 mm**

The monitor nodes are chosen on the tip of the last fin and on the opposite stator wall as indicated in Fig.3.16. INCONEL 718 has been chosen for both rotor and stator. INCONEL physical properties are temperature dependent. The physical properties of INCONEL 718 as a function of temperature are summarised in table 3.1.

	293	477	699	922	1144
$k \left[\frac{W}{m.K}\right]$	11.4	11.8	15.15	18.03	20.92
$Cp \left[\frac{J}{kg.K}\right]$	435	453	480	506	520
$E\ [Gpa]$	211	206.7	189.5	172.25	158.47
$\alpha \left[\frac{\mu m}{m.K}\right]$	12.8	13.5	14	14.9	17.15

Table 3.1: Physical properties of INCONEL 718 as a function of temperature [K] [1].

k is the coefficient of thermal conductivity, C_p the specific heat, E the Young's modulus and α the coefficient of thermal expansion. Between two reference temperatures listed in table 3.1, the physical properties of the material are linearly interpoled. The effect of temperature on the density of INCONEL 718 is very small. Therefore the INCONEL 718 density is supposed constant over the whole range of temperature and equals $8.19 \times 10^3\ kg/m^3$.

To asses the contributions of the different aspects of the problem separately, four different models have been developed.

- Case 1: Baseline model

  The baseline model represents the labyrinth as designed.

- Case 2: Centrifugal force

  Centrifugal force is applied to the rotor (18200 RPM).

- Case 3: Static pressure

  The static pressure of each junction node of the fluid channel acts simultaneously on the stator inner side and rotor outer side. The static pressure on the stator upperside corresponds to the labyrinth outlet pressure. On the inner side of the rotor a pressure of 1.44715 bar is applied.

- Case 4: Temperature

  The nodes on the top of the stator are set at a temperature of 770K, the nodes belonging to the bottom part of the rotor have a temperature of 880K. This is case 4. It is subsequently divided in two subcases. In the first computation only the two previously mentioned boundary conditions have been implemented. This is case 4.1. The labyrinth gap definition is controlled by the displacements of the monitor nodes, but the fluid properties are uncoupled from the thermal problem. The second computation, case 4.2, takes into account the fluid flowing through the labyrinth seal. To this aim, film conditions are applied between the inner side of the labyrinth and the fluid junction nodes. For the geometry given and the flow conditions specified, MTU proprietary data specifies a heat transfer coefficient of $1000W/(m^2K)$ on the stator and a heat transfer coefficient of $3000W/(m^2K)$ on the rotor. The value of the heat transfer coefficient varies in function of fluid properties and geometrical definition. However, as the aim of the computation is to assess the relative importance and effects of the various loads with regard to the coupled problem, heat transfer coefficients on rotor and stator are kept constant. This enables furthermore to be independent from MTU proprietary data for this calculation.

- Case 5: Centrifugal force, pressure and temperature.

  The last model addresses all aspects of the coupled problem: mechanical and thermal loads. This case is labelled case 5.

For each model, the calculation has been performed taking into account the variation of geometry in order

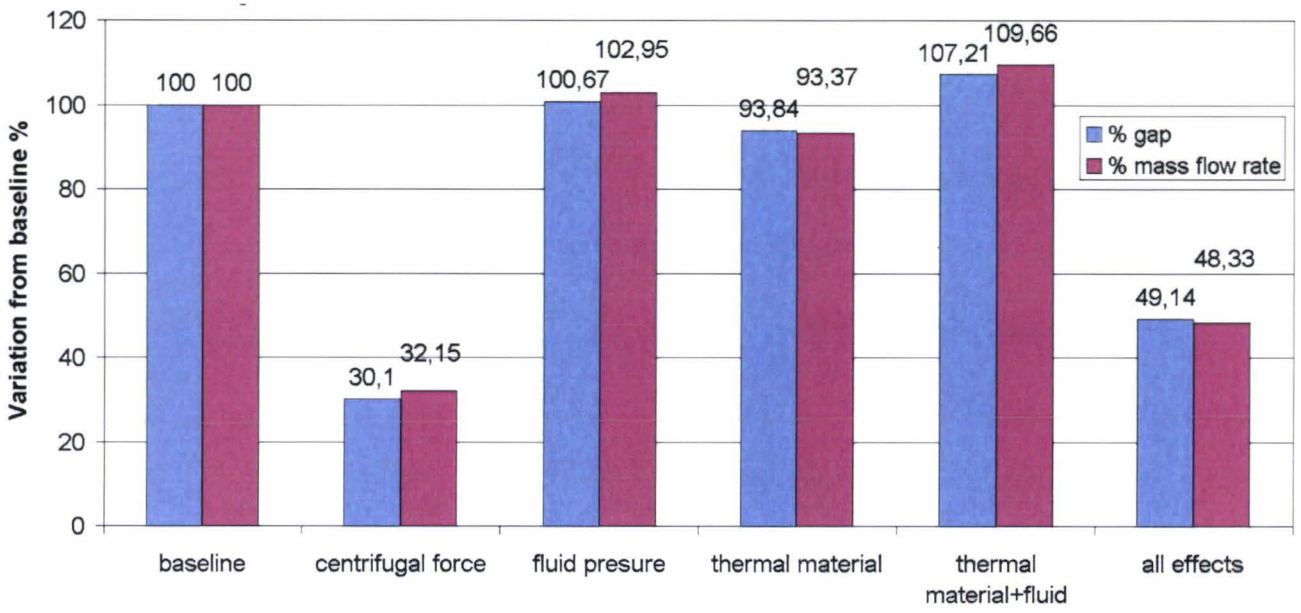

Figure 3.17: Variation of the labyrinth seal mass flow rate and gaps for all models. All results are given in percent relative to the baseline solution

to update the definition of the labyrinth in the fluid channel. Results in terms of mass flow rates and gap definition are given in Fig.3.17.

Results

Fluid pressure acts on the inner side of the labyrinth seal, in the positive radial direction on the stator and negative radial direction on the rotor which increases the initial gap. The displacements of the monitor nodes are respectively 7.33×10^{-7} m on the stator and -3.97×10^{-6} m on the rotor. Due to the small pressure difference between the inner and outer sides of the labyrinth seal, the deformation of the labyrinth due to the pressure of the fluid acting on the structure is negligible in comparison with the deformation generated by the other effects. As shown in Fig.3.17 the gap increases by only 0.67%.

The effect of the centrifugal force acting on the rotor is to move the fins in the positive x-direction thus reducing the gap between rotor and stator. The radial displacement of the monitor node placed on the rotor amounts to 4.89×10^{-4} m. The global rotor radial displacements and the final deformed state of the labyrinth seal are presented in Fig.3.18. The remaining gap is only 30% of the initial gap as as can be seen in Fig.3.17 case 2.

The effect of temperature on the deformation of the labyrinth seal is also important. The displacements and temperature repartition for case 4.1 are presented in Fig.3.19 and in Fig.3.20.

As the fluid is not considered in this case rotor and stator temperature are respectively 880K and 770K due only to conduction phenomena in the solid. As there are no temperature gradients in the structure the

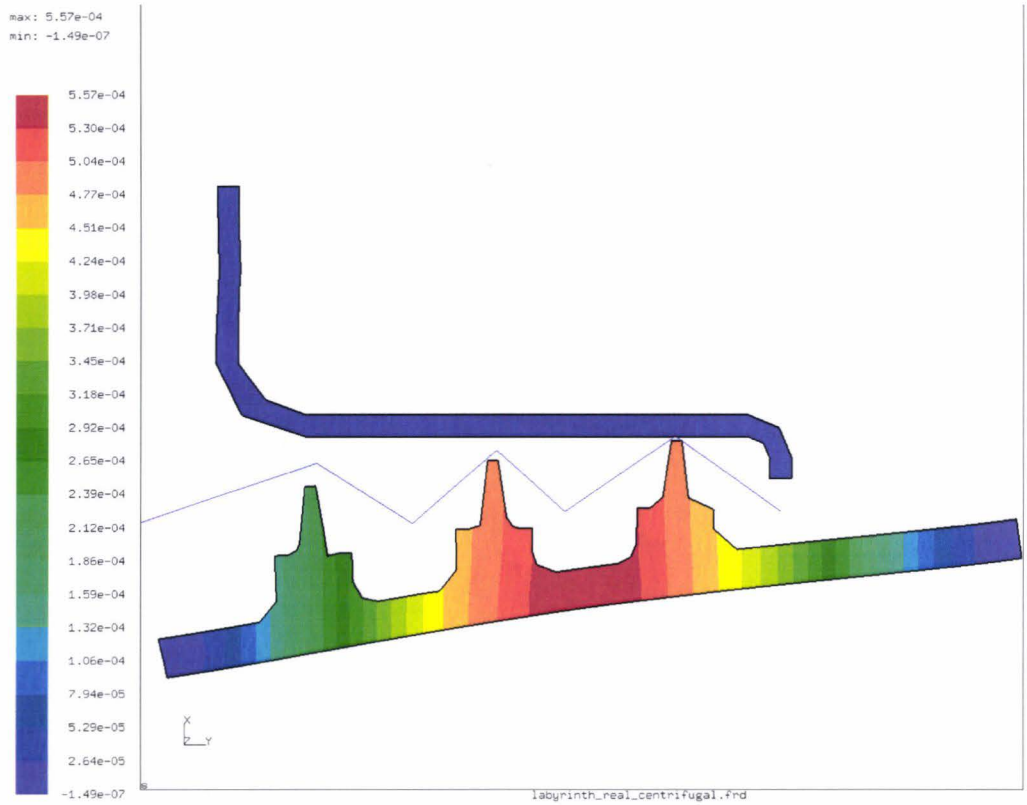

Figure 3.18: Labyrinth seal final deformed state under centrifugal load and corresponding displacements [m]. (case 2).

effect on the labyrinth gap is not differential deformation but global thermal deformation. In the monitor nodes, the displacements for case 4.1 are respectively 1.56087×10^{-3} m for the stator and 1.6039×10^{-3} m for the rotor. As the deformation of the rotor is more important than the stator for the two monitor points considered, the initial gap is reduced to a value of 0.65669×10^{-3} m which corresponds to a mass flow rate of 8.77×10^{-2} kg/s.

For case 4.2, taking into account the fluid as a thermal boundary condition, displacements and temperatures are presented in Fig.3.21 and in Fig.3.22. Due to the presence of the cooler fluid, the temperature distribution in the solid is significantly different from case 4.1. The addition of the fluid has essentially an impact on the rotor due to the higher heat transfer coefficient between fluid and wall but nevertheless affects the stator temperature. The first fin of the labyrinth sees its temperature decrease to 658 K. For the two monitor points the temperatures are respectively 767 K on the stator and 763 K on the rotor.

Displacements due to thermal loads are given in Fig.3.21 for case 4.2. They amount to respectively 1.5537×10^{-3} m for the stator and 1.50321×10^{-3} m for the rotor. This corresponds to an increase of the gap value at 0.7505×10^{-3} m. By comparing the displacements with and without fluid, one can see the impact of fluid temperature on the global displacements is not very important on the stator with about 0.5% relative

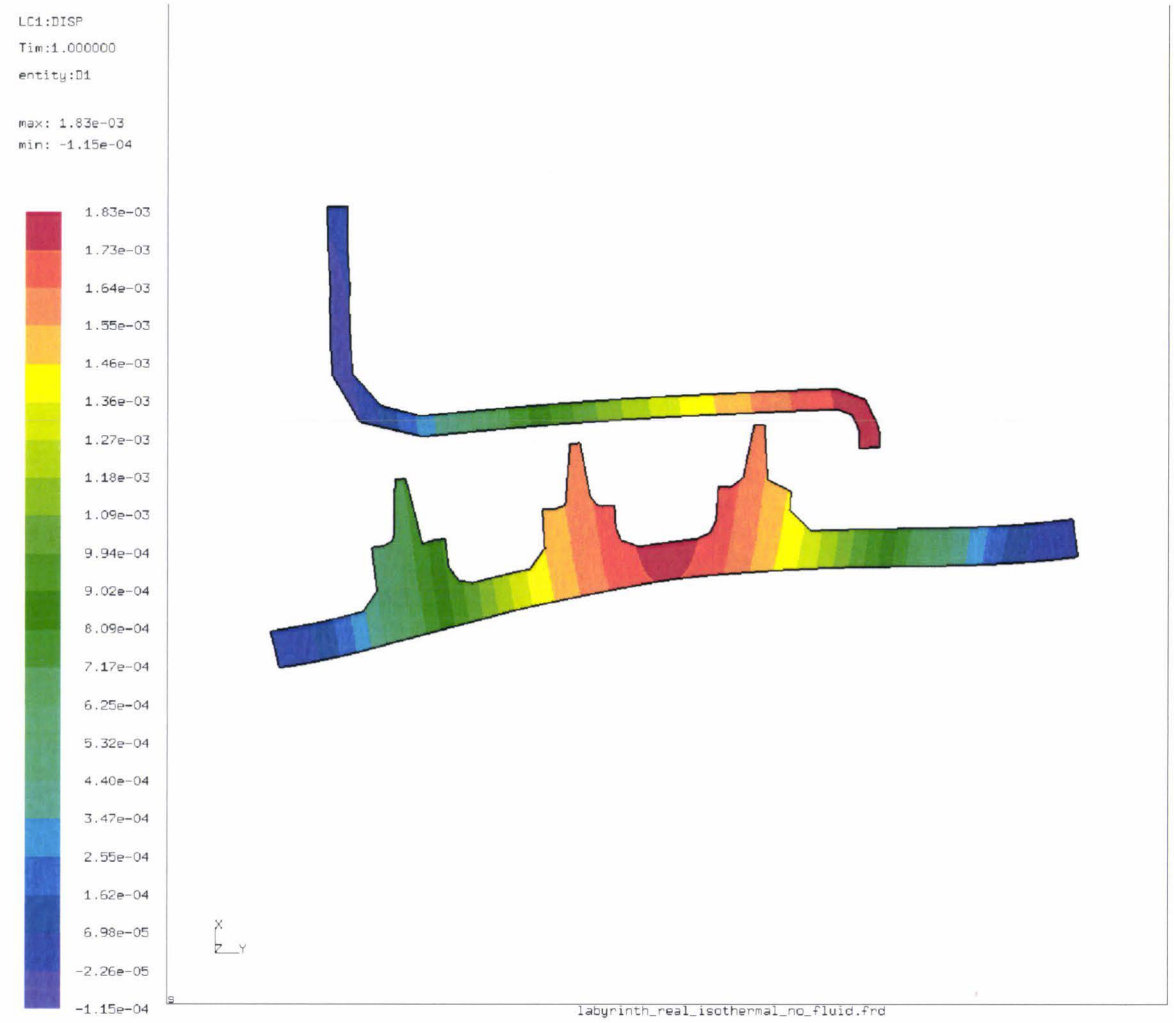

Figure 3.19: Radial displacements due to thermal load [m] (case 4.1).

difference. For the rotor however the introduction of the cooler fluid has for effect to decrease the temperature of the rotor and therefore the displacements. The relative difference on the rotor between case 4.1 and 4.2 amounts to 6.3%. The gap value is increased by 12.5% which results in an increase of mass flow rate by 14.45% at 1.03×10^{-1} kg/s.

Due to the thermal interactions between the fluid and the walls, the temperature of the fluid increases as it progresses inside the labyrinth seal. The nodal temperatures in the fluid canal are: 600 K, 671 K ,719.5 K and 768.5 K.

When combining pressure, centrifugal and thermal loads, as done for case 5, the displacements of the two monitor nodes are respectively 1.56052×10^{-3} m for the stator and 1.916397×10^{-3} m. When compared with the purely thermal computation (case 4.2), the displacements of the stator are very slightly increased by the addition of the pressure on the inner face of the stator as well as the reduction of the coolant mass flow rate. As for case 4.2 conduction phenomena inside the stator are higher than the exchanges between stator

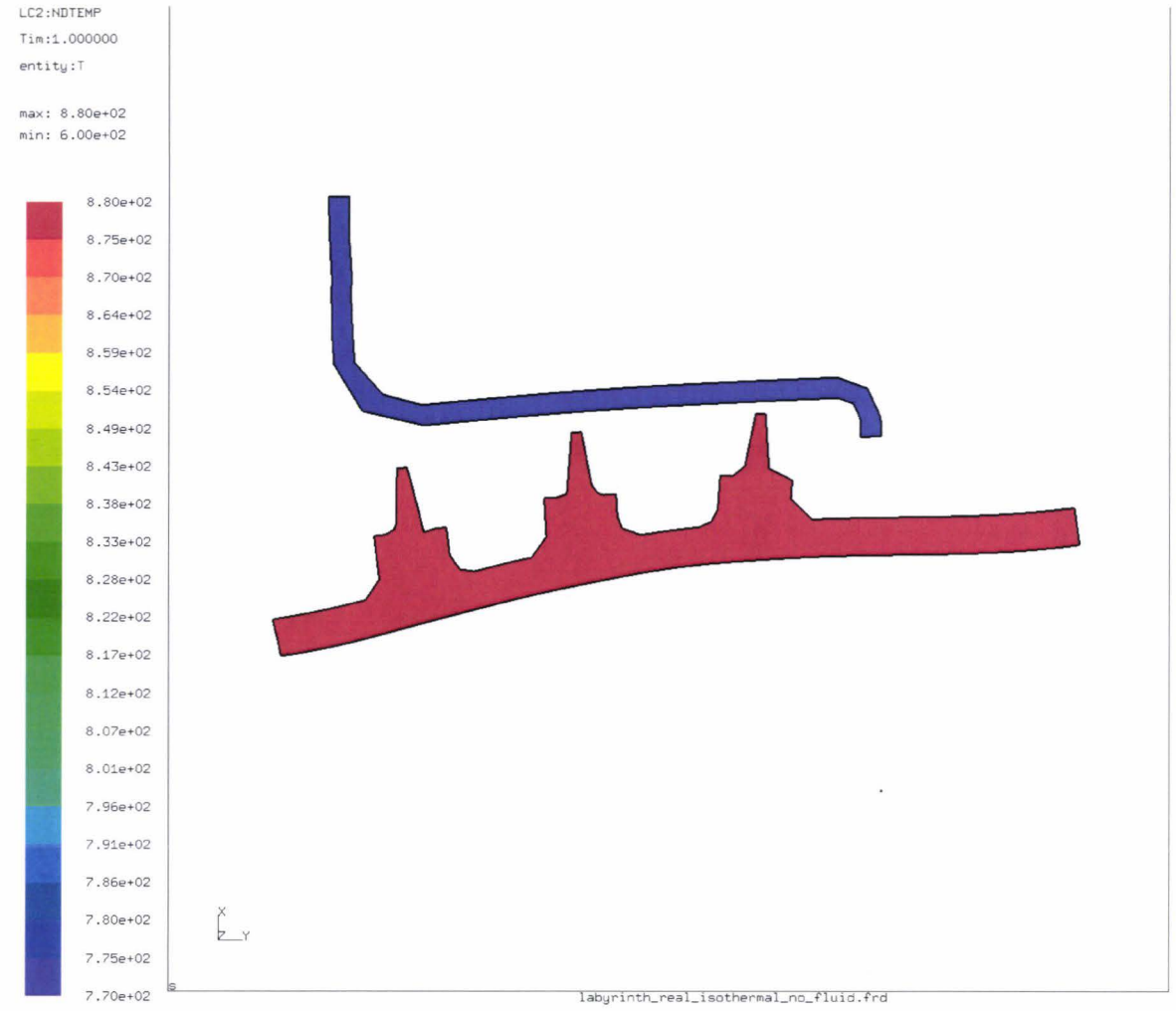

Figure 3.20: Temperature repartition [K] for case 4.1.

and fluid. Therefore the a small temperature gradient exists in the stator between 770 K on the outer face and a minimum of 760 K on the inner face. The effect of combined temperature and centrifugal force on the rotor is to move the rotor toward the stator and thus to reduce the gap. The counter-effect of pressure is only marginal. The resulting displacements obtained using the combined loads are not the direct combination of the different effects taken separately. Finally the gap is reduced by 50.85% at 0.344×10^{-3} m which corresponds to a reduction of 51.65% of the labyrinth seal mass flow.

As the gap is reduced the amount of flow flowing through the labyrinth is reduced. The contribution of the fluid to the solid temperature, and especially the rotor temperature, is therefore reduced. The temperature on the stator monitor point is 772.27 K and 808.9 K on the rotor, which is slightly warmer than for the purely thermal computation (case 4.2). Air temperature is also increased during the crossing of the labyrinth and the nodal fluid temperatures are respectively 600 K, 712.57 K, 773. 23 K and 818.18 K. They are about 6% higher than the fluid temperatures obtained with thermal loads only (case 4.2). The reduction of the

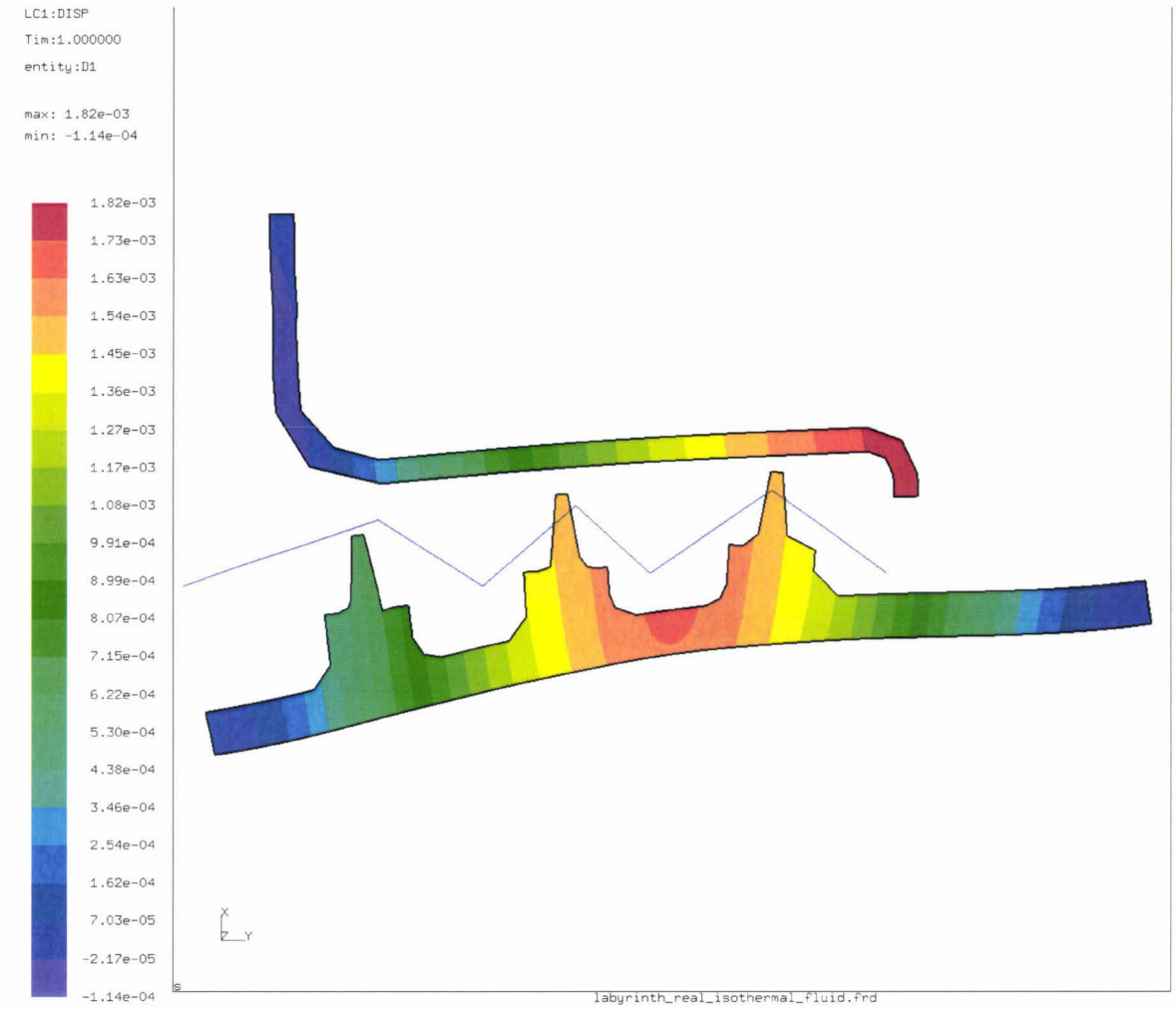

Figure 3.21: Radial displacements due to thermal load [m] (case 4.2).

labyrinth gap reduces the coolant mass flow. In turn the coolant losses part of its cooling potential as its temperature increases. At the right end of the labyrinth seal, the temperature of the fluid is more important than the temperature of 770 K prescribed for the stator.

Conclusion and discussion

For the case considered, the parameter study shows the two main sources of material deformations: thermal loads and centrifugal forces. The contribution of fluid pressures on the global deformations appears to be negligible. The interaction between fluid temperature and solid temperature has been highlighted with regards to temperature distribution in the solid and fluid channel. The impact of fluid temperature on the solid deformation is to be reckoned with. The introduction of the fluid in the thermal problem changes the temperature of the material and therefore changes the displacements. However the contribution of fluid properties to the global displacements is on average quite small when compared to centrifugal forces and

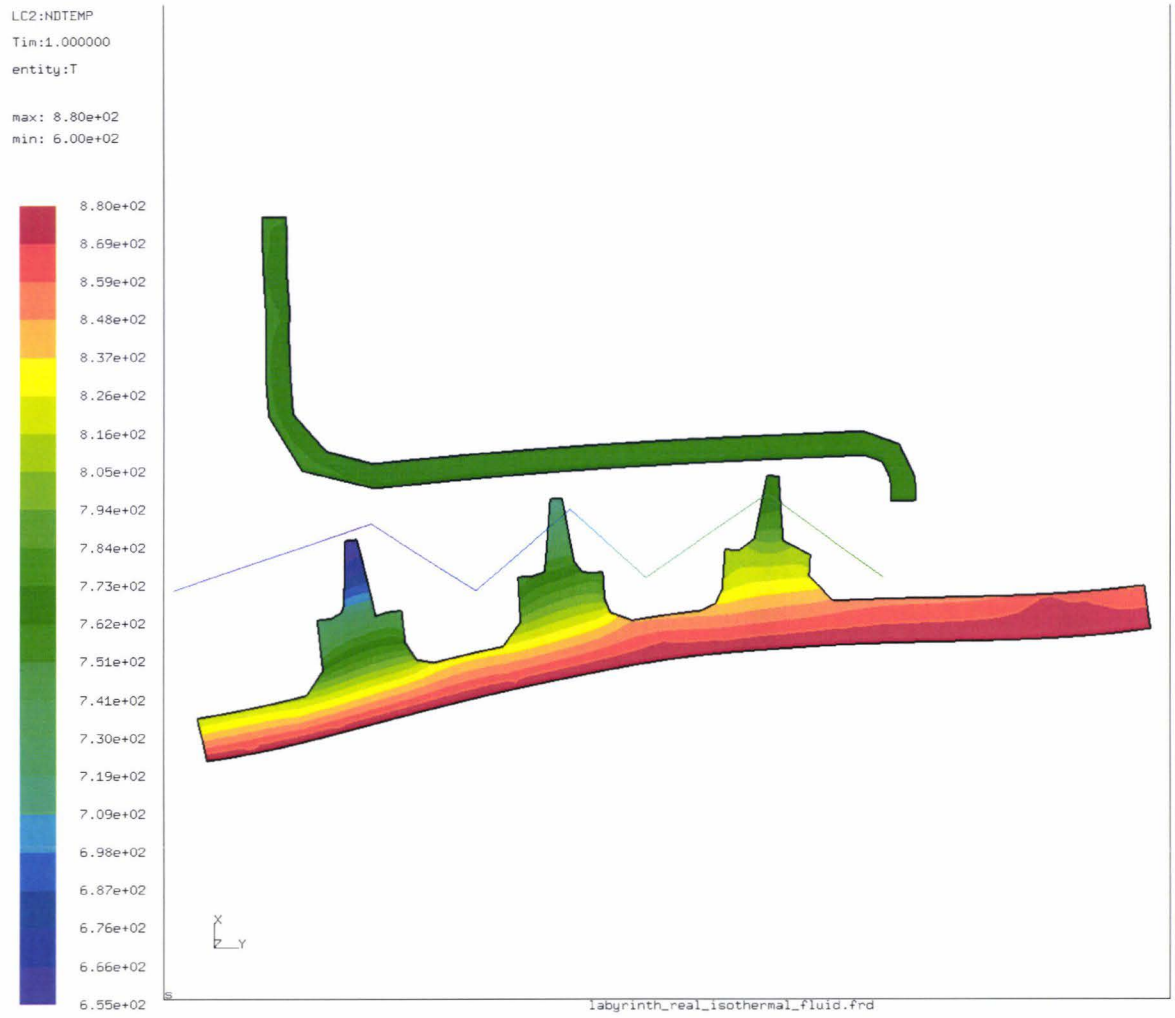

Figure 3.22: Temperature repartition [K] for case 4.2.

conduction phenomena inside the solid.

This raises the question of the pertinence of the present coupling process for the case considered. Indeed in order to be efficient, the procedure should begin with a thermomechanical computation since the effect of the thermal and mechanical loads are predominant in the present case. The secondary air computations should come afterwards using a deformed geometry instead of being considered in the first place, thus giving the priority to secondary phenomena.

As presented in the literature review, secondary air system computations and thermomechanical computations are systematically performed in a sequential way for the analysis of an engine. In comparison to the costs involved to run a thermomechanical computation, performing one secondary air system computation per thermomechanical computation is small and even more so inside a fully automated process. In this regard two cases may be considered

- the secondary air system has no or very little influence on the thermomechanical problem.

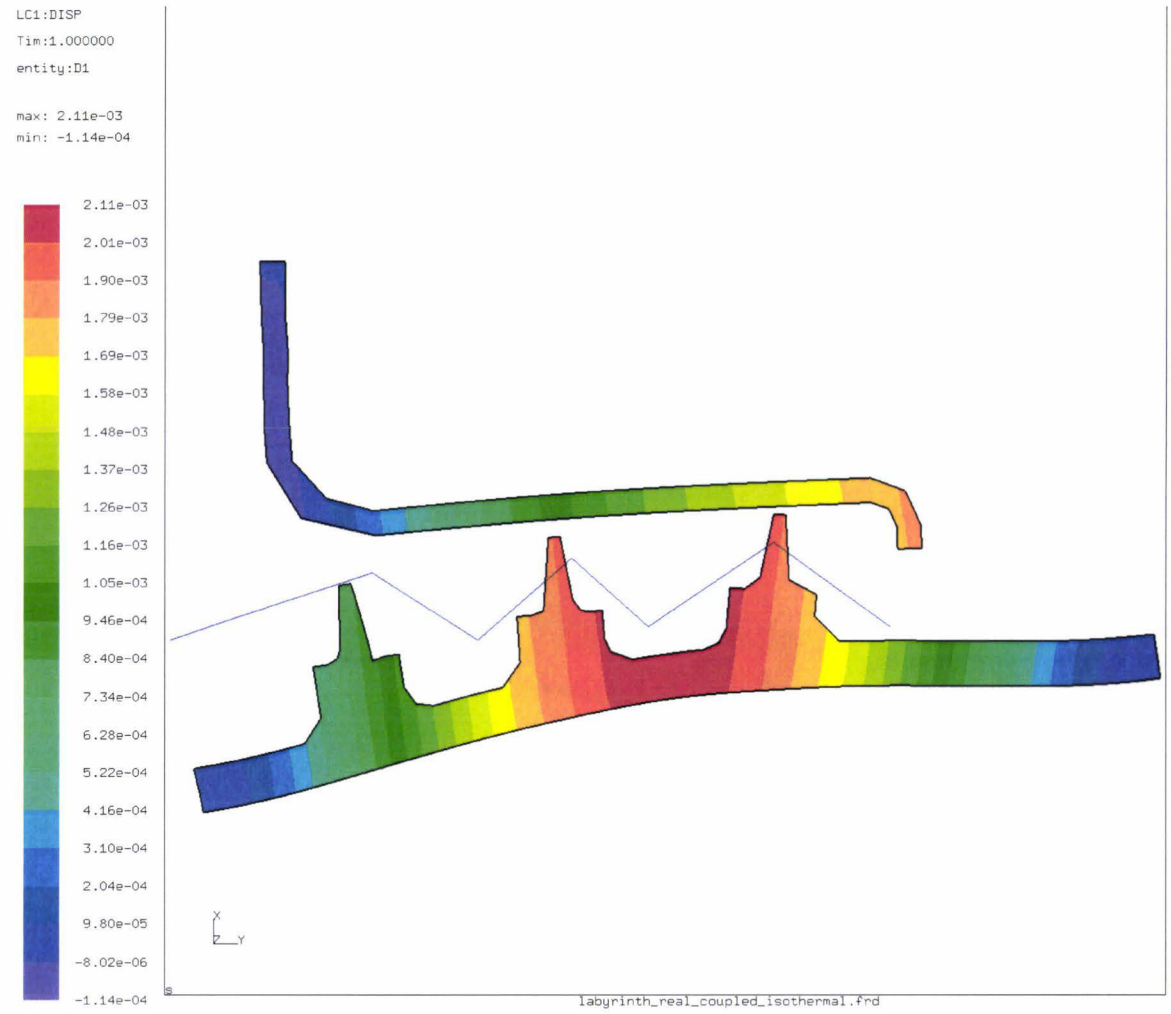

Figure 3.23: Radial displacements due to thermal and mechanical loads [m] and final deformed state of the labyrinth (case 5).

Beginning the iterative process with a secondary air system computation or directly with the thermomechanical computation neither impairs the accuracy of the computation nor increases the resources required to run the following thermomechanical computation.

- the secondary air system has a moderate or high impact on the thermomechanical problem.

  Beginning the iterative process directly with the thermomechanical analysis disregards the secondary air system impact at least in the first iteration. This means that the solution after the first loop will be farther away from the final solution than the one achieved by taking secondary air system into consideration. In turns this means more iterations to obtain the final converged solution thus increasing the global computational cost.

Beginning the coupling process by performing a secondary air system analysis is therefore optimal from a computational point of view, even if it disregards the relative importance of the different loads. Moreover

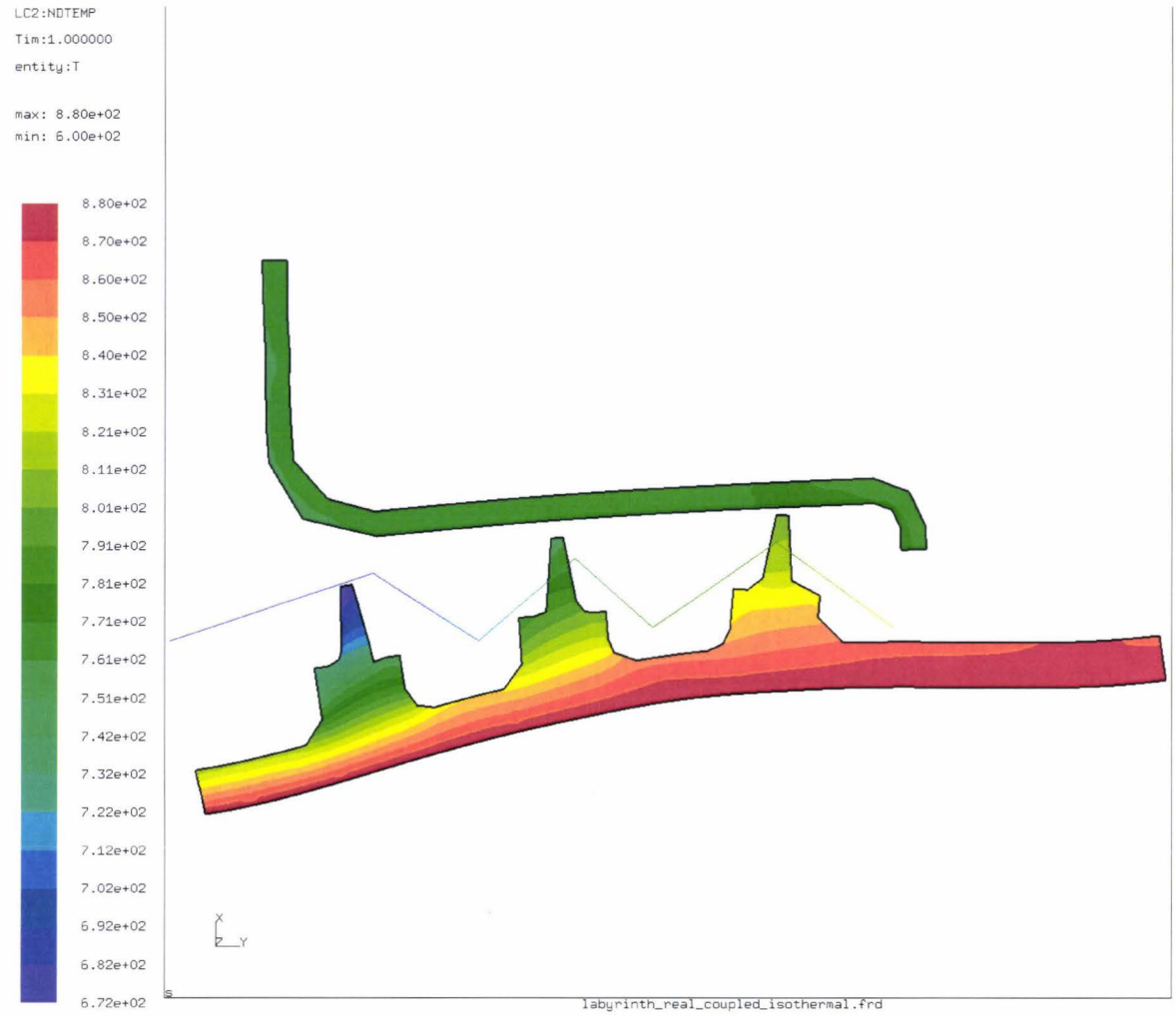

Figure 3.24: Temperature repartition and deformed state of the labyrinth (case 5).

the introduction of an automated tool can only help reducing the amount of resources required for coupled computations in terms of user and machine time.

3.3.3 Investigation of the steady state behaviour of a low pressure turbine

An industrial example of a fully coupled analysis of a low pressure turbine arrangement is proposed as an illustration of the capabilities of the new tool developed during the project and its future possible use.

Model presentation

The model presented here is the complete low pressure turbine of a real engine. As featured on Fig.3.25, it is constituted by a rotor with three blades labelled "blade 1", "blade 2" and "blade 3" and a stator comprised of two nozzle guide vanes labelled "NGV1" and "NGV2". Fig.3.25 represents the complete thermomechanical mesh with embedded secondary air system flow network. The model width is 0.244 m and its height is 0.323 m. The axisymmetric model is meshed with 5370 eight-node quadratic axisymmetric elements of type CAX8R which represents a total of 19700 nodes.

Both rotor and stator are modelled in INCONEL 718 using an isotropic linear elastic behaviour law. The physical properties of INCONEL 718 are temperature dependent and are summed up in table 3.1.

The rotation rate of the rotor is 18194.44 RPM. The investigation focuses on the steady state behaviour of the two stepped labyrinth seals, namely D40 and D50. The labyrinth seals geometrical properties are listed in table 3.2. The honeycomb lining on the labyrinth D40 stator, not represented on Fig.3.25, has been

	D40	D50
gap [mm]	0.8	0.7
diameter [mm]	418	406
fin number	2	3
fin tip breadth [mm]	0.5	0.5
fin height [mm]	1	1
fin interspace [mm]	8	8
fin/stator position [mm]	4	4
honeycomb cell size[mm]	0.7874	0
honeycomb height [mm]	5.258	0
fin tip radius [mm]	0	0

Table 3.2: Geometrical definition of labyrinth seals D40 and D50.

modelled by an offset taken into account when computing the distance between the two monitor nodes.

The secondary air system network, the outline of which is displayed on Fig.3.25, is represented more in details in Fig.3.26 using the graphical user interface. Chamber and boundary condition numbers on Fig.3.26 corresponds to the nodes number on Fig.3.25.

Boundary conditions in terms of pressures and temperatures are implemented in nodes: 1, 2, 3, 4, 6, 7, 8, 10, 11, 12. They are located in the low pressure turbine main stream and have been provided by numerical computations performed in the main flow path. These steady state conditions are defined for the working

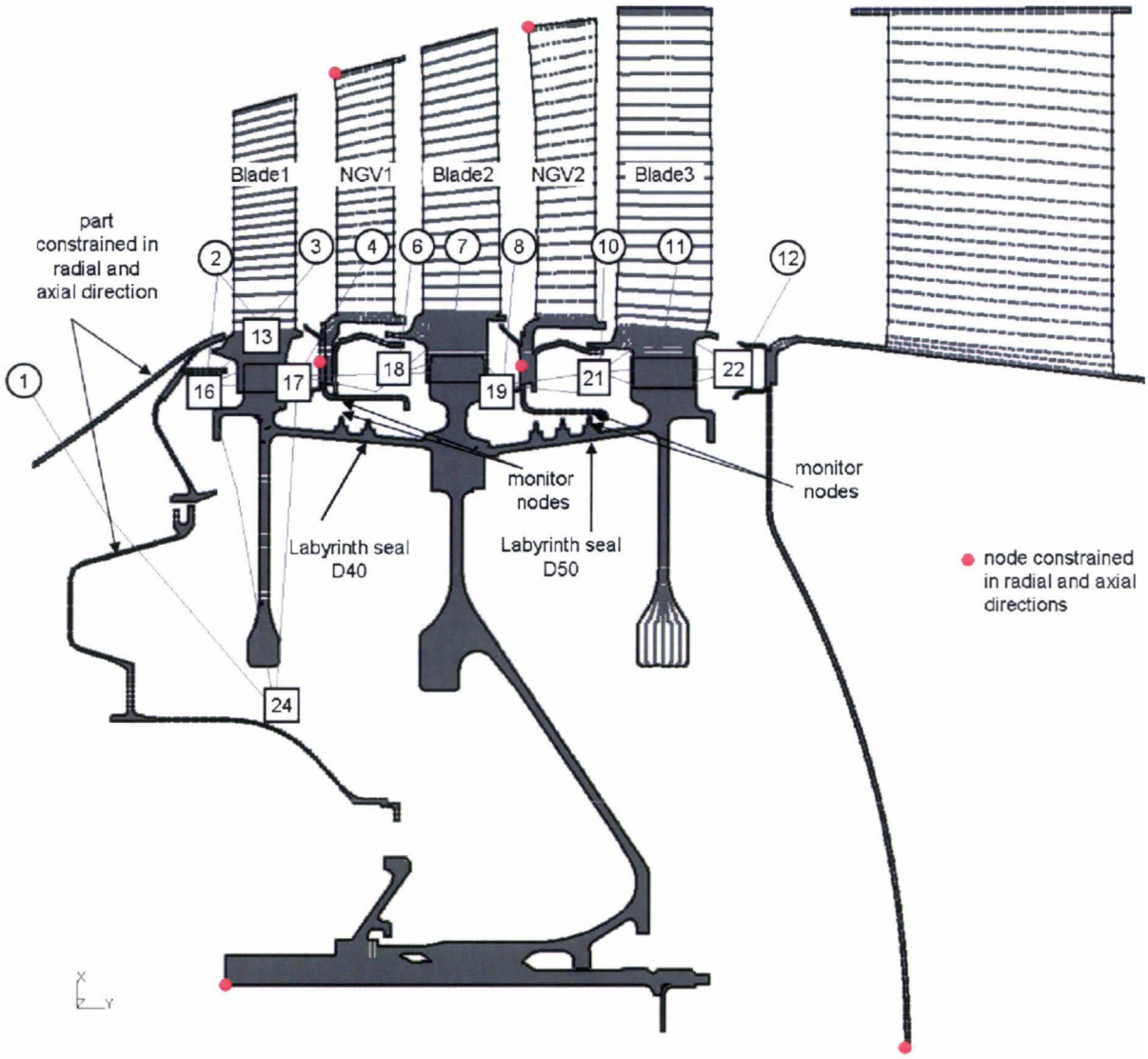

Figure 3.25: Finite element model of the LPT with embedded secondary air system network and structural boundary conditions.

point studied.

In the chambers (13, 14, 15, 16, 17, 18, 19, 21, 22, 23, and 24), temperatures and pressures are to be computed. Mass flow rates in the flow lines linking the different chambers are unknown. The loss elements, representation and nomenclature of which has been highlighted in section 2.5.2, are represented in Fig.3.26. The yellow circles symbolyse inlet or outlet boundary conditions located for this example in the main flow path. The circles contain first of all a label, than a total pressure level written in bar and a total temperature level written in Kelvin. The green squares are the nodes, also designed as SAS chamber, where the total pressure and the total temperature level are to be determined. As for the boundary nodes, they display results in terms of total pressure level in bar and total temperature level in Kelvin. In the oriented flow lines, represented by black arrows and a black label, there is a minimum of one flow element represented by a blue

symbol and an associated label. A red flow line represents a reversal of the flow direction, it is associated with a negative mass flow rate also represented in red. The mass flow rate in $kg.s^{-1}$ is an unknown of the problem in all the flow lines.

For the structural model, nodal flow pressures are considered as distributed loads, fluid temperatures and mass flow rates are used to model convective heat transfer (see Annex C 3.4). For the purpose of the computation an unique heat transfer coefficient of 1000 W/m^2K has been defined for convective heat transfer. Convective heat transfer relationships are set up between the different fluid nodes of the fluid network and the different structural parts.

The rotation rate defines a centrifugal load applied to the rotor of the LPT.

As presented in the Fig.3.25, the bottom left node of the rotor is constrained in the radial as well as in the axial direction to simulate the attachment of the rotor shaft. Both nozzle guide vanes are constrained by their upper left node in axial and radial direction to simulate the attachment to the casing and casing growth. In the bottom part of each nozzle guide vane, the attachment of the floating ring constituting the labyrinth seal stator with a nut and bolt system is modelled by constraining a single node in the axial and radial direction. Labyrinth D40, between chambers K17 and K18 and labyrinth D50 on line D50 between chambers K19 and K21 are subject to gap definition change through thermal and mechanical loads. Monitor points are located on the left fin tip and opposite stator for labyrinth D40 and on the right fin tip and opposite stator for labyrinth D50. The two pairs of monitor nodes are represented on Fig.3.25.

Results and comments

Two fully integrated computation has been carried out

- in the first one variations of geometry due to mechanical and thermal loads are not taken into account in the secondary air system definition.
- in the second one a fully coupled computation is carried out, taking into account thermal and structural coupling between the air system and the structure.

The first model represents the engine as designed. The solution obtained at the end of the first iterative loop therefore constitutes at the same time the first loop of the fully coupled calculation.

The purpose of the investigation is to show the difference between the first model results and the final model results in terms of

- secondary air system variables as pictured Fig.3.27 and Fig.3.28
- structural temperature repartition as shown Fig.3.29 and Fig.3.30

- radial displacements presented in Fig.3.31 and in Fig.3.32

The secondary air system model results for both first (Fig.3.27) and coupled model (Fig.3.28) are presented using the dedicated graphical user interface. Radial displacements and temperature distribution are displayed using the CalculiX graphical user interface.

Convergence for the coupled calculation is achieved after 16 iterations which takes about 20 minutes on an Intel Pentium 4, 3.4 GHz and 512MB RAM machine. This makes the coupled process particularly adapted and attractive for engineering purposes as even for an important problem such as the one currently considered, computational resources are readily available and time to convergence remains small. Initial cold gaps, final gaps and related variation for both labyrinth seal are presented in the following table.

Labyrinth	cold gap [m]	final gap[m]	% variation
D40	8E-4	8E-6	-99%
D50	7E-4	7E-6	-99%

Let consider the secondary air system problem as pictured Fig.3.27 and Fig.3.28.

In view of the mass flow rates in line D40 (0.00025 kg/s) and D50 (0.00012 kg/s), labyrinth D40 and D50 may be considered as closed .

As the mass flow rates in D38 and D48 are equally low, the front part of the LPT comprised of the first rotating blade and static nozzle guide vane, as well as the middle part comprised of the second blade and second nozzle guide vane, can be considered as almost independent from one another as well as from the rest of the LPT from the air system point of view. This tends to explain the difference of flow temperature level between front and rear part presented in Fig.3.28 as well as the few differences between the first model and the fully coupled model for the front part of the LPT as the labyrinth seals are located after the first nozzle guide vane.

In Fig.3.28 the incoming hot flow from P6 has a direct impact on K18 temperature and affects all downstream chambers. This effect is all the more reinforced by the decrease of the labyrinth seal D50 gap by half its value, thus impeding the venting of chambers K18. The same occurs between P10 and chamber K21. In Fig.3.27, as no ingress of hot air occurs in the secondary air system, the flow temperatures in the LPT remain globally even.

The temperature in chamber K22, which in both models is higher than the rest of the temperatures of the adjacent chambers, is explained by the presence of convective boundary conditions in the last rotor cavity

(under the last nozzle guide vane) and also between the last blade foot and the flange.

The coupling effect with regard to material temperature repartition and radial displacements is pictured in Fig3.29 and Fig.3.31 for the basic model and Fig.3.30 and Fig.3.32 for the coupled model. Temperature levels of the labyrinth seal stator for both labyrinth seals are significantly different for both models due to the different fluid temperatures. This results in more important displacements of the stator tip for the coupled model.

Material temperatures and displacements are significantly higher when considering the fully coupled model due to the closure of both labyrinth seals and the almost negligible venting flow between chambers K17 and K18 as well as chambers K19 and K21.

As can be seen on Fig.3.33, the main drive for labyrinth closure is in this case the centrifugal forces acting on the rotor. Temperatures on both labyrinth seal stators tend to move the labyrinth stator in the positive radial direction, and even more so due to higher temperatures in the coupled model, but the displacements are not sufficient enough to maintain the labyrinth seals open. The interaction between fluid-thermal-structure can be summed up as follow: the centrifugal force is closing the labyrinth seals, thus modifying the flow network. The modification of the flow path leads to an increase of the fluid temperatures. In turn fluid temperatures lead to higher material temperatures and larger material deformations.

It is interesting to see on Fig.3.33 that some other parts of the general arrangement are impacted by the thermomechanical coupling. For instance the rim seals between the casing and the first blade as well as between the first and second blades and the first nozzle guide vane and the third blade and the second nozzle guide vane. This would require implementing the coupling procedure for other elements as well.

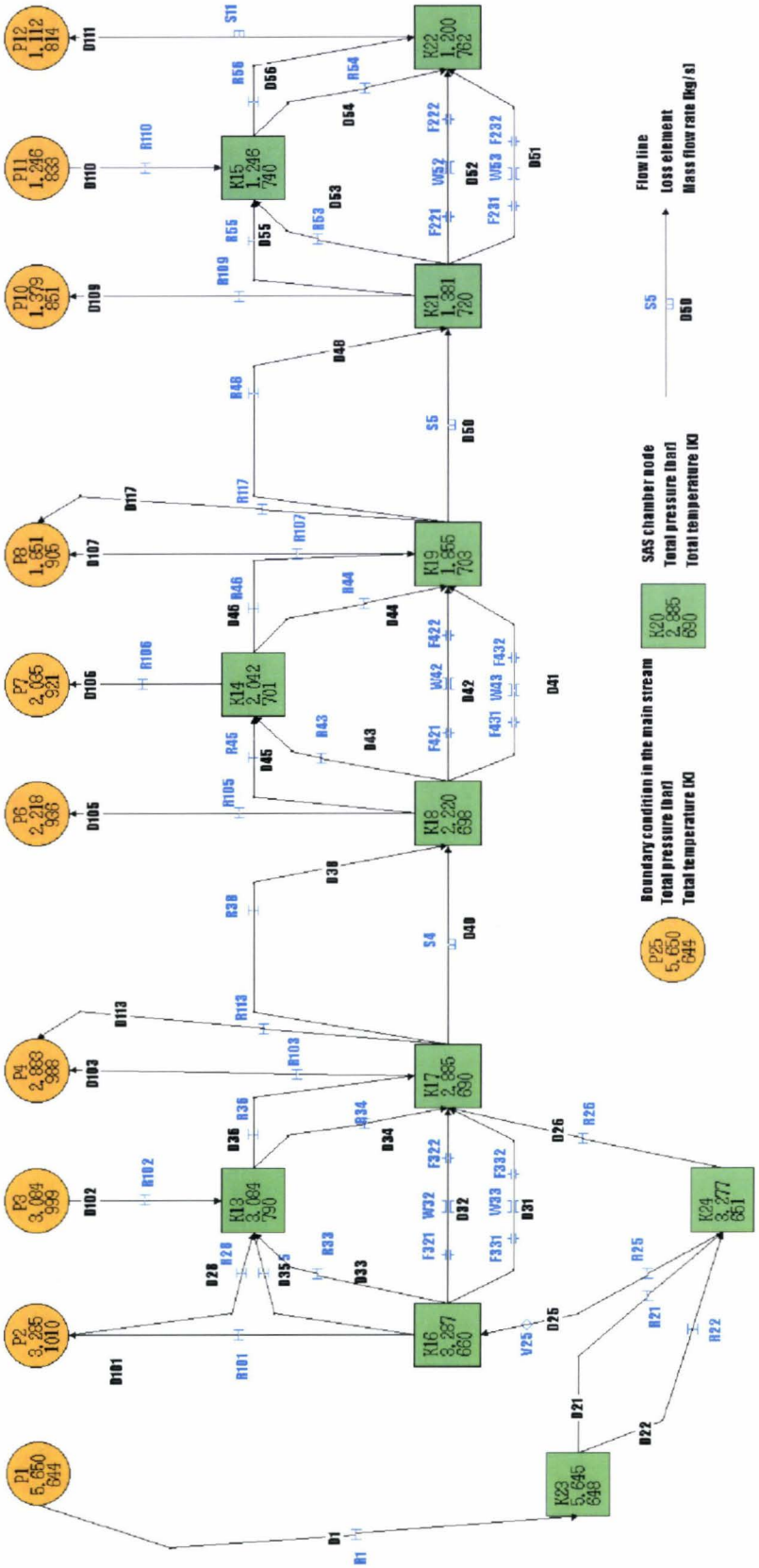

Figure 3.26: Secondary air system model of the LPT.

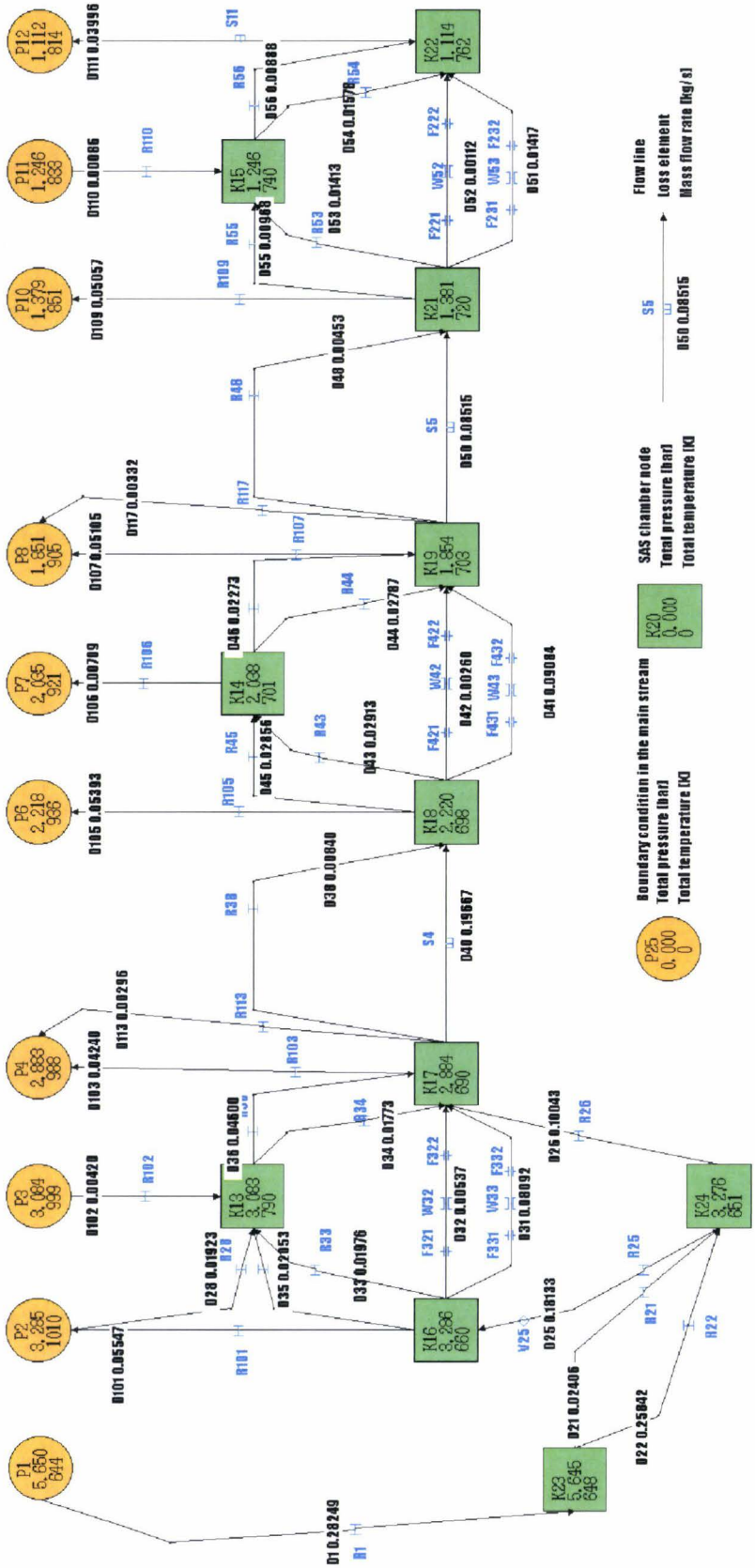

Figure 3.27: Results of the first calculation for the secondary air system .

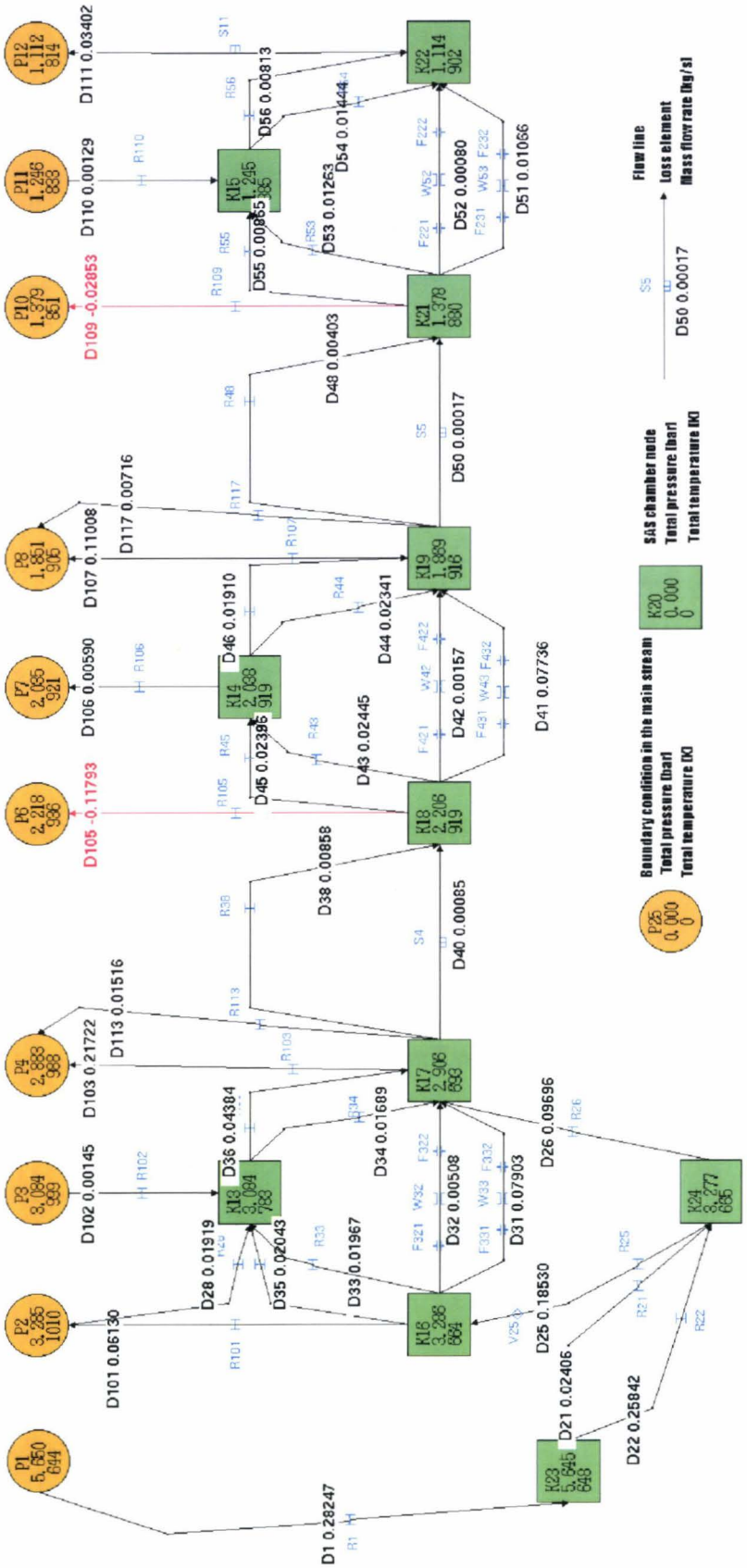

Figure 3.28: Results of the fully coupled calculation for the secondary air system .

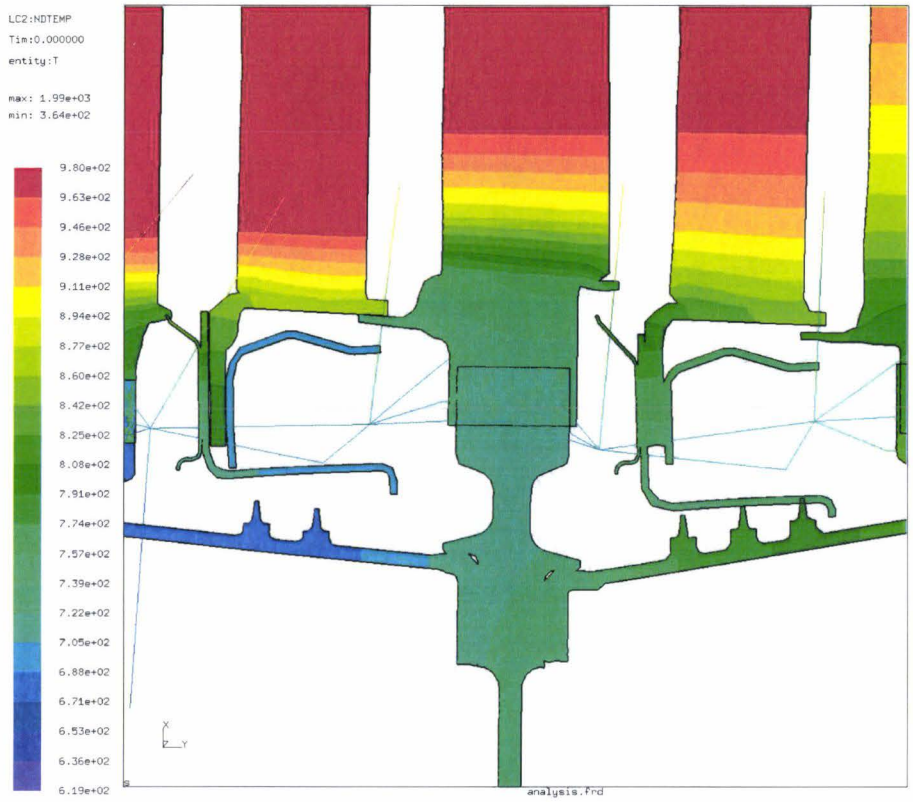

Figure 3.29: Temperature repartition on the first model.

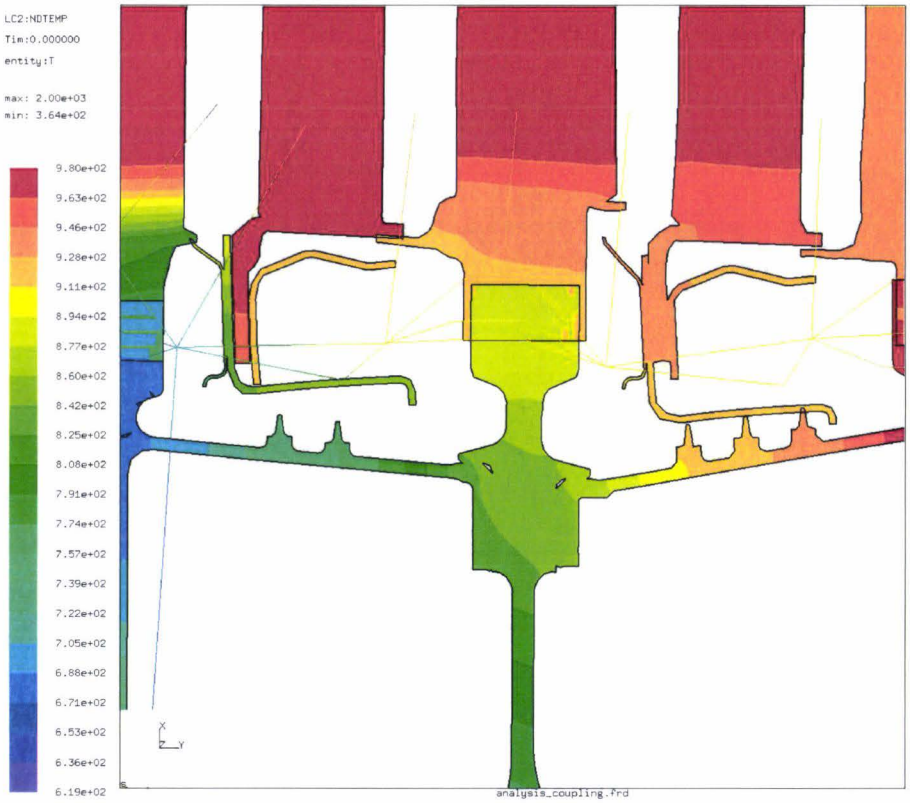

Figure 3.30: Temperature repartition on the fully coupled model.

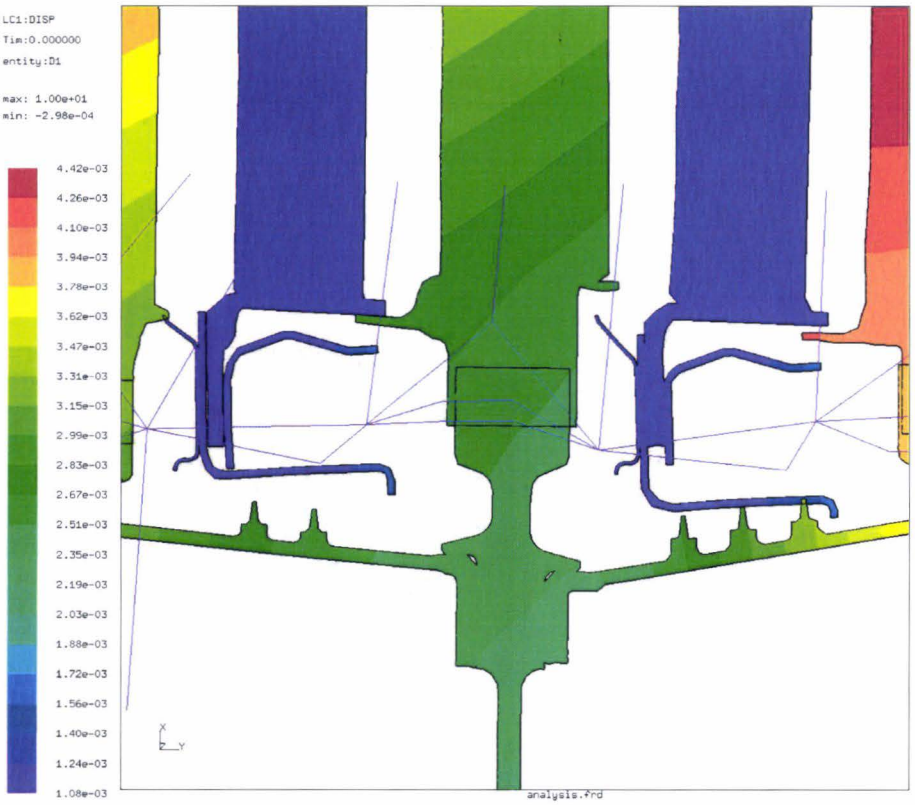

Figure 3.31: Radial displacements on the first model.

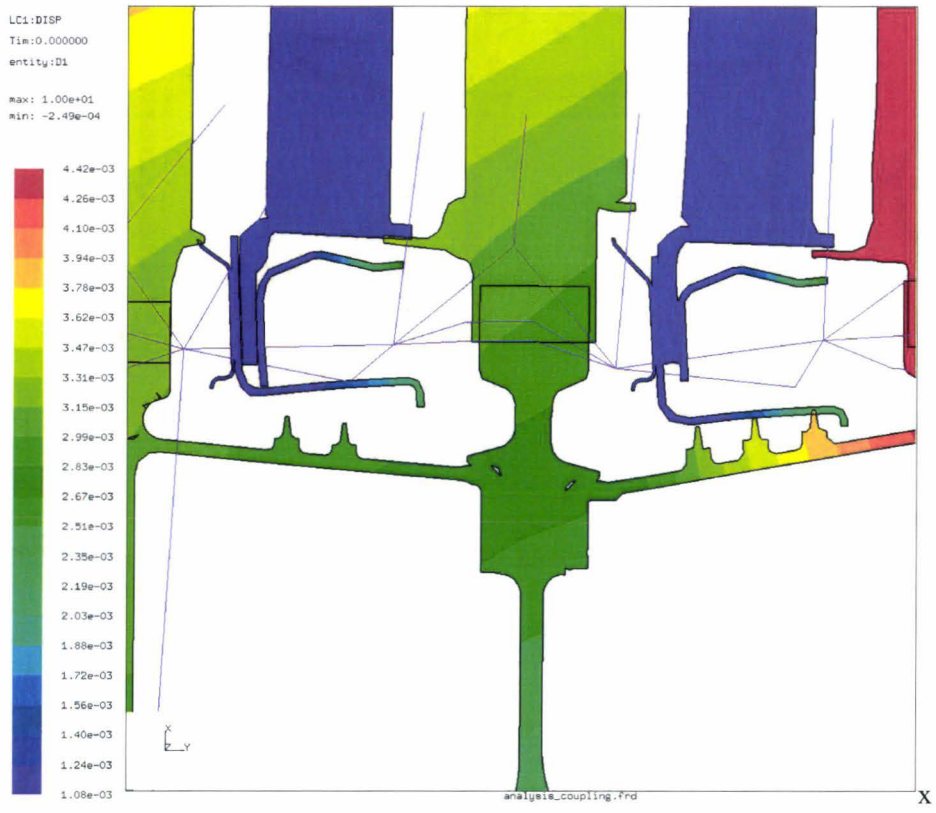

Figure 3.32: Radial displacements on the fully coupled model.

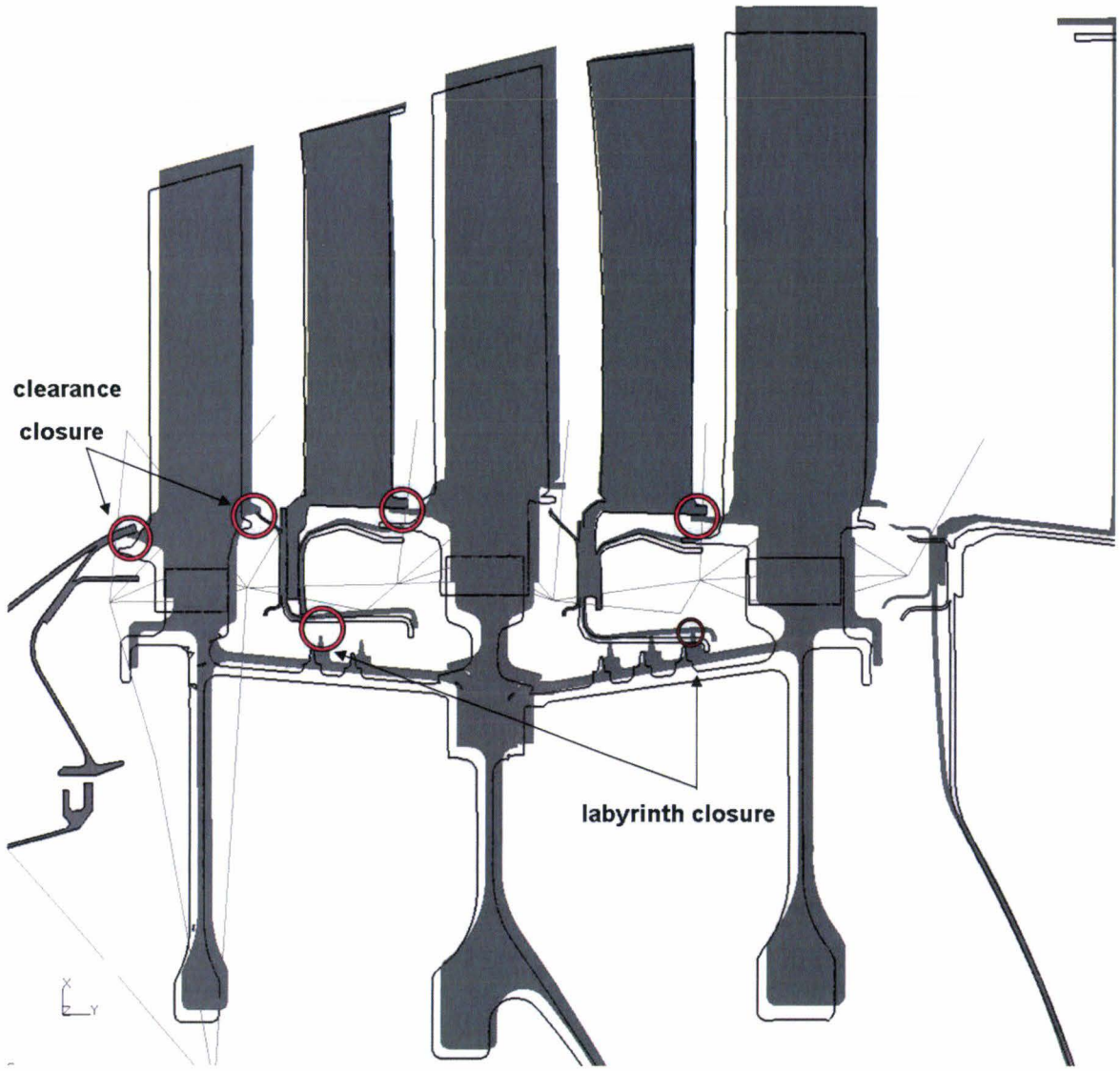

Figure 3.33: Final deformed state of the low pressure turbine showing labyrinth closure.

3.4 Conclusion

The feasibility of the creation of an unique finite element model comprised of the thermomechanical material model and the secondary air system flow network has been presented. Thanks to the new flow network solver module developed in this thesis (see chapter 2.) and the structural and thermal solver developed by Dr. G. Dhondt [12], this unique model can be used to solve the coupled flow-structure problem for secondary air system applications.

Three illustrations of coupled simulations have been presented. They aim at

- demonstrating the coherence of the results obtained for the fluid
- emphasising the effect of thermomechanical phenomena on labyrinth seal gap definition and subsequently labyrinth seal flow and temperature.
- providing insight on the parameters playing a major role in the interaction between fluid and structure in a typical secondary air system seal.
- demonstrating that complex secondary air systems can be modelled and processed thanks to the new integrated suite of CalculiX capabilities.

The first example, a pipe made of rubber-like material with an internal flow, shows that the fluid solution given by CalculiX, using the simplified one-dimensional theory described in chapter 2, enables to accurately represent the fluid behaviour and the interactions between fluid and solid. Validation has been provided by comparing CalculiX results with the simplified theory from Idelchik [22] for fluid properties and linear elasticity theory for mechanical displacements. However, in view of the results it can be postulated that using a material with a higher Young's modulus such as aluminium (78Gpa) or steel (210Gpa) would result in a cancelation of the coupling effect as radial material displacements due to fluid static pressure would be much too small to have an important effect. This has been demonstrated by the study performed on a real labyrinth seal arrangement made of INCONEL 718. The study shows that even if fluid pressure plays a role in material deformation, centrifugal and thermal loads are the driving forces responsible for the largest part of the material displacements and subsequent impact on the fluid properties. As fluid and material temperatures are in interaction through convective heat transfer, the effect of fluid temperature is also to be reckoned with, although its role is secondary.

This example illustrates that if thermal and mechanical loads have a great influence on the geometry and therefore indirectly control the mass flow rate, the effects of air pressure is marginal and the contribution of fluid temperature on solid geometry is one order of magnitude lower than the contribution of centrifugal

loads. This raises the question of the necessity of performing systematically coupled computations for the secondary air system of aero engines. Thermal interaction between fluid and structure cannot be however disregarded. It is furthermore suspected that the effect of the mechanical load from the fluid on the solid may play a more significant role in unsteady states.

The industrial example shows that the new SAS-thermo-mechanical process can be applied successfully to complex multi-physics industrial problems which makes it attractive for engineering applications. It shows furthermore that not only labyrinth seals are subject to thermal deformation and that it would be worth implementing coupled variants for other loss elements to predict as well their impact on the coupled solution.

Conclusions and perspectives

Accurate prediction of gaps and clearances in jet engine sealing applications is crucial for secondary air consumption and design point of view. Secondary air is required to keep the material temperature of the components in the hot flow below the maximum allowable temperature and to ensure that adequate pressure is maintained in the non-flow path regions of the engine for effective sealing (bearing chambers, disk cavities). Requirement of cooling/sealing air must be minimised so that the work done by the machine on each amount of secondary air saved can be used to generate power and increase the engine thermal efficiency. Therefore the selection of cooling and sealing air is of critical importance. As a strong coupling between flow characteristics, material temperatures and displacements is observed in sealing applications, the thesis aimed at improving the current way to predict these mutual interactions.

The goal of the present project has been the creation a new tool enabling to perform coupled fluid-thermal-mechanical analysis for the secondary air system of aero engines accurately using the free finite element software CalculiX.

The work has been divided into three parts:

1. a review of the state of the art
2. a study and creation of a tool dedicated to the analysis of the SAS air flow thermodynamic properties
3. a study of fluid-thermo-structural coupling method

As presented in the literature review, the SAS is a crucial subsystem of an aero engine requiring a series of steady state fluid, heat transfer and structural analysis to determine the optimum cooling air for a given design configuration.

The most straightforward way to represent the secondary air system is to use a 1D nodal network composed of junction nodes and loss elements. Nodes represent locations where the state of the fluid is clearly defined, while loss elements represent the quantity of fluid transported. Flow networks are governed by three equations: conservation of energy and mass in the nodes and the loss element equation in the loss elements. Different methods for solving flow networks have been reviewed.

Conventionally, SAS, heat transfer and structural analysis are performed sequentially. It has been pointed out that this process tends to neglect the mutual interactions between fluid and structure leading to inaccurate prediction and suboptimal design.

Computational resources in the design phase may be used to perform a coupled SAS-heat transfer-structural analysis to achieve a more accurate gap and clearance predictions and avoid costly redesign efforts. It has been highlighted that especially for sealing configurations, which control the amount of air flowing in and out of the secondary air system, performing fully coupled SAS flow-heat transfer-structural analysis would bring an additional degree of accuracy in the prediction of secondary air system design and integration. Possibilities of improving the coupling process in terms of flexibility, efficiency and accuracy have been envisioned under the form of one unique free software, namely CalculiX featuring SAS, heat transfer and structural analysis capabilities, and one unique finite element model gathering the SAS flow model, the thermal model and the structural model.

Taking into account the information gathered through the literature review, the implementation of the secondary air system module into CalculiX has been presented in the second chapter of the present work. At first, a way to make the secondary air system 1D network model compatible with a finite element mesh has been developed. The use of three-node flow elements, representing pressure loss devices enables to blend secondary air network and thermomechanical model into one global entity. The different equations governing the network have been presented in details. To compute the relevant flow network variables, temperatures pressures and mass flow rates, the set of nonlinear equations thus obtained is linearised using the Newton-Raphson method and solved thanks to a free linear algebra solver. The implementation of the Newton-Raphson algorithm in CalculiX has been detailed. The different flow element classes encountered in the SAS have been described and implemented under a modular form which enables easy modification/creation. Four models of varying size and complexity have been proposed, computed with CalculiX and compared with the current SAS tool used at MTU aero engines GmbH showing very good agreement in terms of accuracy and computational resources.

Chapter 3 explained the method chosen to perform the coupling between secondary air flow thermal and structural analysis. The method has been described generally. The special case of labyrinth seals where coupling effects are expected to be strongest has been highlighted. Three illustrations of coupled computations have been provided along with results and comparisons. The different examples emphasised the effect of coupled computations and showed the improvements brought by the use of coupled computation in analysing the secondary air system of aero engines. A parametric study on a labyrinth seal, showed that the main drives for material deformation are centrifugal and thermal loads. In comparison, air pressure role

seems marginal. Air temperature however plays a non-negligible role on the definition of the thermal loads. Nevertheless, neither the contribution of air temperature and mass flow rate to the global thermal loads on the structure nor the influence of structural deformation on the air properties can be completely disregarded. Even a weak coupling between fluid and structure must be addressed in the design phase. As the contribution of the secondary air system may vary from one system to another, there is no telling in advance if the fluid properties will have a strong or weak impact on the global model. In view of the low requirements of secondary air system computation, the systematic use of coupled analysis in the secondary air system of aero engines is an interesting trade-off between analysis requirements and design security. The integrated new tool developed greatly simplifies the current design process, making the coupled computation especially attractive by automating the process and reducing the amount of resource needed.

To qualify the SAS module for productive use it is foreseen to perform a sensitivity study in order to test the software robustness to input variations. In particular, the impact of the initial values on the convergence characteristics is to be accurately assessed. More over the extension of the specific network problem solver to other fields of applications is foreseen. Fluids such as oil or fuel and the corresponding fluid elements are to be investigated and implemented. The special application to blade cooling system, with regards to important rotating effects as well as heat transfer, is also to be investigated in details.

The author is aware that most of the results presented in this study have been obtained from numerical simulations. Concerning the fluid solver, most of the pressure loss correlations taken from the literature are based on test results. It has not been deemed relevant to include them in this thesis. Unfortunately, to the knowledge of the author no literature reference exists for series of different flow elements, or even better fluid networks, to which the solution obtained with CalculiX could be compared. The CalculiX mechanical and thermal analysis module has been in service in the different departments of MTU Aero Engines for more than 5 years. Nevertheless, comparison from alternate sources have been shown whenever possible under the form of empirical methods or using other software.

More work is on the way to fully test the extent and limits of the new tool and compare the results to test data.

Annex A

An overview of CalculiX.

CalculiX [13] is a package designed to solve field problems. It is developed under the terms of the 2nd GNU Public License (see[51]). The method used is the Finite Element Method. [12]

CalculiX enables to build Finite Element Models, solve the finite element problem and post-process the results. The pre- and post-processor, CalculiX Graphics, is an interactive 3D-tool using the openGL API developed by Klaus Wittig. The solver, CalculiX Crunchix, is able to perform linear and non-linear calculations. Static dynamic and thermal solutions are available on a wide range of applications. The solver has been developed by Dr. G. Dhondt. Both solver and graphical user interface can be used independently.

Because the solver makes use of the Abaqus input format it is possible to use commercial pre-processors as well. In turn CalculiX Graphics, the pre-processor, is able to write mesh related data for most analysis tools used today such as Nastran, Abaqus, Ansys, code-aster and for the free-CFD codes duns, ISAAC and OpenFOAM. A vda CAD interface is available.

From a portability point of view, the program is designed to run on Unix platforms like Linux and Irix computers. Convergent Mechanical Solutions has ported the application to the MS- Windows operating system.

In the industrial domain CalculiX is used by Germany's leading engine Manufacturer MTU Aero engines GmbH, but also by the European aerospace consortium EADS. In the academic domain, CalculiX is used in many universities such as Karlsruhe, Paderborn, Cape Town. A discussion forum and news group exist to promote experience sharing and enable a direct communication inside the CalculiX community.

In agreement with the terms of the 2nd GNU Public License, CalculiX source code may be freely downloaded, used, and modified. The secondary air system module has been developed for MTU Aero Engines GmbH purposes integrating proprietary data and methods. For the purpose of the thesis and accordingly with CalculiX policy, a public version has been developed in parallel implementing data and methods taken from the literature. CalculiX CrunchiX is programmed in C for the upper levels of the algorithm and in

FORTRAN for the sub levels. Subsequently the implementation of the secondary air system module is programmed accordingly.

Man Machine interface.

In order to create and modify more comfortably the secondary air system network model, the current secondary air system program possess a graphical user interface. This Graphical User Interface, or GUI, is based on the ILOG Grapher input/output format and has been improved to fit the specific needs and format of the currently used S.A.S program [26]. From model creation to result post-treatment, everything is, from the user point of view, performed through the GUI. In order to keep modifications and adaptations as minimal as possible for future users, as well as simplifying the creation of complex network models and perform more quickly modifications, the GUI has been adapted to CalculiX requirements.

To this end, the creation of several transcription programs is needed: from the GUI to CalculiX and back to the GUI. An overview of the process is presented Fig.3.34.

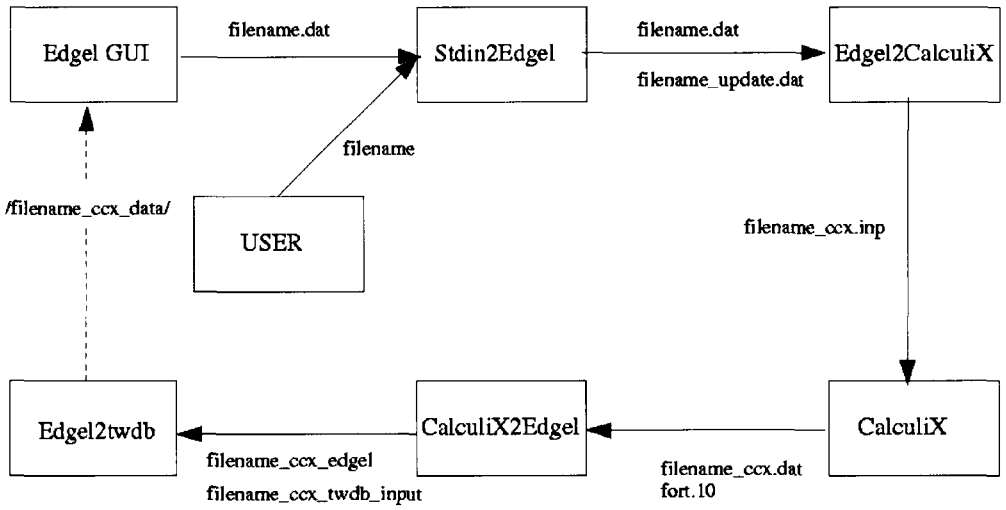

Figure 3.34: Outline of the interfacing process as developed for CalculiX

This process as well as the different programs created are presented in this part. It is important to note that the graphical user interface is not directly involved in the aero-thermo-mechanical iterative process, and that it is not contributing to the transfer of information from one CalculiX module to the other. However, it greatly simplifies the use of the SAS module.

Keeping the same interface between the actual SAS software and CalculiX also enables a swift passage from one solver to the other requiring neither adaptation effort nor training period on the new software.

Stdin2Edgel

The GUI generates a formatted text file, 'filename.dat', containing all relevant topological network information.

- information on the type of calculation and steering values (tolerances...)
- the detailed network topological description (chambers and lines)
- boundary conditions definitions
- element definitions.

Stdin2edgel.exe checks if model updates, defined as separate file to avoid modifying directly the main model, exist. Accordingly, the indicated changes in the network topology are performed.

Edgel2CalculiX

Once the definition file, 'filename.dat', has been processed through Stdin2Edgel.exe, the next task is to translate this file into an input deck file, 'filename_ccx.inp', for CalculiX. This is taken care of by the program Edgel2CalculiX.exe. As explained in section 2.1, CalculiX topology differs from the current network topology. More over, CalculiX possesses its own syntax to define nodes, elements, elements properties, initial and boundary conditions as well as steering parameters for the computational procedure and output creation.

CalculiX

CalculiX solves the problem as presented in chapter 2 using the input deck file 'filename_ccx.inp'. The following data are generated:

- 'filename_ccx.dat' contains the nodal values in the network (total temperatures and pressures as well as mass flow rates).
- 'fort.10' gives a detailed version of the results (nodal values, C_d values, Reynolds number, Mach number, friction coefficient...)

CalculiX2Edgel

As the GUI only accept a special kind of formatted result files, CalculiX2Edgel.exe creates 2 steering files:

- 'filename_ccx_edgel' containing the nodal results under the right format

- 'filename_ccx_twdb_input', steering file for the creation of the result data base.

A company owned program uses both files to convert CalculiX results in a format acceptable for the GUI and after specifying the right path, results in terms of nodal total pressures and nodal total temperatures in the chambers and mass flow rates in the flow lines can be directly post-processed on the GUI. Intermediate inlet and outlet pressures and temperatures as well as additional information not represented on the GUI must be looked up in 'fort.10' file.

In order to make the whole process completely invisible from the user point of view and as smooth as possible, a Linux shell script has been created. This script contains the unified sequential set of commands and checks controlling the process. The script is launched through the graphical user interface and all the instructions are executed automatically.

Annex B

Fluid mechanics

The concept of continuum

At a macroscopic level, matter seems continuous, whereas it is composed of a myriad of molecules in constant motion and collision. By introducing the concept of **fluid particle** it is possible to conciliate the vision of a continuous medium with the one of an ensemble of distinct molecules separated by void. The fluid particle is defined as a volume v_ϵ big enough to contain an important number of particles yet small enough at observation scale to be considered as a single point. The existence of such a fluid particle is not a priori obvious: it is necessary that the macroscopic and microscopic characteristic scales be distinct. If L is the characteristic length scale of the mean motion and l the free mean path between two molecules:

$$l^3 << v_\epsilon << L^3$$

The ratio $Kn = \frac{l}{L}$ called **Knudsen number** is used to define if the continuum hypothesis holds. This is the case if $Kn < 10^{-2}$. The hypothesis does not yield if:

- the mean free path increases as is the case with highly rarefied gases (rocket flight, vacuum technology, electronic tubes)
- the characteristic length scales of the mean motion decreases (through a shock wave for instance).

System and control volume

The three basic principles listed in the following paragraph are always stated in the first instance in terms of a "system". A system is defined as an arbitrary collection of matter. Everything not belonging to the system is called the surroundings. Surroundings and system are separated by the system boundary defined as an imaginary surface. The attention is therefore focused on the system of interest in interaction with its surroundings. Due to the intrinsic nature of the fluid, it is not convenient to work with systems as the

mobility of the fluid makes it difficult to identify the boundaries of a fluid system for any appreciable length of time.

With fluids in motion it is therefore more convenient to consider an arbitrary volume, fixed is space and through which the fluid flows. The identity of the fluid in the control volume changes from instant to instant. This volume is called **control volume**. The surface bounding the control volume is always a closed surface, called **control surface** with either one or several connectivities. The size of the control volume may vary from application to application but is finite.

Fundamental equations of fluid dynamic

All analysis concerning the motion of fluid begin with the statements of the three basic physical laws governing the fluid motion. For a given control volume as presented in the previous paragraph the laws are written as:

- the law of conservation of mass is written

$$\frac{d\rho}{dt} + \rho v^k_{,k} = 0$$

- Newton's second law of motion is written

$$\rho \frac{dv^k}{dt} = \rho f^k + \sigma^{kl}, l$$

- the law of total energy conservation

$$\rho \frac{de_t}{dt} = \rho v^k f^k + (u^k \, \sigma^{kl})_{,l} - q^k_{,k}$$

The three basic principles, are complemented by laws relative to the fluid thermodynamical, mechanical, and thermal behaviour.

Thermodynamical behaviour

A perfect gas is a fluid displaying the following conditions:

- the fluid state equation is defined by two
  - it follows Mariotte equation, which states that at a given constant temperature $\frac{p}{\rho} = cte$

- it follows the law of Gay Lussac $\frac{p}{\rho} = \frac{R_u}{M_{\text{gas}}} T$, where R_u is the universal gas constant and M_{gas} the molecular mass of the considered gas. $R_u = 831.2 \frac{\text{J}}{\text{kmol K}}$. The gas constant of a given gas is defined by $R = \frac{R_u}{M_{\text{gas}}}$. For air, $M_{\text{air}} = 29 \frac{\text{kg}}{\text{kmol}}$ an subsequently $R_{\text{air}} = 287 \frac{\text{J}}{\text{kg K}}$

- the fluid follows Joule laws

$$de = C_v dT \quad \text{and} \quad dh = C_p dT$$

Mechanical behaviour: the Newtonian fluid and the Newton-Stokes model

The modelling of the fluid mechanical behaviour is based on the description of the strain tensor. The description of the strain tensor is empirical taken experimental observations into account. For the usual fluids, the **Newtonian fluid model** is defined according to the following assumptions:

- in the absence of motion the strain tensor reduces to $\sigma^{kl} = -p\delta^{kl}$

- if motion occurs strains are proportional to deformation rate, and in turn the strain tensor is a linear function of the the tensor of deformation rates

- the relationship between strain tensor and tensor of deformation rate is isotropic.

According to the previous assumptions, the strain tensor is written

$$\sigma^{kl} = -p\delta^{kl} + 2\mu S^{kl} + \mu' v^k_{,k} \delta^{kl}$$

where $S^{kl} = \frac{1}{2}(v^k_{,l} + v^l_{,k})$ is the tensor of deformation rates. μ and μ' are the two viscosity coefficients depending only on the fluid thermodynamic state. μ is called dynamic viscosity. The viscosity tension tensor is defined has

$$\tau^{kl} = \mu \left(u^k_{,l} + u^l_{,k} \right) + \mu' v^k_{,k} \delta^{kl}$$

and therefore

$$\sigma^{kl} = -p\delta^{kl} + \tau^{kl}$$

Separating σ^{kl} between the deviatoric part, which trace is null, and spherical part, which is a constant diagonal matrix yields

$$\sigma^{kl} = \tau^{kl} - \frac{\sigma^{kl}}{3} \delta^{kl} - \left(p - \frac{2\mu + 3\mu'}{3} u^k_{,k} \right) \delta^{kl}$$

The spherical part $p' = \left(p - \frac{2\mu+3\mu'}{3} u^k_{,k}\right) \delta^{kl}$ is interpreted as a mechanical pressure. Stokes assumes that this mechanical pressure is identical to thermodynamic pressure and therefore $3\lambda + 2\mu = 0$. This yields

$$\sigma^{kl} = -p\delta^{kl} + \mu(v^k_{,l} + v^l_{,k}) - \frac{2}{3}\mu v^k_{,k}\delta^{kl}$$

This model is subsequently called the **Newton-Stokes model**.

Thermal behaviour: Fourier law of heat conduction

The fluid thermal behaviour is determined through the modelling of the vector of flux density. Only conductive transfer are considered, and, observing that for the usual fluid heat transfer occurs from the hottest point towards the coldest point and therefore in opposition with the thermal gradient, Fourier law of heat conduction is considered:

$$\vec{q} = -\lambda \frac{\partial T}{\partial x^k} \vec{e_k}$$

where λ is the thermal conductivity of the fluid

The Navier-Stokes equations

The three constitutive principles:

- mass conservation;
- momentum conservation;
- total energy conservation;

complemented by

- Newton-Stokes law for the mechanical behaviour;
- Fourier law for the thermal behaviour;
- the state equation of the perfect gas and Joule laws for the thermodynamic behaviour;

enables to establish the Navier-Stokes model. The Navier-Stokes model is written as

$$\begin{aligned}
\frac{d\rho}{dt} &= \rho\frac{\partial u}{\partial x_i} \\
\rho\frac{du_i}{dt} &= \rho f_i - \frac{\partial p}{\partial x_i} + 2\frac{\partial \mu S_{ij}}{\partial x_j} - \frac{2}{3}\frac{\partial \mu \frac{\partial u}{\partial x_i}}{\partial x_i} \\
\rho\frac{d\left(C_v T\right)}{dt} &= -p\frac{\partial u}{\partial x_i} + \frac{\partial}{\partial x_i}\left(\lambda\frac{\partial T}{\partial x_i}\right) + 2\mu S_{ij}S_{ij} - \frac{2}{3}\mu\left(\frac{\partial^2 u}{\partial^2 x_i}\right) \\
\frac{p}{\rho} &= RT
\end{aligned}$$

This system of partial differential equations is:

- nonlinear (advective terms)
- of the first order in time
- of the second order in space (diffusion terms)
- closed (6 equations for 6 unknowns)

It is theoretically possible to solve this system over a given domain, provided initial estimates and boundary conditions are given.

Euler equation

The Euler model is a simplification of the Navier-Stokes model and is used for a compressible perfect fluid. By definition, a perfect fluid is non-viscous. It is further supposed that the fluid is non-heat conductible.

$$\mu = 0 \text{ and } \lambda = 0$$

Therefore for a perfect fluid the strain tensor is reduced to the pressure terms

$$\sigma_{ij} = -p\delta_{ij}$$

Under the previous assumptions, the Navier-Stokes model is written

$$\begin{aligned} \frac{d\rho}{dt} &= \rho \frac{\partial u}{\partial x_i} \\ \frac{du_i}{dt} &= f_i - \frac{1}{\rho}\frac{\partial p}{\partial x_i} \\ C_v \frac{dT}{dt} &= -\frac{p}{\rho}\frac{\partial u}{\partial x_i} \\ \frac{p}{\rho} &= R\,T \end{aligned}$$

This system of equations constitutes the Euler model.

Annex C

The basic principles of thermal analysis

Generalities

The thermal computations of structures usually serves to ensure that the temperatures of the different material parts used remain inside the admissible temperature range and enable to obtain an accurate material temperature repartition subsequently used as boundary condition for the thermal expansion computation and life expectancy prediction. The principal physical phenomena considered are:

- thermal conduction in the material
- convective boundary conditions, which describe the heat transfer with the adjacent moving fluid
- the advection or fluid channel system, which describes the increase respectively decrease of the temperature of the adjacent fluid
- transfer of heat flux boundary conditions, which describes direct incoming heat flux in the material or in the fluid
- Radiative exchange, which couples the material surfaces that are 'seeing' one another.

As only few analytical solutions for simple systems exist, the thermal analysis is usually performed using numerical methods based on the Finite Element Method.

Thermal conduction

Thermal conduction describes the transport of heat inside the material. Conduction related phenomena are modelled by:

$$\rho\, C_p \frac{\partial T}{\partial t} = \lambda_c \frac{\partial^2 T}{\partial x_i^2}$$

The left hand side of the equation represents heat inertia during transient processes, the right hand side describes the heat conduction. The heat flux transferred through conduction is modelled by Fourier's law of

conduction

$$\dot{Q} = -\lambda_c A \frac{\partial T}{\partial x}$$

which is proportional to the thermal conductivity of the material considered, the conduction surface and the temperature gradient.

Convective boundary conditions

Convective heat transfer is not a mechanism in itself. It is an integrated formulation of the conductive heat transfer between a moving fluid and a solid medium, applied whenever the thermal boundary layer is not resolved as is the case for the thermal analysis performed in the design phase. The heat flux directed from the material surface towards the adjacent moving fluid is modelled by:

$$\begin{aligned} \dot{Q} &= h_c A \left(T_{wall} - T_{fluid}\right) \\ &= \overline{h_c} \left(T_{wall} - T_{fluid}\right) \end{aligned}$$

and is proportional to the heat transfer surface, the difference of temperature between solid and fluid. The proportionality factor $\overline{h_c}$, heat transfer coefficient, depends on the fluid velocity, the geometry, the fluid and solid properties as well as the state of the fluid. Heat transfer coefficients are usually defined using correlations based for the most part on empirical methods.

In most cases, all material surfaces accommodate convective boundary conditions. The total temperature in the relative motion is used to define the fluid temperature.

Material temperatures are changed through the heat exchange by convection between structure and fluid and in turn fluid temperatures are impacted by the thermal solution. The part of the heat imparted to the fluid is represented by

$$\dot{Q} = \dot{m}\ C_p\ \left(T_{out} - T_{in}\right)$$

The heat flow is proportional to the mass flow rate the heat capacity at constant pressure of the fluid and the difference of temperature between the outlet and the inlet of the fluid channel. Convection is a global but simplified approach to take into account thermal conduction between a solid and a fluid in movement.

Temperature boundary conditions

With this type of boundary condition the temperature for a specific part is specified. This is the case when temperatures at the frontier of the system are accurately known, for instance the fluid temperatures in the main stream. In this case the heat flow coming out of this part depends on the thermal solution.

Heat flux boundary conditions

Heat flux boundary conditions appear as

- surface based heat fluxes, as for instance radiative heating, inductive heating with minimal penetration depth.
- volume based heat fluxes , as reaction heat
- global heat flux for the heating of the fluid by friction.

In both cases a heat flux value is given. For frictional heating different loss models exist, describing the heat flux similarly to the convective heat transfer coefficient correlations in the simplified approaches.

Radiative exchange

Each material surface absorbs and emits heat in form of electromagnetic radiations. All the material parts that can see one another are involved in radiative heat exchange. The simplified model for the radiative heat flux between two surfaces is given by:

$$\dot{Q} = \sigma_b \, \epsilon_{12} \, A_1 \, \left(T_1^4 - T_2^4\right)$$

It is proportional to the Boltzmann constant, the exchange factor based on the emissivity coefficients of the two surfaces, the view factor, and the difference of both surface temperature to the power of four. The view factor between to surfaces involved in radiative heat exchange depends on the solid angle that defines the relative interaction between the two surfaces.

Annex D

Interactions couplées fluide-structure thermo-mécanique dans le système d'air secondaire de moteurs d'avions: contribution à une méthode d'analyse intégrée.

Le système d'air secondaire ou SAS est un sous système extrêmement important du turbo réacteur. Les tâches qui lui sont affectées ont principalement trait au refroidissement des parties chaudes du moteur comme par exemple les aubes de la turbine haute pression ainsi que l'étanchéité entre flux primaires et secondaires pour éviter l'ingestion de gaz chauds. La prédiction fiable et exacte des jeux et écartements pour les application d'étanchéité d'un turbo réacteur est cruciale pour la détermination des besoins en air du système d'air secondaire ainsi que d'un point de vue de la conception.

Les besoins en air de refroidissement et d'étanchéité doivent être minimisés dans le but de ne pas dégrader les performances globales du moteur en terme de poussée et de consommation spécifique de carburant. Ainsi le choix des écoulement de refroidissement et d'étanchéité revêt une importance capitale. Les applications industrielles, civiles ou militaires, demandent, de manière soutenue, moyens et méthodes d'analyse améliorées pour prédire plus finement le comportement du système d'air secondaire dans de nombreuses conditions de fonctionnement. Les flux d'air contrôlent les températures des matériaux. Par dilatations thermiques et efforts mécaniques les structures sont amenées à se déformer entrainant la modifications des définitions géométriques des joints. Ceci modifie pressions et débits qui à leur tour influencent le problème thermique. Un couplage important entre les propriétés du flux, les températures matériau et les déformations induites est observé pour les applications d'étanchéité du SAS. Cette étude est menée dans le but d'améliorer la prédiction de ces interactions mutuelles entre fluide et structure dans le système d'air secondaire.

Le but premier de la thèse a été la création et l'implémentation d'un nouveau module dédié au calcul/analyse du système d'air secondaire dans le logiciel de calcul élement fini CalculiX (License Gpl2). CalculiX possédant par ailleurs des modules dédiés au calcul thermique et mécanique, la seconde tâche a consisté à combiner les différentes compétences du logiciel (système d'air thermique et mécanique) dans une suite

intégrée, permettant d'accroitre la précision, la liberté de conception, et permettant ainsi une meilleure prévision des interactions mutuelles entre les différentes disciplines.

Le mémoire se subdivise en trois parties : Une recherche bibliographique présentant l'état de l'art. Une étude visant à l'obtenir d'un outil fonctionnel pour la prédiction des propriétés du fluide dans le système d'air secondaire. Une étude présentant la méthode développée pour prendre en compte le couplage aero-thermo-structural ainsi que trois exemples, de complexité croissante, illustrant le problème couplé et démontrant la fonctionnalité ainsi que les apports du nouvel outil créé.

Comme présenté dans l'étude bibliographique, le débit d'air nécessaire au refroidissement/étanchéité est contrôlé par le rapport des pressions, ainsi que les écartements de joint entre les régions du système d' air primaire et secondaire. L'air de refroidissement, à son tour, contrôle les températures de la structure. Les gradients de température du matériau ainsi que la pression du fluide influent sur les contraintes à l'intérieur de la matière et résultent en déplacements qui modifient la définition des écartements et affectent les débits d'air de refroidissement. Pour déterminer de façon réaliste et optimale les débits d'air de refroidissement pour une configuration donnée, une série itérative d'analyse du système d'air secondaire d'un point de vue fluide, transfert thermiques et structure est réalisée.

La méthode la plus pratique et la plus directe de représenter le système d'air secondaire est d'utiliser une représentation de type réseau unidimensionnel. Cette modélisation combine flexibilité, compacité, économie de ressources informatiques. Elle est de ce fait très attractive pour la conception et l'analyse. Les différentes méthodes mathématiques utilisées pour l'analyse de tels réseaux unidimensionnels ont été présentées avec leurs avantages et leurs inconvénients.

Conventionnellement SAS, transfert thermique et analyse mécanique sont menées de manière séquentielle. La rigidité du procédé de couplage entre ces trois disciplines induit de manière générale une unique itération de finalisation de concept. Dans une phase ultérieure, les résultats de tests sont utilisés pour calibrer le modèle. Dans la plupart des cas, cette approche donne naissance à des concepts acceptables. Cependant il arrive que d'importants écarts soient observés entre prédictions et mesures nécessitant un effort important d'amendement de conception dans la dernière phase d'un programme de développement induisant une augmentation des couts et délais. Ces déviations sont en général attribuées à une mauvaise/imprécise prédiction des écartements impactant l'ensemble du processus itératif. Dès la phase de conception, les ressources informatiques peuvent être mises à profit pour réaliser une étude couplées SAS-transfert thermique-mécanique dans le but de prédire plus finement les écartements. Il a été montré , spécialement pour le cas de configurations d'étanchéité qui contrôlent la quantité d'air entrant et sortant du système d'air secondaire, qu'une étude couplée SAS-transfert thermique-mécanique menée jusqu'à son terme, apporte un degrés supplémentaire de

précision dans la prédiction des paramètres du système d'air secondaire tant au niveau de la conception que de l'intégration. Dans le but d'améliorer le processus de couplage inter-disciplines en termes de flexibilité, efficacité et précision, il est envisagé dans ce projet de regrouper les trois disciplines concernées sous forme modulaire au sein d'un logiciel unique, le logiciel d'analyse élément fini CalculiX, et d'utiliser un modèle unique regroupant les modèles du système d'air secondaire, thermiques et mécaniques.

Le chapitre 2, reprenant les informations collectées durant l'étude bibliographique, explicite la création du module dédié à l'analyse du système d'air secondaire pour CalculiX. Dans un premier temps, une méthode visant à rendre compatible le réseau unidimensionnel du système d'air secondaire avec le maillage element fini thermomécanique a été développée. L'utilisation d'un élement topologique comprenant trois noeuds, représentant une perte de charge discrète permet de fondre le réseau unidimensionnel et le maillage thermomécanique jusqu'alors distincts en un unique maillage. Une fois la topologie relative au problème couplé fixée, les différentes équations régissant le réseau d'air sont présentées et modifiées de manière à convenir à la nouvelle formulation du réseau unidimensionnel ainsi qu'au variables préférentielles du système d'air secondaire : pressions, températures et débits massiques. Pour calculer les variables relatives au problème du système d'air secondaire, le système d'équations non linéaires obtenu est linéarisé par la méthode de Newton-Raphson et résolu à l'aide d'une routine dédiée. L'implémentation de l'algorithme de Newton-Raphson est détaillé. Dans l'optique d'obtenir un outil fonctionnel, les différents types de pertes de charges rencontrés dans le système d'air secondaire sont décrits et implémentés dans CalculiX sous forme modulaire de manière à faciliter la création de nouvelles classes d'éléments et/ou leur modification. Pour rendre encore plus aisée l'utilisation du module dédié au système d'air secondaire, l'interface graphique existante pour l'outil d'analyse du système d'air secondaire actuel, est couplée a CalculiX. Elle permet entre autre, la création/modification rapide du modèle unidimensionnel (topologie+conditions limites) ainsi que la visualisation des résultats. Grâce à cette interface, quatre modèles de tailles et complexités différentes sont proposés, résolus à l'aide du nouveau module implémenté dans CalculiX. La diversité des modèles, des éléments de pertes de charge utilisés et des configurations, représentatifs d'un moteur existant, permettent de tester de manière approfondie les capacités du nouveau module et de la nouvelle méthode. Les résultats, comparés à ceux obtenus avec l'outil existant, montrent une excellente concordance tant au niveau de la précision des résultats qu'au niveau de la rapidité des calculs. D'un point de vue utilisateur, l'adaptation au nouvel outil ne requiert pas d'efforts particulier, l'interface graphique ayant été conservée dans sa forme actuelle.

Le troisième chapitre détaille la méthode retenue pour réaliser le couplage entre système d'air secondaire et partie thermomécanique. La méthode est décrite dans un premier temps sous forme générale puis appliquée

à deux exemples. Comparée à la méthode existante, l'apport du nouvel outil/processus est non négligeable : complètement automatisé, il ne requiert plus d'interventions externe de la part de l'utilisateur ni de traitement externe de l'information. Le traitement du transfert de condition limites d'un problème a un autre et géré de manière interne. En outre, un seul fichier de description du modèle est requis pour un seul logiciel au lieu de trois précédemment. Différentes illustrations du couplage sont proposées. Elles insistent sur l'effet du couplage entre fluide, thermique et structure et montrent les améliorations que le nouvel outil apporte tant au niveau de la conception que de l'analyse du système d'air secondaire. Les résultats obtenus avec CalculiX ont été coroborrés par des méthodes alternatives numériques et empiriques.

Dans l'un des exemples présentés, l'effet de couplage relativement faible tend à montrer que certaines configurations peuvent être faiblement influencées par le couplage et que l'utilisation du nouvel outil ne devrait pas être systématique. Cependant, aussi faible soit-il, l'effet de couplage doit être pris en compte. Il n'existe pas à l'heure actuelle de méthode absolument fiable pour determiner apriori si les proprietés du fluide auront une influence importante sur le problème thermomécanique et donc la force du couplage. Aux vue des ressources informatiques nècessaires à l'étude couplée et de l'automatisation du processus de couplage, il est plus sûr de systématiser l'étude couplée lors de la phase de conception et d'analyse, ce qui est en partie réalisé avec le processus existant.

Dans le but de qualifier le nouveau module dédié au système d'air secondaire, une étude de stabilité/sensitivité est envisagée de manière à étudier la susceptibilité de l'algorithme. En particulier, l'impact de la variation des conditions initiales sur la convergence et la précision des résultats sera estimé. En outre, l'extension du nouveau module à de nouveaux types de fluides tels que l'huile ou le carburant pour leurs systemes de repartition respectifs, ainsi qu'à de nouvelles applications telles que le refroidissement des aubages est envisagée. Pour le couplage fluide-thermique-structure, les résultats numériques doivent être comparés à des resultats de tests.

Bibliography

[1] *Aerospace Structural Metals Handbook.* Aerospace Structural Metals Handbook, 1995.

[2] A. ALEXIOU AND AL.: *Discharge coefficients for flow through holes normal to a rotating shaft.* International Journal of Heat and Fluid Flow, vol.21 pp. 701-707, 2000.

[3] R. P. BENEDICT: *Fundamentals of pipe flow.* Wiley-Interscience publication, John Wiley and Sons Inc., 1980.

[4] N.T. BIRCH: *2020 vision: The prospect for large civil aircraft propulsion.* Aeronautical Journal, pp. 347-352, 2000.

[5] C. BREZINSKI AND M. REDIVA-ZAGLIA: *Methodes numeriques iteratives.* Editions Elliplses, 2005.

[6] T. CHMIELNIAK AND AL.: *Coupled analysis of cooled gas turbine blades.* ASME TURBO EXPO 2003, Power for Land, Sea and Air, Atlanta, Georgia, USA, ASME GT2003-38657, 2003.

[7] X. CHUNHUA, S.AND QINGLUAN: *Aerothermal analysis of turbine blades using an unstructured flow solver - U2NCLE.* 38th AIAA Thermophysics Conference, Toronto, Canada, AIAA 2005-4683, 2005.

[8] A. COUTROT: *Technological developments in european programs aimed at reducing air transport noise and emissions.* 40th AIAA/ASME/SAE/ASEE Joint Propulsion Conference and Exhibit, Fort Lauderdale, Florida, USA, AIAA 2004-4227, 2004.

[9] H. CROSS: *Analysis of flow in networks of conduits or conductors.* Bulletin of the engineering experiment station University of Illinois, 1937.

[10] ROLLS ROYCE DERBY UNITED KINGDOM: *The Jet Engine: 6th Edition.* Renault Printing Co. Ltd, Birmingham England, ISBN 0-902121-2-35, 2005.

[11] U. DESIDERI AND F. DIMARIA: *Power pipe: an algorithm for analysis for single-phase, steady state, pipe networks with second-degree boundary conditions.* Proceedings of the Institution of Mechanical Engineers, vol.4, pp. 519-525, 2001.

[12] G. DHONDT: *The Finite Element Method for Three-Dimensional Thermomechanical Applications.* John Wiley & Sons, ISBN 0-470-85752-8, 2004.

[13] G. DHONT: *Online User Manual and source code www.calculix.de.* www.calculix.de, 2007.

[14] M DITTMANN AND AL.: *Discharge Coefficients of a Pre-Swirl System in Secondary Air Systems.* ASME TURBO EXPO 2001, New Orleans, Louisiana, USA, ASME GT2001-0122, 2001.

[15] G. EBENHOCH AND T.M. SPEER: *Simulation of Cooling Systems in Gas Turbines.* International Gas Turbine and Aeroengine Congress, The Hague, Netherlands, ASME 94-GT-049, 1994.

[16] A. EGLI: *The leakage of steam through labyrinth seals.* Transaction of ASME, ASME 57, 1935.

[17] M. P. ERRERA AND S. CHEMIN: *A fluid-solid thermal coupling applied to an effusion cooling system.* 34th AIAA Fluid Dynamics Conference and Exhibit, Portland, Oregon, USA, AIAA 2004-2140, 2004).

[18] J.C. HASAN: *Flow in a Cover-Plate PreSwirl Rotor-Stator System.* ASME 97-GT-243, 1997.

[19] N. HAY AND D. LAMPARD: *Discharge Coefficient of Turbine Cooling Holes: a Review.* International Gas Turbine and Aeroengine Congress and Exhibition, Birmingham, United Kingdom, ASME 96-GT-492, 1996.

[20] A. HESELHAUS: *A Hybrid Coupling Scheme and Stability Analysis for Coupled Solid/Fluid Turbine Blade Temperature Calculations.* ASME 98-GT-88, 1998.

[21] B. HODKINSON: *Estimation of the Leakage Through a Labyrinth Gland.* Proceedings of the Institutional Mechanical Engineering, Vol. 141, pp. 283-288., 1940.

[22] I.E. IDELCHIK: *Handbook of Hydraulic Resistance. 2nd edition.* Hemisphere Publishing Corporation, ISBN 0-899116-284-4, 1986.

[23] A. IDRIS AND AL.: *The influence of incidence angle on the discharge coefficient for rotating radial orifices.* ASME Turbo Expo 2004 Power of land, sea and air, Wien, Austria, ASME GT2004-53237, 2004.

[24] R.W. JEPPSON: *Analysis of flow in pipe networks.* Ann Arbor Science, Ann Arbor, Michigan, USA, ISBN 0-250-40119-3, 1977.

[25] J.H KEENAN AND E.P. NEUMANN: *Measurements of friction in a pipe for subsonic and supersonic flow of air.* Journal of Applied Mechanics, vol.13, No.2l, 1946.

[26] K.J. KUTZ AND T.M. SPEER: *Simulation of the secondary air system of aero engines.* Journal of turbomachinery, 1994, vol. 116, no2, pp. 306-315, 1994.

[27] A. LICHTAROWICZ AND AL.: *Discharge Coefficients For Incompressible Non-cavitating Flow Through Long Orifices.* Journal of Mechanical Engineering Science. 1965, 1965.

[28] J.F. LOUIS AND AL.: *A comparative study of the influence of different means of turbine cooling on gas turbine performance.* International Journal of Turbo and Jet Engines, ASME 83-GT-180, 1983.

[29] A.K. MAJUMDAR, AND AL: *A generalized fluid system simulation program to model flow distribution in fluid networks.* 34th AIAA/ASME/SAE/ASEE Joint Propulsion Conference and Exhibit, Cleveland, Ohio, USA AIAA 98-3682, 1998.

[30] A.K. MAJUMDAR AND K.P. VAN HOOSER: *A General Fluid System Simulation Program to Model Secondary Flows in Turbomachinery.* 31st AIAA/ASME/SAE/ASEE Joint Propulsion Conference and Exhibit, San Diego, California, USA AIAA 95-2969, 1995.

[31] W.F. MCGREEHAN AND M.J. SCHOTSCH: *Flow Characteristics of Long Orifices with Rotation and Corner Radiusing.* ASME Gas Turbine Conference and Exhibition, Anaheim, California, USA, ASME 87-GT-162, 1987.

[32] J.A. MIEDEMA AND B.Q.M. WESTGEEST: *Computation of Mass Flow rates and Pressure Losses in Branched Pipeline Networks.* Netherlands Organisation for Applied Scientific Research, Delft, Netherlands, Netherlands Royal Navy, No.5173202-81-1, 1981.

[33] D.S. MILLER: *Internal Flow Systems.* vol.5 B.H.R.A Fluid Engineering, ISBN 0-900983-78-7, 1978.

[34] B. MILLS AND B.N. COLES: *Compressible Gas flow in Commercial Pipes.* Proc. Inst. Mech. Engrs., 1957.

[35] A. MOORE: *Turbine cooling - A review of the various interface problems.* 2^{nd} International Symposium on Air Breathing Engines, 1974.

[36] A. MOORE: *Gas turbine engine internal air systems: A review of the requirements and the problems.* ASME 75-WA/GT-1, 1975.

[37] J.M. OWEN AND AL.: *Flow and heat transfer in a rotating cylindrical cavity with radial inflow of fluid. Part 1: The flow structure.* International Journal for Heat and fluid flow vol.6 No. 4, 0142-727X/85/040228-07, Butterworth Co.(Publishers) Ltd., 1985.

[38] J.M. OWEN AND AL.: *Flow and heat transfer in a rotating cylindrical cavity with radial inflow of fluid. Part 2: Velocity, pressure and heat transfer measurements.* International Journal for Heat and fluid flow vol.7 No.1, 0142-727X/86/010021-07, Butterworth Co.(Publishers) Ltd., 1986.

[39] J.M. OWEN AND R.H. ROGERS: *Flow and heat transfert in rotating-disc systems Volume 1: rottor-stator systems.* Research Studies Press Ltd., ISBN 0-86380-090-4, 1995.

[40] J.M. OWEN AND R.H. ROGERS: *Flow and heat transfert in rotating-Disc systems Volume 2: rotating cavities.* Research Studies Press Ltd., ISBN 0-86380-179-X, 1995.

[41] D.M. PARKER AND D.M. KERCHER: *An Enhanced Method to Compute the Compressible Discharge Coefficient of Thin and Long Orifices with Inlet Corner Radiusing.* Winter Annual Meeting of the ASME on Heat Transfer in Gas Turbine Engines, HTD Volume 188, 1991.

[42] O. POPP, J. KUTZ AND H. ZIMMERMANN: *CFD-Analysis of Coverplate Receiver Flow.* International Gas Turbine and Aeroengine Congress and Exhibition, Birmingham, UK, ASME 96-GT-357., 1996.

[43] M.J. POWELL: *A Fortran Subroutine For Solving Systems Of Nonlinear Algebraic Equations.* Rabinowitz P.: Numerical Methods For Nonlinear Algebraic Equations Gordon And Breach, 1970.

[44] M.J. POWELL: *A Hybrid Method For Nonlinear Equations.* Rabinowitz P.: Numerical Methods For Nonlinear Algebraic Equations Gordon And Breach, 1970.

[45] B.V. PRASAD AND AL.: *A combined CFD and flow network approach for the simulation of secondary air system of aero engines.* The 10th International Symposium on Transport Phenomena and Dynamics of Rotating Machinery, ISROMAC10-2004-128, 2004.

[46] E REILE AND E. EBERT: *Bridging the gap between structural and thermal analysis in aircraft engine design.* AIAA 2000-4782, 2000.

[47] S. ROYCHOUDHARY AND B. JLIDI: *Coupled Secondary air system - Heat Transfer - Structural analysis of a jet engine sealing application.* 17th International Symposium on Air Breathing Engines, Munich, Germany, ISABE 2005-1079, 2005.

[48] N. SCHOLZ: *Neuere Methoden zur Berechnung von Schaufelgitter.* Maschinenmarkt, 41&54, 1965.

[49] A. H. SHAPIRO: *The dynamic and thermodynamic of compressible fluid flow.* The Ronald press company, New York, vol. 1, 1953.

[50] P.D. SMOUT AND P.N.R CHILDS: *ICAS-GT: A european collaborative research programme on internal cooling air systems for gas turbines.* ASME TURBO EXPO 2002, Amsterdam, Netherlands, ASME GT2002-30479, 2002.

[51] R. STALLMAN: *The GNU Manifesto. Free Software Foundation.* www.gnu.org, 2007.

[52] E. TRUCKENBRODT: *Fluidmechanick Band1 Grundlagen ubd elementare Strömungsvorgänge dichtebeständiger Fluide. 2. Auflage.* Splinger-Verlag, Berlin Heidelberg New York, ISBN 3-540-09499-7, 1980.

[53] A.B. TURNER AND AL.: *A review of some current problems in gas turbine secondary air systems.* International Gas Turbine and Aeroengine Congress and Exhibition, Orlando, FL, USA, ASME 97-GT-325, 1997.

[54] UNIV. OF CALIFORNIA BERKELEY NAG LTD. COURANT INSTITUTE ARGONNE NATIONAL LAB UNIV. OF TENNESSEE AND RICE UNIVERSITY: *LAPACK driver routine (version 3.0).* FORTRAN GPL subroutine, March 31, 1993.

[55] A. VAZSONYI: *Pressure Loss in Elbow and Duct Branches.* Transactions of the ASME, april 1944, 1944.

[56] DÜSSELDORF. VDI: *VDI Wärmeatlas, 10. bearbeitete und erweiterte Auflage.* Berlin: Springer,ISBN 3-540-25503-6, 2006.

[57] J.A. VERDICCHIO AND J.W. CHEW: *Coupled Fluid/Solid Heat Transfer Computation for Turbine Discs.* ASME TURBO EXPO 2001, New Orleans, Louisiana, USA, ASME GT2001-0205, 2001.

[58] A.J. WARD-SMITH: *Internal fluid flow : The fluid dynamics of flow in pipes and ducts.* Oxford University Press, ISBN 0-19-856325-6, 1980.

[59] I. WEISSERT: *Numerische Simulation dreidimensionaler Strömungen in Sekundärluftsystemen von Gasturbinen unter besonderer Berücksichtigung der Rotation.* VDI Fortschrittsbericht, Reihe 7, Nr. 313., 1997.

[60] K. WILLENBORG AND S. KIM: *Effects of Reynolds Number and Pressure Ratio on Leakage Loss and Heat Transfer in a Stepped Labyrinth Seal.* ASME TURBO EXPO 2001, New Orleans, Louisiana, USA, ASME GT2001-0123, 2001.

[61] K.H. WOLFF AND H. ZIMMERMANN: *Air System Correlations Part 1: Labyrinth Seals.* International Gas Turbine and Aeroengine Congress and Exhibition, Stockholm, Sweden, ASME 98-GT-206, 1998.

[62] D.J. WOOD AND A.G. RAYES: *Reliability of algorithms for pipe network analysis.* Journal of the Hydraulic Division, ASCE,Vol. 107,No. HY10, 1981.

[63] H. ZIMMERMANN AND J. KUTZ: *Air System Correlations Part 2: Rotating Holes and Two Phase Flow.* International Gas Turbine and Aeroengine Congress and Exhibition, Stockholm, Sweden, ASME 98-GT-207, 1998.

[64] H. ZIMMERMANN AND K.H WOLFF: *Comparison between Empirical and Numerical Labyrinth Flow Correlations.* International Gas Turbine and Aeroengine Congress and Exhibition, Stockholm, Sweden, ASME 98-GT-206, 1998.

Coupled thermo-mechanical fluid-structure interaction in the secondary air system of aircraft engines: contribution to an integrated design method.

Yannick Muller

Résumé.

Dans un turboréacteur, le système d'air secondaire rempli de multiples fonctions. Les flux d'air secondaire contrôlent les températures des matériaux et l'expansion thermale des parties moteurs, en particulier les écartements des joints d'étanchéité. Pour s'assurer de la réalisation des diverses fonctions dès la phase de développement, les différentes propriétés du gas doivent être correctement prédites.

Actuellement, les calculs aérodynamiques, livrant les débits, les températures et les pressions d'air, sont séparés des calculs thermiques, livrant les températures matériaux. Les interactions dont le traitement nécessite de nombreuses itérations sont ignorées. En effet, un changement de température matériau modifie l'expansion relative des parties moteurs, redéfinissant ainsi l'écartement des joints qui à son tour contrôle les quantités d'air. La définition de l'écartement de joint influant de manière importante sur les pertes de charges, un fort effet de couplage est attendu.

Le but de l'étude est de prendre en compte ces interactions au sein d'un nouvel outil combinant analyse du système d'air secondaire, calculs thermiques et mécaniques. Une serie de modules integrés permet de considérer ces effets dans les cas stationnaires. Un reseau constitué de nodes représentant les chambres connectées par des élements assimilés à des pertes de charges constitue la base du concept. Utilisant une formulation compatible avec la topologie Elément Finis, le reseau est imbriqué dans le modèle Eléments Finis thermo-mécanique au sein d'un modèle unique et résolu grâce au logiciel CalculiX. Températures, pressions et débits de gas sont calculés, basés sur les températures et déformations matériau de l'itération précédente et servent de conditions limites au calcul thermo-mécanique dans l'itération suivante.

Mot-clés: turboréacteur, système d'air secondaire, réseau de fluide, couplage thermomécanique, méthode numérique.

Abstract.

In jet engines, the secondary air system, or SAS, takes care of a variety of important functions. In particular, secondary air flows control material temperatures and thermal expansion of engine parts, especially seal clearances. To check the fulfilment of these functions in the engine design phase, gas properties, temperatures, pressures and mass flow rates, must be accurately predicted.

Up to now, the aerodynamic calculations leading to mass-flow rates, fluid pressures and temperatures and the thermal calculations yielding material temperatures are performed separately. A lot of interactions are

neglected, the treatment of which would require numerous time consuming iterations. Indeed, material temperature changes lead to a modification of the expansion of the interacting parts yielding significant modifications in the gaps which control mass-flow rates. Since gap width has an important influence on the pressure losses, the interaction between aerodynamic, thermal and solid mechanics solution to the problem is expected to be important.

The present investigation aims at taking this interaction into account in a robust analysis tool, combining SAS, thermal and mechanical analysis. An integrated program suite has been created, which allows to calculate these effects steady state. The basic concept is a network consisting of nodes representing the chambers and connected by pressure loss elements. Using a finite-element-compatible formulation, the network is embedded in a thermomechanical finite element model of the engine within an unique model and solved using the free software finite element CalculiX. This is done in the form of a module in which the gas pressure temperature and mass-flow are calculated based on the structural temperature and deformation of the previous iteration and serve as boundary conditions to the thermomechanical model for the next iteration.

Keywords: jet engine, secondary air system, flow network, thermomechanical coupling, numerical method.